Fluid-Structure-Jet Interaction Effects on High-Speed Vehicles

by

Ryan C. Kitson

A dissertation submitted in partial fulfillment
of the requirements for the degree of
Doctor of Philosophy
(Aerospace Engineering)
in the University of Michigan
2018

Doctoral Committee:

Professor Carlos E. S. Cesnik, Chair
Associate Professor Karthik Duraisamy
Professor Peretz P. Friedmann
Associate Professor Eric Johnsen
Dr. Daniel A. Reasor Jr., Air Force Research Laboratory

Ryan C. Kitson

kitson@umich.edu

ORCID iD: 0000-0002-2568-2445

To my family

ACKNOWLEDGEMENTS

This dissertation would not have been possible without the support from so many people. First and foremost, I would like to thank my mother for her endless support. She was always there for me when things were challenging or when it was time to celebrate an accomplishment. I would like to thank all of my family for their encouragement as well.

Next, I would like to sincerely thank my advisor Prof. Carlos Cesnik. He first took a chance on me as an undergraduate student and continued to support me for the following seven years. I am very grateful for having had the opportunity to work with and learn from him. There is no doubt that I developed into the engineer, researcher, and person that I am today because of his advice and guidance.

I would like to thank Dr. Crystal Pasiliao and Dr. Daniel Reasor for their mentorship and funding support. I appreciated the opportunity to develop professional and personal relationships with them and the AFRL engineers at Eglin. I also would like to thank my dissertation committee, Prof. Duraisamy, Prof. Friedmann, Prof. Johnsen, and Dr. Reasor for all of their help to develop a quality dissertation.

The journey through graduate school would not have been the same without the friendships that I made along the way. A special thanks to Dr. Ryan Klock for being a great mentor and friend both in Florida and Michigan. Thank you to Dr. Jessica Jones, Dr. Ziyang Pang, and Chris Lupp for all of their help and friendship. Thank you to all of the current and former A2SRL members for their friendship that made the lab feel like a home away from home. I also need to thank the many friends that I had during my time in Florida. Especially, Emily Dreyer and Michael Sparapany who helped make those summers fun and unforgettable.

This material is based on research sponsored by Air Force Research Laboratory under agreement number FA8651-13-2-0007 with Dr. Crystal Pasiliao and Dr. Daniel Reasor as technical monitors. The U.S. Government is authorized to reproduce and distribute reprints for Governmental purposes notwithstanding any copyright notation thereon. The views and conclusions contained herein are those of the authors and should not be interpreted as necessarily representing the official policies or endorsements, either expressed or implied, of Air Force Research Laboratory or the U.S. Government. The numerical results were obtained primarily using the High Performance Computing Modernization Program DoD Supercomputing Resource Centers.

TABLE OF CONTENTS

LIST OF FIGURES

LIST OF TABLES

LIST OF ABBREVIATIONS

AoA	Angle of Attack
AoS	Angle of Sideslip
ARMA	Autoregressive Moving-Average
CFD	Computational Fluid Dynamics
DACS	Divert and Attitude Control System
DMD	Dynamic Mode Decomposition
EDSD	Explicit Design Space Decomposition
FSI	Fluid-Structure Interaction
FSJI	Fluid-Structure-Jet Interaction
HSV	High-Speed Vehicle
JI	Jet Interaction
LES	Large Eddy Simulation
MAE	Median Absolute Error
POD	Proper Orthogonal Decomposition
PR	Ratio of jet total pressure to free-stream static pressure
RANS	Reynolds-averaged Navier–Stokes
RBD	Rigid-Body Dynamics
ROM	Reduced Order Model
SA	Spalart–Allmaras
SVD	Singular Value Decomposition
SVM	Support Vector Machine
UM/HSV	University of Michigan's High-Speed Vehicle Simulation Framework

LIST OF SYMBOLS

A	System matrix
A_0	Amplitude of F_s applied to the mass-spring system
A_1	Amplitude of F_s deviation away from equilibrium applied to the mass-spring system
A_{ref}	Vehicle reference area, m^2
AoA	Angle of Attack, deg
AoS	Angle of Sideslip, deg
C	Speed of sound, m/s
$\bar{C}$	Damping matrix of the aeroelastic system
C_D	Drag coefficient
C_L	Lift coefficient
C_M	Moment coefficient
C_X	Axial force coefficient
C_Y	Side force coefficient
C_Z	Normal force coefficient
E	Energy per unit length of the jet, J/m
F	Flight conditions (e.g., Mach, Altitude, and Angle of Attack)
F_j	Force component due to jet thrust, N
F_{ji}	Force component due to jet interaction, N
F_s	Force applied to the mass-spring system
H_i^j	Step response corresponding to load j and input i
I	DACS Impulse

J	Jet parameters (total pressure of the attitude and divert jets)
J_0	Blast wave constant
$\bar{K}$	Reduced stiffness matrix of the structural system
K_F	Jet interaction amplification factor of quantity F
L_{ref}	Vehicle reference length, m
$\bar{M}$	Mass matrix of the aeroelastic system
M	Mach number
Q	Generalized forces of the aeroelastic system
R	Shock front distance from the blast origin, m
R_0	Blast characteristic length, m
S	Structural parameters
S_{ref}	Reference Area, m^2
T	Temperature, K, or time period, s
U	Wave propagation velocity, m/s
U_∞	Freestream velocity, m/s
X	Training points for the co-Kriging model
Y	SVD modal amplitudes at the training points for the co-Kriging model
Y_k	Output time history for ARMA modeling
Z	Gaussian process
a	Speed of sound, m/s
b_e	Jet nozzle exit diameter, m
c_s	Damping of the mass-spring system
d	Difference of the cheap and expensive functions quantity
f	Frequency, Hz
f_c	Nonlinear correction factor
h_f	Height of the equivalent forward facing step due to jet interaction, m
h	Normalized grid spacing

h_s	Jet terminal shock height in the free-stream, m
i	Free-free vibration mode index ($i = 1 \ldots n$)
k	Step response time index, 1...n
$\bar{k}$	Reduced frequency, $\frac{\omega L_{ref}}{U_\infty 2}$
k_s	Stiffness of the mass-spring system
m	Total number of structural mode shapes
m_s	Mass of the mass-spring system
n	Total number of time steps
p	Pressure, Pa
$\bar{p}$	Normalized pressure, $\frac{p-p_\infty}{p_\infty}$
p_{0a}	Attitude jet total pressure, Pa
p_{0d}	Divert jet total pressure, Pa
p_b	Back pressure behind the jet, Pa
p_e	Jet exit pressure, Pa
p_{p_1}	First plateau pressure due to a forward facing step, Pa
p_{p_2}	Second plateau pressure due to a forward facing step, Pa
q	Dynamic pressure, Pa
t	Time, s
t_d	DACS time duration
u	Model input
$\bar{u}$	Displacement vector
u^i	Model input corresponding to input i
w	Surface velocity perpendicular to the flow
x	Downstream distance from the jet, m
$x^{(n+1)}$	Co-Kriging next evaluation point
x_s	Oblique shock location due to boundary layer separation, m
x, y, z	Body-fixed axes with x positive aft, y positive right, z positive up

y	Linear model output
$\hat{y}$	Approximate model output
$\hat{y}^j$	Linearized model output corresponding to load j
$\hat{y}^{ss}_{linear}$	Linearized model steady-state output
$\hat{y}^{ss}_{nonlinear}$	Nonlinear steady-state model output
y^+	Dimensionless wall distance
Δ	Change in quantity
Φ	Free-free vibration mode
Ψ	Correlation function
α_s	Deflection angle required to achieve the pressure ratio p_{p_1}/p_∞, rad
β	Rigid body translational velocity vector
γ	Flight path angle
γ_e	Jet exit ratio of specific heats
δ	Offset term of the nonlinear correction factor
δ_1	Attitude jet total pressure, % maximum
δ_2	Starboard divert jet total pressure, % maximum
δ_3	Port divert jet total pressure, % maximum
ζ	Rigid body rotational velocity vector
η	Generalized structural degree of freedom
η_s	Displacement of the mass-spring system
η_1	Lateral first bending mode deformation, % tip deflection
η_2	Longitudinal first bending mode deformation, % tip deflection
ϕ	JI ROM rotation angle
θ	JI ROM rotation angle
μ	Process mean
ρ	Density
ρ_z	Co-Kriging tuning parameter

σ	Configuration parameter, ratio of configuration 1 to 2
σ^2	Process variance
ω	Circular frequency

Subscripts

$_0$	Flow total quantity
$_\infty$	Freestream quantity
$_c$	Cheap function quantity
$_e$	Expensive function quantity
$_j$	Jet quantity
$_{ji}$	Jet interaction quantity
$_{i,j}$	Matrix row and column indexes

Superscripts

$\dot{}$	Time derivative
$\ddot{}$	Second time derivative
$\hat{}$	Fourier transform
$\tilde{}$	Approximate or previously unsampled quantity

ABSTRACT

This dissertation is focused on two design considerations for supersonic intercept missiles: (i) increased structural slenderness and (ii) attitude control jets. The resulting new designs have the potential to increase vehicle performance, but will lead to a coupled fluid-structure-jet interaction that has yet to be studied. Numerical results of the vehicle response across the design space and flight envelope can be used as guidelines for assessment of improved control effectiveness, maneuverability and agility.

First, vehicle models are developed that include slender structures and attitude control jets to conduct flight simulations. The numerical analysis of fluid-structure-jet interaction using these vehicle models provides insight into how this interaction can be leveraged during the design to improve performance.

Next, approximate methods for including jet interaction effects are developed for slender high-speed vehicles. These methods allow for more complex geometry, a range of flight conditions, and varying control inputs. The jet interaction models are developed for flight simulation to maintain accuracy without significant computational cost.

A detailed computational model of the maneuverable vehicle with fluid-structure-jet interaction is created to study the sensitivity to changes in flight conditions. These steady and dynamic results of the nonlinear system identify the conditions that may be difficult to model as well as those that can be exploited for improved performance.

Next, modeling methods for the fluid-structure-jet interaction dynamics in flight are developed and evaluated using aggressive maneuvers throughout the flight envelope. Previous methods are evaluated to identify their effectiveness and a new method

is developed specifically to model the nonlinear vehicle response to aggressive maneuvers.

Finally, fluid-structure-jet interaction effects introduced by a slender missile body and attitude control jets are modeled during flight simulations. Multiple vehicle configurations are considered and the simulation results demonstrate the corresponding design modifications can impact vehicle maneuverability and agility.

Overall, this dissertation explores a new topic in fluid-structure-jet interaction that arises due to new design trends that seek to improve intercept missile performance. New modeling methods were developed to analyze the problem and numerical simulation results identify regions where the fluid-structure-jet interaction significantly affects the vehicle response.

CHAPTER 1

Introduction

This chapter begins with the motivation to analyze fluid-structure-jet interaction of HSVs. A literature review is presented that begins with the current state-of-the-art of HSVs, then goes into the multidisciplinary analysis that can be involved. Fluid-structure interaction and jet interaction with a supersonic crossflow are the primary topics that are included in this dissertation leading to coupled fluid-structure-jet interaction. Additional review of the current reduced order modeling and simulation methods for HSVs is presented. Finally, the dissertation objectives based on the open questions in the literature are presented along with an overview of the content of each chapter.

1.1 Motivation

HSVs used for air-to-air intercept scenarios require a high level of performance in terms of maneuverability, accuracy, and agility to be successful. In addition, a missile that is effective under a wide variety of flight conditions and scenarios is required. Various design trends of HSVs are evident in the literature that have specific impacts on missile performance. Short and medium range air-to-air missiles typically have a slender fuselage with some configuration of control fins used to maneuver the missile within the atmosphere. High-altitude intercept missiles use divert and attitude control jets instead of control fins to maneuver the missile in exo-atmospheric conditions.

Each missile type is well-designed for its respective objective, but a missile that is versatile for both low and high altitude operation might require some combination of the two configurations. Each of the design trends of increased missile slenderness and attitude control jets have the potential to add to the HSV design capabilities. If the slenderness of the missile was increased further, then more missiles could be stored per launcher thereby increasing the capability of the launching aircraft. Adding attitude control jets would maintain control effectiveness at high altitudes and high angles of attack. However, each of these design trends adds complexity and an additional interaction to the system.

Attitude control jets have been previously studied as effective control actuators for flight vehicles due to their control authority at very high altitudes [5], high angles of attack [6], severe aerodynamic heating [2], and fast response times (on the order of milliseconds) [7, 8] compared to conventional control surfaces. In exo-atmospheric conditions, the applied force from the jet is equivalent to the thrust in vacuum, but within the atmosphere there is an interaction between the jet and the freestream flow. This problem is known in the literature as *jet-in-crossflow* or *jet interaction* and occurs in applications beyond flight vehicles. The Jet Interaction (JI) with a supersonic crossflow has been shown to be sensitive to flow parameters such as angle of attack, Mach number, jet total pressure, vehicle geometry, and others [6]. The net effect of JI can either amplify the applied thrust or lead to a control reversal [6], which is motivation for accurately includes these effects during vehicle flight simulations.

Intercept missiles operate in a highly dynamic environment while performing aggressive maneuvers to complete their mission. Modeling and simulation of the vehicle dynamics is critical to accurately predict vehicle performance. Several methods exist for modeling flight vehicle dynamics, but have not been tested for coupled fluid-structure-jet interaction. In addition, there is relatively less known regarding the transient jet interaction response to changes in flight conditions. A method for mod-

eling vehicle dynamics due to transient variations in the flight dynamics, structural deformation, and control jet inputs will need to be developed that accounts for aggressive maneuvers and the variation of flight conditions across the flight envelope.

Fluid-Structure-Jet Interaction (FSJI) arises at the intersection of two maneuverable HSV design trends — the trends of increased vehicle slenderness and attitude control jets. Very slender vehicles improve the vehicle aerodynamics and launcher load-out, but add flexibility to the system. Attitude jets maintain control effectiveness in extreme conditions, but add a complex pressure distribution that may reduce its effectiveness. The complex FSJI effect on vehicle performance is unknown, but the combined effect has the potential to be greater than the sum of each design trend individually. The Fluid-Structure Interaction (FSI) problem and JI with a supersonic crossflow problem are well-developed areas of research. However, the JI with a flexible structure has not been studied and the coupled effect on the flight vehicle dynamics is unknown. The objective of this research is to investigate the effect of FSJI on HSV performance.

The following sections present a summary of the state-of-the-art regarding fluid-structure interaction, jet interaction, and reduced order modeling as it applies to maneuverable HSVs. Research objectives based on the state-of-the-art are developed that address the open research questions that arise due to the coupled FSJI. Finally, an overview of the dissertation is given that addresses these objectives.

1.2 Overview of Maneuverable Intercept Missiles

This dissertation is focused on the modeling, simulation, and analysis of maneuverable supersonic intercept missiles. In general, these vehicles have various combinations of a slender body, wings, control fins, attitude and divert control jets, and main engines for thrust. These missiles can be launched from land or sea and the flight profile can vary

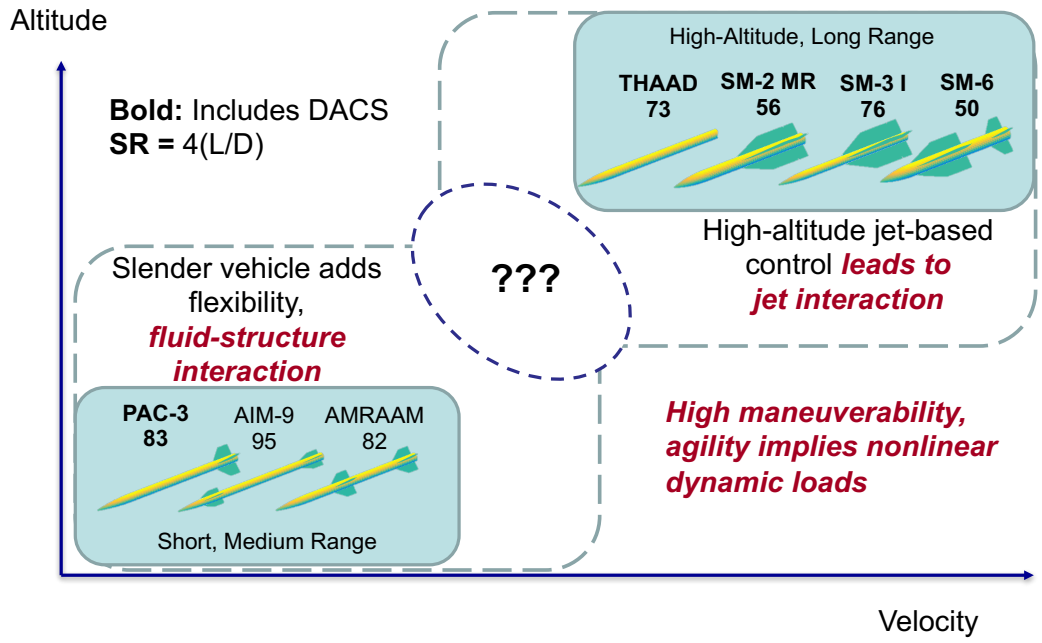

Figure 1.1: Intercept HSVs overview highlighting (**bold**) those that include DACS and slenderness ratio SR, where: $SR = 4 \times (Length/Diameter)$.

significantly in altitude and duration based on the configuration and vehicle design. Finally, there is a terminal phase that typically includes some maneuvers to hit the target. The terminal phase maneuver may be one smooth trajectory that requires significant maneuverability or a series of small adjustments that requires superior agility. Examples of short, medium, and long range intercept HSVs are shown in Figure 1.1. The slenderness ratio is shown along with each vehicle calculated by the length divided by the radius of gyration. For a solid cylinder the radius of gyration, the square root of area moment of inertia divided by cross-sectional area, is the diameter divided by four.

Short range missiles, such as the AIM-9 shown in Figure 1.2, tend to focus on the terminal phase of flight and emphasize design trends that maximize agility. For example, short range missiles within the atmosphere use multiple sets of control fins for rapid modifications to the flight trajectory. In addition, these short range flights do not require a booster or staged flight configuration and are typically designed with

Figure 1.2: Front view of the AIM-9 Sidewinder air-to-air missile. Source: U.S. Air Force.

a single body construction. These short range missiles are most often launched from land or air platforms, which leads to more consideration of total weight and volume of the design.

One medium range missile example is the AMRAAM, which is shown being launched from an F-35 aircraft in Figure 1.3. Medium range high-speed vehicles are similar to the short range configurations with single body construction. The AMRAAM and the AIM-9 are shown together in Figure 1.4 for reference. However, a trade for maneuverability in favor of agility is made with fixed wings that might replace a set of movable control fins. In addition, the vehicles are often long and slender to accommodate additional fuel needed for longer duration flights.

Long range missiles are typically larger in every dimension than the short and medium range ones. The larger configuration is often to accommodate more fuel and leads to a staged configuration where the booster is ejected mid-flight and the payload is equipped with sensing and control to maneuver during the terminal flight

Figure 1.3: Medium range AMRAAM missile launch from an F-35 aircraft. Source: Raytheon.

Figure 1.4: U.S. Airman inspecting an AMRAAM with a AIM-9 in the background. Source: U.S. Air Force photo by Samuel King Jr.

phase. Long range missiles are primarily launched from sea or land-based platforms and operate at high altitudes with low density, which corresponds to less drag and aerodynamic heating at similar Mach numbers. High altitude operation also leads to a change in control actuator from fins to a reaction control jet system due to the lack of dynamic pressure at very high altitudes where the jet thrust maintains control effectiveness compared to the fins. The SM-3 is an example of a long range vehicle used for ballistic missile defense and is shown being launched at sea in Figure 1.5.

Maneuverability and agility are two metrics that are key to HSVs mission success in addition to accuracy and precision. These two qualities can be quantified according to Bitten [9] using multiple quantities of the vehicle response including velocity and the flight path angle. The maneuverability in this work is calculated using the vehicle acceleration normal to the flight path and the time rate of change of the flight path angle. The vehicle agility is calculated using the second time derivative of the flight path angle.

Figure 1.5: Long range SM-3 launch. Source: Missile Defense Agency.

1.3 Fluid-Structure Interaction Effects on Missiles

Aeroelastic analysis of missiles has primarily focused on the vehicle stability under various conditions. However, the long and slender construction of the short to medium range missiles may introduce additional flexibility that leads to significant deformation under applied aerodynamic loads and control inputs. These control inputs include, but are not limited to, the control fins, main engine thrust, vectored thrust, attitude and divert control jets. In addition, missiles are typically classified as spin or fin-stabilized, which refers to a vehicle rotating about the center line to stabilize flight or a non-rotating vehicle with external control surfaces to stabilize flight, respectively.

Adding flexibility could potentially improve vehicle performance compared to a rigid structure. Costello and Argarwalla [10] show how introducing a hinge near the nose could lead to a passive control mechanism that improved stability, but did not address any other hinge locations or multiple hinges similar to a continuous structure. Youn and Silton [11] presents the improved control effectiveness of a bent body compared to a straight or canard-controlled body. These results motivate further research into flexible vehicle dynamics for improved performance.

Although flexibility may lead to larger pitch moments or passive stability, it may result in less precise missile. Yao, Wu, and Yang [12] present an aeroelastic analysis of maneuvering flexible vehicles and the effects of varying vehicle flexibility. Numerical results in this study compared a closed-loop intercept scenario and system-level quantities such as time-to-target and miss-distance between multiple mass and stiffness values of the vehicle. The results suggested that the control effort and vehicle performance are significantly affected by structural stiffness, but this study used constant coefficients with respect to angle of attack and sideslip for the aerodynamic forces and only one particular mode shape was used for the calculations.

The structural degrees of freedom must be accounted for during stability analysis as well as flight simulation of slender high-speed vehicles. Crimi [13] considers the

aeroelastic stability of a high-speed vehicle over a range of flight conditions using a quasi-steady aerodynamics model with finite element structural model. The results show that flutter and divergence were possible instabilities depending on the vehicle spin rate and structural flexibility in addition to the flight conditions. Platus [14] examines the coupling between rigid-body and aeroelastic degrees of freedom of a spinning missile and presented the governing equations of motion. The results in [14] showed that the spinning flexible missile becomes unstable with increasing spin rates and higher structural damping. As flexibility is introduced to improve performance, stability must be considered as well to develop a viable vehicle.

In addition, the effect of control inputs should be considered along with adding flexibility to the missile system. Beal [15] develops an analytical model of the flexible vehicle with an end thrust and presents the stability regions that occur with a constant and pulsating thrust and thrust vectoring. The end thrust caused a change in the frequencies of the rigid-body and flexible modes of the system based on the pulse frequency from the control input, which lead to regions of stability and instability based on total thrust and thrust variation frequency. Chae and Hodges [16] add the aerodynamic effect to the end-thrust problem with a flexible structure to find the critical thrust value of a conventional configuration with control surfaces. The results in [16] show a variation in stability based on the Mach number in addition to the thrust value.

The previous aeroelastic analysis of high-speed vehicles has underscored the need for coupled analysis for studying their stability and performance. However, the previous work has utilized more fundamental aerodynamic models such as slender-body theory or linear coefficient aerodynamics. More detailed analysis would be required as the maneuverability and agility of the vehicle increase, which introduce nonlinear effects due to higher body angles of attack and large angular rates. JI with the external flow is also nonlinear and highly dependent on the flow direction relative to

the jet nozzle exit (i.e., windward or leeward facing). This nonlinearity in addition to the various other parameters such as flight conditions, structural flexibility, and jet conditions that could lead to significant changes in performance.

1.4 Jet Interaction with Supersonic Crossflows

Jet interaction with a supersonic crossflow is composed of a dominant flow interacting with a jet flow that is typically perpendicular or near-perpendicular to the freestream flow with a high pressure and velocity. In this dissertation, the JI problem refers to a control system composed of small actuated jets that produce thrust to maneuver a slender high-speed vehicle. The jet flow is perpendicular to the supersonic freestream flow, which causes an interaction near the jet exit and additional forces applied to the vehicle. This jet-based control system can either replace or add to existing control actuators such as control fins as shown in Figure 1.6.

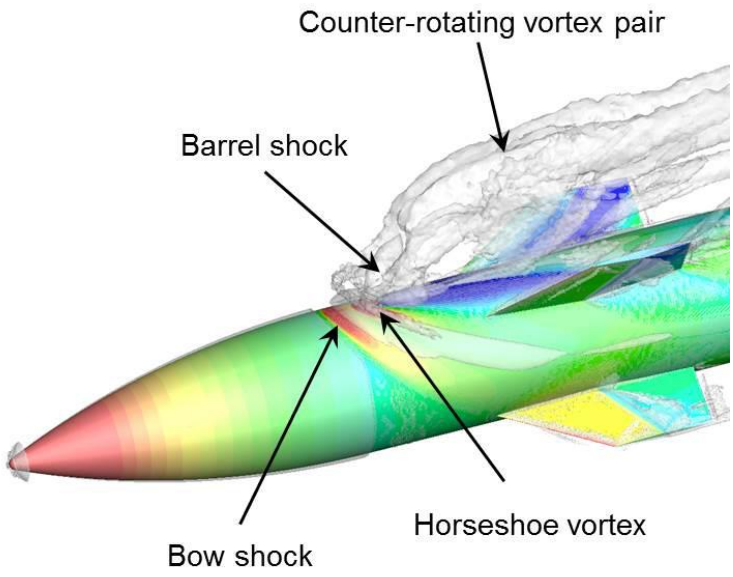

Figure 1.6: Detached eddy simulation results by VanderWyst, Shelton, and Martin [1] the attitude jet interaction with a supersonic flow on a finned vehicle.

There is a flow discontinuity that must be resolved due to the different flow condi-

tions between the jet and freestream. This usually results in boundary layer separation and vortex shedding around the jet exit in subsonic and supersonic flight regimes. In supersonic flow, there are shock waves and expansion waves that form as a result of the freestream flow diverting around the jet flow. This combination of compressibility and turbulence leads to a complex interaction that is difficult to predict based on the flow and jet conditions. Experiments or high-fidelity computations are needed that capture all of these JI effects to analyze resulting flow structure and the net force applied to the vehicle. A diagram of the main JI flow structures is shown in Figure 1.7 and a snapshot from a dynamic computational result is shown in Figure 1.8 with the flow shocks, boundary layer, and vorticity.

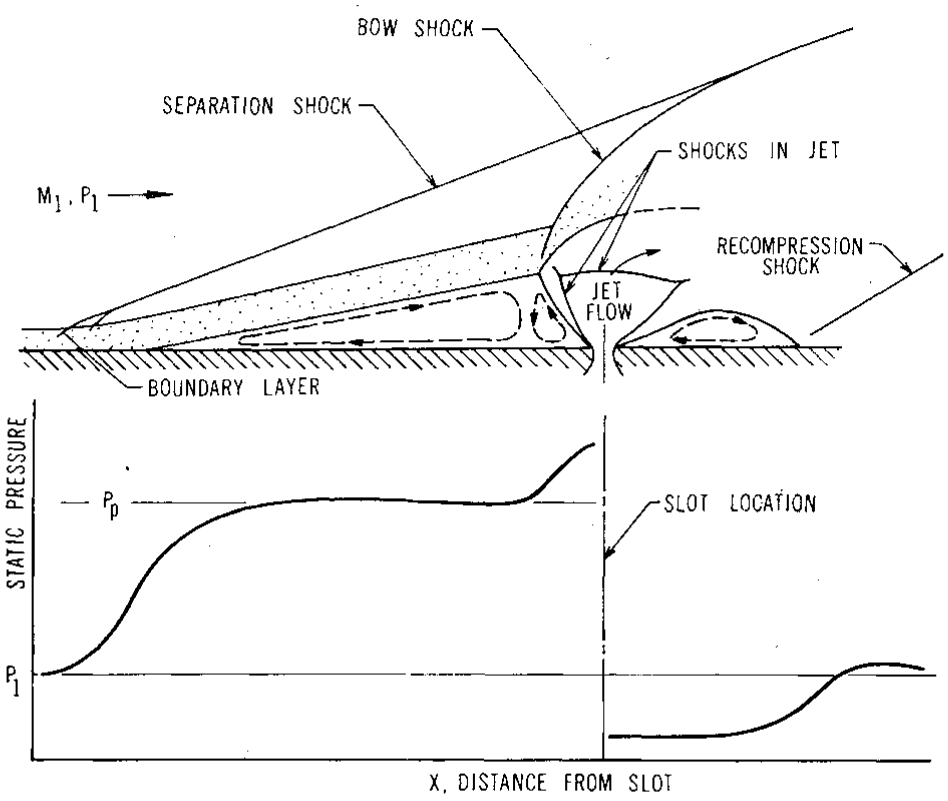

Figure 1.7: Diagram by Spaid and Zukoski [2] of jet interaction with supersonic crossflow highlighting the main flow structures.

Previous experimental studies have been conducted regarding the JI with a supersonic crossflow and the characteristic steady-state flow condition has been well

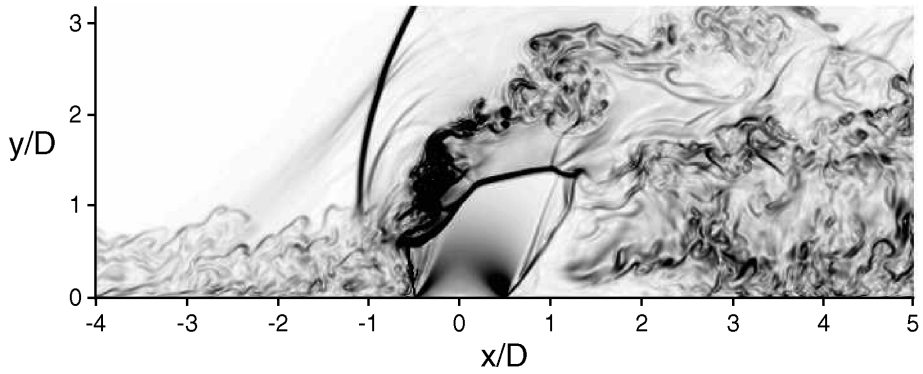

Figure 1.8: Large eddy simulation results by Kawai and Lele [3] of the density gradient magnitude from jet interaction with supersonic crossflow showing the flow structures including shocks and vortex shedding.

documented. Spaid and Zukoski [2], Spaid and Cassel [5], and Zukoski and Spaid [17] experimentally identify the flow structure and developed preliminary models for the interaction. These results also identify the potential increase in jet control authority due to the supersonic flow interaction, which could be leveraged to improve vehicle maneuverability.

Roger [6] summarizes the JI literature of the previous 50 years, collected the common trends and critical parameters, and highlighted the remaining challenges. One of the challenges was the sporadic approach to the problem throughout the literature and a lack of a common methodology that could be used for multiple vehicles, flight conditions, and jet conditions. Another important issue noted by Roger [6] is the "jet-on jet-off transients issue," which refers to the fluid dynamic response as a result of pulsed or throttled jet flow. This summary motivates further research that compares multiple vehicle configurations with more emphasis placed on the jet interaction transient response.

1.4.1 Analytical and Empirical Modeling

Previous work on modeling JI with a supersonic crossflow extends back before computing resources were advanced enough to tackle the problem. Various empirical and theoretical modeling efforts have been made to correlate the flow and jet conditions to the flow velocity or surface quantities [18, 19, 20, 21].

Early experimental results yielded a scaling parameter that is presented by Zukoski and Spaid [17]. This scaling parameter could be used to correlate the jet penetration height into the flow and jet parameters. Experimental results show very good correlation with the scaling parameter and the work is extended to calculate a similar scaling parameter for the total force on the wall. Then, Spaid and Zukoski [2] develop an analytic model based on the characteristic structure of the JI experimental results. The analytic model involved creating a control volume for the jet flow to then calculate useful quantities such as the pressure upstream of the jet as well as the jet penetration height into the flow and amplification factor.

The amplification factor is a useful quantity to measure the relative effect of the JI to the jet thrust and it has been used throughout the JI literature [2, 5, 6, 22]. The jet amplification factor K for quantity F is calculated as,

$$K_F = \frac{F_j + F_{ji}}{F_j} \tag{1.1}$$

where F_j corresponds to the contribution from the jet thrust alone, F_{ji} is the contribution of the interaction with the external flow. An amplification factor greater than 1 indicates that the loads due to jet interaction amplifies the net forces and moments, less than 1 indicates a reduction in the net forces and moments, and less than 0 indicates control reversal. This quantity is used throughout the dissertation to quantify the jet interaction effect on the vehicle model.

Later results are tied to more complex flow quantities of interest, such as Young

[20] that presents a solution procedure to calculate the boundary layer separation distance and amplification factor. These amplification factor results compare well to previous experiments including Spaid and Zukoski [2]. The whole two-dimensional JI flow structure can be modeled following Werle, Driftmyer and Shaffer [19] using a series of flat plate experiments. The model presented by Werle, Driftmyer and Shaffer [19] calculates the surface pressure distribution due to the characteristic JI features such as boundary layer separation, normal shock, flow turning, and re-compression shock by relating the various flow and jet parameters.

The previously discussed results are primarily focused on the flat plate results and the longitudinal jet plane, which neglects the three-dimensional effects. Broadwell [23] includes the three-dimensional effects by considering JI and the resulting shock formation similar to the propagation of a blast wave due to a high energy explosion. The blast wave propagation in air had been developed previously by Taylor [24] and Sakurai [25, 26] for intense explosions. Broadwell [23] then considers the blast wave to propagate with the free-stream flow to calculate shock wave propagation downstream between the jet flow and free-stream flow. The model developed by Broadwell [23] compares well with experiments when calculating the total force applied to the plate by the JI.

Overall, the previous work in JI analytic modeling has been shown to correlate well with experimental results for integrated quantities or two-dimensional pressure distributions, but a three-dimensional analytic model would still be needed when considering more complex geometries and varied flow conditions.

1.4.2 Computational Modeling

Detailed computational modeling has the ability to simulate the JI problem for complex geometry, flow and jet conditions [27, 28, 29, 30, 31, 32, 33, 34, 35]. Cassel [36], Demuren [21] and Margason [22] all review the numerical modeling approaches and

results that focus on solving the governing equations for the jet-in-crossflow problem. Cassel [36] summarizes the computational literature on JI with supersonic crossflow along with experimental and flight test results. Cassel [36] notes that JI analysis using computational methods introduces additional complexity such as turbulence modeling, mesh refinement, and shock-capturing that are critical to the solution. Vehicle simulation models including jet interaction must be sensitive to these compressible and turbulent effects in the flow to accurately model the resultant loads.

Warfield [27] compares the numerical simulation results to experiments and noticed that the turbulence model had a significant effect on the predicted flow separation region. DeSpirito [30, 33] investigates this turbulence modeling issue further by comparing several available models to experimental results for flat plate experiments and axisymmetric vehicles for varying flow and jet conditions. The numerical results of DeSpirito [30, 33] demonstrate the wide variance between turbulence models in the ability predict the separated flow around the jet nozzle exit. In addition, there was not a consistently accurate model across all test cases, which adds to the complexity of JI numerical modeling.

Several research studies [37, 3, 38] have used a Large Eddy Simulation (LES) approach to more accurately model the turbulence in the flow and capture the vortex shedding, shear layer and barrel shock among other JI features. Despite capturing these effects, one major conclusion was that the turbulence level of the inflow conditions had a significant impact on the solution. The computational studies of JI have shown that it is possible to match the experimental conditions, but it is difficult to know what computational method is suitable *a priori*. In addition, these methods are computationally expensive and would be prohibitive for studying early design iterations of a vehicle.

Computational modeling also highlights important phenomena such as the jet transient forces [7, 8, 34]. It is critical to understand the dynamics of the JI with

varying flow and jet conditions considering a maneuverable vehicle in a dynamic flight environment. Some experimental and computational work has focused on the transient issue of firing a jet into a supersonic crossflow. Randolph, Chew, and Johari [39] fired a pulsating jet into a crossflow and noted a significant difference in the penetration of the jet into the crossflow to improve mixing in combustion applications. Experimental results by Naumann et al. [8] show significant oscillation in the applied forces due to the JI effect, which would become critical to model during vehicle maneuvers with varying jet thrust. Ebrahimi [7] also presents the oscillation and variation of the resultant JI forces and moments due to turning the jet on and off with a characteristic time to develop the steady state on the order of milliseconds. LES results of the supersonic JI problem by Génin and Menon [40] show unsteadiness in the flow field itself with large-scale vortices from the windward side of the jet leading to significant deviations from the time-averaged flow. DeSpirito [34] examines the transient behavior of the JI with a full vehicle model and the results show that the integrated forces reach the steady-state value before the pressure distribution. This effect can be neglected for rigid flight vehicles, but the pressure distribution is critical to calculating the structural response. These transient results in combination with the findings by Roger [6] emphasize the need for more understanding of the jet interaction dynamics as wells as modeling methods for these effects.

The transient jet interaction effects on vehicle flight response are observed in computational work by Sahu, Fresconi, and Heavey [29]. Flight simulations of a rigid projectile with control jets are completed with a coupled Computational Fluid Dynamics (CFD) and rigid-body dynamics model. The total angle of attack is below 20 degrees at Mach 2, the pulsed time is short (2-20 ms) and the total flight time was limited to one second. The jet was fired once with varying initial angular rates and showed the control authority to divert the projectile from its path. An aerodynamic and jet interaction model is developed by Sahu et al. [29] that compared favorably to

the coupled CFD/Rigid-Body Dynamics (RBD) flight simulation results. The authors conclude that the JI had a significant effect on the projectile trajectory and further study would be required to ensure the accuracy of the projectile. However, the jet effects are incorporated using the integrated force and moment amplification factors, which does not directly include the pressure distribution due to jet interaction. The pressure distribution would be required for aeroelastic analysis to model the correct load distribution and resulting structural deformation.

Previous research regarding the JI with a supersonic crossflow for high-speed vehicles has demonstrated a variety of trends enabled by numerical simulation using CFD. DeSpirito [33] and Graham and Weinacht [28] used computational modeling to investigate a wide variety of vehicle design choices such as surface geometry, jet location, and jet nozzle-exit-to-throat ratio. The numerical results by DeSpirito [32] of the lateral JI with the Army-Navy Basic Finner model demonstrate how the total applied force is strongly dependent on the jet location as well as the proximity to the fins. Cassel [36] alludes to this in a review of JI technology as well. Therefore, the prevailing wisdom has been to place the attitude control jets at the tail end of the vehicle to remove the low-pressure expansion region from the vehicle surface, maintain the high pressure region, and maximize the applied moment to the vehicle.

Computational analysis continues to further the understanding of JI, but the computational cost increases and robustness decreases as the modeling methods become more complex. The majority of JI analysis has focused on steady-state flow and jet conditions with a rigid vehicle. Additional considerations are required for the vehicle control applications such as the intermittent pulsing of the jet, the vehicle attitude, and vehicle dynamics that all affect the flow and resulting JI. In addition, slender high speed vehicles have added flexibility that will lead to FSI due to larger structural deformations under large aerodynamic loads.

These results and intuition have been developed with rigid vehicle models or con-

sidering each physical domain separately. A vehicle model that includes structural degrees of freedom in addition to the JI effect is needed to fully understand the impact on slender vehicle performance and stability with attitude control jets. If the attitude control jet was placed at the tail of the vehicle, then the applied moment would cause a structural deformation that decreases the control effectiveness. However, if the attitude control jet is located near the nose of the vehicle the attitude jet would cause a favorable structural deformation. If the jet location is intelligently chosen, then the high and low pressure regions of the JI could both have a favorable impact on the vehicle deformation that mitigate the loss in effectiveness due to the low pressure region.

1.5 Reduced Order Modeling and Simulation of Fluid-Structure-Jet Interaction

The ROMs used in this work are focused on modeling the loads applied to the vehicle due to aerodynamics, structural dynamics, and jet interaction with the external flow. Several different approaches have been used in the literature to develop ROMs for this application with varying levels of accuracy, robustness, and computational cost. The aerodynamics and jet interaction dynamics are nonlinear, which requires more complex modeling approaches. The flight dynamics of the vehicle are also nonlinear and the interaction with the fluid and jet dynamics could lead to a complex interaction for developing a ROM. Another complication is the time-dependence of the HSV applied loads and the dynamic environment due to a maneuvering vehicle. Unlike other aerospace vehicles that operate in a steady cruise regime for long time periods, the trajectory of an HSV may not be known *a priori*. This implies that the domain for computational modeling cannot be significantly reduced to near-cruise conditions.

High-fidelity multidisciplinary analysis tools, such as Kestrel [41], are available to

analyze maneuvering flexible vehicles. However, these tools have a high computational cost, complexity and possible robustness issues. For example, Sahu et al. [29] analyzed the effect of jet interaction on a free-flight projectile by coupling the RBD to the CFD solution, but the simulation times are limited by the computational resources. A long duration flight simulation capability with jet interaction is required to understand the jet effect on vehicle performance.

A modeling approach is required that reduces the computational cost of approximating the vehicle loads due to jet interaction. Reduced order modeling based on high-fidelity solutions is an effective way to capture the relevant physical phenomena and couplings of the full problem while significantly reducing computational cost and complexity and increasing computational robustness. Reduced order aerodynamic models have been shown to achieve a high level of accuracy with a low computational cost [42, 43, 44] and can include the jet interaction effects as well. VanderWyst et al. [45] developed a ROM approach to approximate the vehicle loading due to aerodynamics and jet interaction. This ROM approach to modeling the jet interaction is able to predict the vehicle pressure distribution and can be extended to include a variety of input degrees of freedom such as structural deformation. VanderWyst et al. [1] presented the use of a multi-fidelity method known as co-Kriging to develop a surrogate jet interaction model for a high-speed vehicle based on solutions of the Euler and Reynolds-averaged Navier–Stokes (RANS) equations. This multi-fidelity approach can potentially be extended to the jet interaction problem itself by leveraging the analytic models and the high-fidelity computational models. Reduced order modeling frameworks that couple the aerodynamic and structural ROMs for unsteady aeroelastic problems have been used for vehicle design [46, 47], but these frameworks are not configured to the extreme flight conditions a maneuvering vehicle might experience (e.g., large flow incidence angles and high angular rates). A reduced order modeling framework presented by Klock and Cesnik [48] couples the ROMs of

various disciplines to simulate the flexible vehicle flight response and is modified for this study to include a jet interaction capability for the DACS.

There is a significant number of previously developed unsteady aerodynamics modeling methods that can be applied to the current fluid-structure-jet interaction problem of a slender high-speed vehicle. One approach is to use linear convolution with the vehicle step or impulse response to approximate the loads with an arbitrary input during flight simulations [49, 42]. The linear convolution technique breaks down as the arbitrary input becomes significantly larger than the training step input, which is why Skujins and Cesnik [42] implemented a nonlinear correction factor based on nonlinear steady-state analysis *a priori*. The nonlinear correction factor proved to be quite accurate over multiple Mach regimes and may be a successful approach to modeling the nonlinear jet interaction over a wide range of flow and jet conditions. Another approach is to use an Autoregressive Moving-Average (ARMA) model that is fit to a characteristic vehicle response then used to approximate the vehicle loading with an arbitrary input [50]. The number of retained coefficients in the ARMA model determine the relative gains in memory storage and loss of information relative to the convolution approach. An unsteady loads model of the coupled fluid-structure-jet interaction problem should be developed that captures the nonlinear effects such as control reversal and the jet transient loads in a dynamic flight environment. The previously developed methods have not been tested with the fluid-structure-jet interaction and new methods may be required for aggressive maneuvers.

1.6 Dissertation Objectives

The primary focus of this dissertation is to fill the gap in the literature regarding the interaction between a jet-in-crossflow and a flexible vehicle in flight. As mentioned in the literature review, there is a body of work regarding jet interaction with rigid flight

vehicles and another regarding flexible missiles without jet actuation. It is difficult to determine what the net effect the combined fluid-structure-jet interaction will have on vehicle flight performance based on the previous work.

An effective FSJI model is required to conduct flight simulations. The literature includes models effective for canonical geometries such as flat plates, and high-fidelity approaches for complex geometries. New modeling methods are required to approximate FSJI effects for flight simulation.

A maneuvering intercept missile in the supersonic regime operates within a dynamic environment and may perform aggressive maneuvers to complete its mission. A model of the vehicle dynamics is required to accurately predict the vehicle response. There is a large gap in the research on jet interaction dynamics especially including flight dynamics. The FSJI dynamics must be included into a flight simulation model, but the sensitivity to changes in vehicle conditions is unknown.

An appropriate modeling method for the FSJI dynamics is required in addition to identifying the sensitivity effects on vehicle performance. The literature includes several approaches to modeling vehicle dynamics, but the highly dynamic nature of the intercept missile or the nonlinearity of FSJI may cause these methods to be less effective.

Finally, the net effects of jet interaction, structural flexibility, and FSJI on vehicle performance are unknown. Some best practices and design trends can be inferred from the literature, but these are based on conventional vehicles with control fins and low levels of structural flexibility. There is a lack of understanding on how to leverage FSJI for improved performance.

With the goal of better understanding the interplay of FSJI in flexible supersonic vehicles, the objectives of this dissertation are summarized as:

1. Create representative high-speed vehicle models that include the advanced design concepts of structural flexibility and jet interaction.

2. Develop new modeling methods of jet interaction effects for arbitrary flight conditions, geometries, and jet conditions.

3. Identify the sensitivity of FSJI to static and dynamic changes to vehicle conditions and control inputs.

4. Develop modeling methods for FSJI dynamics that apply to aggressive maneuvers throughout the flight envelope.

5. Measure the net FSJI effect on vehicle performance and deliver some additional insight on how to leverage these effects for improved performance.

1.7 Dissertation Overview

This dissertation is organized based on the overarching research objectives. The chapters are focused on more specific topics related to fluid-structure-jet interaction effects on HSVs. It concludes with a summary of the findings, conclusions, and key contributions of this dissertation. The description of each subsequent chapter is as follows:

Chapter 2 discusses the numerical methods investigated and used to analyze flexible flight vehicles. Previously available methods are presented in the context of including FSJI effects and new methods are presented that have been developed specifically for modeling FSJI of a maneuvering missile. Parts of this chapter were published previously in [51, 52, 53, 54, 55, 56, 57, 58].

Chapter 3 presents the HSV models used throughout the dissertation to fulfill Objective 1. Parts of this chapter were published previously in [51, 52, 53, 54, 55, 56, 57, 58].

Chapter 4 evaluates the approximate jet interaction modeling methods that have been developed according to Objective 2. Parts of this chapter were published previously in [52, 55].

Chapter 5 presents the sensitivity of fluid-structure-jet interactions to changes in the flight conditions, fluid dynamics, structural dynamics, and jet dynamics following Objective 3. Parts of this chapter were published previously in [53, 54, 56].

Chapter 6 examines the previously available and newly developed vehicle dynamics modeling methods for aggressive maneuvers across the flight envelope. These results are associated with Objective 4. Parts of this chapter were published previously in [54].

Chapter 7 evaluates the performance and stability of HSVs with respect to flexibility and fin size. These results can be used as guidelines for advance HSV concept development and support Objective 5. Parts of this chapter were published previously in [51, 55, 57, 58].

Chapter 8 evaluates the FSJI effects on performance of maneuverable HSVs. These results can also be used as guidelines for advanced HSV concept development. These results also contribute to Objective 5. Parts of this chapter were published previously in [57, 58].

Chapter 9 summarizes results and presents the key contributions of this dissertation. In addition, the broader impacts of this work and suggestions for future study are discussed.

CHAPTER 2

Numerical Methods

This chapter presents an overview of the methods that are used to develop physics-based models of HSVs. The fluid-structure-jet interaction coupled with the flight mechanics involves several physical disciplines and interactions that need to be modeled for accurate flight simulation. These methods span the range of physical disciplines required for FSJI analysis. First, the UM/HSV is presented that is used to simulate the full aeroelastic models in flight. The framework is broken up into modules that correspond to different physical disciplines and interactions, which can be modeled with varying fidelity. Next, the modeling methods that were either adapted to the FSJI problem or developed for this dissertation are presented. These methods account for steady-state and transient aerodynamic and JI effects. Finally, post-processing methods to quantify vehicle performance and stability are presented. Overall, these approaches aim to maximize computational speed, accuracy, and robustness to enable flight simulation of HSVs with FSJI.

2.1 University of Michigan's High-Speed Simulation Framework

The aerothermoelastic propulsive simulation framework that has been previously developed by Frendreis and Cesnik [59], Falkiewicz *et al.* [60], and Klock and Cesnik

[48] is used here and takes a partitioned approach to analyzing the vehicle. The following sections describe structural and aerodynamic models used in the simulation framework. The last section describes the coupled aeroelastic and flight mechanics equations of motion that are marched forward in time to simulate flexible vehicles in free flight. The full description of UM/HSV capabilities is presented by Klock [4] and the code framework is presented in Figure 2.1. Jet interaction models developed later in this dissertation are designed to be compatible with this modular simulation framework, as shown by the DACS ROM block in Figure 2.1.

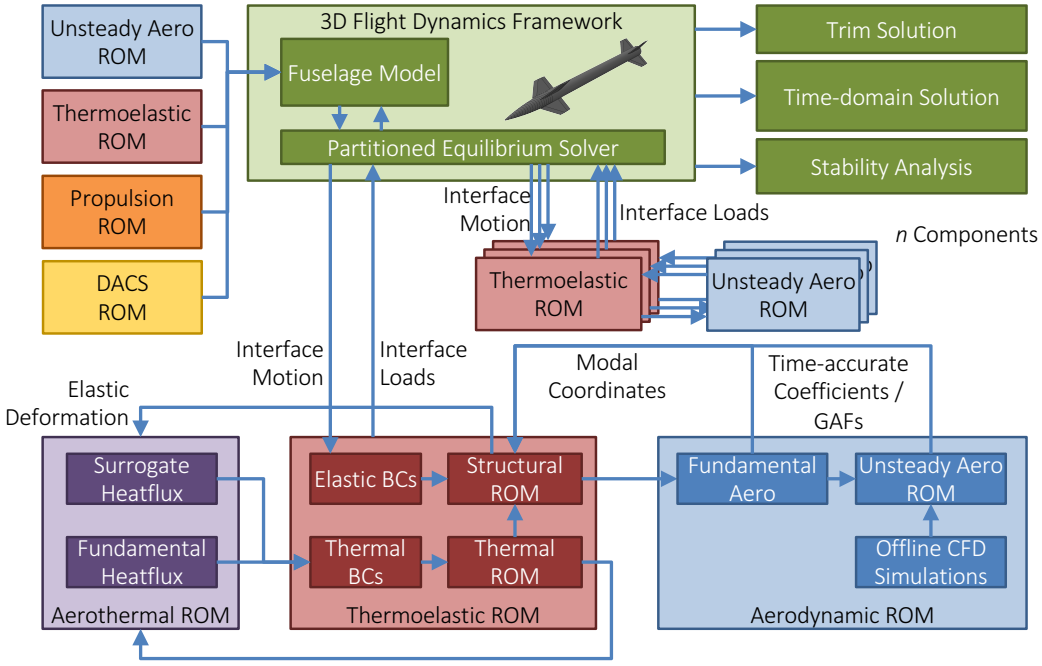

Figure 2.1: UM/HSV code framework adapted from [4] and updated to include DACS ROMs.

The structural equations are reduced using the normal mode method with the free-free vibration mode shapes [61]. The displacement of the structure is represented as a linear combination of the mode shapes, i.e.,

$$\bar{u}(x,y,z,t) = \sum_{i=1}^{m} \Phi_i(x,y,z)\eta_i(t) \tag{2.1}$$

where $\bar{u}$ is the displacement vector, Φ_i is the mode shape of mode i, and η_i is the amplitude of mode i. The free-free vibration mode shapes are eigenvectors and therefore form an orthogonal set of basis vectors to represent the displacement. The method reduces the structural equations to the number of degrees of freedom equal to the number of free-free vibration modes included (m).

The aeroelastic equations of motion are written as

$$\left[\bar{M}\right]\begin{Bmatrix}\dot{\beta}\\ \dot{\zeta}\\ \ddot{\eta}\end{Bmatrix}+\left[\bar{C}\right]\begin{Bmatrix}\beta\\ \zeta\\ \dot{\eta}\end{Bmatrix}+\left[\bar{K}\right]\left\{\eta\right\}=\begin{Bmatrix}Q_\beta\\ Q_\zeta\\ Q_\eta\end{Bmatrix} \tag{2.2}$$

for a flexible structure as presented by Frendreis and Cesnik [59]. The vehicle dynamics are expressed in the body frame using the column vectors β, ζ, and η. The quantity β is a three-element column vector containing the x, y, and z body frame translational velocities. The quantity ζ is a three-element column vector containing the body frame rotational velocities about the x, y, and z axes. The column vector η contains the amplitudes of each structural mode and its length corresponds to the number of modes chosen to represent the structure. The matrices $\bar{M}$, $\bar{C}$, and $\bar{K}$ represent the reduced mass, damping, and stiffness of the vehicle. At each time step in the simulation the external forces Q_β, Q_ζ, and Q_η are calculated and used with the current state of the vehicle to integrate the equations of motion according to a fourth-order Runge–Kutta scheme.

The aerodynamic loads are calculated using the vehicle outer mold line geometry that is represented by a coarse triangular mesh approximating the vehicle surface. The loads are calculated at each mesh element according to the user-defined model.

There are different options on aerodynamic load sources in the UM/HSV framework. The low-fidelity method used in this dissertation for supersonic aerodynamics is the analytic shock-expansion approach with a piston-theory **??** correction for un-

steady effects. The shock-expansion approach is derived from the governing equations, but is complicated to apply to complex geometries, neglects viscous effects and does not account for three-dimensional effects. This leads to an over-prediction of the vehicle surface pressure compared to viscous CFD solutions. The piston-theory approach has shown good agreement with CFD [62], but again makes some assumptions such that the Mach number is sufficiently high and viscosity can be neglected. The advantage of this analytic approach is the equation-based formulation that makes it exceptionally fast to compute and robust to the wide range of flight conditions.

A CFD-based surrogate modeling approach is used throughout this dissertation that approximates the accurate high-fidelity solution with the speed and robustness of the equation-based model. The Kriging predictor is a numerical method to approximate a nonlinear function given a sample set of data. Martin and Simpson [63] provides a detailed description of the method for further reading. The popularity of the method has increased due to its ability to capture local and global nonlinear features in a data set. Several aerospace applications [44, 64, 65] that feature the Kriging method involve approximating aerodynamic data, but can be applied to any input-output data set from a deterministic computer simulation.

The computer simulation of interest is the solution to the RANS equations with the Spalart–Allmaras (SA) turbulence model. The NASA Langley FUN3D CFD code [66] is used to solve the equations for a wide range of flight conditions, structural deformations, and jet conditions. FUN3D is a node-based finite volume formulation for compressible flows on three-dimensional unstructured grids assuming calorically perfect gas. The spatial discretization scheme is second-order accurate and the second-order accurate method for time integration is used for dynamic simulations. The advantages to using FUN3D in this dissertation are the previously developed capabilities to handle rigid-body motion, structural deformation, and prescribed boundary conditions used for the jet exit conditions. The built-in aeroelastic module of FUN3D

removes any offline mesh deformation for aeroelastic analysis and is taken advantage of in the later chapters of this dissertation. The CFD approach can be very accurate relative to experimental results, but requires significant amount of computational resources and is not robust enough to incorporate into a flight simulation. Long duration flight simulations with CFD in the simulation loop are not feasible at this time and other aerodynamic modeling methods are preferred for preliminary design.

The surrogate modeling approach in this dissertation pairs a pseudo-random sampling method, such as Latin Hypercube Sampling [67] or Halton sequences [68], to generate sample points across the domain of interest. These sample points are then used as inputs to the CFD code and the output to each sample is collected. The Kriging model then fits the input-output data of the CFD simulation using a global regression and local correlation function to approximate the simulation output at un-sampled points. The model quality can be calculated using a variety of cross-validation techniques or compared to additional sample points reserved for testing.

Reduced order modeling approaches based on matrix decomposition methods are also used to decompose the physics of the problem that takes a slightly different approach than the surrogate model. In these approaches, the set of degrees of freedom are selectively chosen to represent the full solution using several methods such as Proper Orthogonal Decomposition (POD), SVD and eigenvalue decomposition. The advantage of these methods is that the resulting set of degrees of freedom are orthogonal to each other that allows for decomposing the full problem. Similar to the Kriging surrogate model, the degrees of freedom chosen to represent the full solution must be carefully chosen such that the approximation is accurate enough. A select few degrees of freedom can often be chosen based on physical intuition of the problem, which greatly reduces the computational cost of the model. The formulation for these methods and numerical results including high-speed applications have been presented previously in the literature [69, 70, 71, 72].

2.2 FSJI Dynamics Modeling Methods

Some additional methods are used beyond the UM/HSV framework to included the transient effects due to FSJI dynamics. The first method is based on the linear convolution of the vehicle step response and uses the steady-state aerodynamic surrogate model to apply a nonlinear correction. The second approach is a method to calculate the effective dynamics of the vehicle response and is especially useful for aggressive maneuvers and nonlinearity that may not be captured by the convolution-based model.

2.2.1 Linear Convolution with Nonlinear Correction Factor

For a linear system, the step response corresponding to a particular input can be convolved with the input time history to calculate the system output. This an approximation for nonlinear systems and it is accurate for small perturbations about the linearization point. The convolution implementation used in this paper is based on the work by Raveh and Mavris [49] that showed how a step response from CFD could be used to calculate unsteady aerodynamic loads. For example, the angle of attack history of an airfoil, u, can be convolved with the step response, H, using the discrete version of Duhamel's integral to calculate the aerodynamic load at the current time step $y[n]$ as [42]

$$y[n] = u[0]H[n] + \sum_{k=1}^{n}(u[k] - u[k-1])H[n-k] \tag{2.3}$$

The first term $u[0]H[n]$ represents the steady aerodynamic load at index 0 while the second term is the unsteady component due to an arbitrary input from index 1 to n. Therefore, the steady term can come from a more accurate source such as a steady-state CFD solution and the unsteady contribution of the most recent time steps can be calculated using convolution. The result is a linear approximation of the dynamics

about a nonlinear reference point.

A steady-state CFD solution can be used to correct the approximated unsteady loads using the nonlinear correction factor approach presented by Skujins and Cesnik [42]. The method is based on the assumption that the ratio of the nonlinear to linear unsteady prediction is approximately equal to the ratio of nonlinear to linear steady prediction. Therefore, at each time step the vehicle state is used to approximate the steady-state solution y^{ss} using the nonlinear CFD surrogate and linear convolution models. The ratio of these steady-state approximations is known as the *nonlinear correction factor*, f_c. The corrected unsteady approximation $\hat{y}$ can be written as

$$\hat{y} = f_c y \tag{2.4}$$

where y is the linear convolution of step response and input history in Eq. (2.3), and f_c is defined as

$$f_c = \frac{y^{ss}_{nonlinear}}{y^{ss}_{linear}} \tag{2.5}$$

To avoid division by zero, an offset term δ can be introduced that still preserves the effect of the nonlinear correction factor such as

$$f_c = \frac{y^{ss}_{nonlinear} + \delta}{y^{ss}_{linear} + \delta}. \tag{2.6}$$

2.2.2 Volterra Series in the Time Domain

The Volterra series is a nonlinear expression of the system response to a given input. In this dissertation it is implemented in the time domain using the first and second-order kernels of the Volterra series to approximate the system output. The expression for a single-input-single-output system is [73]

$$y(t) = \int_0^t h_1(t-\tau)u(\tau)d\tau + \int_0^t \int_0^t h_2(t-\tau_1, t-\tau_2)u(\tau_1)u(\tau_2)d\tau_1 d\tau_2, \tag{2.7}$$

where h_1 and h_2 are the first and second order kernels, tau_1 and tau_2 are the time variables of integration. In a linear system the first-order kernel is equal to impulse response. The first and second-order kernels for a weakly nonlinear system are calculated by [73]

$$h_1(t) = 2y_0(t) - \frac{1}{2}y_2(t)h_2(t, t - T_1) = \frac{1}{2}\left(y_1(t) - y_0(t) - y_0(t - T_1)\right), \tag{2.8}$$

where y_0 is the unit impulse response, y_2 the response to two time the unit impulse, T_1 is the period shift. The second-order kernel is then a two-dimensional function identified using several values of T_1.

2.2.3 Effective Dynamics Approach

The new effective dynamics approach is developed here to calculate the system dynamics from the high-fidelity simulation itself as opposed to identifying the linearized dynamics of the vehicle about a given flight condition. This alternate approach alleviates some concerns with identifying the dynamics in the traditional way and introduces some others. However, in a nonlinear coupled case such as the dynamic FSJI of high-speed vehicles it may be more effective to use the information contained directly in the high-fidelity simulation as opposed to guessing the structure of the problem *a priori*.

First, a maneuver is selected as an input to the high-fidelity CFD simulation. The time-marched solution associated with the known input can then be used to identify the equivalent dynamics that are contained in the problem. The problem is assumed to be of the form of a Volterra series, which is a nonlinear model of dynamical systems. The Volterra series is written in terms of multiple inputs for each output. With respect to the high-speed vehicle the inputs include flight parameters such as angle of attack, structural deformation, attitude jet conditions, etc. The outputs can

include lift, drag, moment, generalized aerodynamic forces, etc.

Given an input, a high-fidelity solver yields an output that is specific to that case. However, the goal is to approximate the output given an arbitrary input to the high-fidelity solver. Therefore, the objective is to identify the underlying nonlinear system that represents the input-output relationship. In the previous sections the dynamics model was identified using step responses with the high-fidelity solver and assuming these step responses were valid throughout the simulation as the vehicle fluid, structure, and jet parameters were varying with time. The effective dynamics approach does not make this assumption. Instead, the dynamics are directly calculated based on high-fidelity solutions of a maneuver with time-varying fluid, structure, and jet inputs.

The effective dynamics follows the previous convolution method except in the frequency domain and can be extended to nonlinear terms as in the Volterra series. The Volterra series formulation relies on a set of kernels that must be identified, such that any new input time series can be used to calculate the system response. Traditionally the kernels are identified in either the frequency [74] or time domain [73, 75]. Representing the Volterra series in the frequency domain transforms the expressions from convolution integrals of functions to products of functions. The identification of the kernels is then formulated as a least-squares problem with the known inputs and outputs, solving for the effective step response frequency component. Identifying the higher-order kernels relies on choosing a maneuver that sufficiently excites all higher-order dynamics in the problem.

The linear convolution and superposition of FSJI dynamics with n inputs is written in the form

$$y(t) = \sum_{i=1}^{n} \int_{-\infty}^{t} H_i(\tau) u_i(t-\tau) d\tau \tag{2.9}$$

where H is the vehicle step response, u is the time derivative of the input, and y is the predicted output. For example, the step response to a change in angle of attack

could be convolved with the derivative of the angle of attack history to predict the vehicle lift coefficient as a function of time without any additional inputs.

Linear convolution and superposition in the frequency domain of n inputs becomes

$$\hat{y}(\omega) = \sum_{i=1}^{n} \hat{H}_i(\omega)\hat{u}_i(\omega) \tag{2.10}$$

where $\hat{(\cdot)}$ indicates the Fourier transform and ω is the complex frequency. This is a least-squares problem to solve for the effective dynamics for each frequency component. Linear convolution in the frequency domain is represented using zero-padded signals in the time domain [76]. The input signal is zero-padded at the end as expected. The known output is prepended by the inverse of the output with a shift such that the two halves meet. This is shown in Figure 2.2

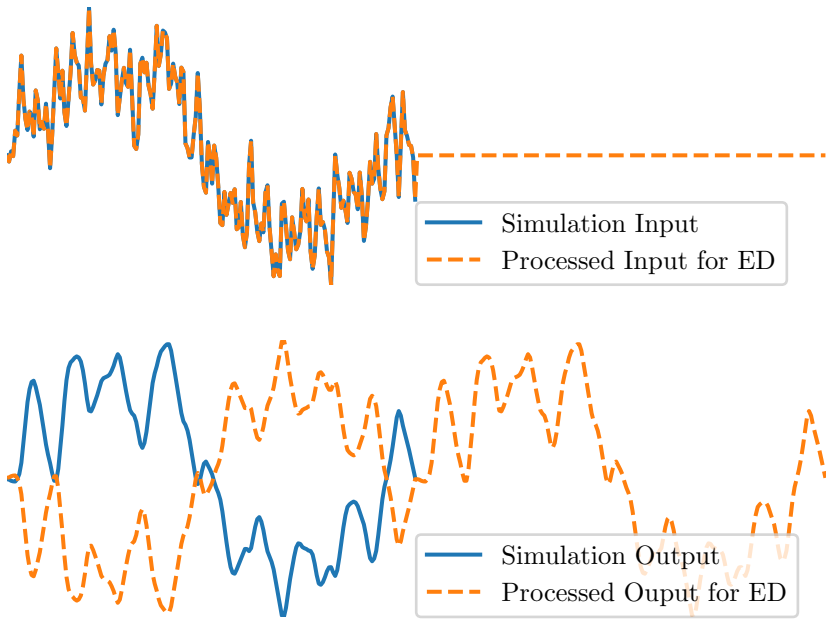

Figure 2.2: Processing of the time-domain simulation input and output signals for calculating the effective dynamics. The processed signals are twice the length of the simulation input and output signals.

This method is extremely powerful due to its simplicity. The pre-processing of step responses for each input has been removed and replaced with a single time-domain solution as long as the input maneuver excites the dynamics of each input. In addition, parameters that have a significant effect on the dynamics such as Mach number, total angle of attack, etc. can be included directly in the identification process.

Nonlinear terms from the Volterra series can also be included and solved for using least-squares. The linear and second-order terms in the time-domain of the Volterra series with a single input are written as

$$y(t) = \int_{-\infty}^{t} H(\tau)u(t-\tau)d\tau + \int_{-\infty}^{t}\int_{-\infty}^{t} H_2(\tau_1,\tau_2)u(t-\tau_1)u(t-\tau_2)d\tau_1 d\tau_2 \quad (2.11)$$

where $H_2(\tau_1, \tau_2)$ is the second-order kernel. Typically this is a complex term to identify in the time domain, but can also be solved for using the least-squares method in the frequency domain. The nonlinear terms can be transformed to the frequency domain for a discrete system as [77]

$$\hat{y}[k] = \hat{H}[k]\hat{u}[k] + \sum_{m} \hat{H}[m, k-m]\hat{u}[m]\hat{u}[k-m] \quad (2.12)$$

where $\hat{u}$ is the Fourier transform of the input function, m and k are the discrete frequencies that vary from $-1/(2\delta t)$ to $1/(2\delta t)$ and have length n.

This can also be extended to multiple inputs and a system two inputs and a single

output would be written as [78]

$$\hat{y}[k] = \hat{H}_1[k]\hat{u}_1[k] + \hat{H}_2[k]\hat{u}_2[k] \tag{2.13}$$

$$+ \sum_m \hat{H}_1^2[m, k-m]\hat{u}_1[m]\hat{u}_1[k-m] \tag{2.14}$$

$$+ \sum_m \hat{H}_{12}^2[m, k-m]\hat{u}_1[m]\hat{u}_2[k-m] \tag{2.15}$$

$$+ \sum_m \hat{H}_{21}^2[m, k-m]\hat{u}_2[m]\hat{u}_1[k-m] \tag{2.16}$$

$$+ \sum_m \hat{H}_2^2[m, k-m]\hat{u}_2[m]\hat{u}_2[k-m] \tag{2.17}$$

The process of calculating the effective dynamics begins with choosing a maneuver that excites the dynamics of interest to the degree of interest. For example, a maneuver for the high-speed vehicle to excite FSJI would include varying angle of attack, structural deformation, and jet actuation at a reference flight condition. To account for the large parameter space of Mach number, altitude, and angle of attack, these parameters could be varying in addition to the dynamic FSJI input. The high-fidelity solution is run using the input maneuver and the parameters of interest (e.g., force coefficients and generalized aerodynamic forces) are collected as the output. The input history $u_i(t)$ for inputs 1 through n and output history for outputs $y_j(t)$ for outputs 1 through m are transformed to the frequency domain. The least-squares solution is used to calculate either the effective step or impulse responses depending on the application. The input u_i is used directly to calculate the effective impulse responses and its derivative with respect to time is used to calculate the effective step responses. Finally, the effective dynamics are transformed to the time domain and correlated with the time-varying parameters (e.g., Mach number, total angle of attack and total jet pressure).

In practice multiple maneuvers that excite similar dynamics are used to calculate the kernels. The solution for each component of the kernels is broken down into a

least-squares solution by frequency. For example, the kernels for a 2^{nd}-order single-input-single-output system are calculated by

$$\begin{bmatrix} \hat{u}_k & \hat{C}_k \end{bmatrix}_{N\times O} \begin{Bmatrix} \hat{H}_k \\ \hat{H}_{2k} \end{Bmatrix}_{O\times 1} = \begin{Bmatrix} \hat{y}_k \end{Bmatrix}_{N\times 1}, \tag{2.18}$$

where N is the number of sampled maneuvers, O is the number of kernels, $\hat{H}_{2k}$ is the vector of 2^{nd}-order kernel coefficients associated with k, and C_k is the k^{th} row of the $N \times N$ matrix with the first, middle, and last rows calculated as

$$\hat{C} = \begin{bmatrix} \hat{u}[0]\hat{u}[n/2]\ldots & \hat{u}[n/2]\hat{u}[0] & 0 \\ \vdots & \vdots & \vdots \\ \hat{u}[0]\hat{u}[n]\ldots & \hat{u}[n/2]\hat{u}[n/2]\ldots & \hat{u}[n]\hat{u}[0] \\ \vdots & \vdots & \vdots \\ 0 & \hat{u}[n/2]\hat{u}[n]\ldots & \hat{u}[n]\hat{u}[n/2] \end{bmatrix} \tag{2.19}$$

2.3 Jet Interaction Modeling Methods

This section introduces the modeling methods that were developed to include jet interaction into the UM/HSV framework. The first approach is a semi-empirical model that is closer to an engineering-level method that is not tied to a specific geometry and does not require significant pre-processing. Second, the Kriging surrogate method is developed to include jet interaction effects with a process to reduce the model size while accounting for surface pressure distribution. Finally, a multi-fidelity modeling method is presented that is a combination of the two previous methods that has the potential to reduce high-fidelity function evaluations and improve robustness of the model.

2.3.1 Semi-Empirical Jet Interaction Model

The semi-empirical jet interaction model is based on empirical and theoretical representations of the jet interaction with a supersonic crossflow. It is used to provide a fundamental understanding of the problem with minimal computational cost. The objective of the model is to calculate the pressure distribution due to jet interaction for the baseline high-speed vehicle. This is a three-dimensional problem and must account for the varying flight conditions, structural deformation, and varying jet conditions.

The reaction control system of the baseline high-speed vehicle consists of attitude and divert jets that exhaust perpendicular to the body. The effective force on the vehicle is a combination of the aerodynamic force without the jet, the force applied from the momentum transfer at the jet nozzle, as well as the jet interaction that causes regions of higher pressure fore and lower pressure aft of the nozzle. Within the simulation framework the aerodynamic loads are solved for based on the current fluid and structural states. The jet interaction problem is solved for a value p/p_1 where p_1 is the pressure due to aerodynamic loading only and p is the pressure due to jet interaction. This factor is then used to calculate the final pressure distribution along the surface at the given time step.

The semi-empirical model consists of two major components, the jet interaction in the stream-wise direction in the longitudinal plane of the jet and in the lateral direction. These two components are shown in Figure 2.3 and described in the sections to follow.

2.3.1.1 Stream-wise Jet Interaction Model

The jet interaction model in the stream-wise direction is based on the work by Werle, Driftmyer and Shaffer [19]. The first region in the flow to be modeled is the boundary layer separation region ahead of the jet. This region has a very similar pressure profile

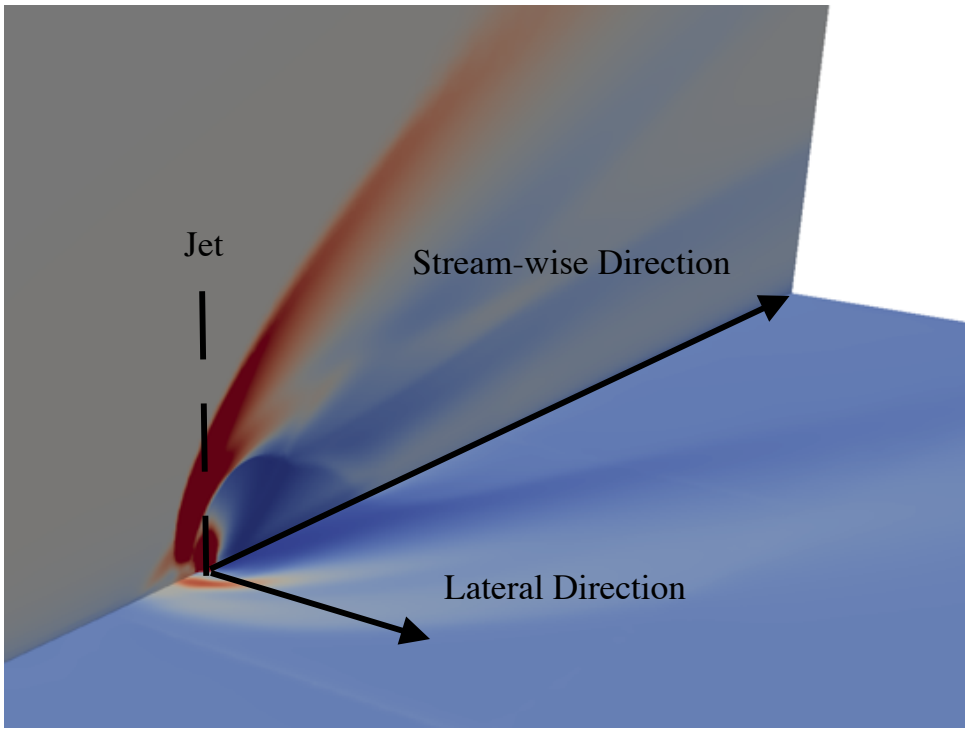

Figure 2.3: Sample numerical solution of jet interaction with a supersonic crossflow showing the stream-wise and lateral directions to be modeled.

to a forward-facing step that characteristically has two plateau pressures [19]. The first plateau pressure can be approximated by

$$p_{p_1} = (M_\infty/2 + 1)p_\infty \tag{2.20}$$

according to experimental results reviewed by Zukoski [79] and the second plateau pressure can be approximated by

$$p_{p_2} = 1.3(p_{p_1} - p_\infty) + p_\infty. \tag{2.21}$$

Then, the back pressure p_b is approximately equal to p_{p_2}. With the back pressure, flow, and jet conditions the height of the jet terminal shock in the free-stream can be calculated by

$$h_s/b_e = 0.7(\gamma_e M_e^2 p_e/p_b)^{1/2}, \tag{2.22}$$

where h_s is the height of the jet terminal shock in the free-stream, b_e is the jet exit diameter, and γ_e, M_e, p_e are the ratio of specific heats, Mach number, and pressure at the jet nozzle exit, respectively.

The height of the jet terminal shock, h_s, is used to calculate the equivalent step height h_f by

$$h_f = 1.36(h_s) \tag{2.23}$$

and the location of the oblique shock in front of the jet x_s is calculated using the step height h_f as

$$x_s = h_f / \tan \alpha_s, \tag{2.24}$$

where the angle α_s is the deflection angle required to achieve the pressure ratio p_{p_1}/p_∞.

Once the shock location x_s and jet terminal shock height h_s have been calculated, the pressure profile ahead of the jet can be approximated by the profile shown in Figure 2.4. Similarly, the region behind the shock in the flow-straightening region can be approximated by the profile shown in Figure 2.5.

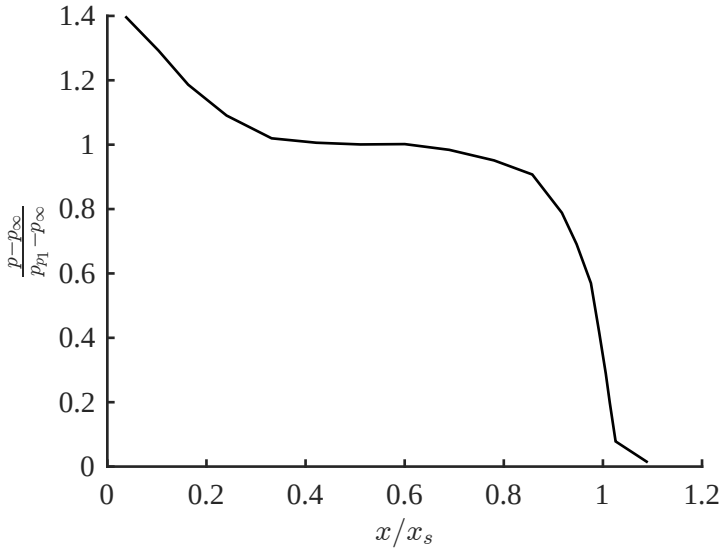

Figure 2.4: Pressure profile ahead of the jet based on empirical data.

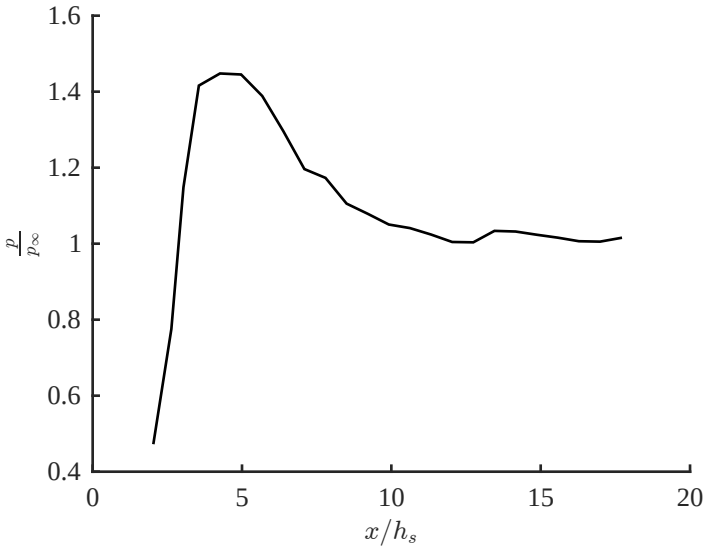

Figure 2.5: Pressure profile behind the jet in the flow-straightening region.

2.3.1.2 Lateral Jet Interaction Model

The lateral jet interaction pressure profile is adapted from the analysis regarding blast waves and applied to a wave in a supersonic flow. The distance of the shock front is represented in terms of C, the speed of sound in the free-stream, U, the wave propagation velocity, R_0 a characteristic length based on the energy of the blast, and the constant J_0, which is a function of the ratio of specific heats and the dimensionality of the problem. The shock front distance R is represented by

$$\left(\frac{C}{U}\right)^2\left(\frac{R_0}{R}\right)^3 = J_0 \tag{2.25}$$

for a spherical blast wave according to Sakurai [25].

Following the work of Broadwell [23], the propagation velocity U is rewritten as $\frac{dR}{dt}$. Solving for R yields

$$R = \left(\frac{C^2 R_0^3}{J_0}\right)^{1/6}(2t)^{1/2} \tag{2.26}$$

where t is expressed as x/V_∞, the distance downstream of the shock front over the

free-stream velocity.

The constant J_0 for specific heat ratio $\gamma = 1.4$ and a spherical shock wave is equal to 0.596 according to the calculations by Sakurai [26]. The characteristic distance R_0 is calculated according to the cylindrical form of Broadwell [23] as

$$R_0 = \sqrt{E/(2\pi p_\infty)} \tag{2.27}$$

where E is the energy per unit length of the jet.

The shock front as a function of position defines the boundary of the stream-wise jet interaction model. Outside of the boundary a pressure profile that is the same as the forward-facing step profile is used. To calculate the profile at each span-wise point along the shock front, the first plateau pressure is defined as 10/13 times the pressure within the shock front at that chord-wise station.

2.3.2 CFD-Based Jet Interaction Reduced Order Modeling

The vehicle surface pressure is described in terms of orthogonal vectors and the predicted coefficients of each vector are then used to reconstruct the surface pressure due to jet interaction. The Kriging inputs are the F, S, and J parameters corresponding to the atmospheric, flow, structure, and jet conditions. The outputs are the m coefficients of the orthogonal vectors in the surface mesh N-dimensional space, where N is number of cells in the surface mesh and m is the number of orthogonal vectors. The SVD of the surface pressure snapshots is used to calculate the orthogonal vectors. First, a matrix A is created with each column vector representing a particular CFD solution,

$$A = p_{CFD},$$

where the first dimension of A is equal to N and the second dimension is equal to the number of CFD snapshots. The SVD of this matrix yields the orthogonal basis U, singular values Σ and orthogonal basis V, where $AV = U\Sigma$. The singular values represent the energy associated with each vector and all singular values are retained in this work. This process is related to the proper orthogonal decomposition of the matrix A where the matrix of basis vectors is equal to the retained vectors of $U\Sigma$ and the coefficients are equal to the retained rows of V. Each row of V represents the coefficients at flight condition. Therefore, if the coefficients of V can be predicted at alternate input conditions as $\tilde{V}$, an approximation of the surface pressure is $\tilde{A} = U\Sigma\tilde{V}^T$ [60].

2.3.3 Multi-Fidelity Modeling of Jet Interaction

This section presents a method that combines the accuracy of the CFD solution with the computationally inexpensive semi-empirical model. The result is a robust jet interaction model that can be included into the UM/HSV simulation framework.

The reduced order jet interaction model is developed using a CFD-based surrogate model for aerodynamic loads, the semi-empirical jet interaction model, and the high-fidelity RANS CFD solution of the vehicle with jet interaction. This approach can leverage the fundamental understanding from the aerodynamics-only surrogate model such as the one developed by Zettl *et al.* [80] and the semi-empirical jet interaction model that has been developed in this work. These solutions are then augmented by the prediction with CFD solutions of the jet interaction using the co-Kriging method. In this study, both the CFD-based surrogate and additional jet interaction CFD solutions used the NASA FUN3D CFD code [66] to solve the RANS equations with the SA one-equation turbulence model.

The literature regarding co-Kriging[81, 82] describes a *cheap* function that is inexpensive to sample, but approximates an *expensive* function of interest that is sparsely

sampled. A CFD surrogate model created from samples without jet interaction in conjunction with the semi-empirical jet interaction model represents the *cheap* function in this work as the models have already been completed, but approximates the full jet interaction solution. Therefore, the additional jet interaction FUN3D solutions represent the *expensive* function of interest.

The jet interaction data-fusion model predicts the surface pressure of the vehicle for varying flight conditions, structural deformations, and jet conditions. These input conditions are grouped by discipline and listed in Table 6.3, where F refers to the fluid parameters, S the structural parameters, and J the jet parameters. The surrogate model of the aerodynamic loads takes the F and S parameters as inputs and outputs the pressure due to aerodynamic loads along the vehicle surface. The jet interaction model takes the F and J parameters as inputs and outputs the pressure ratio of jet interaction to aerodynamic solutions. The total *cheap* pressure distribution, p_c, is the combined solution from the aerodynamic surrogate and semi-empirical jet interaction model. The full set of F, S, and J parameters are used as inputs to the CFD solver to calculate the surface pressure distribution, p_e.

Table 2.1: Input parameters for the CFD solver and co-Kriging model.

Category	Parameter
Flight, F	Mach Number
	Angle of Attack
Structure, S	Structural Mode Amplitudes
Jet, J	Attitude jet total pressure, p_{0a}
	Divert jet total pressure, p_{0d}

The vehicle surface pressure is described in terms of orthogonal vectors and the predicted coefficients of each vector are then used to reconstruct the surface pressure due to jet interaction. The co-Kriging inputs are the F, S, and J parameters and the outputs are the m coefficients of the orthogonal vectors in the surface mesh N-dimensional space, where N is number of cells on the surface mesh and m is the number of orthogonal vectors. The SVD is used to calculate the orthogonal vectors

and then truncated to retain the m vectors with the most energy. First, two matrices are created for the cheap solution and the jet interaction CFD solution. The cheap model and CFD solution matrices are

$$p_{c,ij} = p_c(x_i, y_i, z_i, F_j, S_j, J_j)$$
$$p_{e,ij} = p_e(x_i, y_i, z_i, F_j, S_j, J_j),$$

where p_c refers to the pressure distribution of the *cheap* CFD surrogate aerodynamic model combined with the semi-empirical JI model and p_e refers to the *expensive* CFD solution of the jet interaction.

Taking the SVD of the matrix p_e yields the orthogonal basis U_e, singular values Σ_e and orthogonal basis V_e where $p_e V_e = U_e \Sigma_e$. The singular values represent the energy associated with each vector and the number of vectors kept is determined when a specified amount of the total energy is retained. This process is related to the proper orthogonal decomposition of the matrix p_e where the matrix of basis vectors Ξ is equal to the retained vectors of $U_e \Sigma_e$ and the coefficients are equal to the retained rows of V_e. In this case all of the singular values are retained. Each row of V_e represents the coefficients at each set of expensive F, S, and J conditions. Therefore, if the coefficients of one column of V_e^T can be predicted at alternate input conditions as $\hat{\nu}$, an approximation of the surface pressure is $\hat{p} = \Xi \hat{\nu}$. The corresponding amplitudes of the Ξ basis vectors from the cheap solution V_c^T are calculated by

$$U_e S_e V_c^T = p_c \tag{2.28}$$
$$S_e V_c^T = U_e^T p_c \tag{2.29}$$
$$V_c^T = S_e^{-1} U_e^T p_c. \tag{2.30}$$

For the co-Kriging approximation the inputs (X) and outputs (Y) are expressed as

$$X = \begin{bmatrix} X_c \\ X_e \end{bmatrix} = \begin{bmatrix} F_c, S_c, J_c \\ F_e, S_e, J_e \end{bmatrix}$$
$$Y = \begin{bmatrix} Y_c \\ Y_e \end{bmatrix} = \begin{bmatrix} V_e \\ V_c \end{bmatrix}$$

The co-Kriging approximation follows the work of Forrester *et al.* [81] and Kennedy and O'Hagan [82] where the value of the expensive function is the sum of the Gaussian process Z_d, the difference between cheap and expensive functions, and ρ_z times the Gaussian process of the cheap function Z_c, i.e.,

$$Z_e(x) = \rho_z Z_c(x) + Z_d(x). \tag{2.31}$$

Using this form the co-Kriging approximation of the expensive function in the j^{th} dimension y_{ej} given inputs $X = \{X_c, X_e\}^T$ and calculated outputs $Y = \{Y_c, Y_e\}^T$ is

$$\hat{y}_{ej}(x^{(n+1)}) = \hat{\mu} + c^T C^{-1}(Y_j - \mathbf{1}\hat{\mu}), \tag{2.32}$$

where $\mathbf{1}$ is a $n \times 1$ column vector of ones,

$$c = \begin{Bmatrix} \rho_z \sigma_c^2 \psi_c(X_c, x^{(n+1)}) \\ \rho_z^2 \sigma_c^2 \psi_c(X_e, x^{(n+1)}) + \sigma_d^2 \psi_d(X_e, x^{(n+1)}) \end{Bmatrix}, \tag{2.33}$$

$$C = \begin{bmatrix} \sigma_c^2 \Psi_c(X_c, X_c) & \rho_z \sigma_c^2 \Psi_c(X_c, X_e) \\ \rho_z \sigma_c^2 \Psi_c(X_e, X_c) & \rho_z^2 \sigma_c^2 \Psi_c(X_e, X_e) + \sigma_d^2 \Psi_d(X_e, X_e) \end{bmatrix}, \tag{2.34}$$

and $\hat{\mu} = \mathbf{1}^T C^{-1} y_{ej} / \mathbf{1}^T C^{-1} \mathbf{1}$. The variance of each function is σ^2 and ψ and Ψ are vectors and matrices, respectively, of the correlation functions. The subscripts c, d,

and e refer to the *cheap*, *difference* and *expensive* functions, respectively.

The process for finding an optimal value of ρ_z can expand very quickly depending on the dimension of the output. A new method to approximate this value for high-dimensional data has been developed to mitigate the computational cost of optimizing ρ_z. First, the input and output cheap and expensive data is normalized by subtracting the mean and dividing by the standard deviation. Then, a Kriging model is calculated using the cheap training data with a third-order polynomial regression function and Gaussian correlation function. The cheap approximation at the expensive training input data $\hat{Y}_c(X_e)$ is then calculated. As opposed to solving an optimization problem, the parameter ρ_z is calculated by

$$\rho_z = \frac{\hat{Y}_c(X_e)^T Y_e}{\|\hat{Y}_c(X_e)\|\|Y_e\|} \tag{2.35}$$

and the difference Y_d as

$$Y_d = Y_e - \hat{Y}_c(X_e)\rho_z \tag{2.36}$$

Finally, a second Kriging model is created using the expensive training input data and Y_d using third-order polynomial regression and Gaussian correlation functions. The DACE toolbox [83] was used for the hyperparameter fitting with bounds on the correlation parameters of [1,200].

Figure 2.6 provides a block diagram of the full jet interaction modeling process in the pre-processing block. The simulation block of Figure 2.6 shows how an arbitrary set of fluid, structure, and jet parameters during simulation is collected into the set $\hat{X}$ for the co-Kriging model to approximate the amplitudes of the SVD vectors. Then, the approximated amplitudes, $\hat{\nu}$, are used with the basis set Ξ to calculate the approximate pressure distribution on the vehicle surface $\hat{p}$.

The ROM evaluation process involves cross-validation using the existing data set. This involves remove a set of samples during the model training process to then

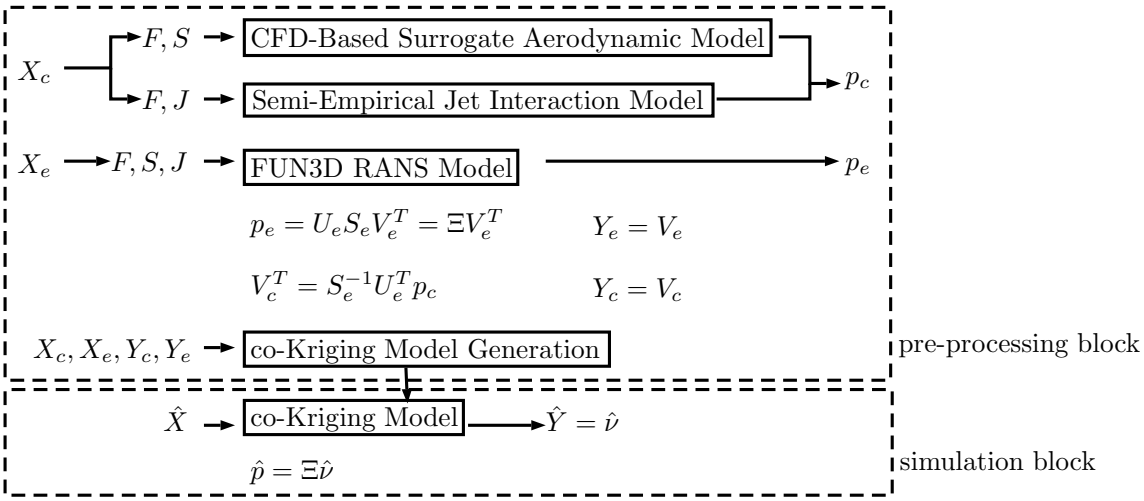

Figure 2.6: Block diagram of the jet interaction modeling process.

evaluate the model approximation at these known samples. Repeatedly following this process across multiple groups of samples quantifies the model quality to approximate unsampled data during simulation. Specifically, a leave-one-out method was applied that removes one sample, trains the model on the remaining samples, and evaluates the model approximation error at the remaining sample point. This is repeated for each sample throughout the sample set. The error is calculated for the pressure distribution measured using L_2-norm, the integrated forces, integrated moment, and the generalized aerodynamic forces all normalized by the reference value. The median is calculated to evaluate the central tendency of these errors and 95% confidence intervals are calculated using the bootstrap method with iterations equal to 100 times the number of samples [84].

2.4 Time-Domain Stability Analysis

The UM/HSV code has several post-processing modules that include trim analysis, time-domain flight response, and stability analysis. However, some additional methods were adapted to use the time-domain flight response to analyze stability and

performance. These were required to include the effects of FSJI dynamics that are modeled in the time domain.

2.4.1 Support Vector Machine

The support vector machine (SVM) is a data analysis method that is fit to a set of data for classification or regression purposes. In this work it is used to classify a set of simulation results that are labeled as stable or unstable. The SVM calculates the boundary that separates the labeled data with the least amount of error (misclassification). The boundary can be linear or nonlinear. The SVM is typically done for two-dimensional data for visualizing the data, but can be extended to higher dimensions as well. The CODES toolbox [85] was used to calculate the SVM for aeroelastic stability analysis.

2.4.2 Explicit Design Space Decomposition

Once the vehicle stability has been calculated from the vehicle response, Explicit Design Space Decomposition (EDSD) can be used to efficiently bisect the domain of a system into two regions, stable and unstable. Basudhar and Missoum [86] presents an EDSD approach using SVM to converge to a refined boundary between two discrete values in a meta-model. The process begins with an initial sample set across the domain of interest. Then, a boundary is fit to the current data set and new sample points are calculated to maximize new information. This process iterates until user-defined convergence is reached. This work used the default values of $\epsilon_1 = 4 \times 10^-3$ and $\epsilon_2 = 5 \times -4$ for the error tolerances. Dribusch and Missoum [87] applied the EDSD and SVM approach to an aeroelastic stability problem to identify the boundary between stability regions. A similar approach is used in this work that refines the stability boundaries in a multi-dimensional input domain with successive samples of the vehicle model. This approach is included in the CODES toolbox [85], which was

used to determine next best flight conditions to sample during aeroelastic stability analysis.

2.4.3 Autoregressive Moving-Average

An ARMA model is used to study the time domain response of the vehicle and determine the stability of the system. This approach was chosen because modeling the unsteady aerodynamics with the convolution technique as described above requires a time domain solution. McNamara and Friedmann [88] have shown the ARMA model to be accurate and computationally effective compared to other time domain methods. The method of calculating flutter using an ARMA model was first presented by Pak and Friedmann [89]. The method begins by taking the vehicle response in the time domain and fitting the M autoregressive coefficients and N moving-average coefficients to the response data as

$$y_k + \sum_{i=1}^{M} a_i y_{k-i} + \sum_{i=1}^{N} b_i u_{k-i} = 0 \tag{2.37}$$

where y_k is the output at index k, a_i is i^{th} autoregressive coefficient, b_i is the moving-average coefficient. Following Pak and Friedmann [89], the ARMA model can be re-written as a linear system:

$$Y_{k+1} = AY_k \tag{2.38}$$

where

$$A = \begin{bmatrix} -a_1 & 1 & 0 & \dots & 0 \\ -a_2 & 0 & 1 & \dots & 0 \\ \dots & \dots & \dots & \dots & \dots \\ -a_{2M-1} & 0 & 0 & \dots & 1 \\ -a_{2M} & 0 & 0 & \dots & 0 \end{bmatrix} \tag{2.39}$$

and

$$Y_k = \left\{ \begin{array}{c} y_0 \\ y_1 \\ \vdots \\ y_{k-1} \end{array} \right\}. \tag{2.40}$$

The moving-average coefficients are dropped for stability analysis. The eigenvalues of this system are calculated for increasing values of dynamic pressure until the system becomes neutrally stable, which determines the flutter boundary. Throughout the work a (2,1) ARMA model, 2 autoregressive and 1 moving average coefficients were used.

2.4.4 Dynamic Mode Decomposition

The Dynamic Mode Decomposition (DMD) method developed by Schmid [90] is another technique used to extract the modes and frequencies of the structural response for stability analysis. The method is based on the assumption that the dynamic response is modeled as a linear system such that each snapshot is a linear function of the previous time step. Snapshots from a time-domain simulation are collected into a matrix V with each column v_i representing the state of each degree of freedom at time step i. The snapshot matrix of n snapshots is then split into V_1^{n-1} and V_2^n where V_1^{n-1} is the collection of snapshots from step 1 to $(n-1)$ and V_2^n is the collection of snapshots from 2 to n. The objective is to calculate the matrix A such that

$$V_2^n = AV_1^{n-1} \tag{2.41}$$

The SVD is used to solve for A by calculating the SVD of V_1^{n-1}, $V_1^{n-1} = U\Sigma W^T$, rearranging terms in Eq. 2.41, and defining S to be equal to $U^T AU$. S is calculated

by

$$U^T V_2^n W \Sigma^{-1} = S \tag{2.42}$$

and the system matrix A is calculated by the transformation of S,

$$A = USU^T \tag{2.43}$$

The eigenvalues and eigenvectors of A can then be used to calculate the stability, stability margin, and associated modes that are correspond to the original time-domain flight simulation data. This process eliminates the need to fit a model to the data (as in ARMA) and has an optional feature of choosing the number of retained singular values to potentially reduce noise in the data. Throughout this work, there was no reduction in the SVD stage and all singular values were retained.

CHAPTER 3

High-Speed Vehicle Models

Following the first research objective, this chapter introduces the high-speed vehicle models that are used throughout the dissertation to investigate the effect of multi-physics interactions on vehicle performance and stability. First, the vehicle structural definition and flight conditions are presented that are representative of a slender high-speed vehicle operating within a wide range of altitudes and Mach numbers. Second, the high-fidelity CFD model is presented that is prepared for use with the NASA FUN3D CFD code[66]. Overall, the vehicle models that have been developed include the high slenderness, increased flexibility, and jet interaction characteristics that are of interest. The models are relatively simple, but exercise the same physical phenomena as a high-speed vehicle in development for real-world applications. Maintaining a simple design allows for rapid numerical experimentation, modeling, and simulation that ultimately results in a greater understanding of the impacts on the vehicle performance.

3.1 Baseline HSV Model

A new vehicle was created for this study and designed to be representative of slender high-speed maneuverable vehicles. It is used as a baseline and it will be modified later to experiment with different designs. The basic dimensions and flight conditions for the vehicle are summarized in Table 3.1. The outer mold line of the baseline

model, shown in Figure 3.1, was chosen to incorporate the high-slenderness and finless structure that has the potential to improve vehicle performance. It follows a typical cone-cylinder-flare geometry with a tangent ogive nose cone and a flare to move the center of pressure aft of the center of gravity at the mean Mach and altitude condition. The resulting static margin is approximately 7% at the mean flight condition of Mach 3 at 21.3 km (70 kft) as calculated using the shock-expansion theory aerodynamics model. Markers for the center of pressure (C.P.) and center of gravity (C.G.) are shown in Figure 3.1 based on the results of the baseline vehicle. Conventional fin surfaces are not included in the baseline model. Instead, attitude and divert control jets are located at 25% and 50% of the vehicle length, respectively. This system provides the additional forces and moments needed to control the vehicle orientation. The attitude jets are aligned with the body z-axis and aligned with the center line of the vehicle. The divert jets are aligned with the body z-axis, but offset from the body centerline to produce a roll moment if needed. The baseline configuration in the study has a uniform mass and stiffness distributions, therefore the free-free vibration mode shapes in Figure 3.2 are similar to a uniform free-free beam.

Table 3.1: Basic properties and flight conditions for the baseline vehicle.

Property	Value	Unit
Length, L_{ref}	3	m
Diameter at mid-length	0.13	m
Reference Area, S_{ref}	0.39	m^2
Pitch Moment Reference	1.5	m
Total mass (uniform distribution)	85	kg
First bending mode frequency	25	Hz
Mach	2–4	
Altitude	12.2–30.5	km

The free-free vibration mode shapes in Figure 3.2 are used to reduce the structural equations of motion. This choice allows for rapid experimentation with the overall stiffness and stiffness distribution of the vehicle. The reduced modal stiffness matrix

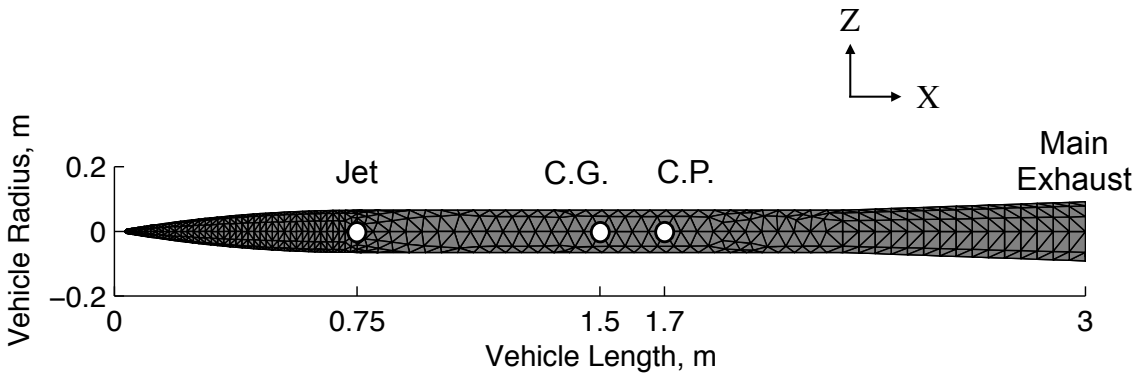

Figure 3.1: Side view of the undeformed axisymmetric baseline vehicle.

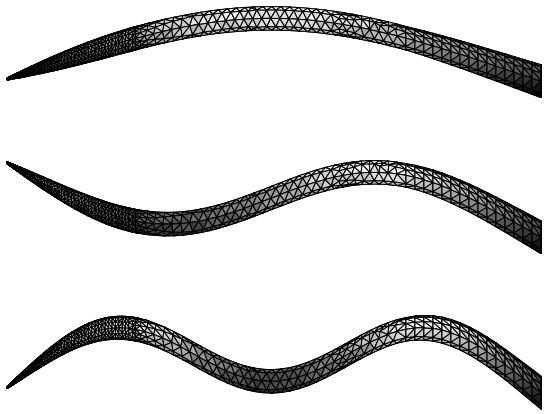

Figure 3.2: Free-free vibration mode shapes of the baseline vehicle with uniform mass and stiffness distributions.

is a diagonal matrix of the free-vibration frequencies squared using mass-normalized modes. Scaling this stiffness matrix corresponds to stiffening the whole structure. In addition, varying the mode shapes corresponds to varying the stiffness distribution along the vehicle length. This is important for modeling real-world configurations where the stiffness can significantly vary from nose to the tail.

3.2 Additional Varied Fin Configuration Model

Another vehicle model is considered representing the current conventional configuration for maneuverable high-speed vehicles in addition to the baseline model rep-

resenting a finless concept vehicle to compare the performance benefit of different design parameters. The overall vehicle outer mold line is kept as similar as possible to maintain similar aerodynamic performance with the exception of control surfaces on the conventional vehicle and a flare for the axisymmetric vehicle. The outer mold lines for each configuration are shown in Figure 3.3 and based on the representative high-speed vehicle geometry used in previous chapters. Both vehicles are modeled with structural deformation and attitude control jets that represent the introduction of slenderness and alternative control systems. The range of operating conditions for each vehicle model are listed in Table 3.1. The nonlinear unsteady applied loads due to aerodynamics, structural dynamics, and jet interaction will be modeled following the methods presented in Chapter 2.

(a) Conventional Configuration (b) Advanced Concept Configuration

Figure 3.3: Vehicle model outer mold lines for the state of the art and concept configurations being considered.

3.3 Computational Fluid Dynamics Model

The discretization of the computational domain was done using Pointwise [91] and used with the NASA FUN3D CFD code [66]. The code was used to solve the RANS equations with the SA turbulence model for the vehicle at various flow conditions. These modeling methods were chosen based on the previous results in the literature demonstrating their effectiveness. The computational grids are refined to ensure a converged solution and presented along with the verification of the solver itself to capture the jet interaction with supersonic crossflow.

This dissertation focuses on the fluid-structure-jet interaction effects in the longitudinal plane of motion. This corresponds to varying body angle of attack, structural deformation in the longitudinal plane, and jet interaction due to the attitude jet that is located quarter-length of the vehicle with positive orientation downwards. Each of these FSJI parameters can be varied via the input file to FUN3D prior to simulation for either steady-state or dynamic fluid and aeroelastic solutions. The mesh deformation and linear elastic solvers enable aeroelastic analysis of the vehicle given in the mode shapes and corresponding frequencies provided by the user in the input file and the linear elastic equations of motion are solved for in a loosely-coupled scheme. The user can also prescribe the mode shape amplitudes, which is useful for analyzing sensitivities and model development. High-performance computing resources were used to run the code and several different solutions in parallel. This capability reduces the wallclock time for each solution to enable rapid generation of databases that capture the variation in the fluid-structure-jet dynamics. These high-fidelity CFD solutions form the basis for the reduced order modeling methods described in the previous chapter.

A grid convergence study was completed that uses a full three-dimensional grid and these results are presented in Figures 3.4–3.6. The grid spacing values are listed in Table 3.2 as well as the conditions used for the study in Table 3.3. The farfield domain is an ellipsoid located L_{ref} away from the vehicle surface to minimize the number of points located upstream of the leading shock. This also limits the number of points downstream of the vehicle that do not affect jet interaction dynamics that are being investigated. The undeformed vehicle at a nonzero angle of incidence with the attitude jet on is used to create an asymmetric condition for the jet interaction. Surface slices were chosen to highlight the convergence of the jet interaction profile as shown in Figure 3.4. The integrated force and moment coefficients presented in Figures 3.5–3.6 start to converge around normalized grid spacing equal to 2 and

follow second-order convergence as shown in Figure 3.6, corresponding to the spacial accuracy of the FUN3D code. The lengthwise slice coordinate is normalized by L_{ref} and the spanwise coordinate is normalized by the diameter of the vehicle. The finest grid with normalized spacing equal to 1 is used to obtain the numerical results in this study. The normalized grid spacing of 0 corresponds to the Richardson extrapolated value.

Table 3.2: Grid spacing for the grid convergence study with the baseline vehicle.

Normalized Grid Spacing (h)	y^+	Surface Spacing	Farfield Spacing
4	4	$L_{ref}/150$	$L_{ref}/8$
2	2	$L_{ref}/300$	$L_{ref}/16$
1	1	$L_{ref}/600$	$L_{ref}/32$

Table 3.3: Conditions for the grid convergence study with the baseline vehicle.

Parameter	Value	Units
L_{ref}	3.0	m
Length Reynolds Number	3.49×10^7	1/m
Mach	3.0	
Angle of Attack	10	deg
Angle of Sideslip	10	deg
Jet Total Pressure	17.5	MPa
Jet Total Temperature	2700	K
Jet Exit Mach Number	1	

Similar grid development and convergence studies were completed using the baseline vehicle with control fins to eventually compare the results with the baseline vehicle. The conditions used for the grid convergence study are listed in Table 3.4 and the solution from the finest grid is shown in Figure 3.7. The contours of Mach number are shown in the longitudinal plane along with the contours of normalized surface pressure, which highlight the boundary layer separation extending laterally out to the control fins. This effect will lead to the most significant differences related to jet interaction between the axisymmetric and finned configurations.

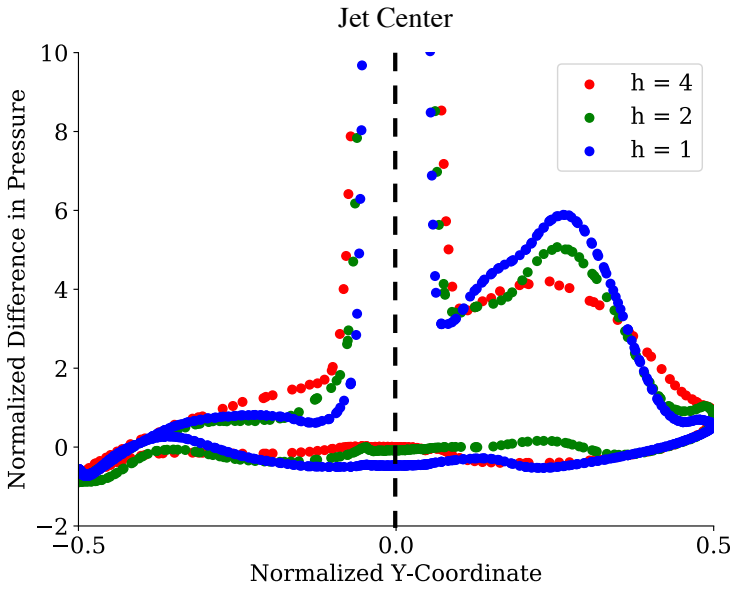

(a) Spanwise Slice Through Jet

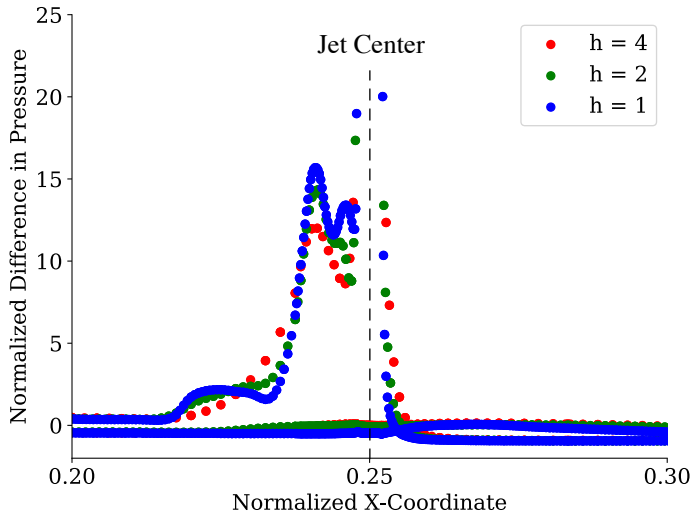

(b) Lengthwise Slice Through Jet

Figure 3.4: The baseline vehicle surface distribution with varying grid spacing.

The grid convergence study is conducted with successively refined grids with a refinement ratio of $\sqrt{2}$. The grid properties are listed in Table 3.5. The Reynolds number used to calculate the y^+ values is 1.37×10^7 and the farfield grid is a cylinder L_{ref} away from the vehicle surface. The integrated forces of lift, drag, and pitch moment are used to calculate the relative error compared to the finest grid spacing. In addition, the surface pressure distribution near the jet exit is monitored to ensure

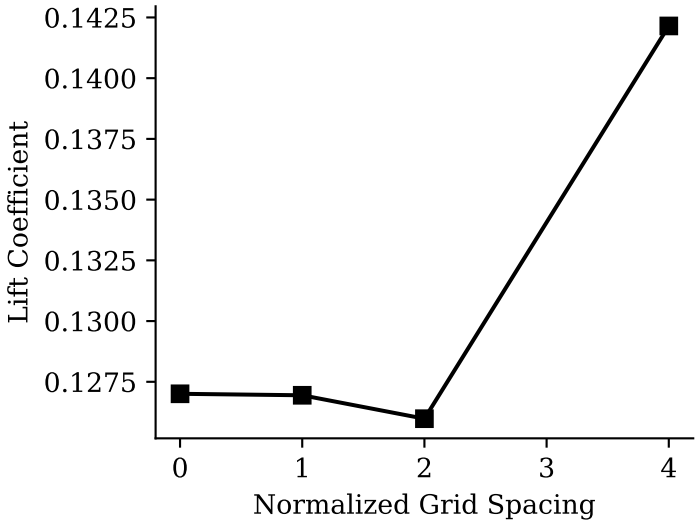

(a)

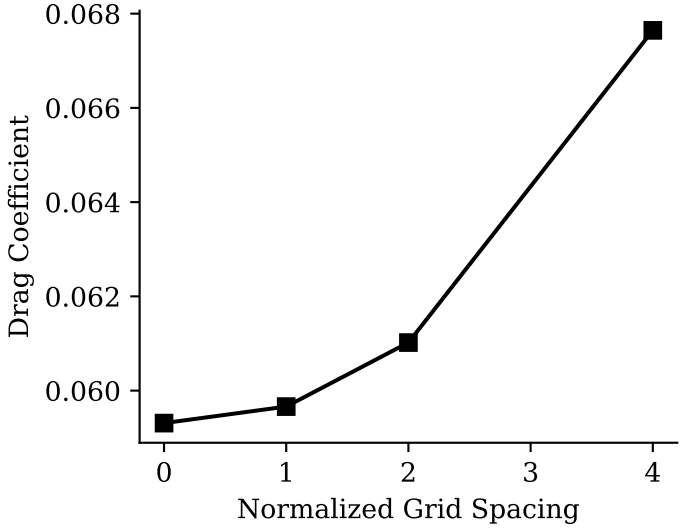

(b)

Figure 3.5: The integrated coefficients convergence with refined grid spacing.

that the jet interaction pressure profile was captured. The results in Figure 3.8(a) show the normalized pressure $\bar{p}$ of the longitudinal plane for each grid near the jet exit, which is centered at $L_{ref}/4$. Figure 3.8(b) shows the convergence of the integrated forces with decreasing normalized grid spacing that correspond to the second-order spatial accuracy of the FUN3D CFD code. Grid 4 is chosen based on a balance of

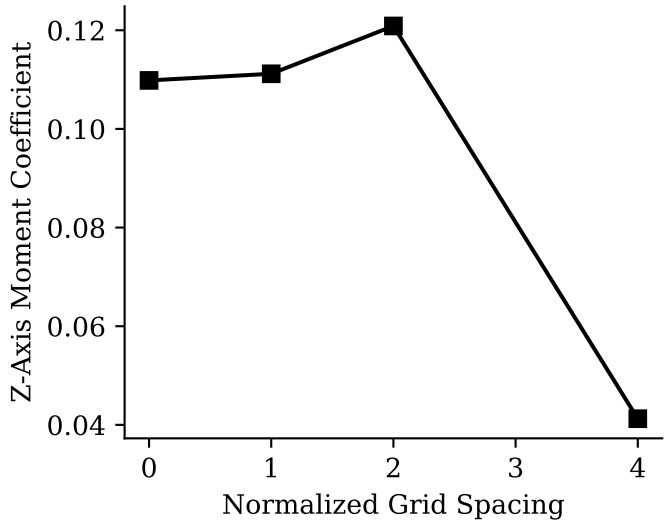

(a)

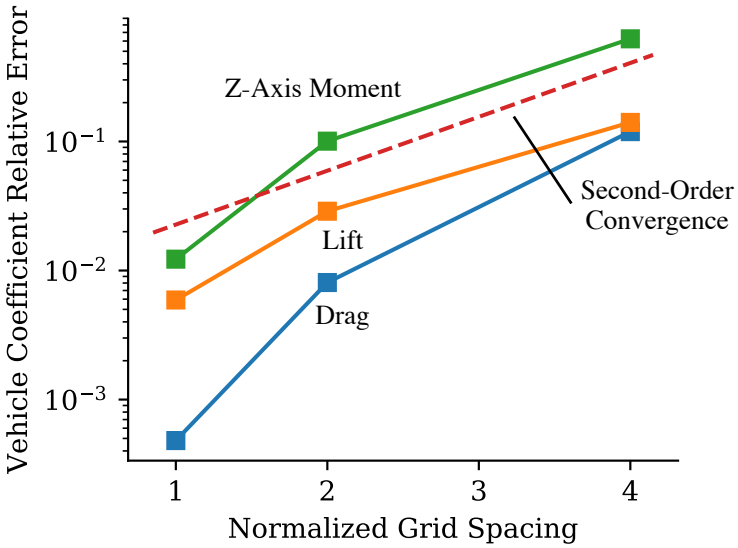

(b)

Figure 3.6: Moment coefficient and relative error converge with refined grid spacing.

accuracy and computational size for creating reduced order models with several CFD snapshots.

Table 3.4: Conditions for the grid convergence study with the finned vehicle.

Parameter	Value	Units
L_{ref}	3.0	m
Length Reynolds Number	4.408 $\times 10^6$	1/m
Mach	3.0	
Angle of Attack	0	deg
Jet Total Pressure	17.5	MPa
Jet Total Temperature	2700	K
Jet Exit Mach Number	1	

Table 3.5: Grid spacing for the grid convergence study with the finned vehicle.

Grid	Normalized Grid Spacing (h)	y^+	Surface Spacing, L_{ref}	Farfield Spacing, L_{ref}
1	1	2	1/300	1/32
2	$\sqrt{2}/2$	$\sqrt{2}$	1/424	1/45
3	1/2	1	1/600	1/64
4	$\sqrt{2}/4$	$\sqrt{2}/2$	1/849	1/91
5	1/4	1/2	1/1200	1/128

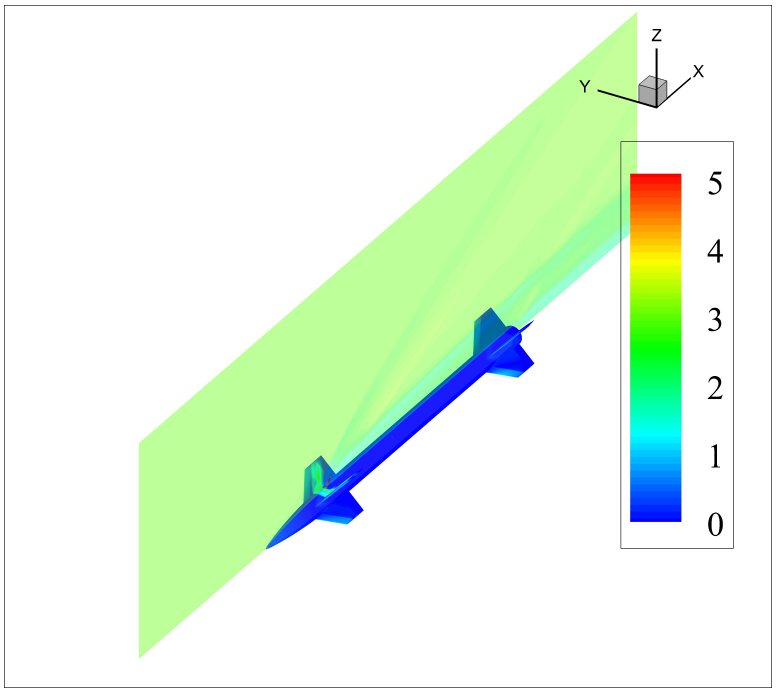

(a)

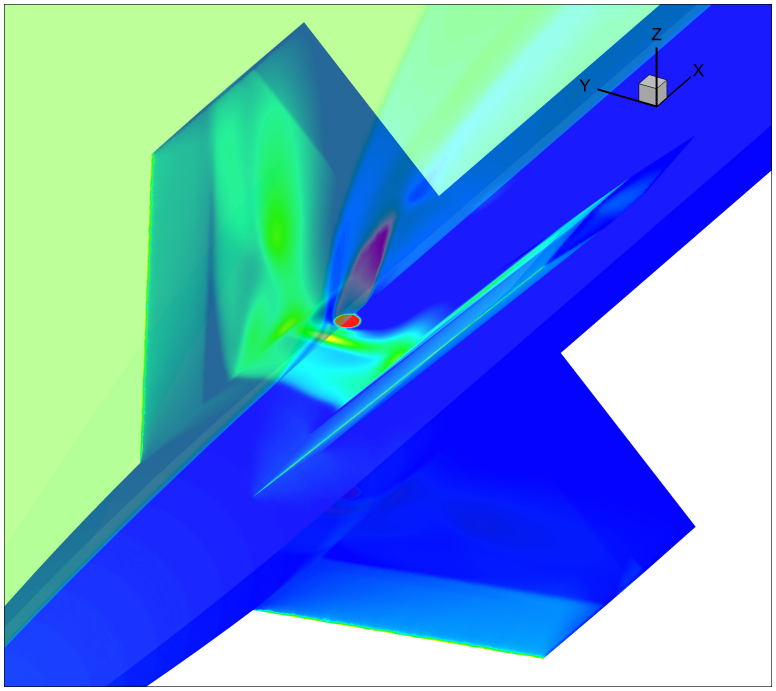

(b)

Figure 3.7: Visualization of Mach number contours in the longitudinal cut plane and normalized pressure $\bar{p}$ along the finned vehicle surface.

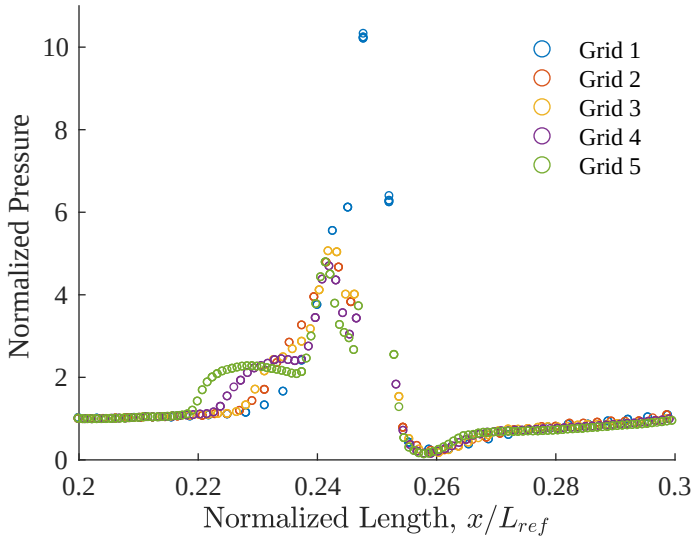

(a)

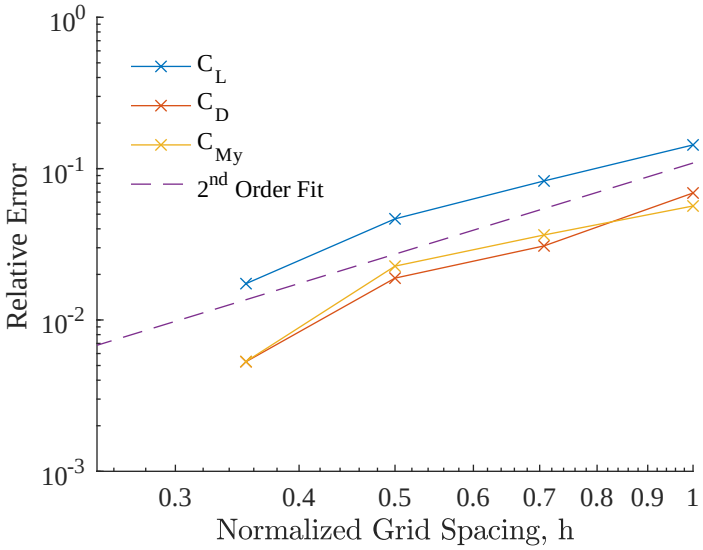

(b)

Figure 3.8: Visualization of Mach number contours in the longitudinal cut plane and normalized pressure $\bar{p}$ along the finned vehicle surface.

CHAPTER 4

Jet Interaction Model Evaluation

Following the second research objective, the modeling methods for jet interaction with a supersonic crossflow are evaluated in this chapter. First, the semi-empirical jet interaction model that approximates pressure distribution along a surface for a range of fluid and jet parameters. Second, a CFD-based surrogate model using steady-state solutions is developed that models the surface pressure distribution more efficiently with a modal basis. Finally, the CFD-based loads model that leverages the semi-empirical model, an aerodynamics surrogate model, and CFD solutions using a data-fusion approach. These modeling methods are developed for the flight simulation of the representative high-speed vehicle. The approaches expedite the simulation of the large parameter space of fluid, structure, and jet conditions for the high-speed maneuverable vehicle.

4.1 Semi-Empirical Jet Interaction Model Verification

The semi-empirical JI model was developed based on flat plate studies and the pressure distribution in the flow direction with a correction to account for three-dimensional effects. The numerical flat plate solutions presented by DeSpirito [33] and the experimental results by Dowdy and Newton [92] are used to verify the im-

plementation of the model. The flat plate test case flow and jet parameters are listed in Table 4.1 for two test cases. These two test cases were chosen as a low-PR and high-PR case to test the range of applicability of the semi-empirical JI model.

Table 4.1: Test conditions of the flat plate with jet in supersonic crossflow.

Test	M_∞	p_∞, kPa	T_∞, K	T_{0j}, K	PR
1	2.01	18.8	131	296	75.5
2	2.61	6.73	133	296	308

DeSpirito [33] compared the computational results with various turbulence models to an experimental result. The new semi-empirical model is compared in Figures 4.1 and 4.2 to the experimental pressure distribution [92] and the computational solution calculated with the Spalart–Allmaras CFD solution by DeSpirito [33].

The semi-empirical JI model is able to capture the general locations of the various flow features, but the magnitudes are different. In the stream-wise direction, the lack of information immediately behind the jet results in an over-prediction of the surface pressure and the boundary layer separation point is miscalculated for the high PR condition. In the transverse direction, the shock location is generally well estimated by the model, but the pressure at the shock boundary and the pressure distribution outside the shock are not well represented. The model over-predicts the pressure distribution due to flow separation in both test cases and the pressure due to the bow shock in the transverse direction is under-predicted in both test cases. Overall, the new semi-empirical JI model captures the basic qualitative features of the problem, but additional data from CFD or experiments are needed to quantitatively improve the solution.

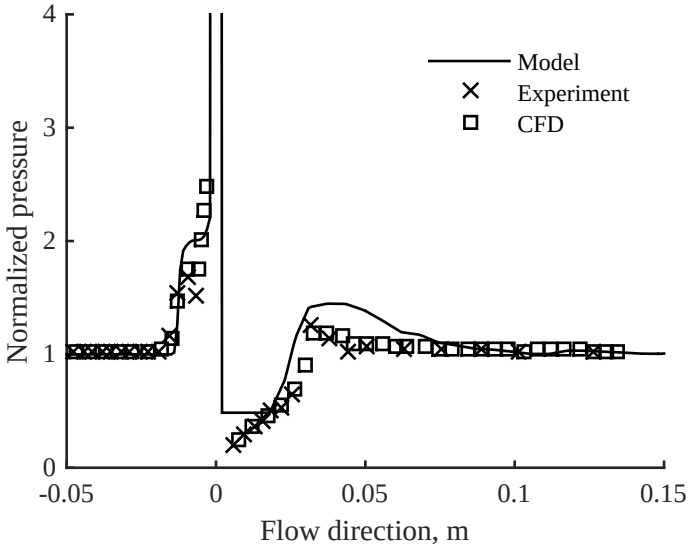

(a)

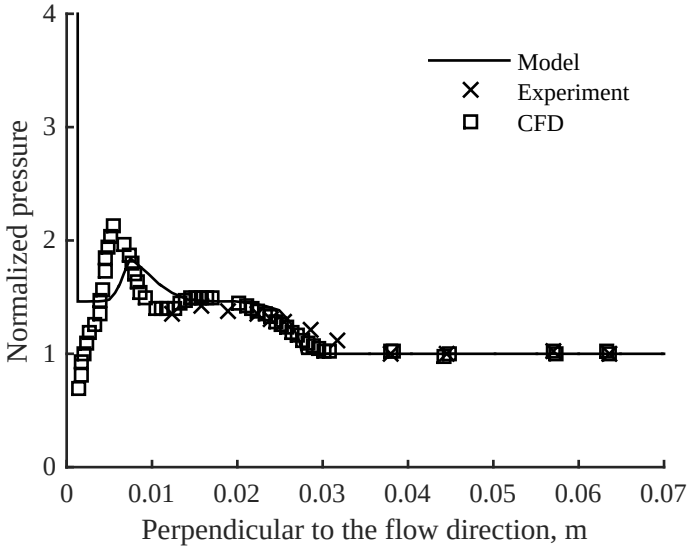

(b)

Figure 4.1: Pressure distribution due to JI as calculated by the new semi-empirical JI model ("Model"), computational ("CFD") and experimental results from the literature for Test 1 conditions.

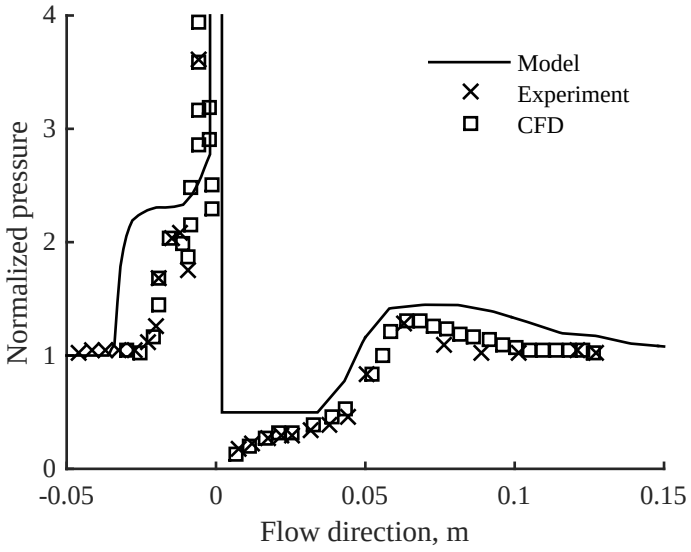

(a)

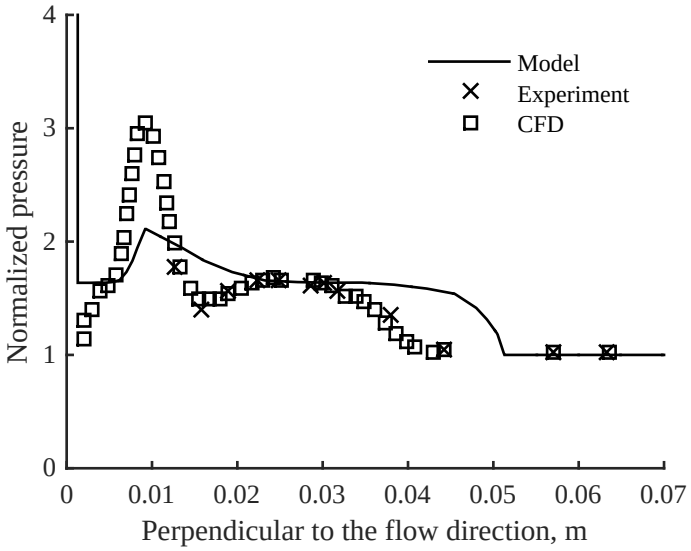

(b)

Figure 4.2: Normalize pressure (p/p_∞) distribution due to JI as calculated by the new semi-empirical JI model ("Model"), computational ("CFD") and experimental results from the literature for Test 2 conditions.

4.2 Multi-Fidelity Jet Interaction Model Verification

First, the high-fidelity solutions to the jet interaction problem are presented with high AoA and moderate structural deformation, which are characteristics of interest for the slender high-speed vehicle. The force coefficients and the amplification factors are selected to show the degree to which the jet interaction will have an effect in the steady-state solution. Second, the jet interaction model development is presented using the data-fusion and surface domain methodology presented in the previous sections. The ability of the model to approximate the vehicle surface pressure distribution is presented, which is critical to future aeroelastic analysis.

Figure 4.3 shows the CFD solution of the vehicle with the attitude or divert jets on and at either positive or negative 45 degrees AoA. The normal force coefficient, pitch moment coefficient, and the corresponding amplification factors are presented in Figure 4.4. The moment amplification for the attitude jet initially increases with AoA up to approximately 1.4 until an AoA of approximately 20 degrees. Beyond this AoA, there is a reduction in control effectiveness, that is the force and moment amplification factors of the attitude and divert jets decrease below 1 for high AoA. The contour plots in Figure 4.3 show a large expansion region that occurs at high AoA that acts in the opposite direction of the applied jet thrust. The jet interaction due to the divert jets has an effect on the pitch moment, but it does not have a moment amplification factor because the location coincides with the center of mass.

Figure 4.5 shows the CFD solution of the jet interaction problem with positive or negative 5% tip bending with the attitude or divert jets on. The force and moment coefficients along with the respective amplification factors are presented in Figure 4.6. The results show that the jet interaction is not significantly affected by positive tip deflection with amplification factors approaching unity. However, the negative

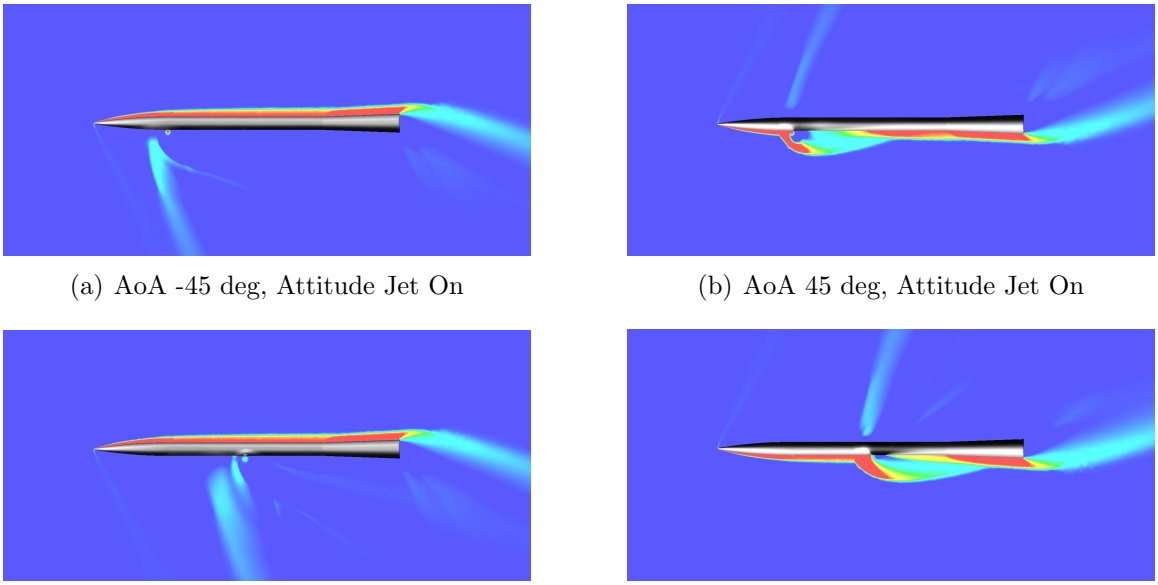

(a) AoA -45 deg, Attitude Jet On

(b) AoA 45 deg, Attitude Jet On

(c) AoA -45 deg, Divert Jets On

(d) AoA 45 deg, Divert Jets On

Figure 4.3: Contours of $\frac{p-p_\infty}{p_\infty}$ at Mach 3, 50,000 ft, and jet pressure ratio (PR) of 1500 with varying AoA.

tip deflection causes a reduction in the force amplification due to a larger expansion region downstream of the jet and slight increase in the moment amplification factor for the attitude jet due to a larger boundary layer separation region upstream of the jet. In addition, the jet interaction due to the divert jets increases the moment coefficient for all levels of deformation due to the upstream boundary layer separation ahead of the center of gravity combined with the expansion region behind the center of gravity. This effect is larger for negative deformations that place more of the vehicle surface in the expansion region.

Figure 4.7 shows the CFD solution along with several models using different approaches. The first (far right) is a surrogate built using 300 CFD solutions without any information from the semi-empirical model using a Kriging surrogate to predict the surface pressure at each surface panel. Zero-order regression and Gaussian correlation functions were used to create the Kriging using the DACE [83] toolbox. The second from the right is the *cheap* solution, the aerodynamic-only surrogate with semi-empirical model. This solution is a rough approximation moving away from an

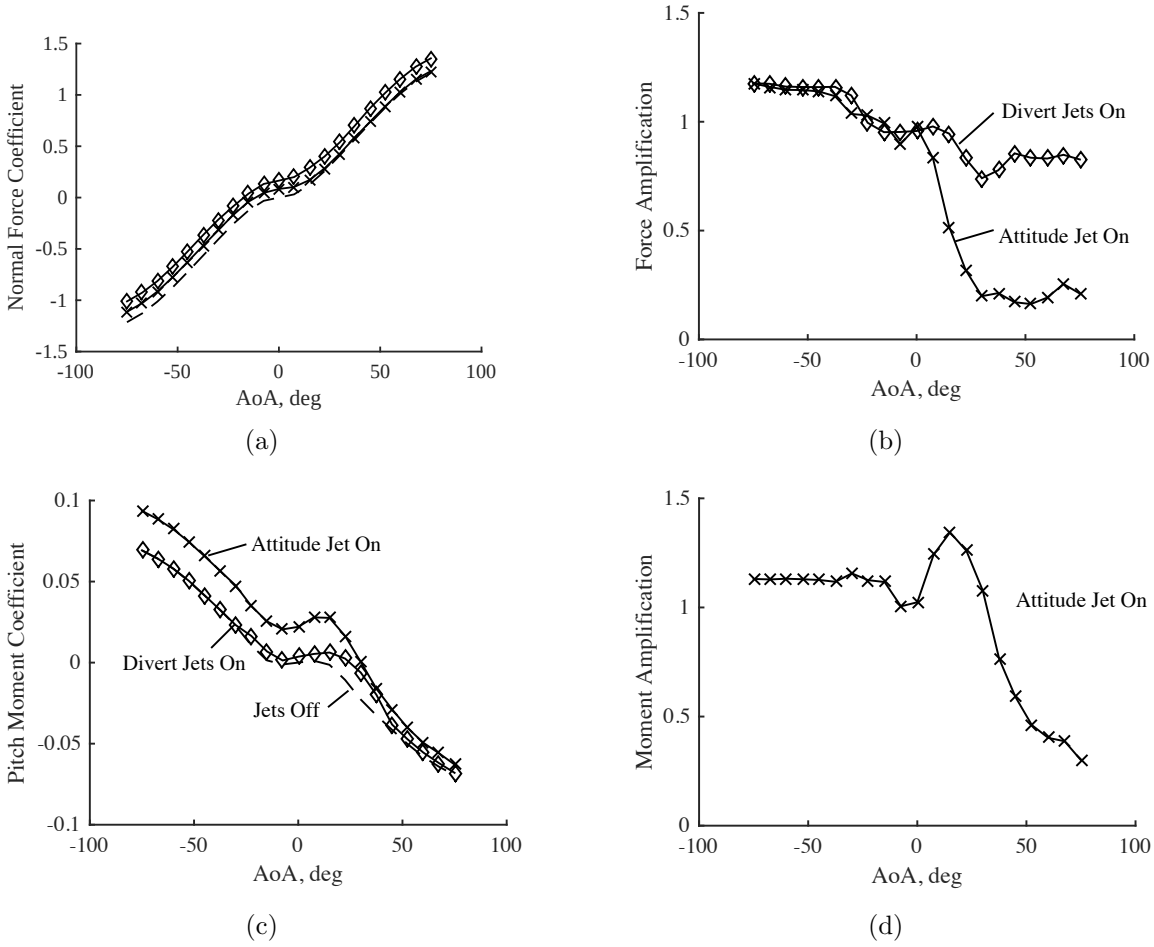

Figure 4.4: Force coefficients and the amplification factors due to jet interaction with varying AoA and no structural deformation. Flight conditions: Mach 3, 50,000 ft. Jet Conditions: PR 1500. (dashed) Jets Off, (×) Attitude Jet On, (◇) Divert Jets On.

aerodynamic-only solution towards the full JI solution. The last (second from the left) is the multi-fidelity model that is another step closer to the reference CFD solution. The same 300 samples were used to compare to the ordinary Kriging model. This model follows the procedure described in Chapter 2 where the pressure distribution is decomposed using SVD. There was no reduction during the multi-fidelity model development modal decomposition. However, fewer modes could be used to decrease the model size without significant loss in accuracy. This is shown by the result in Figure 4.8, the relative energy of singular values from the SVD of the CFD solutions. This model used a third-order regression and Gaussian correlation function

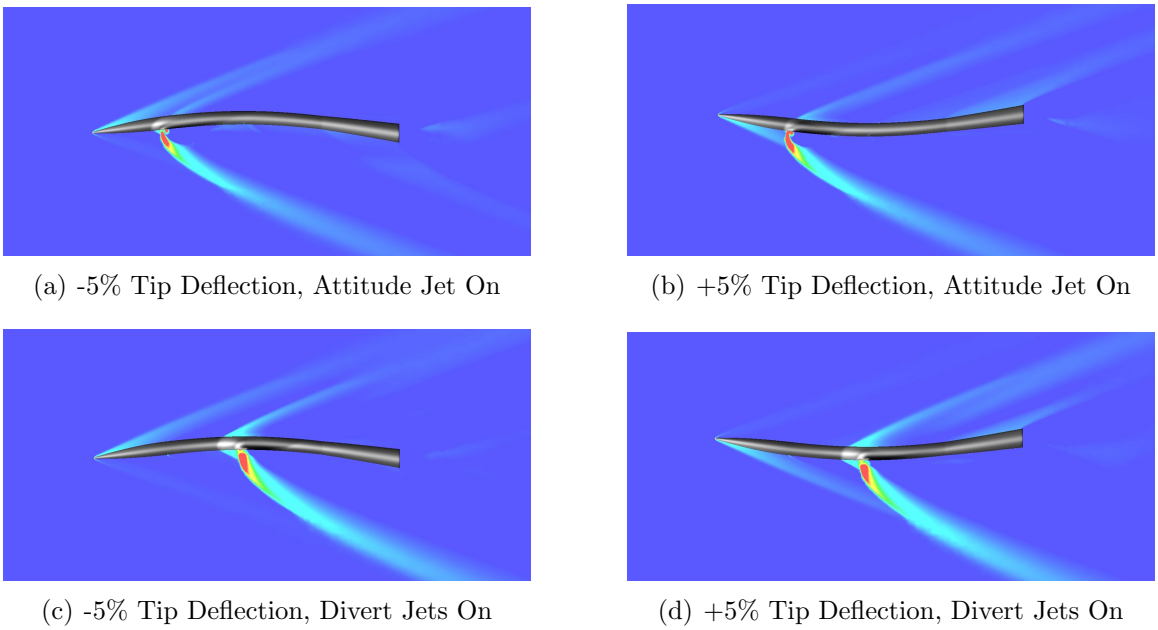

(a) -5% Tip Deflection, Attitude Jet On

(b) +5% Tip Deflection, Attitude Jet On

(c) -5% Tip Deflection, Divert Jets On

(d) +5% Tip Deflection, Divert Jets On

Figure 4.5: Contours of $\bar{p}$ at Mach 3, 50 kft., and jet PR of 1500 with varying structural deformation

with correlation hyperparameter set to 10 and 20 for the cheap and expensive layers of model. The relative error of these models calculated using the L_2-norm are 27%, 99%, and 5% for the Kriging surrogate, the *cheap* solution of the co-Kriging, and the data-fusion co-Kriging model for the conditions listed in Figure 4.7. These results show that the multi-fidelity approach is the most valuable with very limited expensive sample points. As the number of expensive samples increases, there is little to no difference between an ordinary Kriging model. One situation where the method is most effective is very high-dimensional input domains that require exponentially large numbers of expensive samples for ordinary Kriging models.

A cross-validation was done to measure the quality of the data-fusion model by creating the data-fusion model without one of the CFD solutions and then measuring the error between the predicted solution at that point and the known CFD solution [84]. This leave-one-out process is repeated for every training point and avoids additional CFD runs for measuring model quality. For each high-fidelity test condition the surface pressure L_2 error norm, applied force error, applied moment error, and

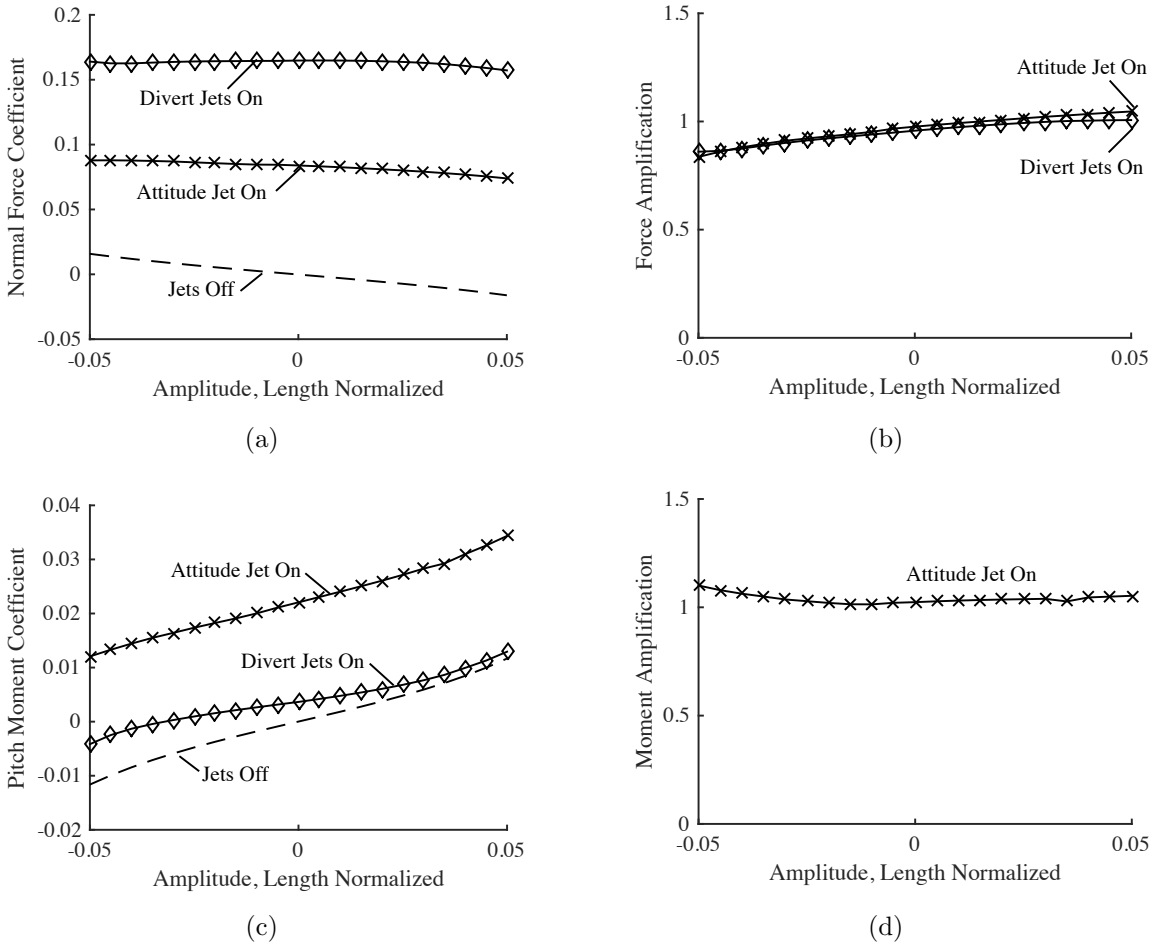

Figure 4.6: Force coefficients and the amplification factors due to jet interaction with varying tip deflection. Flight conditions: Mach 3, 50,000 ft. Jet Conditions: PR 1500. (*dashed*) Jets Off, ($\times$) Attitude Jet On, ($\diamond$) Divert Jets On.

generalized force error were calculated and then normalized by the values associated with the validation point. The 95% confidence interval of the median for each error metric is presented in Table 4.2 calculated using bootstrap samples a total of 1000 times the number of leave-one-out evaluations. Each CFD solution used as training points and leave-one-out error calculation are independent, which is a critical assumption for cross-validation. The jet interaction model includes 1030 solutions across 5 dimensions and further sampling is expected to improve the accuracy of the model.

The results show that model is converging to the reference solution within 10% for all metrics except the moment coefficient. The moment coefficient is particularly

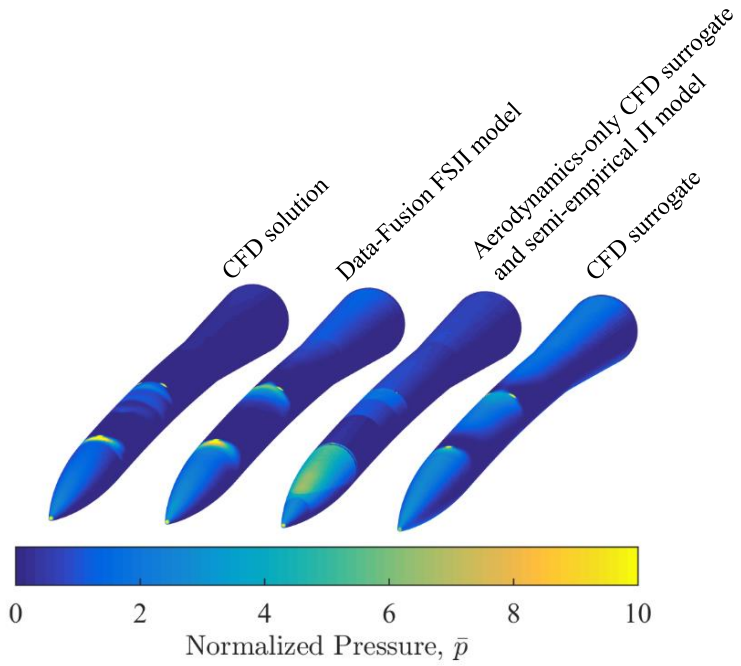

Figure 4.7: Normalized pressure distribution ($\bar{p}$) of the cheap model, CFD solution, multi-fidelity model, and CFD surrogate. Input conditions: Mach 3.1, 16 deg flow incidence angle, 1% tip deflection (first bending mode), Attitude Jet PR 1500, Divert Jets PR 1000.

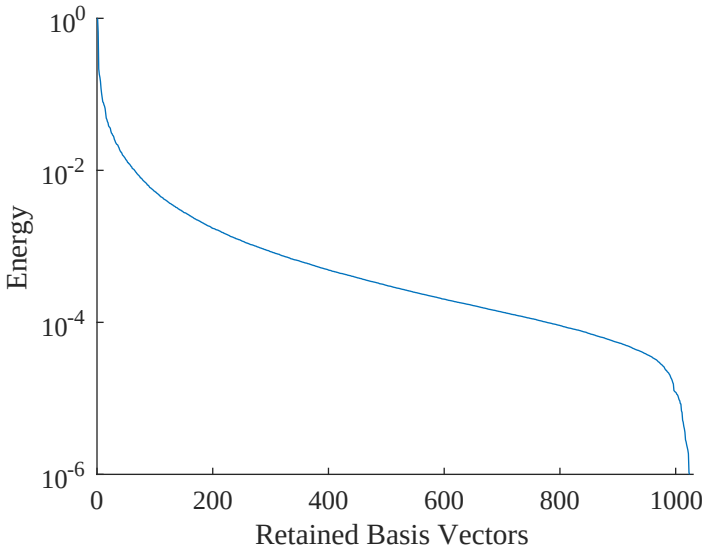

Figure 4.8: The decay in energy with the number of modes retained during the multi-fidelity modeling approach that leverages SVD. All modes were retained for the multi-fidelity model.

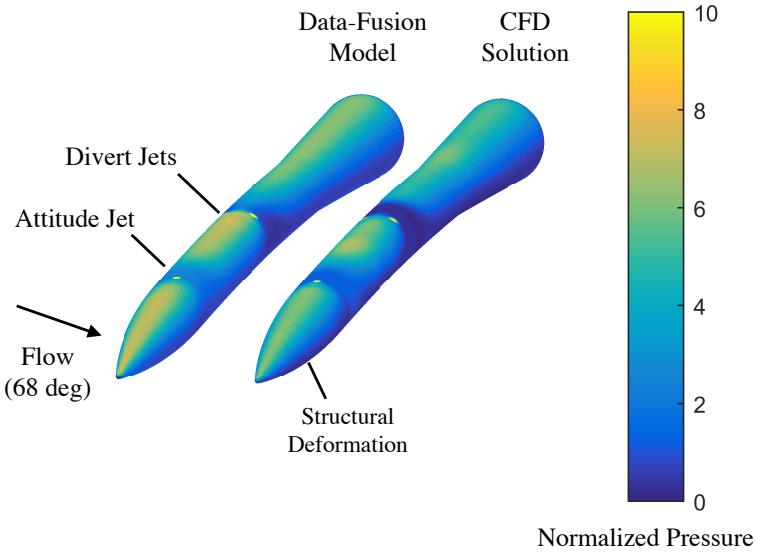

Figure 4.9: Normalized pressure distribution ($\frac{p-p_\infty}{p_\infty}$) of the data-fusion model and CFD solution. Input conditions: Mach 2.11, 68 deg flow incidence angle, 1% tip deflection (first bending mode), Attitude Jet PR 690, Divert Jets PR 1350.

Table 4.2: 95% confidence intervals of the median for the two surface pressure error metrics.

Error Metric	Lower Bound	Upper Bound
Normalized L_2-Norm	0.027	0.029
Applied Force Relative Error	0.061	0.073
Applied Moment Relative Error	0.113	0.139
Generalized Force Relative Error	0.036	0.045

sensitive to the magnitude and location of the jet interaction profile on the vehicle surface (*i.e.*, shocks and flow separation). This is the result of predicting the surface pressure distribution required for aeroelastic equations of motion as opposed to modeling the force and moment coefficients directly. Overall, the multi-fidelity modeling approach is a viable approach to modeling the pressure distribution due to JI over a wide range of flight conditions.

4.3 Flight Simulation Results

Flight simulation results capture the effect of making various modeling assumptions for high-performance vehicles. Specifically, the high-speed slender vehicle is modeled using either engineering-level or CFD-based surrogate models with a rigid or elastic model. The vehicle model is then simulated using the UM/HSV framework in free-flight by integrating the coupled aeroelastic and flight mechanics equations. Step and impulse functions are used to measure the response of the various vehicle models and the vehicle response is analyzed to measure the performance in response to the control input. Performance quantities of interest are the vehicle normal acceleration and pitch rate. For reference, the angle of attack and vehicle deformation are reported along with the jet amplification factors. The jet amplification factor is the ratio of the combined jet interaction and jet thrust loads to the jet thrust.

Shock-expansion theory is the engineering-level aerodynamics model for steady-state pressure distribution. The unsteady pressure due to vehicle dynamics and vibration is accounted for using a third-order piston-theory approximation [93]. The two models combine for an unsteady aerodynamic prediction of the vehicle as it maneuvers and deforms during the flight simulations.

The aerodynamic CFD-based surrogate is that developed in the previous section without any jet input. This aerodynamic surrogate model approximates the vehicle surface pressure distribution over a wide range of angles of attack and structural deformation from a training set of steady CFD solutions. The piston-theory correction is applied here as well to account for the unsteady flow contribution to the surface pressure. The input to the model during simulation is the instantaneous flight conditions (Mach number and AoA), structural deformation (first-bending mode amplitude), and attitude jet total pressure (PR). The output is the surface pressure distribution that is then used to calculate generalized force for the aeroelastic equations of motion and integrated forces and moments to solve for the flight mechanics.

The engineering-level jet model is the ideal jet, which is simply a point force equal to the jet thrust. This is a first approximation that neglects the interaction of the jet flow with the external flow and the associated change in pressure distribution along the vehicle surface. The CFD-based jet interaction surrogate model is the multi-fidelity model developed in the previous section that uses a combination of the semi-empirical jet interaction model with CFD solutions of RANS equations for the slender high-speed vehicle. The input to the multi-fidelity model uses the flight conditions (Mach number and AoA),structural deformation (first bending mode amplitude), and attitude jet pressure (PR) with the *cheap* and *expensive* components of the co-Kriging model. The *cheap* layer of the surrogate calculates the pressure distribution based on the semi-empirical model of JI with three-dimensional and flow separation corrections. The *expensive* layer of the surrogate calls on the sampled CFD solutions with varying flight conditions, structural deformation, and jet pressure.

The following sub-sections describe the vehicle response to an impulse and step input from the control jet. The vehicle modeling of the aerodynamics and jet interaction is varied to measure the effect of the modeling approach on the predicted vehicle response. The highest fidelity model available that is used as the reference model is the CFD-based surrogate used for aerodynamics and jet interaction coupled to the elastic equations of motion for the vehicle. A select few combinations of models are chosen to directly compare the aerodynamic, structural, and jet interaction modeling approaches. The first is the elastic vehicle with the engineering-level model for the aerodynamic and jet interaction solutions, which corresponds to shock-expansion/piston-theory aerodynamics with the ideal jet assumption. The next modeling approach uses the CFD-based aerodynamic surrogate with the ideal jet assumption, which directly compares the ideal jet approximation to the reference solution and compares the engineering-level aerodynamic solution to the RANS approximation. The final model compared is a rigid model with the CFD-based sur-

rogates for aerodynamics and jet interaction that evaluates the impact of modeling the vehicle without any structural degrees of freedom on predicted performance. In addition, the change in vehicle performance due to elasticity can be assessed from comparing the reference model to the rigid model. The models are designated with a three-letter acronym for the aerodynamic model, jet interaction model, and structural model. The key is listed in Table 4.3.

Table 4.3: Acronym key for simulation results.

Acronym	Aerodynamic Model	Jet Interaction Model	Structural Model
SSF (Ref.)	CFD-Surrogate	CFD-Surrogate	Elastic
EEF	Shock-Expansion + Piston theory	Ideal Jet	Elastic
SEF	CFD-Surrogate	Ideal Jet	Elastic
SSR	CFD-Surrogate	CFD-Surrogate	Rigid

4.3.1 Impulse Response

The vehicle response to an impulse input from the attitude jet is used to measure the change in performance associated with accounting for higher-order effects such as vehicle elasticity and jet interaction. The impulse properties are listed in Table 4.4 and the vehicle response is presented in Figures 4.10–4.12.

Table 4.4: Impulse and step input properties.

Parameter	Value	Units
Altitude	15	km
Mach	3.0	-
Jet Impulse PR	3000	-
Impulse Period	0.04	s
Jet Step PR	500	-
Input Start Time	1.0	s

The impulse responses reveal some trends in the vehicle response when comparing the various modeling strategies. The impulse response highlights the difference between the aerodynamic models and the structural models as the jet interaction does

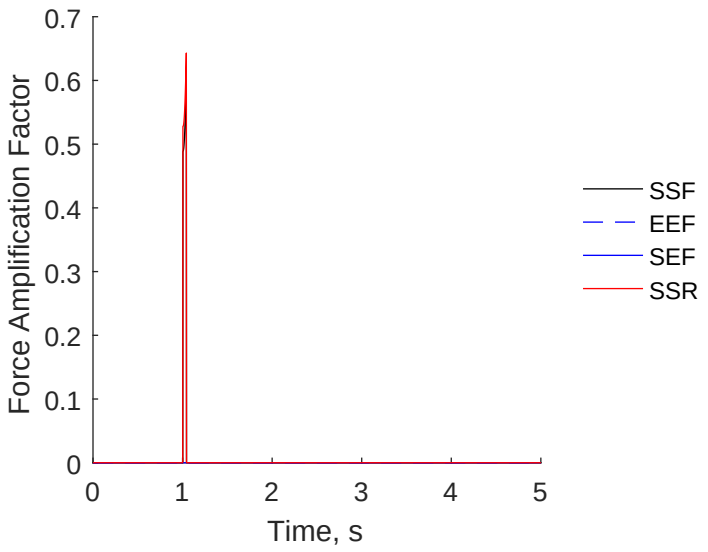

(a)

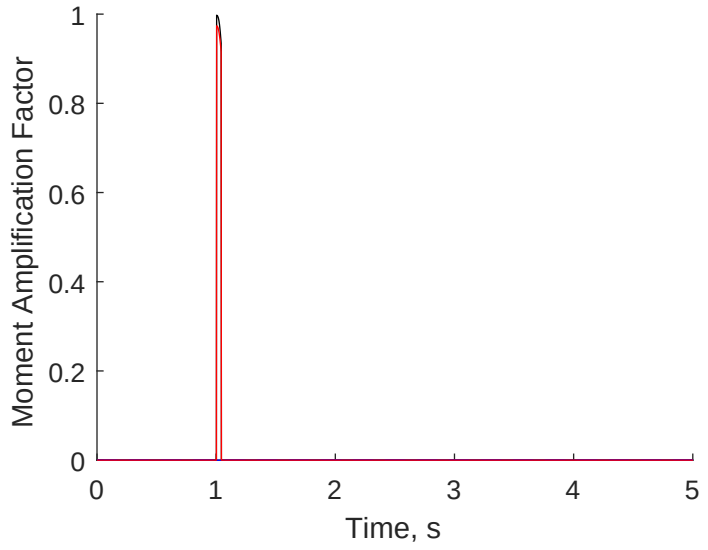

(b)

Figure 4.10: Impulse response jet amplification factors.

not have much time to take effect. The overall trend in the aerodynamic model is that the engineering-level model has a higher aerodynamic stiffness that can be seen in the lower angles of attack and higher frequency (Figure 4.11a). This effect leads to acceleration levels (Figure 4.12b) that are about the same as the reference solution initially, but decays faster as the angle of attack decays. The rigid vehicle does not

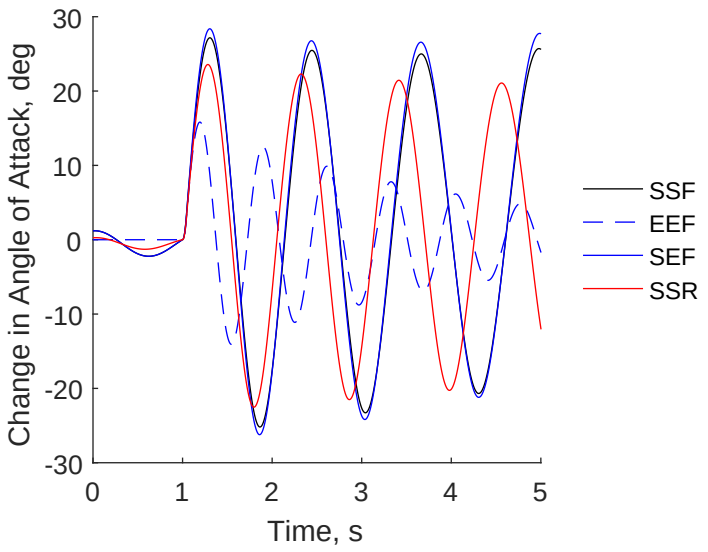

(a)

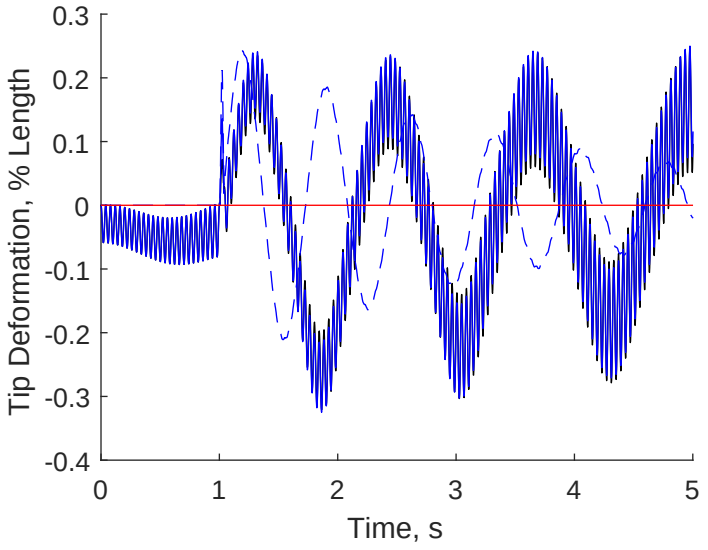

(b)

Figure 4.11: Vehicle response to attitude jet impulse input.

reach the same peak accelerations or angles of attack as the elastic vehicle. The lower maneuverability can be attributed to the lack of deformation. The vehicle deformation leads to a higher pitch moment that amplifies the response of the elastic vehicle. The comparison between the ideal jet and jet interaction model with the elastic vehicle reveals that the jet interaction effect has little to no effect when applied in short

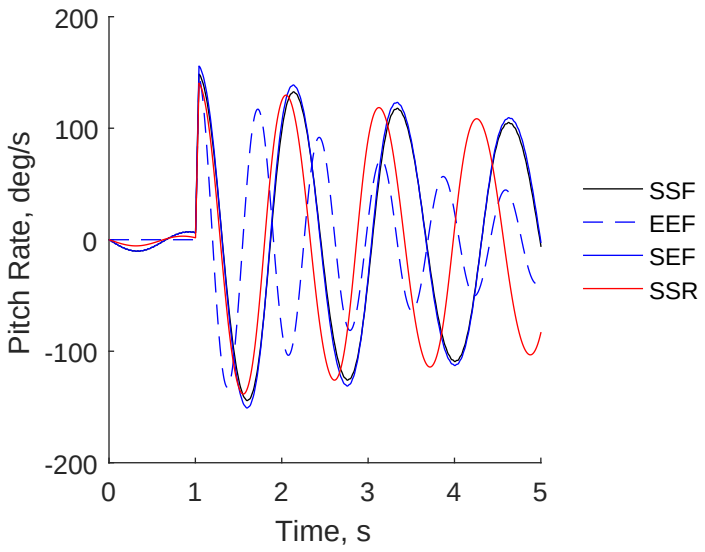

(a)

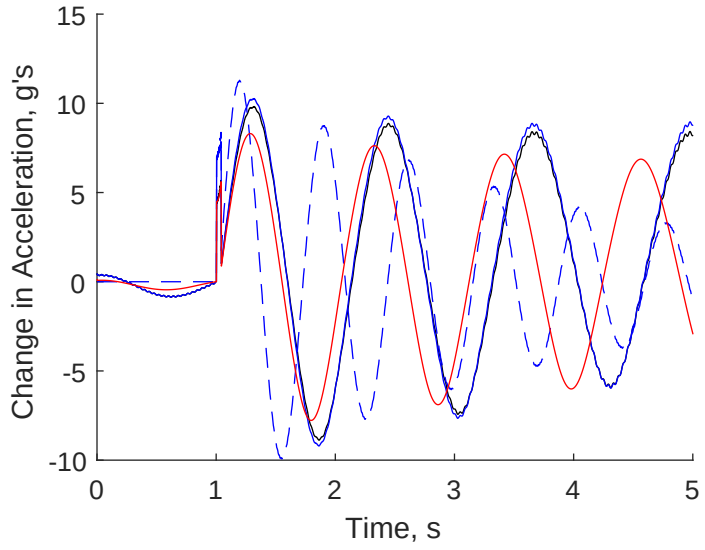

(b)

Figure 4.12: Vehicle maneuverability metrics due to the attitude jet impulse input.

bursts. Therefore the ideal jet model, which is simple to implement, may be sufficient for impulse-like inputs from the reaction control system. However, the jet interaction pitch moment amplification factor at this flight condition is approximately equal to one and this must be taken into consideration before using the ideal jet model for all maneuvers.

4.3.2 Step Response

The vehicle response to a step input from the jet is simulated and compared for the various modeling approaches. The flight simulation results show the effect of jet interaction and elasticity on the vehicle performance. The step input properties are given in Table 4.4 and the vehicle response presented in Figures 4.13 through 4.15.

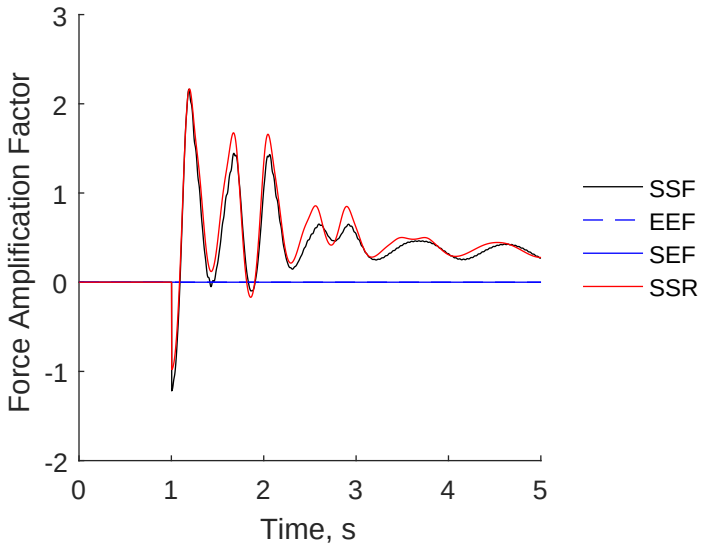

(a)

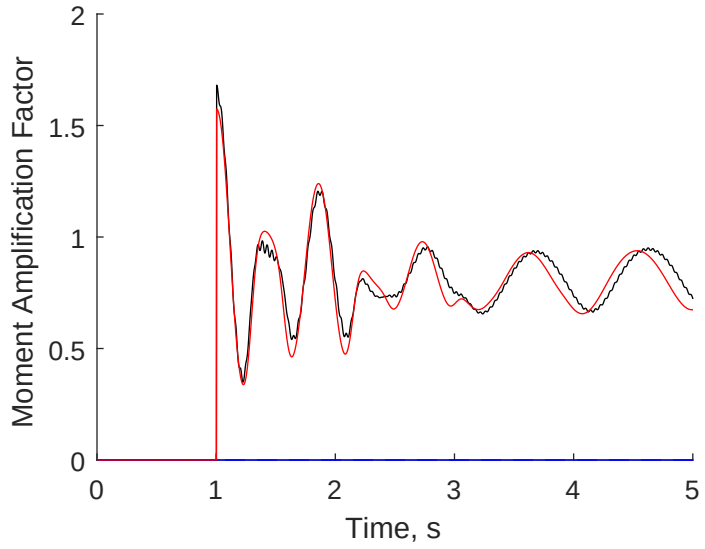

(b)

Figure 4.13: Step response jet amplification factors

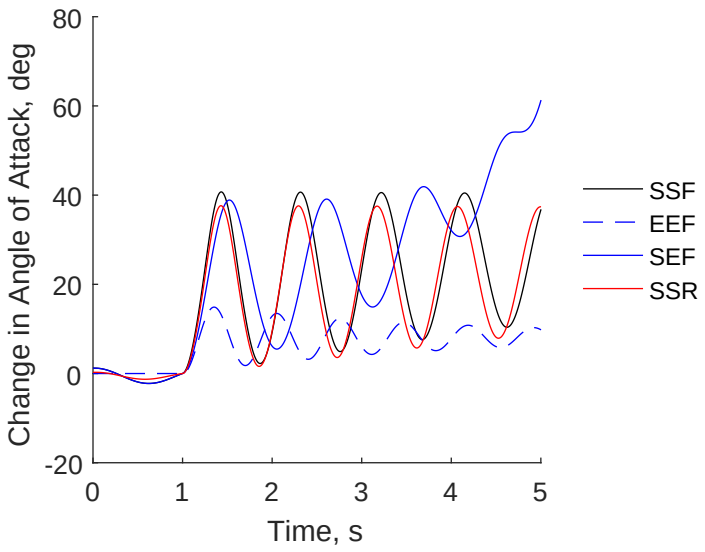

(a)

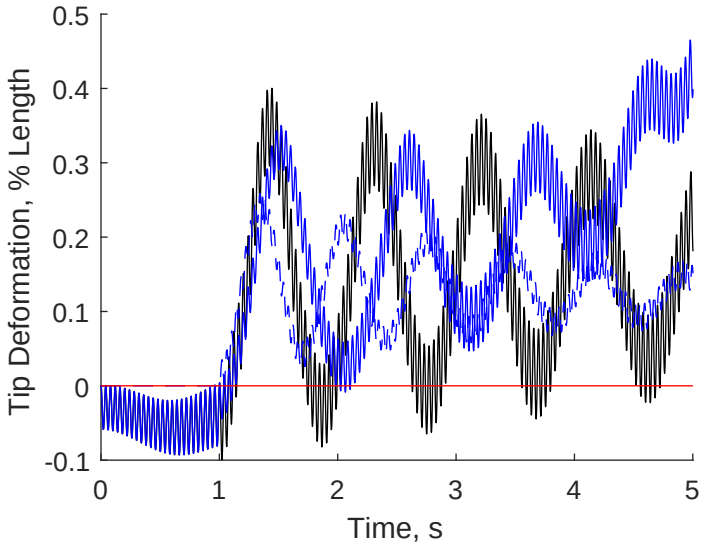

(b)

Figure 4.14: Vehicle response to step input

The step response shows a greater difference between the various modeling strategies as the jet interaction model has an accumulating effect over time. The engineering-level aerodynamic model with the ideal jet model shows similar high oscillation and lower amplitudes as in the impulse response. Compared to the CFD-based aerodynamic surrogate model and ideal jet model this leads to a lower level of acceleration

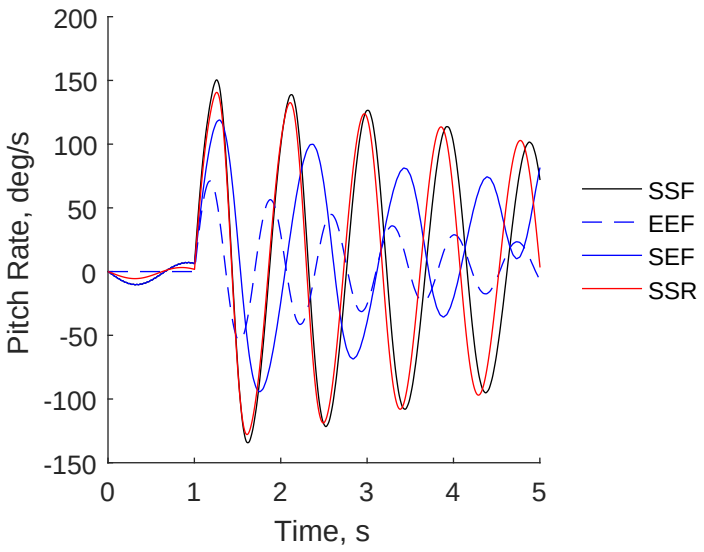

(a)

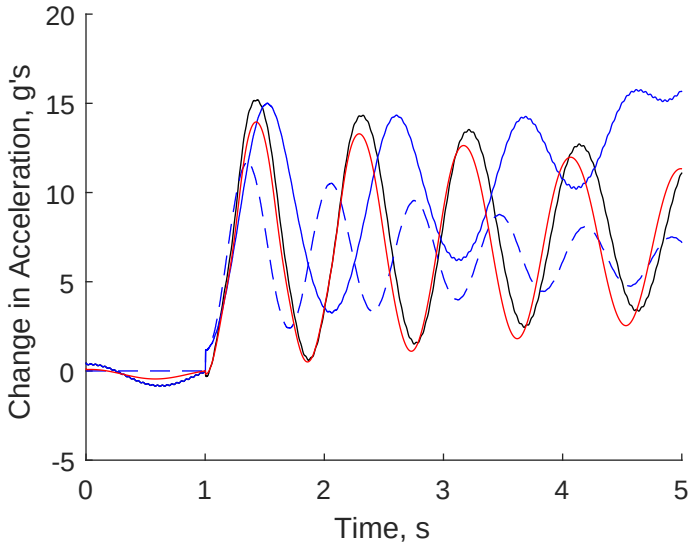

(b)

Figure 4.15: Vehicle maneuverability metrics due to the attitude jet step input

and pitch rate. As the vehicle deforms the CFD-based model continues to pitch upwards with the jet thrust applied. The simulation is stopped at 5 seconds, which corresponds to the 60-degree angle-of-attack limit on the CFD-based surrogate model used for this simulation. The ideal jet model with the CFD-based aerodynamics does not account for the jet interaction effect, which is shown to trend towards a value

less than unity for the normal force and pitch moment amplification factors (Figure 4.13). The jet interaction has a restoring effect at this pressure ratio due to the loss in control effectiveness (Figure 4.13). The ideal jet model should not be used in this case due to over-prediction of the effectiveness. The elastic model with CFD-based jet interaction and aerodynamics compared to the rigid vehicle model shows that the jet interaction has a very similar effect, but due to the change in aerodynamics the elastic model reaches higher angles of attack (Figure 4.14a) and thus higher accelerations normal to the flight path (Figure 4.15). The rigid model therefore under-predicts vehicle performance and adding elasticity to the system would increase maneuverability for these two-dimensional maneuvers.

4.4 Concluding Remarks

This chapter presented multiple modeling approaches to the jet interaction problem. The first modeling method is a new semi-empirical model that is constructed by combining analytical approximations from previous work found in the literature. The foundation is a two-dimensional semi-empirical model derived using flat plate experimental results. This part of the model is responsible for calculating the pressure distribution in the longitudinal plane of the jet due to boundary layer separation, shocks, and expansion waves. However, the results are only in relation to the flow direction and do not provide a three-dimensional pressure profile, which is desired for flight vehicle analysis. The second component of the new semi-empirical model is the combination of the blast wave equations with free-stream propagation. The blast wave equations are responsible for calculating the pressure distribution within the wave and the location of the propagating blast wave as a function of time. Taking into account the freestream propagation, the shock front due to the jet interaction along the surface is calculated as a function of distance in the flow direction. The

new model calculates the jet interaction pressure distribution in three dimensions for a range of flow and jet conditions by combining the 2-D semi-empirical flat plate model and the 3-D blast wave relations. The final aspect of the model is the use of the boundary layer separation profile from the 2-D model to approximate the pressure distribution ahead of the blast wave. Overall, the model that is presented in this chapter is a new contribution to the jet interaction modeling community that is capable of calculating the pressure distribution around a jet interacting with a supersonic crossflow and does not depend on surface geometry, flow conditions, or jet conditions.

The second approach follows a more traditional surrogate model development by recording snapshots of the CFD solution corresponding to various fluid, structure, and jet conditions. However, the model must accurately output the pressure distribution for the structural dynamics equations of motion in addition to traditional integrated quantities (e.g., lift, drag, and pitch moment). Therefore, the pressure distribution is first decomposed and represented using modal basis calculated using the SVD of the CFD surface solutions. The surrogate model then approximates the mode amplitudes and their relation to the input parameters. This approach greatly reduces the size of the surrogate model itself which is stored in memory and repeatedly evaluated during flight simulations.

Flight simulations of the vehicle with various modeling approaches for the aerodynamics, structural deformation, and jet interaction are presented. The simulation results reveal some trends in the vehicle response and performance that depend on the modeling approach and vehicle design. Specifically, the aerodynamic model comparison between the engineering-level and CFD-based surrogate reveals that the aerodynamic stiffness is over-predicted by the engineering-level approach and leads to incorrect amplitudes and frequency in the vehicle response. The jet interaction model has a significant impact during the step response and leads to an overall loss

in control effectiveness compared to the ideal jet model at the simulation conditions. The ideal jet model was sufficient for modeling the impulse input, but does not account for the change in flow conditions or structural deformation that changes the net force applied. The rigid vehicle model comparison to an elastic model reveals the change in performance predictions based on accounting for structural deformation and adding elasticity to the vehicle design. The overall trend is that the elastic vehicle deforms in the direction of the turn, which leads to a decrease in the restoring pitch moment compared to the rigid vehicle. The elastic vehicle then achieves higher angles of attack and accelerations compared to the rigid vehicle.

The third approach to jet interaction modeling is the multi-fidelity model that leverages the new semi-empirical model with sparsely sampled CFD solutions to improve the accuracy of the approximation without increasing run-time computational cost. The model development requires a sampling scheme that avoids a brute force approach and cross-validation with the selected high-fidelity samples. One of the main challenges to building a multi-physics model is the high-dimensionality of the model input that requires exponential increases in the number of samples required to cover the entire domain. Furthermore, the wide range and strong nonlinear behavior of a flexible supersonic flight vehicle with jet interaction places a further emphasis on nonlinear approximation methods. The advantage to using the co-Kriging approach is that the model regresses to the trend provided by semi-empirical approximation, which has some information about the aerodynamic and jet interaction physics and is not a capability afforded by simple Kriging.

Overall, the modeling approaches presented in this chapter address the previous gap in jet interaction model that exists between low and high-fidelity methods. The jet interaction modeling methodology presented demonstrates how data-fusion techniques can be used to reduce the additional computational cost to converge to a new jet interaction model from a purely aerodynamic model. In addition, the surface do-

main decomposition techniques using singular value decomposition reduced the highly dimensional surface mesh into jet interaction mode shapes that further reduced the number of degrees of freedom that needed to be approximated by the jet interaction model. Using a flight simulation framework enables the comparison of various designs and modeling approaches early in the design and development of high-speed vehicles. This work provides initial insight into the FSJI problem and a modeling methodology that can be built upon for further aeroelastic analysis of flexible high-speed vehicles with jet interaction.

CHAPTER 5

Fluid-Structure-Jet Interaction Sensitivity

This chapter addresses the third research objective presenting the sensitivity of the FSJI problem to changes in the fluid, structure, and jet parameters. Steady-state and dynamic high-fidelity simulations are presented to establish the sensitivity and level of interaction between disciplines prior to any model development. In addition, the variation of the FSJI dynamics across the flight envelope is presented. Finally, a modeling approach is presented and evaluated using the representative high-speed vehicle configuration.

5.1 Approach

The objective is to study the sensitivity of the FSJI problem under various flight conditions and jet conditions as well as structural deformations of a high-performance slender vehicle. This includes large angles of attack, sideslip angles, Mach number variations, altitude variation, jet total pressure, and moderate structural deformations (tip deflections up to 5% length). An exhaustive search of the domain space is not necessary for this analysis and a mean condition can be chosen about which the operating conditions can be varied. This provides the sensitivity of the vehicle load distribution to the operating conditions. The sensitivity is beneficial in identifying the system characteristics as well as determining how to efficiently model the system over a wide design space.

The operating conditions of the vehicle in Table 5.1 represent the bounds of the sensitivity analysis and surrogate modeling. Each of these parameters is varied to determine the change in the vehicle loads about the mean vehicle flight condition, as is listed in Table 5.2 for reference. CFD simulations of the vehicle are used to calculate the integrated forces and moments from the pressure and shear stress distribution. The *jet amplification factor* is used to understand the relative effect of the additional pressure distribution from the jet interaction with the external flow compared to the applied jet thrust.

Table 5.1: High-performance vehicle range of operating conditions.

Input	Minimum	Maximum	Units
Altitude	40	100	kft
Mach	2	4	-
Total Angle of Attack	-90	90	degrees
Roll Angle	-180	180	degrees
Structural Deformation (total tip displacement)	0	5	% length
Jet Total Pressure	0	10	MPa

Table 5.2: High-performance vehicle reference operating condition.

Input	Value	Units
Altitude	70	kft
Mach	3	-
Total Angle of Attack	0	degree
Roll Angle	0	degree
Structural Deformation (total tip displacement)	0	% length
Jet Total Pressure	*Off*	-

The numerical results begin with steady-state solutions to assess the sensitivity without dynamic effects. Next, simulations of the vehicle response to step changes in the fluid, structural, and jet conditions are presented. These results highlight the range of linearity about a reference condition. In addition, the step responses are calculated for various initial conditions and various step sizes. These results demonstrate the degree to which the dynamics vary across the flight envelope as well as extreme changes to the vehicle (e.g., large angles of attack and large jet pulses).

Finally, the vehicle response to various frequency inputs is presented along with model predictions. These results reveal the FSJI sensitivity to input frequency as well as the ability of a model to capture these effects.

Overall, the sensitivity of the vehicle load distribution is calculated as efficiently as possible for such a wide range of input parameters and a high-dimensional input domain. The sensitivity of each parameter can be calculated for its significance of including into a loads surrogate model. In addition, the transient jet interaction can be compared against the other components of the aeroelastic system to determine if a dynamics model is required or if the steady-state model will suffice.

The numerical results highlight the sensitivity of the steady-state and unsteady fluid-structure-jet interaction. First, the steady-state solution is computed for a range of fluid, structure, and jet parameters to calculate the jet amplification factor. These steady-state solutions provide the basis of the nonlinear correction term in the unsteady model. Second, the step response of the vehicle loads to changes in the fluid, structure, and jet parameters are calculated. The step responses are recorded for each discipline input individually with multiple amplitudes and multiple combinations. These step responses highlight the nonlinearity of the coupled dynamic interactions. These step responses are also calculated from varying initial conditions to asses the sensitivity of the dynamics to flight conditions. Next, the vehicle response to various frequencies of rigid-body motion, structural deformation, and jet pulses are evaluated that help define the boundary between quasi-steady and unsteady flow conditions. Finally, the unsteady model is developed using the step responses and steady-state solution. The model is then compared to the frequency sweep simulation results to assess the feasibility of the approach to the FSJI problem.

The L_2-norm relative error metric is used throughout to quantify the difference between different simulation results. For example, the percent relative error RE of

simulation output y_1 to y_0 is calculated as

$$RE = \frac{\|y_1 - y_0\|_2}{\|y_0\|_2} \times 100$$

5.2 Steady-State FSJI Sensitivity

The sensitivity of the steady-state solution was calculated about the mean flight condition of the vehicle model, which corresponds to Mach 3 at an altitude of 21 km. The angle of attack is varied up to 60 degrees, the structure is deformed using the first free-vibration bending mode up to 5% tip deflection, and the jet total pressure is varied up to 10 MPa. Tip deflection of 5% vehicle length is an upper bound and corresponds to a 76 g maneuver for this slender vehicle concept. The amplification factor for each simulation is calculated and presented for the lift and pitch moment coefficients in Figure 5.1. A decision boundary was calculated using a linear SVM with the presented data to help visualize the variation in jet interaction effects. This provides a best-fit separator between simulations with increased and decreased jet interaction amplification factor, which corresponds to increased and decreased control effectiveness across the various input parameters.

The results in Figure 5.1 show that the jet interaction at positive angles of attack has negative effect on the total lift coefficient with a peak reduction of about 50% for the cases studied. However, when the jet is on the leeward side of the vehicle the JI effect on the lift coefficient has a much smaller effect. The deformation of the vehicle has a limited effect on the lift, but a pronounced effect on the vehicle pitch moment coefficient. The jet interaction effect leads to a significantly reduced applied moment at high angles of attack, which is similar to the lift coefficient. This is due to a reduction in the boundary layer separation effect and a larger low-pressure expansion region acting on the vehicle. However, the jet interaction effect can lead

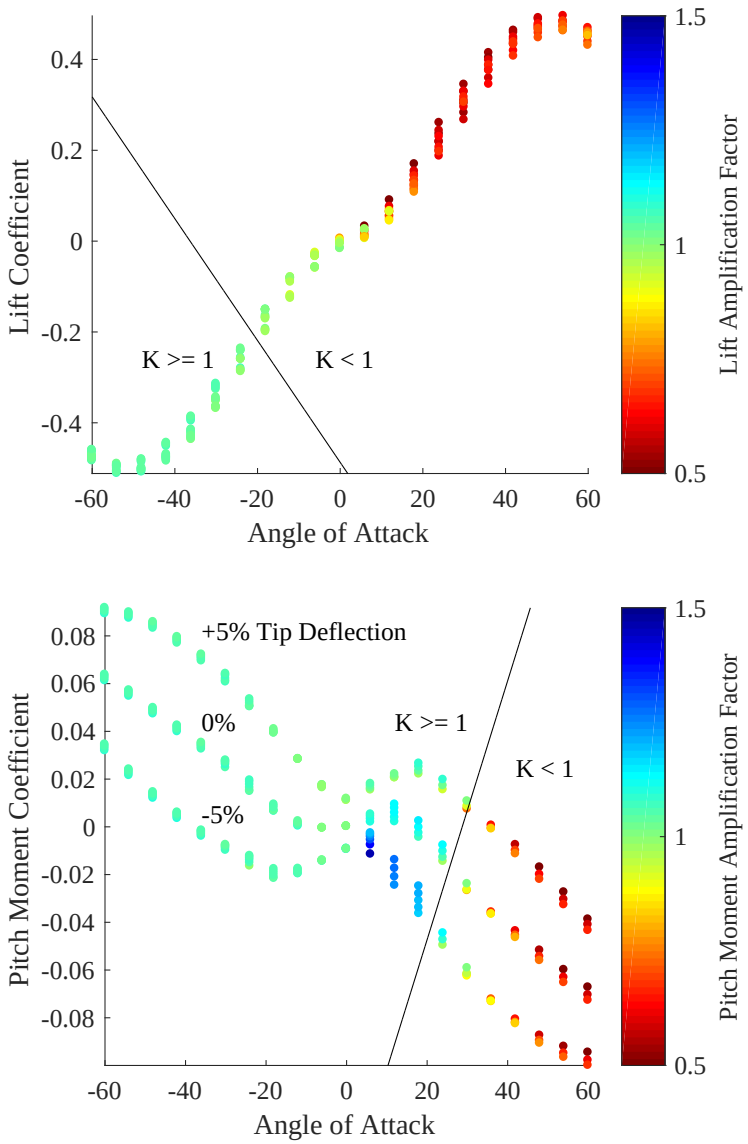

Figure 5.1: Amplification factor as a function of angle of attack, deformation, and jet total pressure. The lower attitude jet is used such that a positive AoA corresponds to a windward jet location. Red indicates a decrease in control effectiveness while blue indicates an increase in control effectiveness. The black line is a SVM fit to the data to highlight boundary between gain and loss in control effectiveness.

to a significant increase in the applied moment for tip-down deformation at small angles of attack. This effect is due in part to the placement of the jet. At these conditions there is significant boundary layer separation ahead of the jet exit, but the body is deformed away from the low-pressure expansion region behind the jet. The jet location for this vehicle configuration was chosen at quarter-length for simplicity,

but these results demonstrate that the location can be used to further exploit jet interaction with a flexible structure.

5.3 FSJI Step Responses

Step responses of the baseline vehicle to changes in the fluid, structure, and jet parameters are presented to identify the dynamics, asses the level of nonlinearity, and identify the coupling between each component associated with FSJI. The step input amplitudes are listed in Table 5.3, but to test the linearity of the dynamics the response to twice the step input was recorded as well. For a linear system the step response to twice the step input should equate to twice the amplitude of the single step response. The vehicle lift and moment coefficient response to each double step input are presented in Figures 5.2–5.4 from the CFD solution and linear approximation. These results highlight the level of nonlinearity at these conditions. The step responses represent the fluid dynamics response only without jet interaction except in the case of the jet step response.

Table 5.3: Amplitudes of the step inputs.

Domain	Parameter	Amplitude	Units
Fluid	Angle of Attack	5	deg
Structure	First Bending Mode	0.5	% L_{ref}
Jet	Attitude Jet Total Pressure	500	kPa
	PR	111	

Table 5.4 shows the L_2-norm relative error associated with the presented step response simulation results. The results of Figure 5.2 show that the fluid dynamics response to structural deformation is well approximated using a linear model. The jet interaction simulation results in Figure 5.3 shows some variation in the dynamics and steady-state value as the input is varied, which could have significant implications for a throttled jet as opposed to a constant amplitude jet. There is some level of nonlinearity to changes in the rigid-body motion as seen in Figure 5.4. These nonlinear

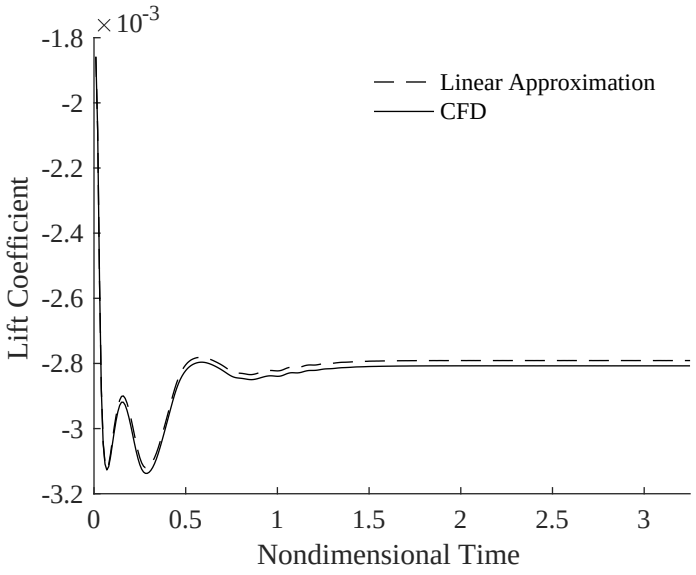

(a)

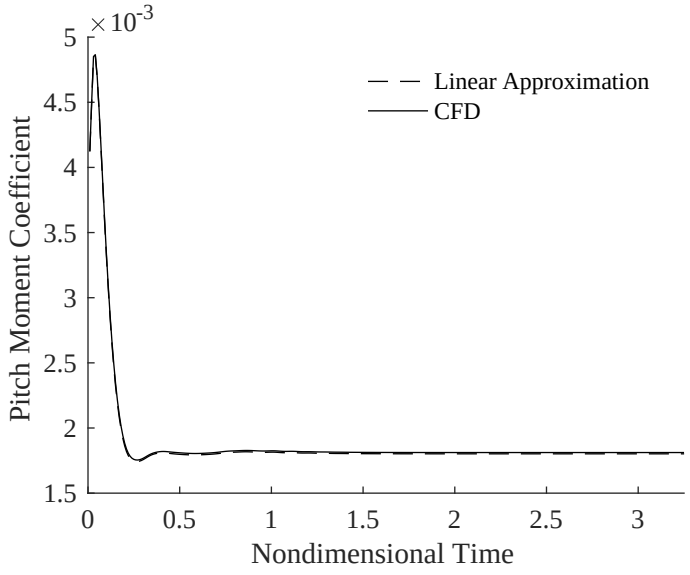

(b)

Figure 5.2: Linear approximation and CFD solution to a 1% L_{ref} step change in structural deformation.

dynamics will have an effect when modeling rigid-body dynamics coupled with the dynamics of the structure or jet.

Figures 5.5–5.7 show the coupled fluid dynamics and jet interaction response to simultaneous step changes in each of the fluid, structure, and jet parameters. The results in Figures 5.5 show that the coupled fluid-structure and structure-jet dynamics

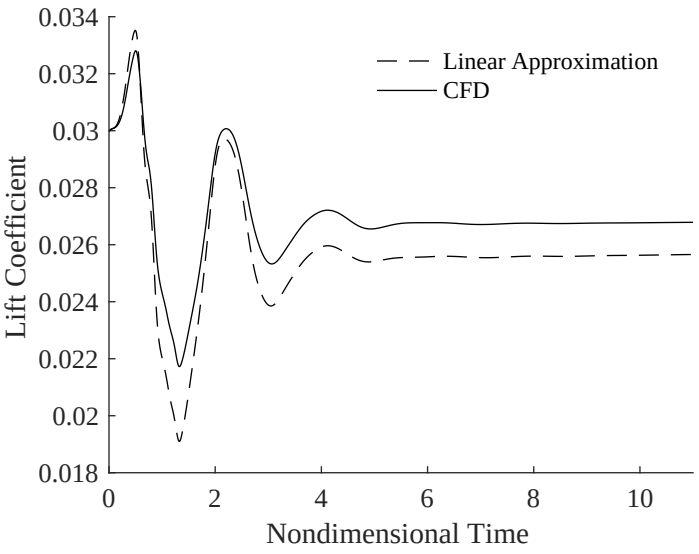

(a)

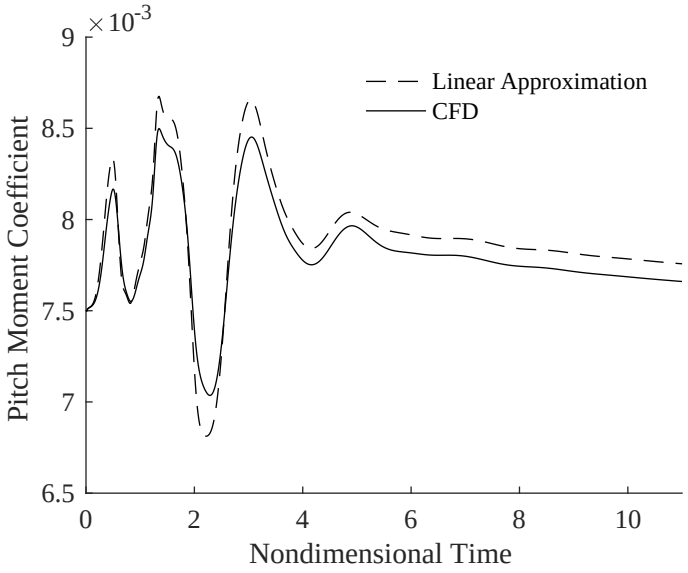

(b)

Figure 5.3: Linear approximation and CFD solution to a 1-MPa change in jet total pressure.

are well approximated by a linear model at these conditions. However, the fluid-jet response in Figures 5.6–5.7 shows some nonlinearity in the form of a delay in the response and significantly different amplitudes. The fully coupled fluid-structure-jet interaction step response is presented in Figure 5.8, which includes the same nonlinear features seen in the fluid-jet and structure-jet responses. The relative error

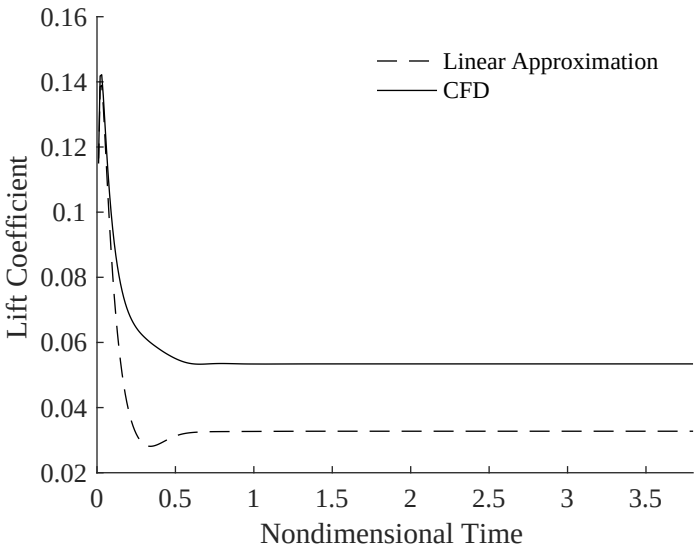

(a)

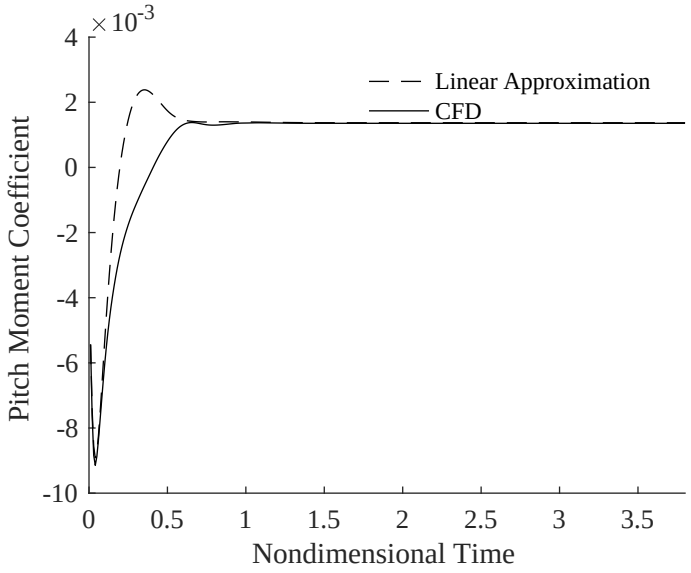

(b)

Figure 5.4: Linear approximation and CFD solution to a 10-degree step change in angle of attack.

in the coupled step response simulations compared to using a linear approximation is listed in Table 5.5. Overall, the jet interaction dynamics are more significantly affected by the a step change in the angle of attack compared with the step change in structural deformation. This translates to accurately modeling flexible vehicles with jet interaction and with rigid-body dynamics that are quasi-steady. As the

unsteadiness in the rigid-body dynamics increases this will lead to degradation in the reduced order model approximation.

Table 5.4: Relative error of the linear approximation to the CFD solution of step inputs.

Step Input	Lift Relative Error	Pitch Moment Relative Error
Structural Deformation (Fig. 5.2)	0.5%	0.5%
Jet Total Pressure (Fig. 5.3)	4.7%	1.5%
Angle of Attack (Fig. 5.4)	37%	43%

Table 5.5: Relative error of the linear approximation to the CFD solution of coupled step inputs.

Step Input	Lift Relative Error	Moment Relative Error
Fluid-Structure (Fig. 5.5)	5.2%	16%
Fluid-Jet (Fig. 5.6)	37%	29%
Structure-Jet (Fig. 5.7)	4.2%	7.2%
Fluid-Structure-Jet (Fig. 5.8)	38%	21%

5.3.1 FSJI Step Response Sensitivity to Flight Conditions

The variation of the step responses across the flight envelope is required for long-duration flight simulations. The ultimate goal is to simulate the flight dynamic response during aggressive maneuvers along an arbitrary flight path. If the underlying system dynamics are changing as a result of varying or extreme flight conditions, then the model must take this into account. The sensitivity of the FSJI dynamics is assessed by examining the step responses using varying step size and initial conditions. The step size and initial conditions are listed in Table 5.6. All sweeps include 21 points spaced according to Table 5.6 using the finned vehicle configuration.

The angle-of-attack step response across the flight envelope is presented first using a step size of 8.8 degrees. The altitude is varied first with a constant Mach number of 3, the steady-state solution is calculated, then the step response is calculated. The

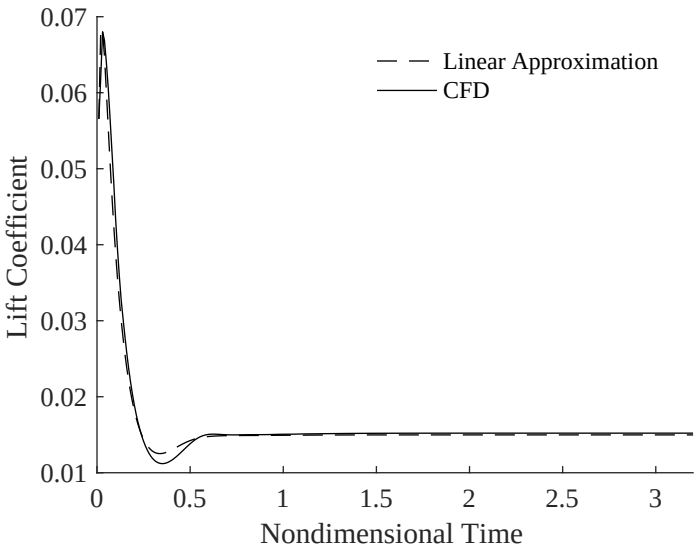

(a)

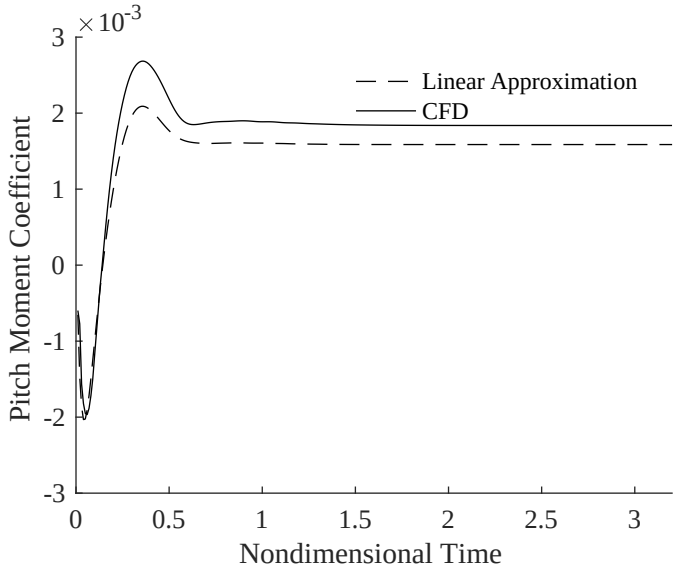

(b)

Figure 5.5: Coupled step responses to step changes in angle of attack (5 deg) and structural deformation (0.5% L_{ref}).

vehicle is kept at the undeformed condition with the jets off. The lift and moment coefficients are presented in Figure 5.9. Next, the Mach number is varied while the altitude is fixed at 70 kft and presented in Figure 5.10.

The angle-of-attack step response has negligible variation with altitude, but varies considerably with Mach number. The steady-state variation is approximately 30%,

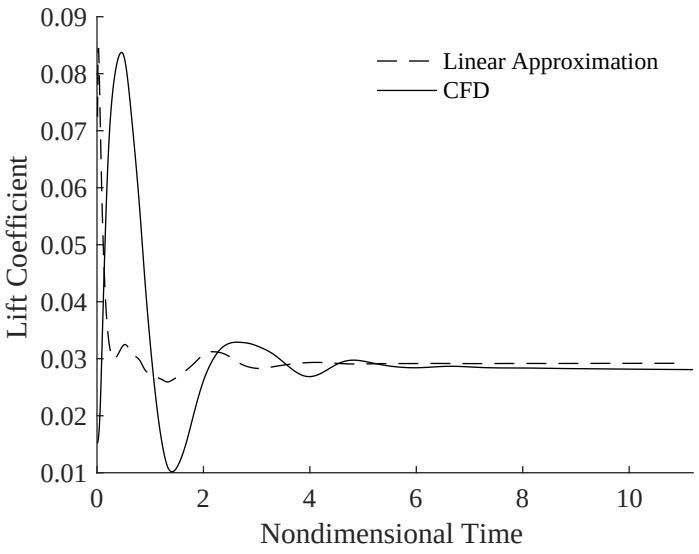

(a)

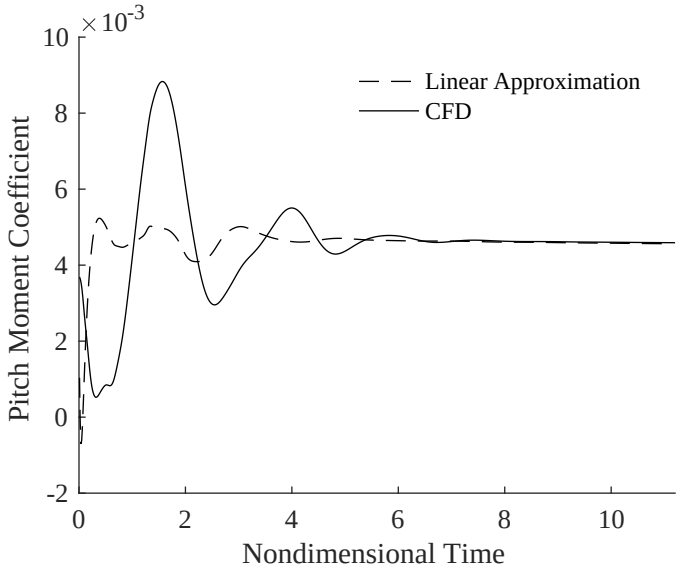

(b)

Figure 5.6: Coupled step responses to step changes in angle of attack (5 deg) and jet total pressure (500 kPa).

but the transient response varies significantly up to 50%. In particular, as the vehicle loses speed and Mach number decreases, the effect of the fins becomes more apparent. High-frequency maneuvers will require a detailed model that tracks how the fluid dynamics are changing due to Mach number.

Next, the angle-of-attack step response is calculated from varying initial angles

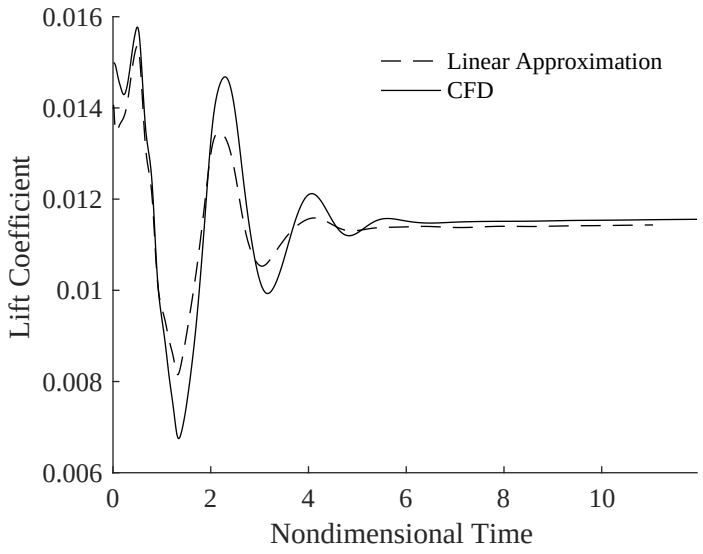

(a)

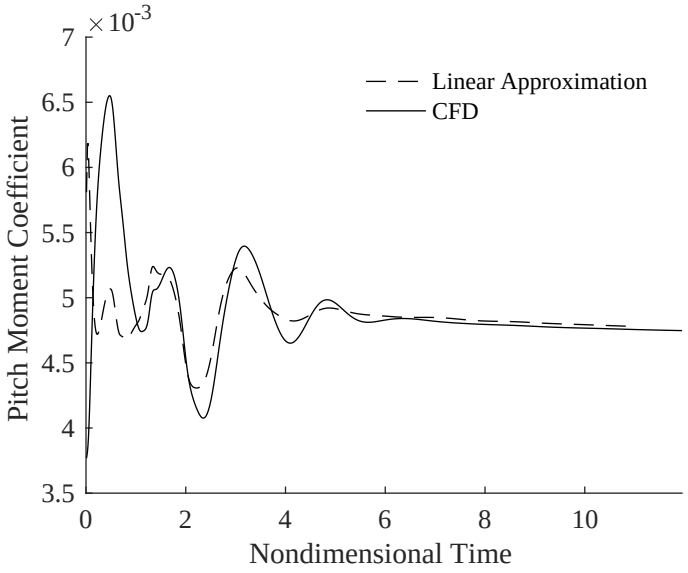

(b)

Figure 5.7: Coupled step responses to step changes in structural deformation (0.5% L_{ref}) and jet total pressure (500 kPa).

of attack and attitude jet pressures. These results indicate how the vehicle transient loads vary throughout a maneuver. The altitude and Mach number are kept constant at 70 kft and Mach 3 and the vehicle is restricted to the undeformed condition. The lift and pitch moment step responses to step changes in angle of attack with varying initial angle of attack and attitude jet pressure are shown in Figures 5.11 and 5.12.

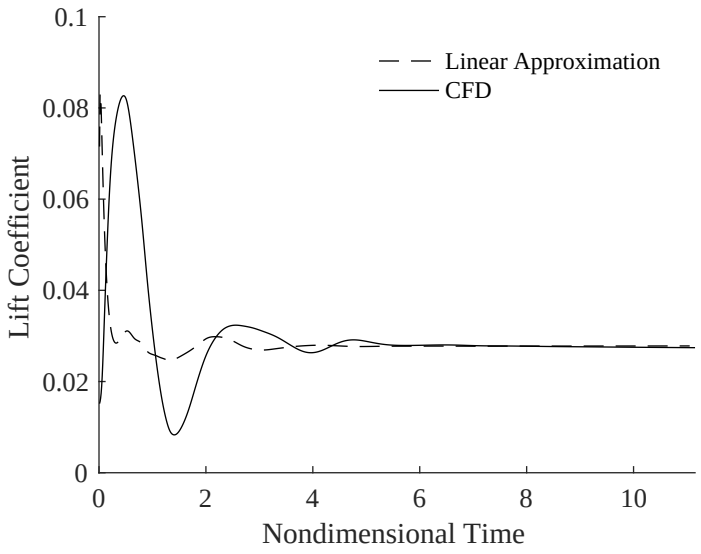

(a)

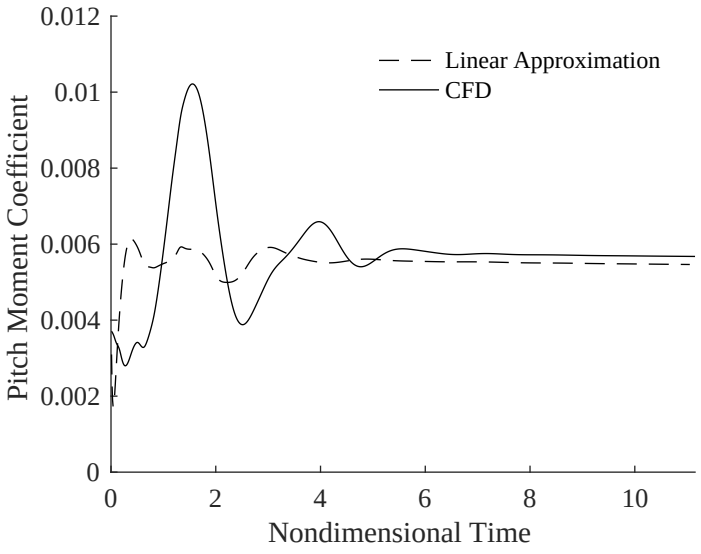

(b)

Figure 5.8: Coupled step response of simultaneous changes in angle of attack, structural deformation, and jet total pressure.

The results in Figures 5.11 show significant variation in the angle-of-attack step response as the initial angle of attack increases. The trend follows the steady-state results where the derivative of lift coefficient with AoA initially increases with AoA then decreases approaching the stall condition. Theses results suggest that aggressive maneuvers with high angle of attacks may require more detailed modeling schemes to

Table 5.6: Bounds for exploring the angle of attack and attitude jet step response sensitivity for the finned vehicle configuration.

Parameter	Minimum	Maximum	Units	Spacing
Mach	2	4		uniform
Altitude	40	100	kft	uniform
Angle of Attack	0	60	deg	cosine
Attitude jet total pressure	0	10	MPa	cosine

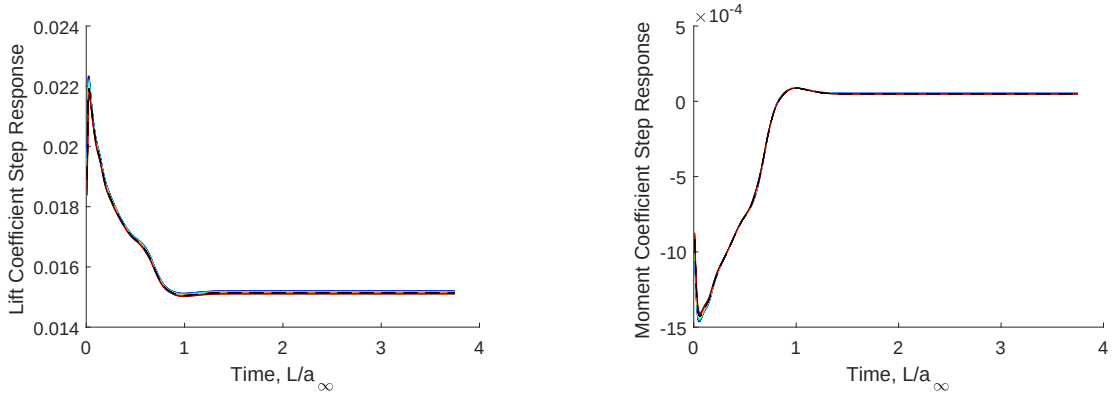

(a) Lift Step Response (b) Pitch Moment Step Response

Figure 5.9: Angle-of-attack step responses with varying altitude at Mach 3 for the finned vehicle configuration, red is high altitude, blue is low altitude.

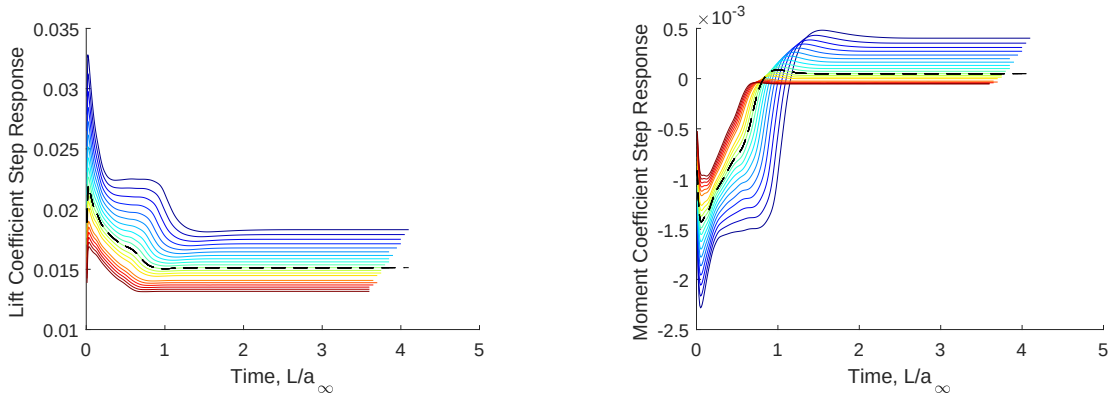

(a) Lift Step Response (b) Pitch Moment Step Response

Figure 5.10: Angle-of-attack step responses with varying Mach number at 70 kft for the finned vehicle configuration. Dashed line corresponds to Mach 3, red is high Mach number, blue is low Mach number.

simulate the vehicle response. The results in Figure 5.12 show that the jet interaction significantly affects the transient loads response to angle of attack perturbation. The steady-state values in Figure 5.12 converge to a similar level, but the transient re-

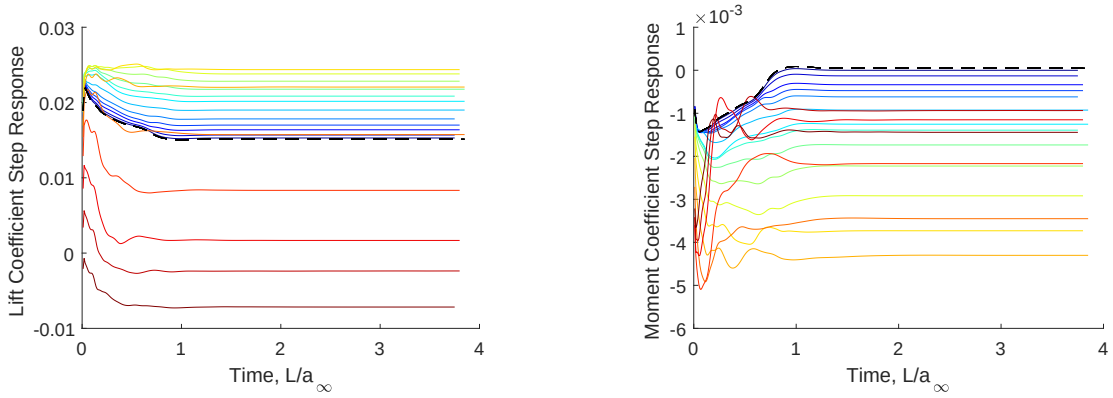

(a) Lift Step Response (b) Pitch Moment Step Response

Figure 5.11: Angle-of-attack step responses with varying initial angle of attack for the finned vehicle configuration. Dashed line corresponds to zero angle of attack, red is high angle-of-attack, blue is low angle-of-attack.

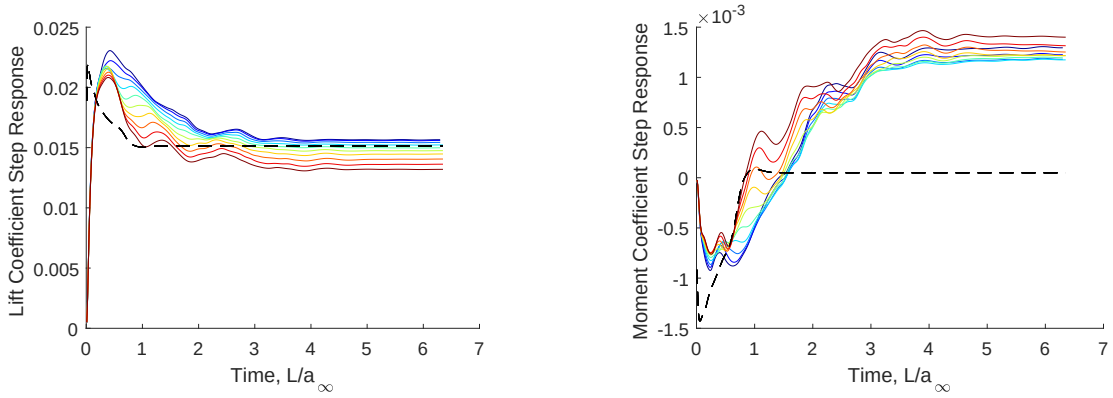

(a) Lift Step Response (b) Pitch Moment Step Response

Figure 5.12: Angle-of-attack step responses with varying attitude jet pressure for the finned vehicle configuration. Dashed line corresponds to the jet off, red is high jet pressure, blue is low jet pressure.

sponse is more sensitive to the attitude jet pressure. Closer examination around time equal to one suggests that this variation is due to the stronger jet-fin interaction.

Next, the attitude jet step response across the flight envelope is examined for the finned vehicle configuration varying flight conditions. The attitude total pressure step size is kept constant at 1.47 MPa. The altitude and Mach number are varied similarly to the angle of attack, the structure is kept at the undeformed condition, and the angle of attack is kept at zero. The lift and pitch moment step responses for varying altitude

and Mach number are presented in Figures 5.13 and 5.14, respectively.

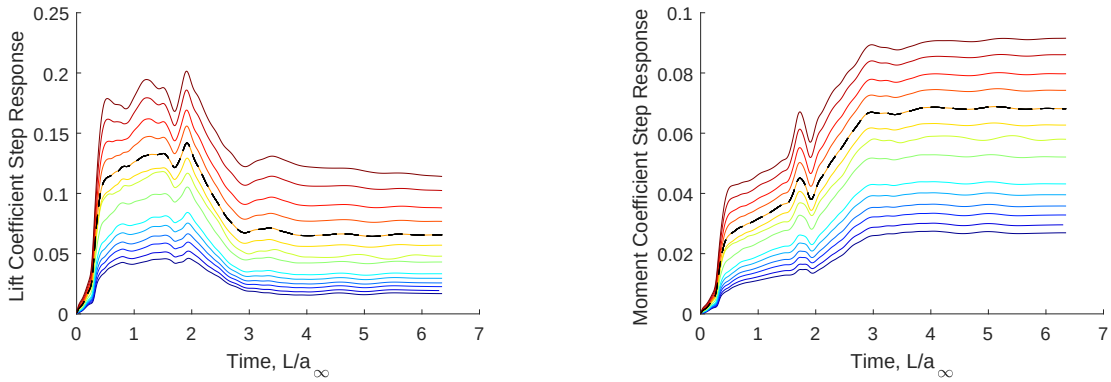

(a) Lift Step Response (b) Pitch Moment Step Response

Figure 5.13: Attitude jet step responses with varying altitude at Mach 3 for the finned vehicle configuration. Dashed line corresponds to 70 kft, red is high altitude, blue is low altitude.

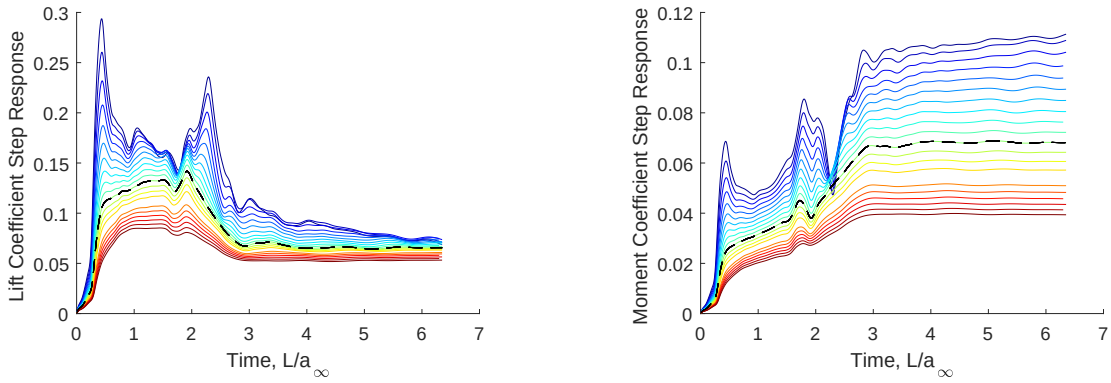

(a) Lift Step Response (b) Pitch Moment Step Response

Figure 5.14: Attitude jet step responses with varying Mach number at 70 kft for the finned vehicle configuration. Dashed line corresponds to Mach 3, red is high Mach number, blue is low Mach number.

The results in Figures 5.13 and 5.14 show a wide variation in the lift and pitch moment due to jet interaction across the flight envelope. The transient response oscillates significantly for low Mach number and high altitude conditions. The control authority also is the highest at these conditions, which would be the opposite trend of deflecting the fins at the same conditions. Overall, there is a significant variation in the steady-state and transient response that requires Mach number and altitude

to be included in jet interaction modeling ROMs. The jet interaction step response sensitivity to freestream flow conditions poses a challenge for modeling pulsed jets during vehicle maneuvers. Methods that do not rely on using a constant step response during maneuvers may be required to develop an accurate model such as the effective dynamics approach as introduced in Chapter 2

Next, the attitude jet step responses are calculated from varying initial angle of attack and jet pressure similar to the angle of attack study. The lift and pitch moment responses corresponding to the varying initial angle of attack and jet total pressure are presented in Figures 5.15 and 5.16, respectively.

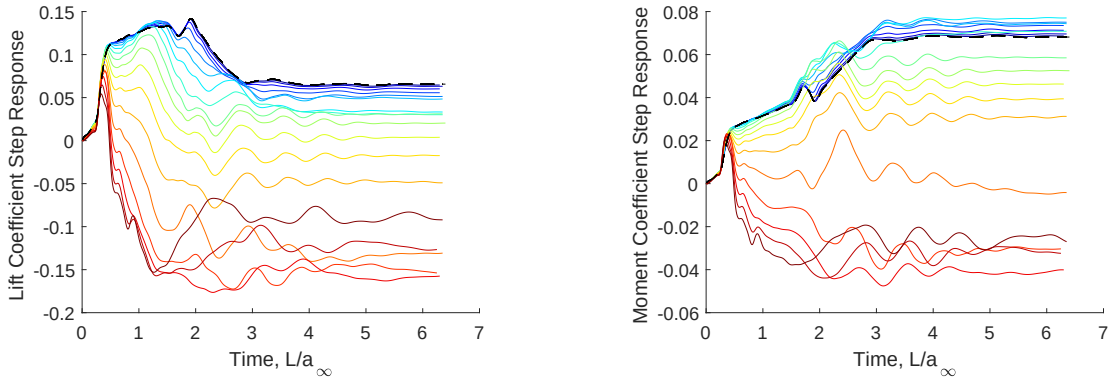

(a) Lift Step Response

(b) Pitch Moment Step Response

Figure 5.15: Attitude jet step responses with varying initial angle of attack for the finned vehicle configuration. Dashed line corresponds to zero angle of attack, red is high angle of attack, blue is low angle of attack.

The jet step responses with varying initial angle of attack (Fig. 5.15) show that the transient and steady-state responses are consistent at low angles of attack. If the jet is only fired at low angles of attack, then this could be taken into account during model development and reduce the angle of attack dependence. However, the jet step responses at high angles of attack vary significantly from the reference zero angle of attack response. When the jet is fired at a high angle of attack, there is an initial positive force and moment component due to jet interaction that decays over time and may become negative. These negative values indicate a loss in control effectiveness.

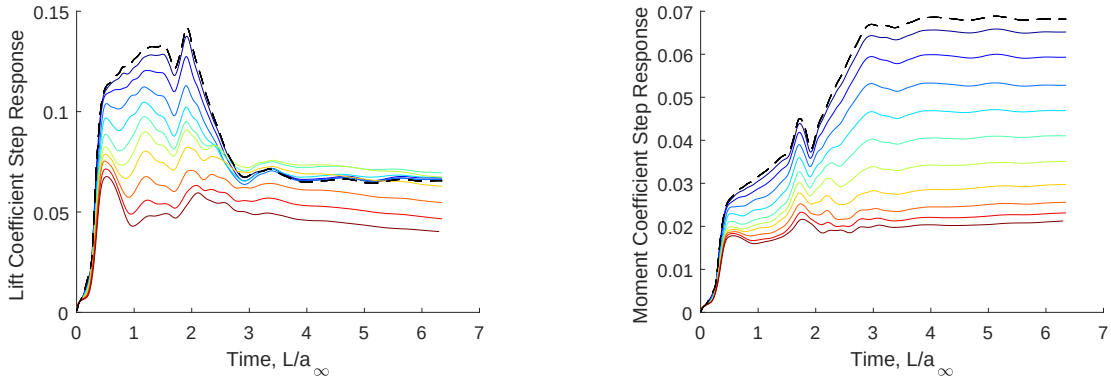

(a) Lift Step Response

(b) Pitch Moment Step Response

Figure 5.16: Attitude jet step responses with varying attitude jet pressure for the finned vehicle configuration. Dashed line corresponds to the jet off, red is high jet pressure, blue is low jet pressure.

The jet lift and pitch moment coefficient at these conditions due to thrust alone are equal to 0.045 and 0.034, respectively. Therefore, firing the jet at the highest angles of attack leads to control reversal.

The jet step responses with increasing jet total pressure (Fig. 5.16) show something similar to a throttled jet, increasing the jet thrust when the jet is already providing some thrust. The results show that the sensitivity to the same step input varies significantly with an approximately 50-60% decrease in the applied force and moment. There are diminishing returns in the favorable jet interaction effects at the higher jet total pressures. This effect could be used to size the attitude jet required for maneuvering. By leveraging the favorable JI for low thrust values, the jet system could be smaller and still effective. Also, depending on the purpose of the jet, *i.e.*, provide lift or pitch moment, the high frequency pulses that excite the transient response would increase lift while steady-state responses would be better for generating pitch moment.

5.4 Dynamic FSJI Sensitivity

The dynamic vehicle response using the finless configuration is calculated for varying frequency rigid-body pitch motion, structural deformation, and jet pulses. Reduced frequencies of 0.01, 0.1, and 1.0 were chosen to compare quasi-steady and unsteady conditions. Reduced frequency $\bar{k}$ is calculated as,

$$\bar{k} = \frac{\omega L_{ref}}{2U_\infty} \tag{5.1}$$

where ω is the circular frequency, L_{ref} the vehicle length, and U_∞ the freestream velocity. The results in Figures 5.17–5.19 show that the unsteady effects are significant for reduced frequencies above 0.1. The effect of jet interaction changes at high frequencies of rigid-body motion with the peak reduction in lift coefficient shifting to a lower rigid-body pitch angle. The jet interaction effect is relatively unchanged for high frequency structural deformation and the peak increase in applied moment is consistently at the maximum tip-down deformation.

Figures 5.20 and 5.21 show the step response normalized by the input cycle time of the jet. The response to turning the jet off is inverted to overlay onto the jet-on response and shows very similar behavior. The responses are consistent at low frequencies at or below $\bar{k} = 0.1$. However, at high frequencies the amplitude of the response increases to approximately twice the peak value of the quasi-steady responses and the peak reduction is approximately half of the quasi-steady response. This is due to the high-pressure region ahead of the jet exit due to the normal shock and boundary layer separation developing faster than the low-pressure expansion region. This effect can be visualized using the Mach contours of the y-symmetry plane shown in Figure 5.22. Each snapshot from the simulation is marked as a fraction of the force input period T where

$$T = \frac{2\pi}{\omega}. \tag{5.2}$$

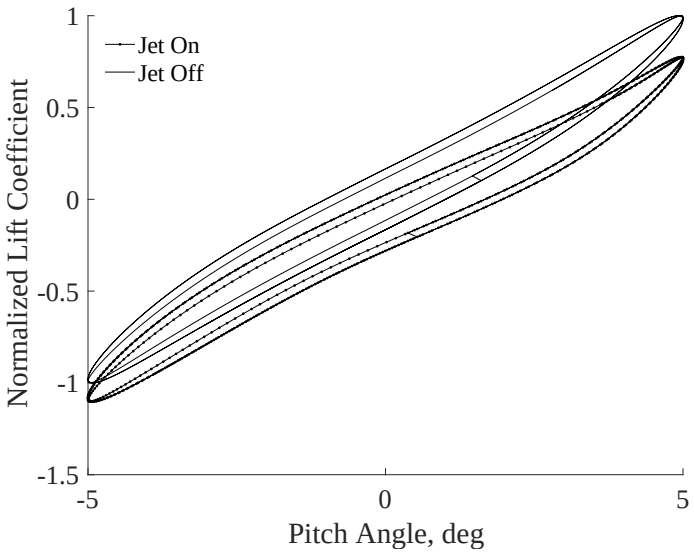

(a)

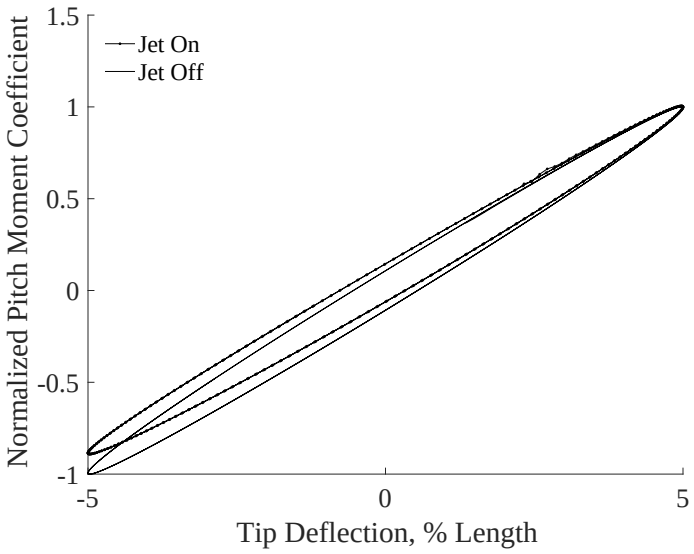

(b)

Figure 5.17: Frequency sweep of rigid-body motion and structural deformation at reduced frequency $\bar{k} = 0.01$. Coefficient values are normalized by the maximum absolute value of the quasi-steady solution for comparison.

At $t = \frac{1}{8}T$ after the jet is turned on the normal shock is fully developed while the low pressure expansion region is still developing and covers a small portion of the vehicle. At $t = \frac{4}{8}T$ the jet is turned off and for $t > \frac{4}{8}T$ the low pressure expansion region is seen being convected downstream while the high pressure region dissipates.

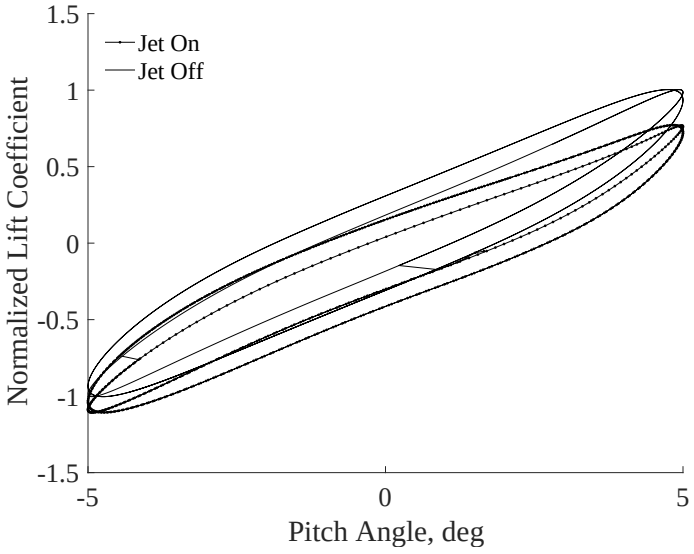

(a)

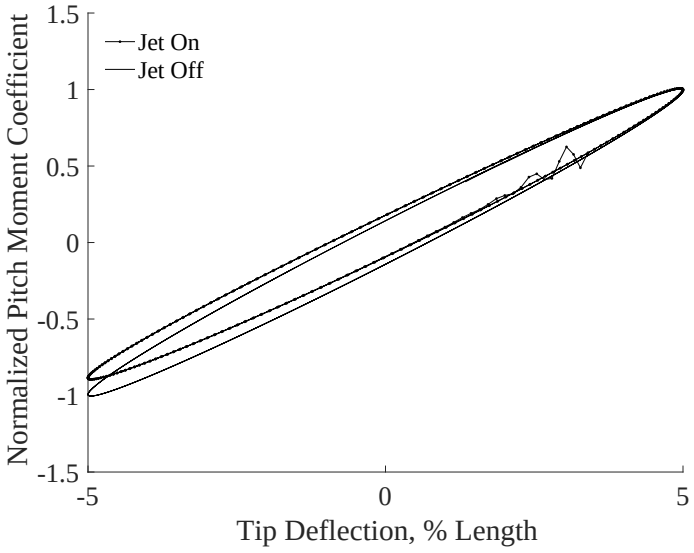

(b)

Figure 5.18: Frequency sweep of rigid-body motion and structural deformation at reduced frequency $\bar{k} = 0.1$. Coefficient values are normalized by the maximum absolute value of the quasi-steady solution for comparison.

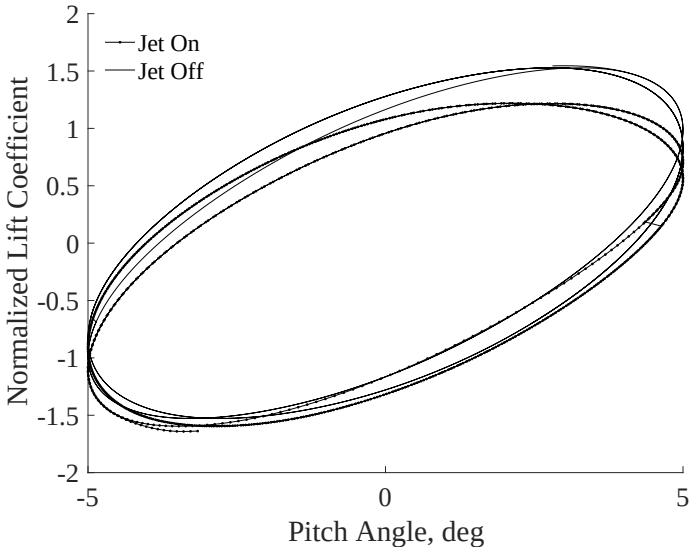

(a)

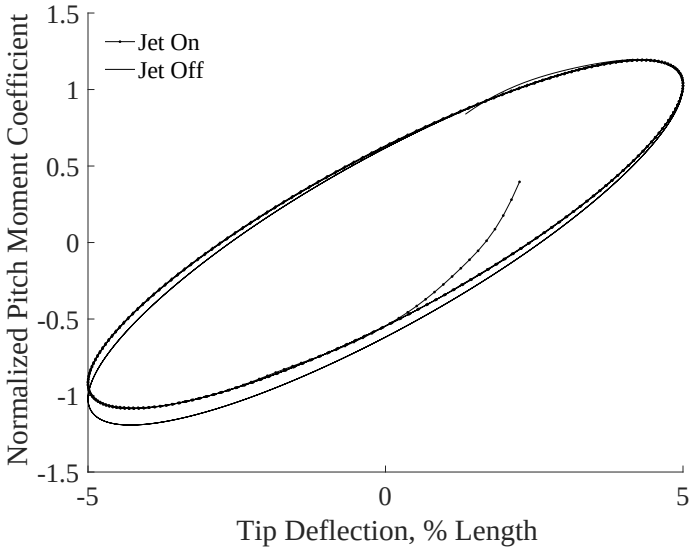

(b)

Figure 5.19: Frequency sweep of rigid-body motion and structural deformation at reduced frequency $\bar{k} = 1.0$. Coefficient values are normalized by the maximum absolute value of the quasi-steady solution for comparison.

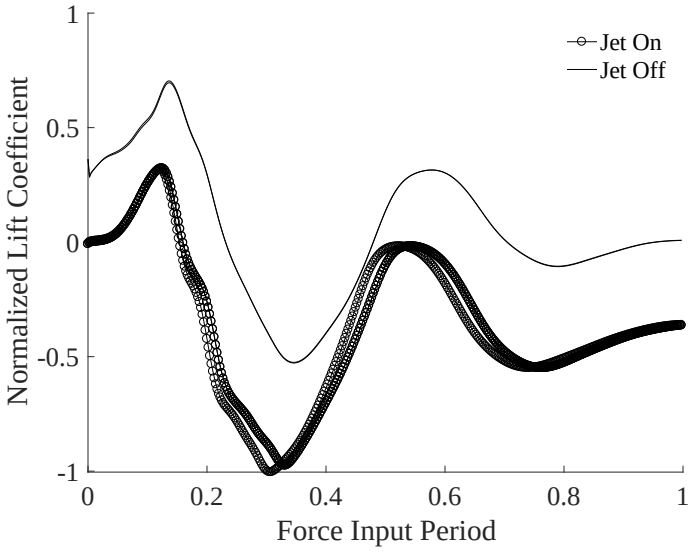

(a) $\bar{k} = 0.01$

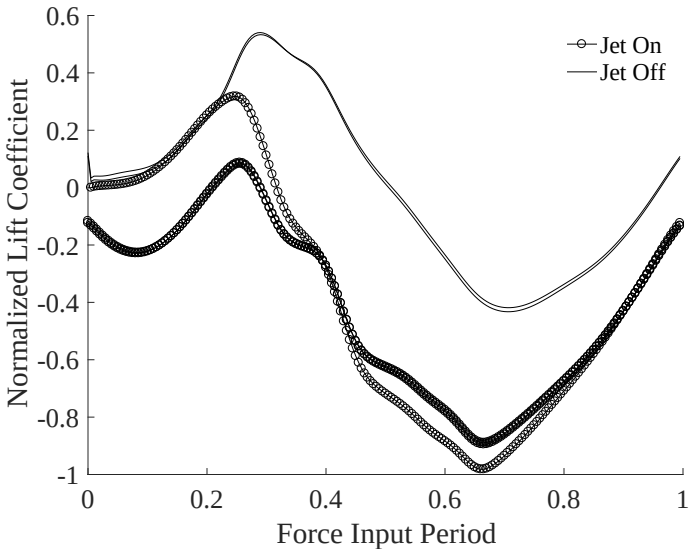

(b) $\bar{k} = 0.1$

Figure 5.20: Frequency sweep of jet pulses from the attitude control jet. The jet-off values have been multiplied by a factor of -1 to align with the jet-on values and coefficient values are normalized by the maximum absolute value of the quasi-steady solution for comparison. Multiple curves are shown due to overlay of the results from each of the three cycles.

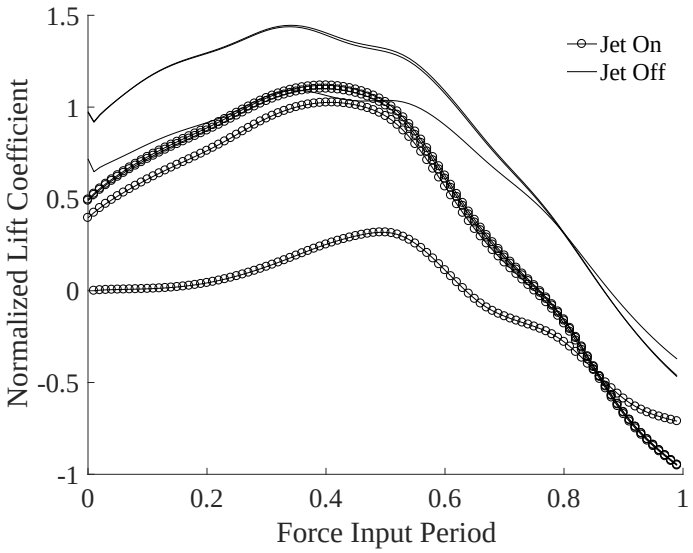

(a) $\bar{k} = 1.0$

Figure 5.21: Frequency sweep of jet pulses from the attitude control jet. The jet-off values have been multiplied by a factor of -1 to align with the jet-on values and coefficient values are normalized by the maximum absolute value of the quasi-steady solution for comparison. Multiple curves are shown due to overlay of the results from each cycle.

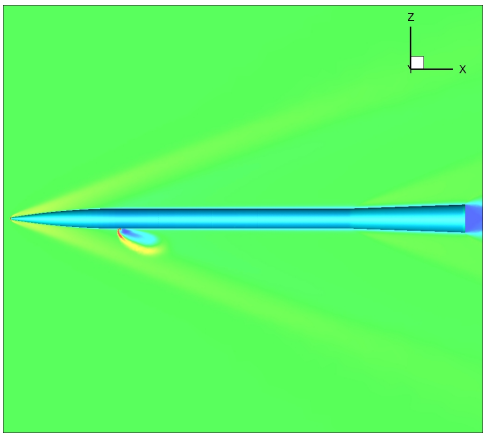

(a) $t = \frac{1}{8}T$

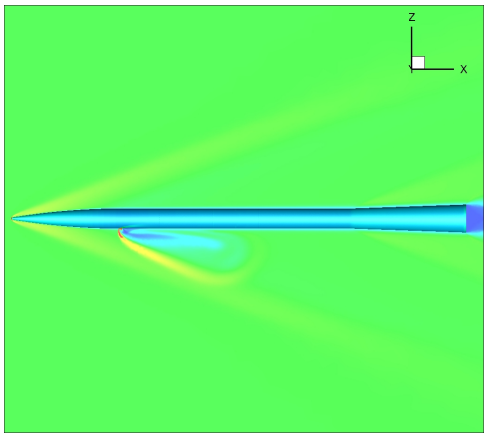

(b) $t = \frac{2}{8}T$

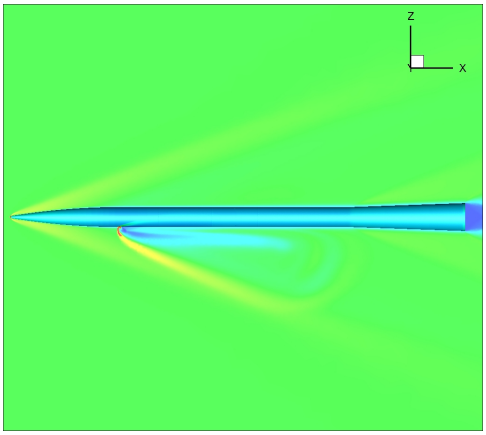

(c) $t = \frac{3}{8}T$

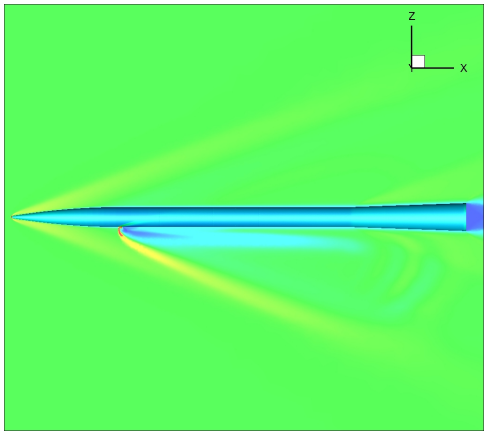

(d) $t = \frac{4}{8}T$

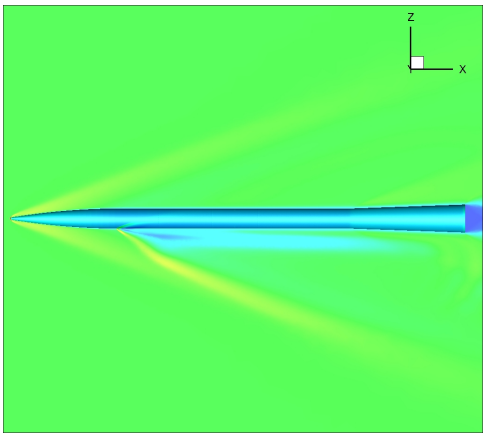

(e) $t = \frac{5}{8}T$

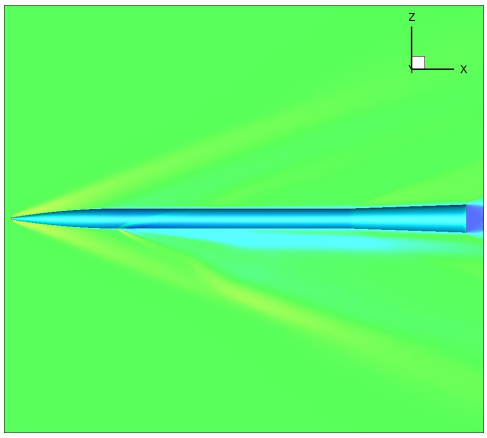

(f) $t = \frac{6}{8}T$

Figure 5.22: Mach contours at several simulation snapshots of the dynamic jet input at the highest frequency $\bar{k} = 1.0$ where T is the period.

5.5 Concluding Remarks

First, the steady-state jet interaction sensitivities to large angles of attack, structural deformation, and jet total pressure were presented. The results showed that the jet interaction has a large effect when the jet is located on the windward side of the vehicle that leads to decreases in the applied force and moment to the vehicle. However, specific combinations of structural deformation and angle of attack lead to significant increases in the applied moment due to jet interaction. Overall, the structural deformation has a small effect on the normal force, but a significant effect on the vehicle pitch moment. In particular, the applied moment is amplified in the direction of the tip deformation, which can be exploited with control inputs to the jets that induce this type of deformation.

Second, the dynamic sensitivity of the problem due to step responses in the flow, structure, and jet were presented. The results demonstrated that a linear model can be used to accurately model the fluid response to structural dynamics, but may not be adequate for rigid-body and jet dynamics. In addition, these results indicated that the transient jet interaction response time may be much longer than the aerodynamic response time. The step responses to changes in angle of attack and attitude jet pressure were presented for different flight conditions as well as initial angle of attack and attitude jet pressure. The results show that there is a significant variation in the dynamic responses even for small differences in initial conditions, which must be taken into account for flight simulation models. The results also highlight the regions in the flight envelope as well as particular flow and jet conditions that can greatly affect the control effectiveness of the jet. Reduced control effectiveness and control reversal was observed as well at high angles of attack using a moderate amount of jet thrust. These cases would require larger thrust values than expected to maintain control effectiveness in an aggressive maneuver with JI taken into account.

Time-accurate dynamic simulations of the finless vehicle with dynamic fluid, struc-

ture, and jet inputs were presented to study the effect of a dynamic environment on the FSJI problem. The vehicle response for low frequency inputs, reduced frequency approximately less then 0.1, did not exhibit significant unsteadiness. Reduced frequency of 1.0 led to significant unsteady effects in the flow and particularly for the jet pulses. The high-frequency jet response led to a significant increase in the applied load leveraging the lag in the jet interaction flow structure. These results help identify the bounds for when an unsteady loads model may be required for a maneuvering vehicle. Jet interaction dynamics may always require a dynamic model due to the longer time scale compared to the fluid dynamics response to rigid-body motion and structural deformation.

Overall, the fluid-structure-jet interaction sensitivity to changes in flight conditions and control inputs was assessed . The angle of attack and attitude jet pressure in particular have a significant nonlinear effect on the transient and steady-state loads on the vehicle. The transient response to jet interaction dynamics and the effect of rigid-body dynamics on jet interaction was largely missing in the literature. This sensitivity study fills the gap in these two areas by introducing rigid-body dynamics and large angles of attack with transient jet pulses.

CHAPTER 6

Modeling Unsteady Fluid-Structure-Jet Interactions over Multiple Flight Regimes

This chapter addresses the fourth research objective, modeling the dynamics of a highly-maneuverable supersonic vehicle over a range of flight and maneuver conditions. Specifically, a model for the fluid-structure-jet interaction problem is developed based on current state-of-the-art and newly developed methods to evaluate the viability of these approaches for a highly nonlinear high-dimensional problem. First, an extension of the convolution-based dynamics modeling method is presented that focuses on identification of vehicle dynamics at selected points throughout the flight envelope. Second, the effective dynamics approach is used with a sample numerical problem to highlight the relative strengths and weaknesses for modeling nonlinear dynamics. Due to the nature of a maneuverable high-speed vehicle with arbitrary trajectory, these approaches are critical to accurately predicting the FSJI dynamic loads throughout the flight simulation.

6.1 Steady-State and Dynamic FSJI Modeling

First, a steady-state model is developed to account for nonlinear effects since the convolution-based modeling approach is based on the linear dynamics. The steady-state model approximates the load distribution to calculate rigid-body and structural

forces on the vehicle at a combination of fluid, structure, and jet conditions within the flight envelope. This section details the steady-state modeling development from initial sampling to cross-validation.

The surrogate model is based on several samples of the CFD steady-state solution of the vehicle. Latin-Hypercube Sampling [67] was used to calculate the sample coordinates within the 9 dimensions for the model input. This approach was selected to develop a pseudo-random sampling of the input domain as opposed to a uniform grid sampling. In addition, the parameters were processed to produce a sample set that creates clusters near the mean condition expected for the vehicle. Table 6.1 lists the 9 pre-processed inputs and Table 6.2 the final inputs for the model. Figure 6.1 shows the distribution of the final inputs that features the clusters near the origin of the flow, structure, and jet parameters.

The flow and structure input parameters are clustered using a polar coordinate system based on the total value (e.g., total deformation) and an angle to relate two of the dimensions in the final surrogate model. The jet parameters are related using an artificial spherical coordinate system. The *jet throttle* is the coordinate from 0 to 1 that corresponds to the minimum and maximum jet total pressure. A negative jet throttle value corresponds to the jet located on the opposite side in the body z-coordinate direction. The three reference jets *attitude*, *divert 1*, *divert 2* are the jets on the positive-z vehicle surface that correspond to positive y-rotation, negative x-rotation, positive x-rotation using the body-fixed coordinate system with x-axis out the nose, y-axis starboard, z-axis forming a right-handed system (Figure 3.1).

The unsteady component of the vehicle loads is required to accurately represent the dynamic flow, structure and jet conditions. These unsteady effects vary depending on the flight conditions, which must be accounted for in the surrogate model development. The linear convolution of step or impulse responses has been used in the past [42, 49] to approximate the response at unsampled flight conditions. This

Table 6.1: Latin hypercube sample parameters and their sampling ranges.

Parameter	Range	Units
Altitude	12–30 (40–100)	km (kft)
Mach	2–4	
Total incidence angle	0–120	deg
Roll angle	−180–180	deg
Total structural deformation	0–5	% L_{ref}
Deformation body-frame angle	−180–180	deg
Jet throttle	0–10	MPa
Jet lateral angle, θ	−180–180	deg
Jet vertical angle, ϕ	0–180	deg

Table 6.2: Surrogate model inputs and their corresponding sampling ranges. Negative jet pressure indicates reverse orientation.

Parameter	Min	Max	Unit
Altitude	12	30	km
Mach	2	4	
Angle of Attack	−120	120	deg
Angle of Sideslip	−120	120	deg
Longitudinal first bending mode normalized tip displacement	−5	5	% L_{ref}
Lateral first bending mode normalized tip displacement	−5	5	% L_{ref}
Attitude jet throttle	-10	10	MPa
Divert jet 1 throttle	-10	10	MPa
Divert jet 2 throttle	-10	10	MPa

chapter examines the applicability of the convolution with nonlinear correction factor approach by Skujins and Cesnik [42] to the unsteady FSJI problem over its flight envelope.

In this study the inputs are parameters from the fluid, structure, and jet domains listed in Table 6.3. For each input, a step change equivalent to 1% of the max amplitude of the input parameter is applied and the change in the vehicle loads is calculated. The unsteady loads, y, are approximated using a linearized model during the simulation. The nonlinear loads, $y^u_{nonlinear}$, are then calculated by using the nonlinear correction factor approach described in Chapter 2.

The time history of each input, u^i, is convolved with the step response, H^j_i, to approximate the change in output, y^j, during the flight simulation. Finally, the

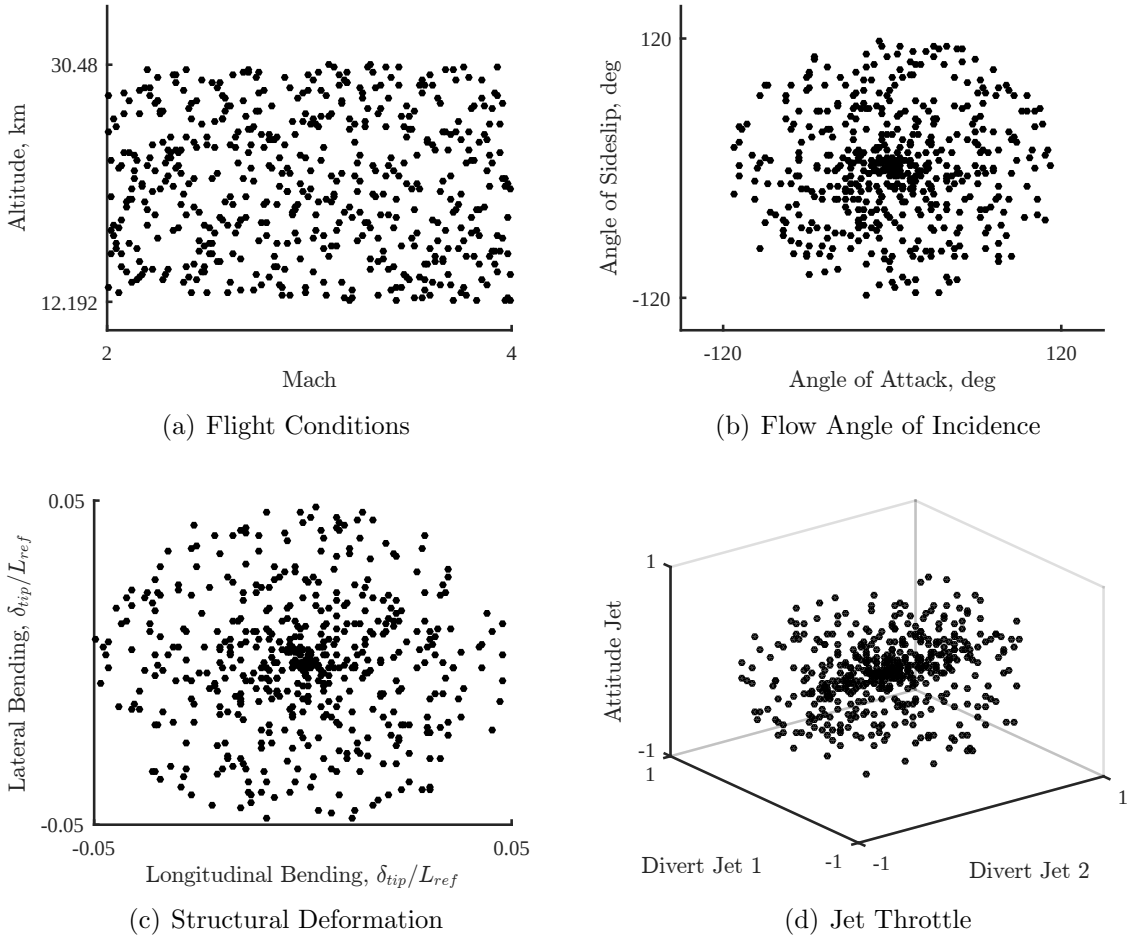

(a) Flight Conditions

(b) Flow Angle of Incidence

(c) Structural Deformation

(d) Jet Throttle

Figure 6.1: Ranges of the steady-state CFD samples across 9 model input dimensions of the flow, structure, and jet parameters across the flight envelope.

Table 6.3: Input parameters for the unsteady FSJI surrogate model construction.

Parameter	Range	Units
Altitude	12–30 (40–100)	km (kft)
Mach	2–4	
Angle of Attack	0–120	deg
Angle of Sideslip	0–120	deg
Normalized Tip Displacement	0–5	%
Jet Total Pressure	Off–10	MPa

vehicle loads at time index n are evaluated as the linear combination of all the step response convolutions in addition to the original steady-state loads. The load $y^j[n]$

is expressed as,

$$y^j[n] = y^j[0] + \sum_{i=1}^{m} \sum_{k=1}^{n} H_i^j[n-k] \left(u^i[k] - u^i[k-1] \right) \tag{6.1}$$

where m is the number of inputs. The step responses are known at the sampled flight conditions, but must be approximated as the vehicle maneuvers and the conditions change. Therefore, a Kriging model for how the step responses vary is created using the flight conditions, altitude, and Mach number to approximate the step responses $\tilde{H}_i^j$.

6.2 Steady-State and Dynamic FSJI Model Evaluation

The quality of the steady-state surrogate model and the linear unsteady models is assessed in this section using a cross-validation approach. Then, the combined unsteady nonlinear approximation is compared against a CFD simulation with varying flight conditions.

The leave-one-out approach is used as the cross-validation technique, which recursively removes one of the training samples to create a new surrogate model. The new model is then evaluated at the removed training point and the known removed solution is used as the reference to measure the level of error. This approach is especially useful with expensive simulations that limit additional sampling for verification and test purposes.

The first CFD verification maneuver is a forced motion simulation of the vehicle over a range of flight conditions. The vehicle orientation is prescribed at each time-step to simultaneously vary the angle of attack with a time-varying frequency. No structural deformation is prescribed during the simulation due to limitations on the

code.

A second CFD verification maneuver that includes structural deformation along with the jet interaction component is presented. The structural deformation is prescribed as a sinusoidal signal with constant frequency and increasing amplitude at an unsampled flight condition. This simulation tests the capability of the nonlinear correction factor approach in addition to the quality of the steady and unsteady surrogate models.

6.2.1 Steady-State Model Verification

The steady-state model is used to approximate the applied loads to the high-speed vehicle due to changes in the flight conditions in addition to the flow, structure, and jet parameters. Specifically, this model calculates the approximate surface pressure applied to the vehicle surface, which can then be integrated to calculate the six rigid-body forces and moments and the generalized loads for each structural deformation mode. The leave-one-out method is used to measure the quality of the surrogate steady-state model using the Median Absolute Error (MAE) in the pressure normalized by the freestream dynamic pressure as well as the MAE of the integrated forces. The relative errors in the integrated forces, moments, and generalized forces are deleted for each leave-one-out evaluation. The statistics of these errors are described in terms of the 95% confidence interval of the median for each error metric and presented in Table 6.4. A sample from the cross-validation of the surface pressure surrogate model is presented in Figure 6.2 with the conditions listed in Table 6.5.

Table 6.4: Steady-state model leave-one-out relative error summary statistics.

Vehicle Load Quantity	p/q_{ref}	C_X	C_Y	C_Z	C_{MX}	C_{MY}	C_{MZ}
Median MAE	0.051	0.044	0.027	0.065	0.506	0.107	0.055
95% Confidence Lower Bound	0.049	0.039	0.022	0.057	0.408	0.088	0.047
95% Confidence Upper Bound	0.054	0.050	0.034	0.074	0.606	0.128	0.065

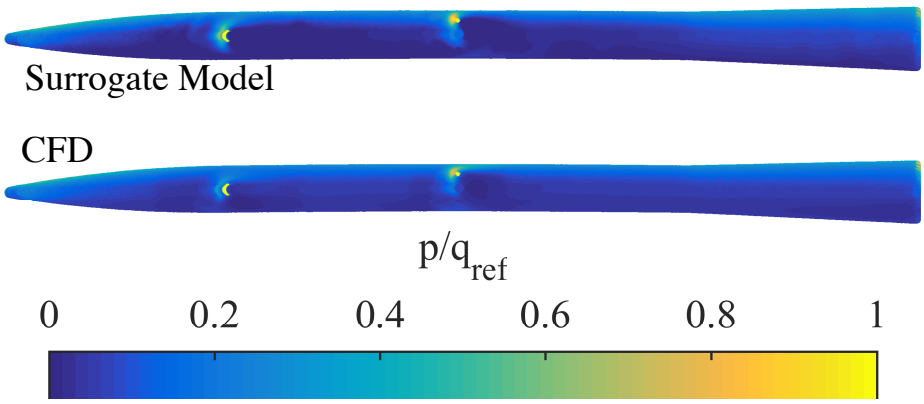

Figure 6.2: Pressure distribution of the model and CFD solution from one sample cross-validation point.

Table 6.5: Sample cross-validation conditions of Figure 6.2.

Parameter	Value	Unit
Altitude	19.5	km
Mach	3.87	
AoA	-8.88	deg
AoS	-21.8	deg
Lateral bending, η_1	0.593	% Tip Displacement
Longitudinal bending, η_2	-1.12	% Tip Displacement
Attitude jet, δ_1	21.9	% Maximum
Divert jet 1, δ_2	-24.0	% Maximum
Divert jet 2, δ_3	32.0	% Maximum

The relative error in the pressure distribution is approximately 5%, which is critical for calculating the forces applied to the structure as well as the integrated body forces and moments. The force coefficients (C_X, C_Y, C_Z) are also approximately 7% or less due to the low error in pressure distribution. However, the moment coefficients (C_{MX}, C_{MY}, C_{MZ}) are much more sensitive to errors in the pressure distribution, which leads to higher relative errors. C_{MX} for the axisymmetric vehicle is very small in general and leads to much larger relative errors during normalization, but is not expected to significantly impact flight simulation results.

6.2.2 Linear Unsteady Model Verification

The unsteady model is based on the step response of the vehicle to changes in each input. However, these step responses are identified at select flight conditions, which then need to be interpolated to approximate the step response at unsampled flight conditions during flight simulation. The output is the full step response at each time step and can be used directly with the time-history of the vehicle conditions to approximate the total unsteady loads using superposition. The collection of step responses collected from step changes in the angle of attack, tip displacement, and jet total pressure are presented along the left column in Figure 6.3. The L_2-norm relative error obtained for each flight condition is calculated against the known solution for each modeling approach and the 95% confidence interval on the median error is presented in Table 6.6. Samples from the cross-validation are presented along the right column of Figure 6.3 that compare the predicted step response to the training set.

Table 6.6: Linear unsteady model cross-validation statistics.

Step Input	Δ AoA	$\Delta\eta_1$	$\Delta\delta_1$
L_2 relative error	0.039	0.022	0.679
95% Confidence Lower Bound	0.018	0.015	0.434
95% Confidence Upper Bound	0.064	0.086	0.938

The results in Table 6.6 show that the fluid-dynamic response to rigid-body motion and structural deformation can be modeled accurately across the desired range of flight conditions. This is in large part due to the consistency of the responses. The jet interaction dynamic response is significantly different at different sample conditions and has a much longer response time. The complexity of the jet interaction response may require more sample points to converge to similar levels of accuracy as the angle-of-attack and structural-deformation step responses. The L_2 error in the jet interaction response is also much larger due to the longer response time for error to accumulate. The peak-to-peak error in the cross-validation sample is approx-

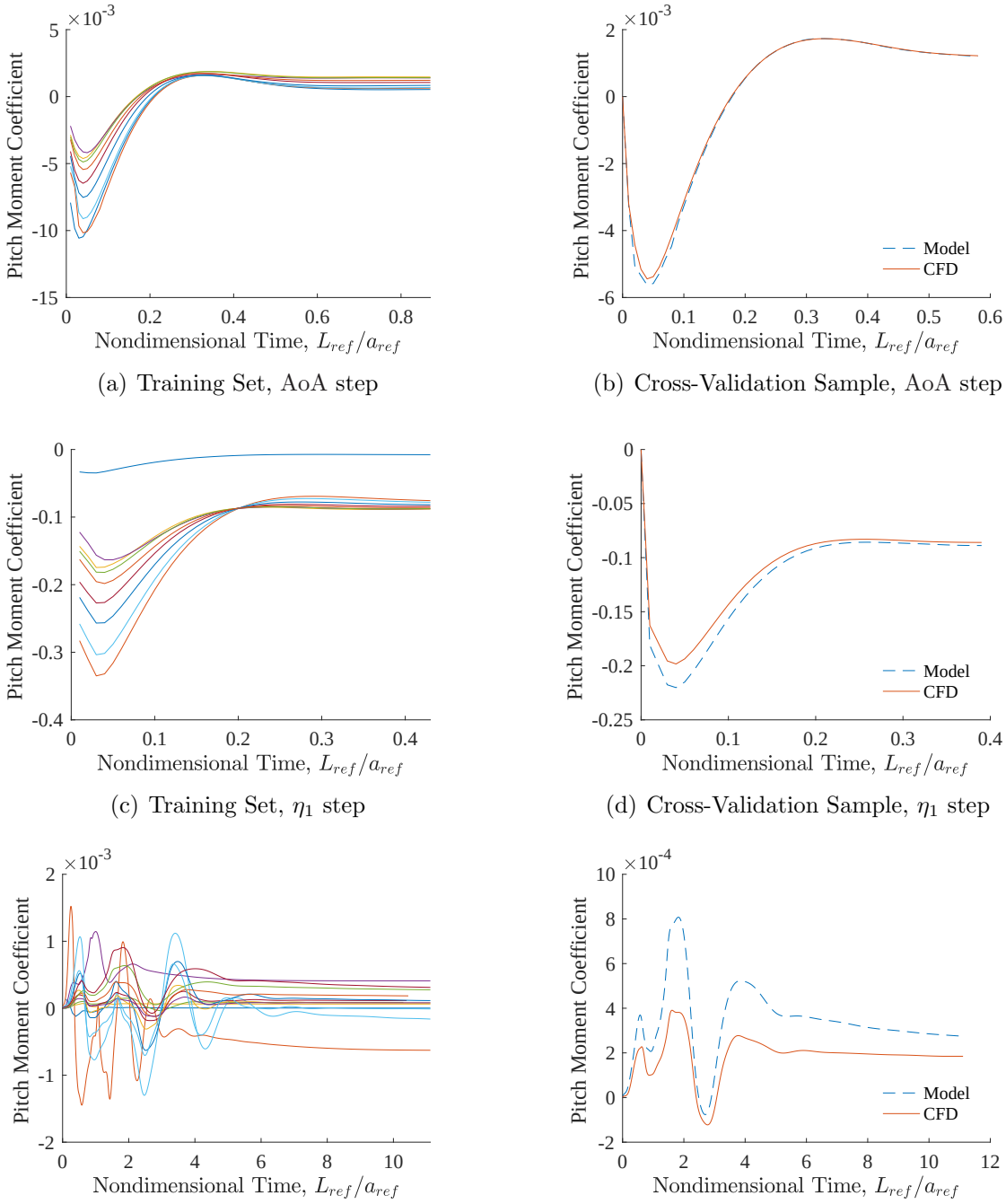

(a) Training Set, AoA step

(b) Cross-Validation Sample, AoA step

(c) Training Set, η_1 step

(d) Cross-Validation Sample, η_1 step

(e) Training Set, δ_1 step

(f) Cross-Validation Sample, δ_1 step

Figure 6.3: Step responses to changes in AoA, η_1, and δ_1 along with samples from the cross-validation of the training set.

imately 200%, which indicates the JI dynamics surrogate requires more samples or an alternate modeling approach.

6.2.3 Unsteady Model Verification

The unsteady model is compared against the time-accurate CFD simulations with jet interaction to asses the feasibility for modeling FSJI problems. These results evaluate the linear superposition assumption and the overall accuracy of the linear convolution with nonlinear correction factor approach.

The step responses and steady-state solutions of the vehicle at the mean flight condition are used to create the model. For comparison, the quasi-steady rigid-body motion and structural deformation with reduced frequency $\bar{k} = 0.01$ and $\bar{k} = 1.0$ are presented with the approximation of the unsteady model in Figures 6.4–6.6. The results show that the linearized unsteady model with steady-state nonlinear correction captures the amplitude of the response due to rigid-body motion and structural deformation. In addition, the general effect of unsteadiness is captured using the unsteady model, but does not exactly match the CFD solution at the highest frequency.

The jet interaction with varying frequency of pulse duration is presented in Figures 6.7 and 6.8 with the unsteady model approximation. The results of Figure 6.7 show that the unsteady model approximates the high-fidelity CFD solution very well and captures the unsteady effects at the highest frequency. In particular, the amplitude gain effect at higher frequencies is captured by the model. Table 6.7 lists the L_2 norm relative error of the reduced order model approximation compared with the CFD solution for each frequency sweep of fluid, structure, and jet parameter that was presented. Overall, the error increases with the frequency of the input, but the relative error increases more significantly for the fluid and structural input. This implies that the model would perform better for vehicles with lower pitch rates and structural vibration. The reduced order model maintains the same level of error approximating dynamic jet inputs, which is advantageous for steady-state as well as pulsed applications.

The unsteady nonlinear FSJI is approximated using a combination of the linear

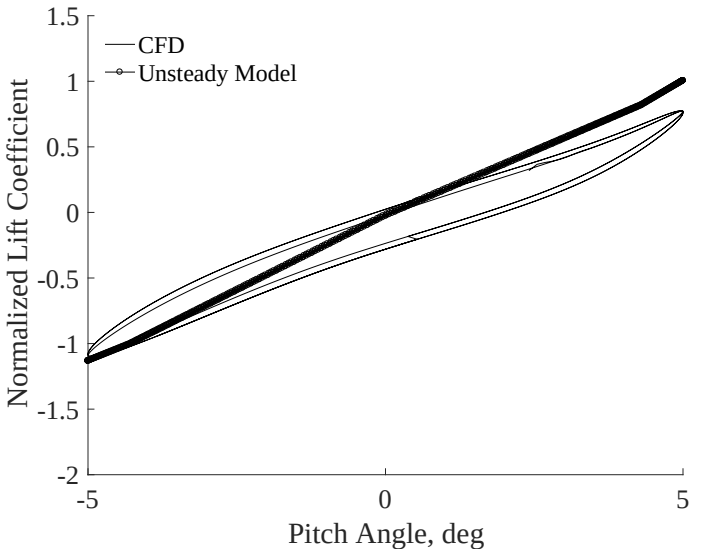

(a)

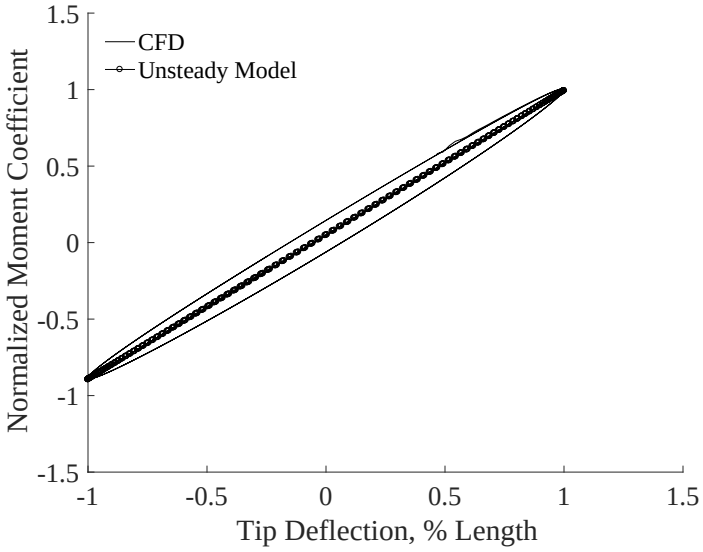

(b)

Figure 6.4: Unsteady model verification against the jet interaction CFD solutions with dynamic rigid-body motion and structural deformation at reduced frequency $\bar{k} = 0.01$. Coefficient values are normalized by the maximum absolute value of the quasi-steady solution for comparison.

unsteady model and the nonlinear steady-state model. The quality of each surrogate model is been presented, but the function of interest is the solution from time-accurate CFD simulation of varying flow, structure, and jet conditions. Three verification maneuvers were chosen to evaluate the nonlinear correction factor approach in addition

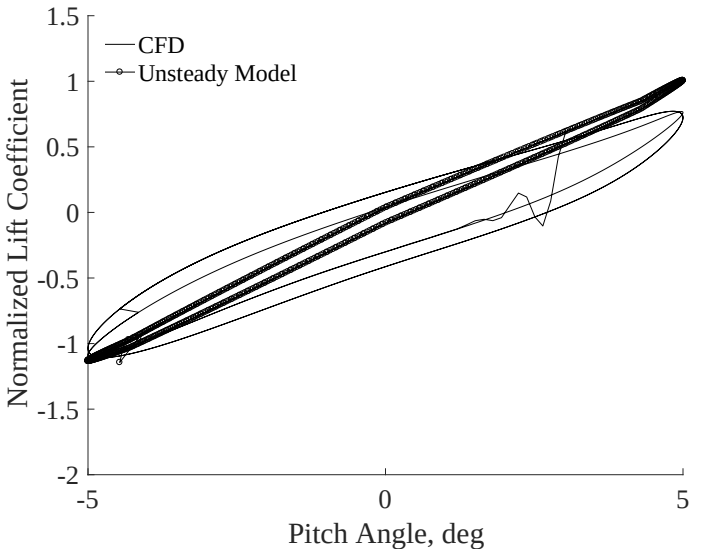

(a)

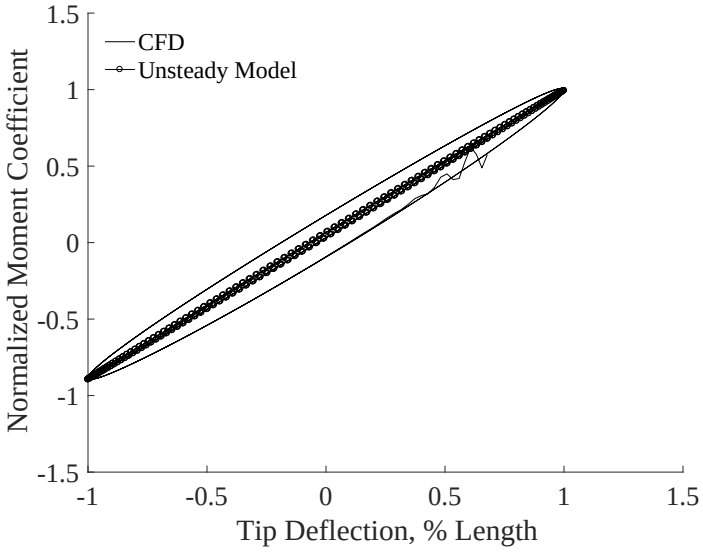

(b)

Figure 6.5: Unsteady model verification against the jet interaction CFD solutions with dynamic rigid-body motion and structural deformation at reduced frequency $\bar{k} = 0.1$. Coefficient values are normalized by the maximum absolute value of the quasi-steady solution for comparison.

to its ability to capture unsteady FSJI effects at unsampled flight conditions. Similar to the steady-state model verification results, the relative errors in the integrated forces and moments are presented in Figure 6.9.

The first verification maneuver is the prescribed motion of an undeformed vehicle

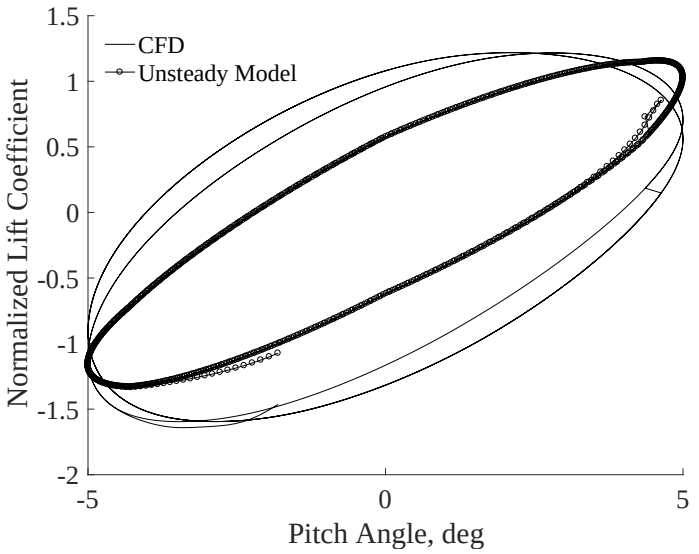

(a)

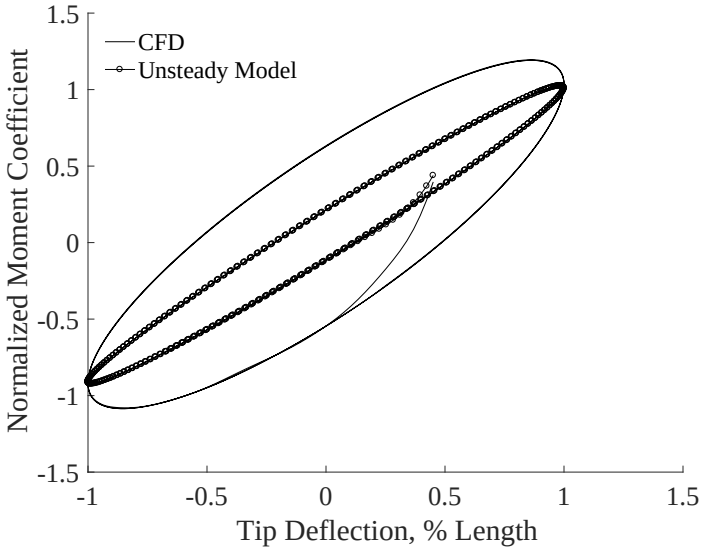

(b)

Figure 6.6: Unsteady model verification against the jet interaction CFD solutions with dynamic rigid-body motion and structural deformation at reduced frequency $\bar{k} = 1.0$. Coefficient values are normalized by the maximum absolute value of the quasi-steady solution for comparison.

with varying flight conditions. The Reynolds number, deformation, and jet conditions relative to the farfield conditions are kept constant and listed in Table 6.8. The rotation is then prescribed at each time step to follow a sinusoidal maneuver with a moderate amplitude, 7.2 degrees, and increasing frequency as a function of time,

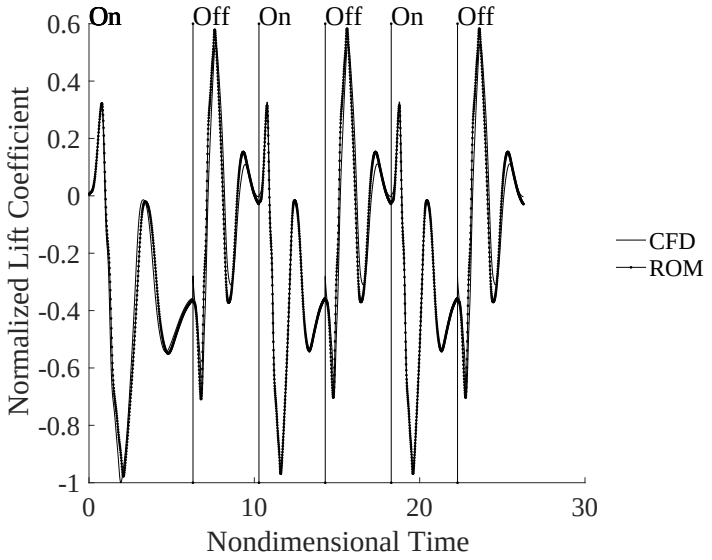

(a) $\bar{k} = 0.01$

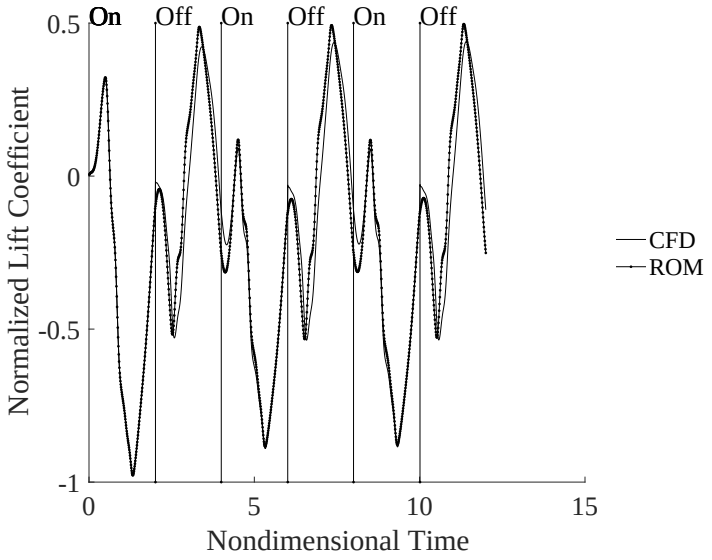

(b) $\bar{k} = 0.1$

Figure 6.7: Unsteady model verification against the jet interaction CFD solutions with pulsating input from the attitude control jet. Coefficient values are normalized by the maximum absolute value of the quasi-steady solution for comparison.

quadratically from 1 to 10 Hz. The second verification maneuver is the prescribed structural deformation of the first longitudinal bending mode, ±5% tip deflection, as a function of time, quadratically from 1 to 10 Hz, at constant flow and jet conditions listed in Table 6.8. The third maneuver is the response of a flexible vehicle, with a

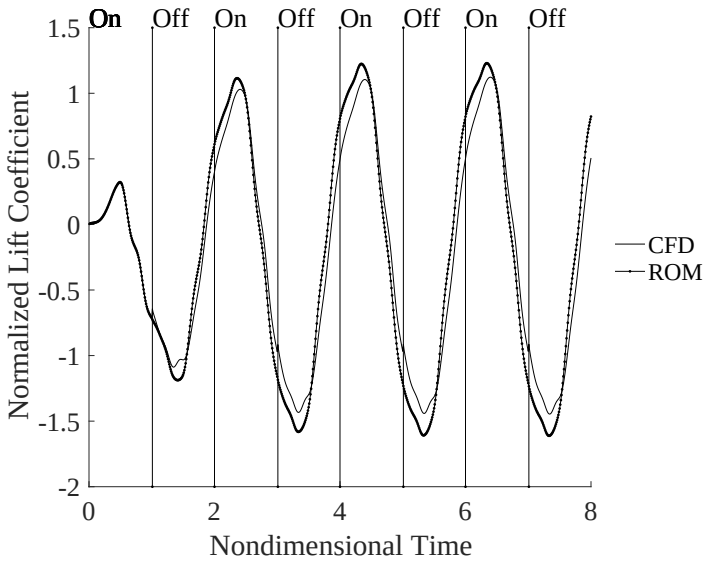

(a) $\bar{k} = 1.0$

Figure 6.8: Unsteady model verification against the jet interaction CFD solutions with pulsating input from the attitude control jet. Coefficient values are normalized by the maximum absolute value of the quasi-steady solution for comparison.

Table 6.7: Relative error of the dynamic FSJI reduced order model for varying frequency inputs (Figures 6.4–6.7).

Unsteady Input	$\bar{k} = 0.01$	$\bar{k} = 0.1$	$\bar{k} = 1.0$
Angle of Attack	32%	35%	44%
Structural Deformation	10%	13%	38%
Jet Total Pressure	18%	21%	22%

first bending mode frequency of 10 Hz, to a step change in the jet total pressure of 1% of the maximum available total pressure and flight conditions listed in Table 6.9. A first bending mode frequency of 10 Hz is chosen specifically at the low end of the spectrum to have the structure deform under the applied loads. The vehicle response is then approximated using each of the modeling methods and compared to the CFD time-accurate solution for each maneuver.

Table 6.8: Dynamic rigid-body and structural deformation simulation conditions.

Altitude, km	Mach	Jet Total Pressure, MPa
21.3	3.0	17.5

For each simulation the flight conditions are used to approximate the step response

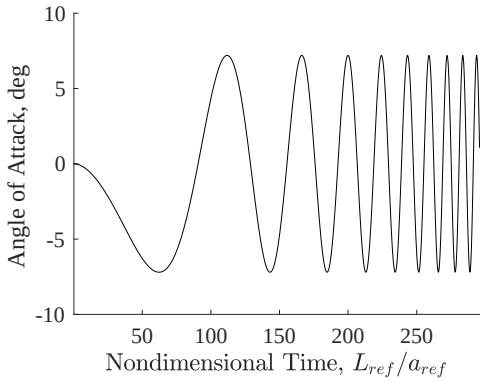

(a) Rigid-Body Input

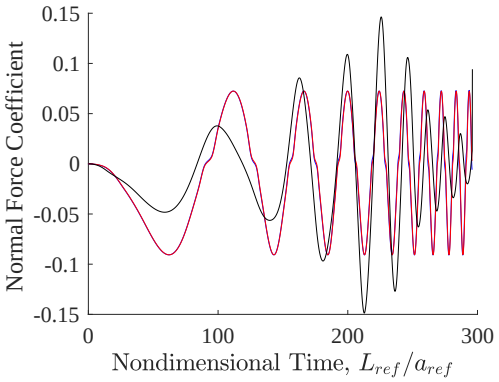

(b) CFD Solution and Model Output

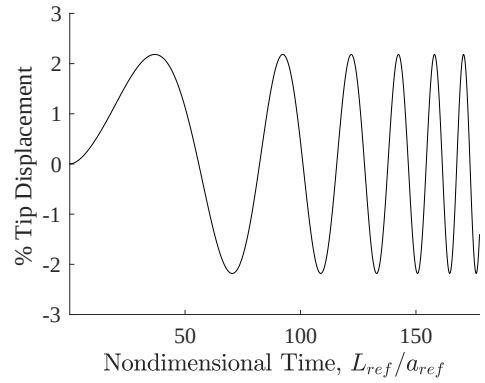

(c) Structural Deformation Input

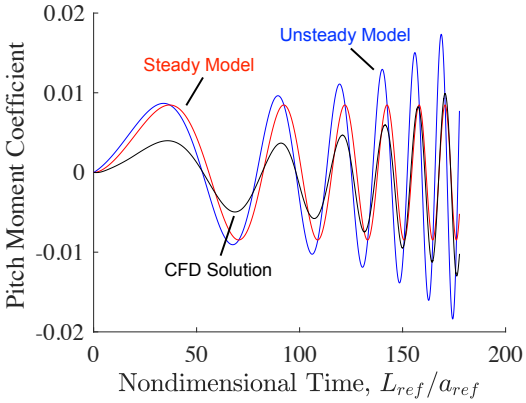

(d) CFD Solution and Model Output

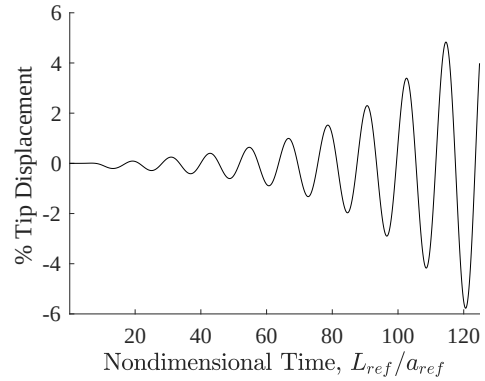

(e) Structural Deformation Response to Jet Step

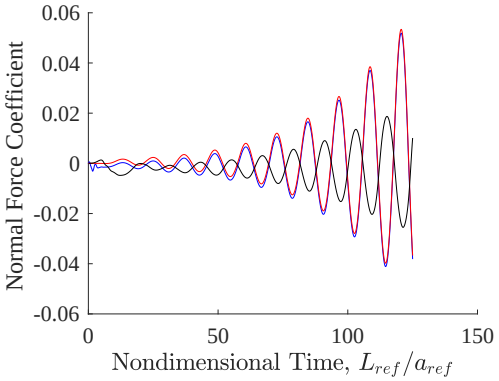

(f) CFD Solution and Model Output

Figure 6.9: Comparisons to CFD simulations of forced pitch oscillation, forced structural deformation, and elastic response to transient jet actuation at the mean flight condition of 21.34 km at Mach 3.0. **CFD solution**, Steady-State Model, Unsteady Model.

Table 6.9: Dynamic jet step simulation conditions.

Altitude, km	Mach	Jet Step ($t = 0$)	Jet Step Total Pressure ($t > 0$), MPa
21.3	3.0	*Off*	0.1

of the system to changes in the fluid, structure, and jet conditions. These responses are then convolved with the input time history of each simulation to calculate the linearized model response. In the case of the final simulation with a jet step and flexible vehicle response these linearized outputs are summed together to reach the total linearized model response. Then, the nonlinear correction factor is calculated for all time steps by evaluating the steady-state surrogate model (*Steady* in Figure 6.9) and linearized model steady-state values. This correction factor is applied to the linearized model output and is referred to as the *Unsteady Model* in Figure 6.9.

The results in Figure 6.9 show that the steady and unsteady models do an adequate job of approximating the FSJI solution to rigid-body and structural deformation inputs. In addition, the unsteady model augments the steady-state solution further in the structural deformation case to better match the amplitude increase that is observed in the CFD solution. At worst, the the unsteady model matches the steady-state prediction and does not degrade the solution. The transient jet interaction solution of the third simulation is misidentified by the surrogate leading to an incorrect transient solution and eventual phase difference in the signal. This is most likely due to the insufficient sampling of the jet step response and larger relative errors. Despite this error the strategy overall captures the frequency and amplitude growth of the vibrating vehicle in the presence of jet interaction. The unstable response that is observed is not indicative of the true vehicle response because the thrust of the jet itself is not accounted for due to the replacement of the nozzle exit with the inflow boundary condition. Therefore, the jet interaction with the flow is the driver that leads to an instability that amplifies the generalized force on the structure similar to the results in the jet sensitivity study.

The differences between the unsteady and steady model come from the unsteady component being excited and having an additional contribution, which is seen in the structural deformation case (Figure 6.9(c)-(d)). The differences between the unsteady model and the CFD solution are additional effects that are not fully captured using the linear convolution approach. This effects may include the nonlinearity of the jet interaction at higher jet total pressure, the sensitivity of the jet interaction effects to unsteadiness in the flow, and nonlinearity introduced by the combination of unsteadiness and stronger interactions between the jet and fluid. These effects may be addressed by a nonlinear representation of the system using a Volterra series and other approaches.

6.3 Effective Dynamics Evaluation

The effective dynamics motivation and approach can be demonstrated with a simple one-dimensional mass-spring-damper system. The parameters of this system are chosen to emulate the nonlinear dynamics about a reference condition that occurs as a result of FSJI of HSVs. The steady-state results capture the nonlinear stiffness near the equilibrium point. Dynamic simulations where the system deviates from the reference point highlight the breakdown in the convolution-based modeling methods. This motivates the effective dynamics approach to calculate the system dynamics in the presence of nonlinearity. Finally, an alternate maneuver is used to evaluate the robustness of the effective dynamics model.

The system properties are listed in Table 6.10 that are used with steady-state and dynamic simulations to evaluate the various dynamics modeling approaches. The parameters correspond to the governing equation

$$m_s\ddot{\eta}_s + c_s\dot{\eta}_s + k_s(\eta_s)\eta_s = F_s, \tag{6.2}$$

Table 6.10: Properties of the sample mass-spring-damper system.

Parameter	Value	Unit
f	5	Hz
k_{s0}	$(2\pi f)^2$	
k_{s2}	$k_{s0}^3/8$	
c_s	$(0.01)k_s$	
m_s	1	

where m_s, c_s, k_s, and F_s are the generalized mass, damping, stiffness, and force, respectively. The single degree of freedom η_s is the output of interest that will be modeled as function of the force input. The stiffness is a function of the state,

$$k_s(\eta_s) = k_{s0} + k_{s2}\eta_s^2 \tag{6.3}$$

where k_{s0} and k_{s2} define the parabolic stiffness and are defined in Table 6.10. The damping coefficient is also state-dependent due to its stiffness-proportional nature. The system dynamics are particularly sensitive to the ratio of k_{s2} to k_{s0} with small ratios leading to a weakly-nonlinear system reasonably captured by linear convolution methods. The ratio chosen here is to ensure that the accuracy of the linear convolution based methods degrades and explore how to model system dynamics in this situation.

Steady-state results of the spring to a range of force inputs are presented in Figure 6.10 to highlight its nonlinear nature. Dynamic results of the system are presented in Figure 6.11 of the unit impulse and step responses using very small perturbations in F_s equal to 1.0 and 0.1, respectively. These functions form the basis of the convolution modeling approaches that are considered next. Figure 6.12 shows the first several components of the second-order kernel in the Volterra series identified through lagged impulse responses of the mass-spring-damper system.

However, inspecting the unit responses with larger amplitude input shown in Figure 6.13 reveals how the dynamics of the mass-spring-damper system change with them. The convolution methods rely on the step or impulse response kernels to be

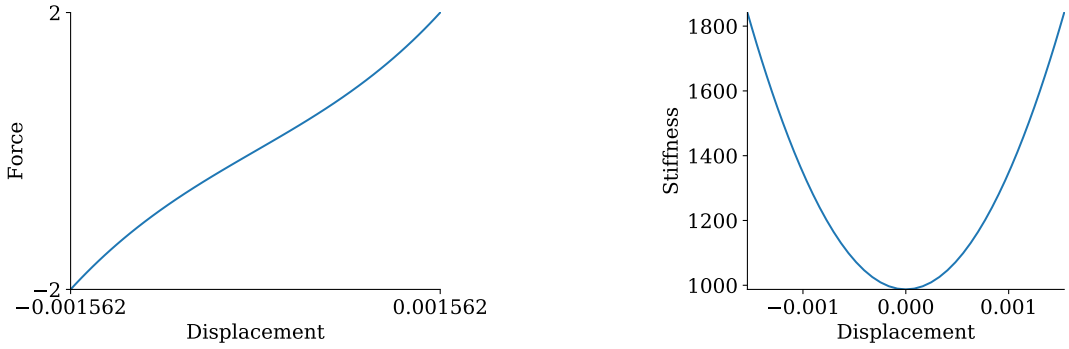

(a) Static Response

(b) Stiffness Function

Figure 6.10: Steady-state characteristics of the nonlinear spring system.

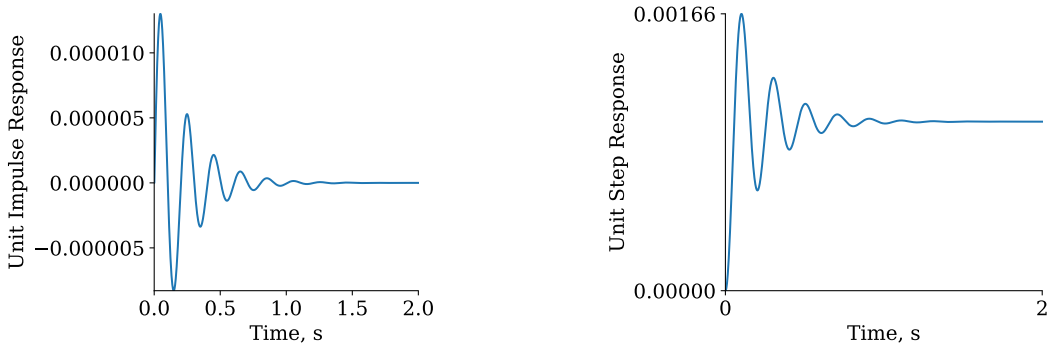

(a) Impulse Response

(b) Step Response

Figure 6.11: Unit responses of the mass-spring-damper system.

accurate. If the underlying dynamics change during typical operating conditions of the system, then the accuracy of the convolution models will degrade.

6.3.1 Effective Dynamics Numerical Approach

The effective dynamics approach begins by transforming the chosen reference solution input and output signals into the frequency domain using the Fourier transform. The first and second order kernels are identified using a least-squares solution for each frequency component fit using multiple simulation samples. These kernels can be used to approximate the response to new input signals by first converting the input to the frequency domain, element-wise multiplication of the first and second order

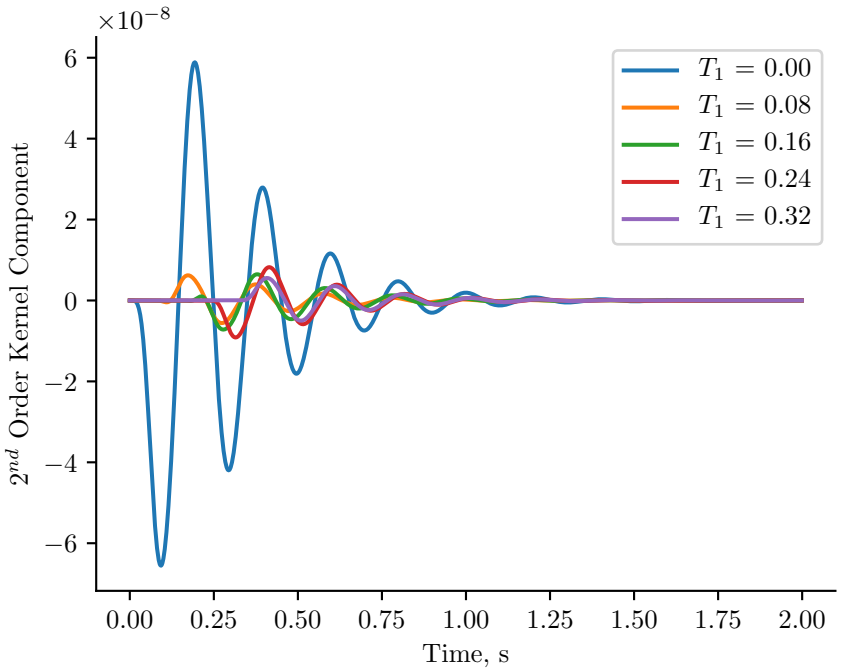

Figure 6.12: Components of the second-order Volterra kernel identified using lagged impulse responses of the mass-spring-damper system in the time domain.

inputs with the corresponding kernels, sum the components, and convert back to the time domain. This process is based on a set of maneuvers of interest to identify the dynamics. Additional maneuvers can be used to calculate the effective dynamics, which lends itself to creating an effective dynamics surrogate model.

Although the approach can be extended to higher orders, this may result in less accurate kernels. For example, a single-input-single-output system as in the mass-spring-damper system becomes inaccurate using a third-order kernels and above. Using a single first-order kernel fit to the reference solution would be very accurate in the vicinity of this maneuver, but adding information in the form of a second-order kernel may add robustness to the model away from the reference solution.

A force is applied to the mass-spring-damper system that oscillates about the reference condition, $F_s = 0$. This simulation is meant to explore the range for which

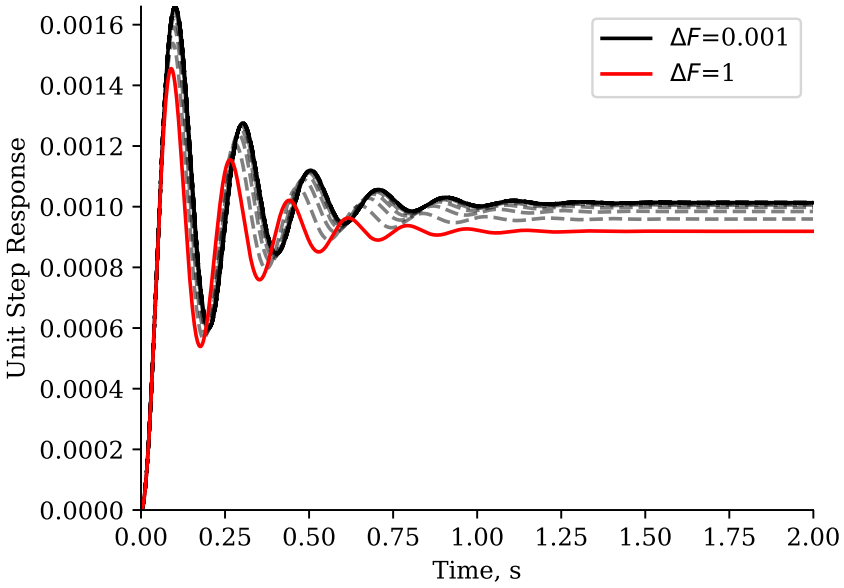

(a) Varying Step Input for $\eta_{s0} = 0$

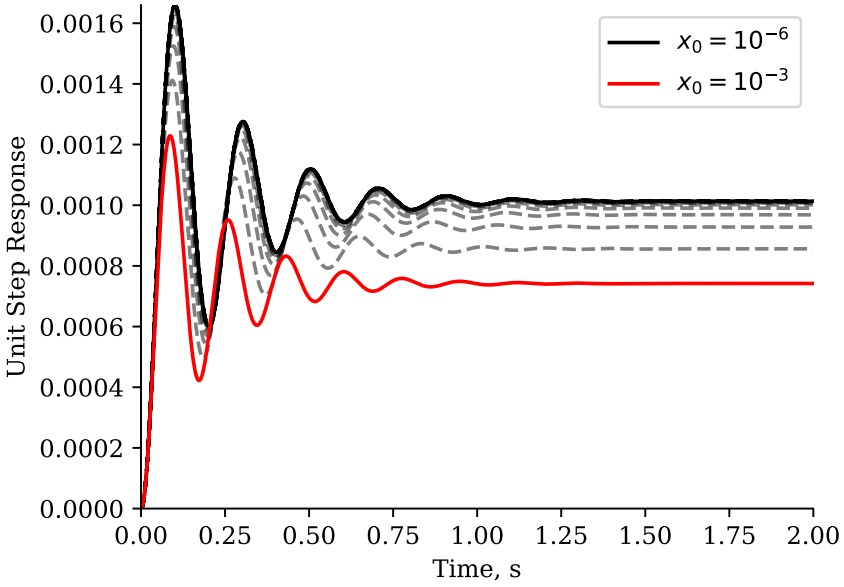

(b) Varying Initial Condition for $\Delta F_s = 0.001$

Figure 6.13: Unit responses of the mass-spring system with varying step input and initial condition.

the convolution method can be applied. The dynamics that were identified should be valid considering that the force remains near the reference point that was used to identify the step responses. The applied force is a summation of cosine functions with frequencies from $\frac{f}{2}$ to $10f$. The phase is randomly sampled from a uniform distribution $[0, 2\pi]$ and the amplitude is randomly sampled from a uniform distribution $[0, \omega]$, where ω is the circular frequency of the signal component. The input is shifted to zero at the initial time step, the peak-to-peak amplitude of the signal summation is then adjusted to the value of A_0, and an additional sine signal with amplitude A_1 and period of two seconds is added to simulate deviation from a reference point. The total force applied is written as

$$F = \frac{A_0}{\sum_{i=1}^{N} a_i} \sum_{i=1}^{N} a_i \cos(\omega_i t + \phi_i) + A_1 \sin(\pi t), \tag{6.4}$$

where N is the number of signal components, a_i the randomly generated amplitude, and ϕ_i the randomly generated phase. The solution is calculated using a forward Euler integration scheme with a time step equal to $1/(200f)$. The following models are compared against the simulation results (Ref): convolution (CV), convolution with nonlinear correction factor (NLC), Volterra series (Vol), linear effective dynamics (ED), linear effective dynamics with steady-state correction (EDC), nonlinear effective dynamics (EDV), and nonlinear effective dynamics with steady-state correction. Linear and nonlinear effective dynamics refer to solving for just the linear kernel or the linear and 2^{nd}-order nonlinear kernels. The steady-state correction for the effective dynamics approaches uses the nonlinear steady-state solution to calculate the zero-frequency amplitude of the signal.

For each set of simulation results the simulation input and output are sampled at 500 Hz ($100f$) prior to calculating the effective dynamics. At this sampling rate, 200 samples are required to span the frequency range of interest up to 50 Hz ($10f$). Using

Table 6.11: Summary of dynamics modeling methods.

Symbol	Domain	Linear or Nonlinear	Steady-State Correction
CV	Time	Linear	No
NCF	Time	Nonlinear	Yes
Vol	Time	Nonlinear	No
ED	Frequency	Linear	No
EDC	Frequency	Linear	Yes
EDV	Frequency	Nonlinear	No
EDVC	Frequency	Nonlinear	Yes

200 random samples creates a determined system to solve for the 2^{nd}-order kernels in the nonlinear effective dynamics approach.

First, the range of linearity is calculated using the reference solution and defined when the nonlinear steady-state response is more than 10% different than the linear solution. Figure 6.14 shows the nonlinear and linear solutions to increasing input along with the calculated range of linearity. These results are used to identify the bounds of A_0 to avoid extrapolating the range of identified kernels in the convolution-based models.

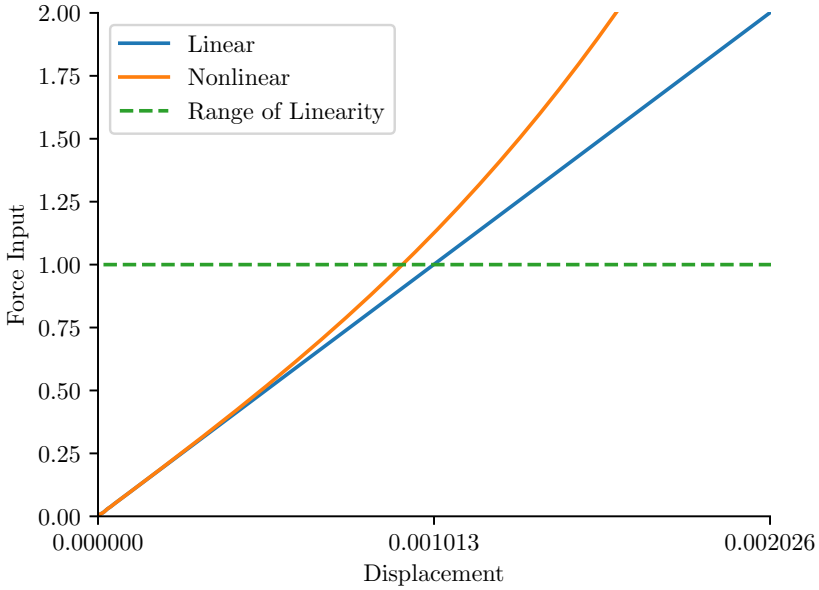

Figure 6.14: Range of linearity for the mass-spring-damper system, where inputs greater that 1 lead to nonlinear response.

6.3.2 Simulation Results

Two hundred randomly generated signals with $A_0 = 0.1$ and $A_1 = 0.2$ are used to calculate the effective dynamics model and an additional verification input signal to compare the response of the various models is shown in Figure 6.15. The simulation result along with the model predictions are presented in Figure 6.16. With the low amplitude about the reference condition, the convolution methods capture the reference solution and the Volterra series approximation is nearly identical the reference solution in this case. The linear and nonlinear effective dynamics results show the ability to capture the reference solution dynamics and the steady-state model is used to shift the DC component of the signal for an improved approximation. The nonlinear kernel further improves the effective dynamics approximation. The steady-state corrected linear and nonlinear solutions are shown in Figure 6.17 that capture the low amplitude response of the system.

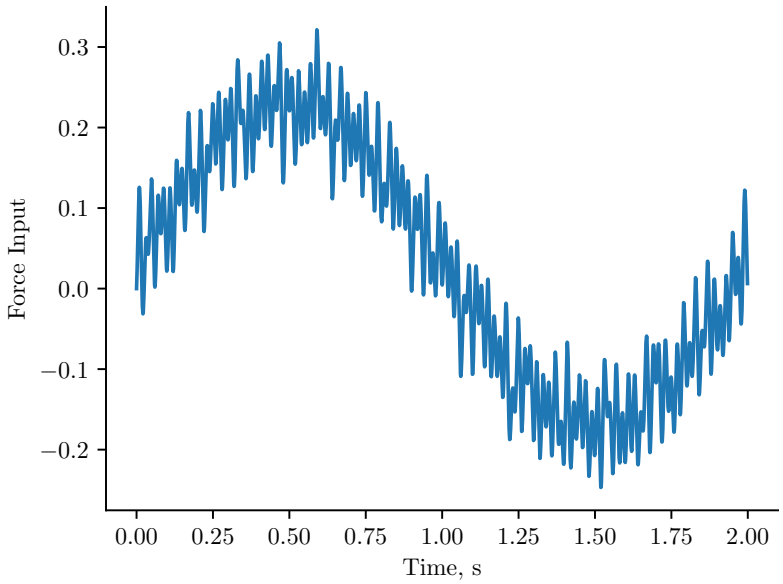

Figure 6.15: Force input with $A_0 = 0.1$ and $A_1 = 0.2$

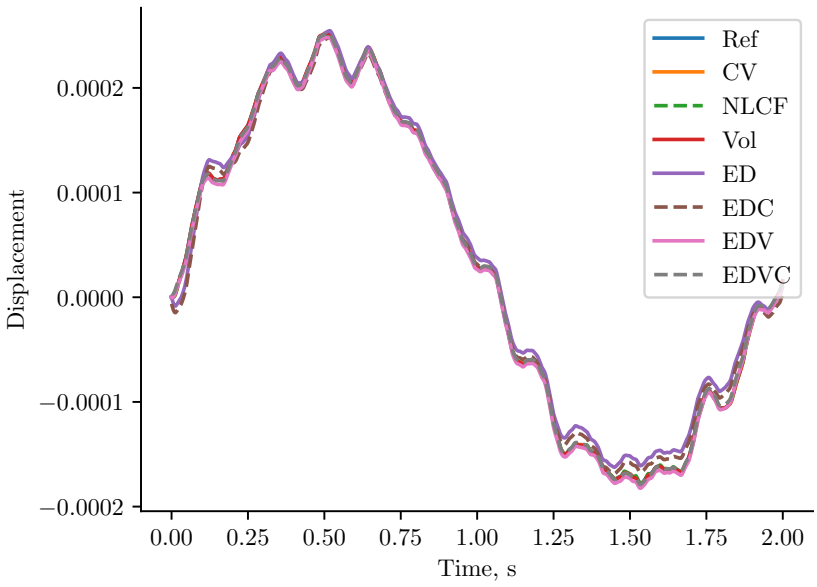

Figure 6.16: Comparison of the models against the reference solution with $A_0 = 0.1$ and $A_1 = 0.2$.

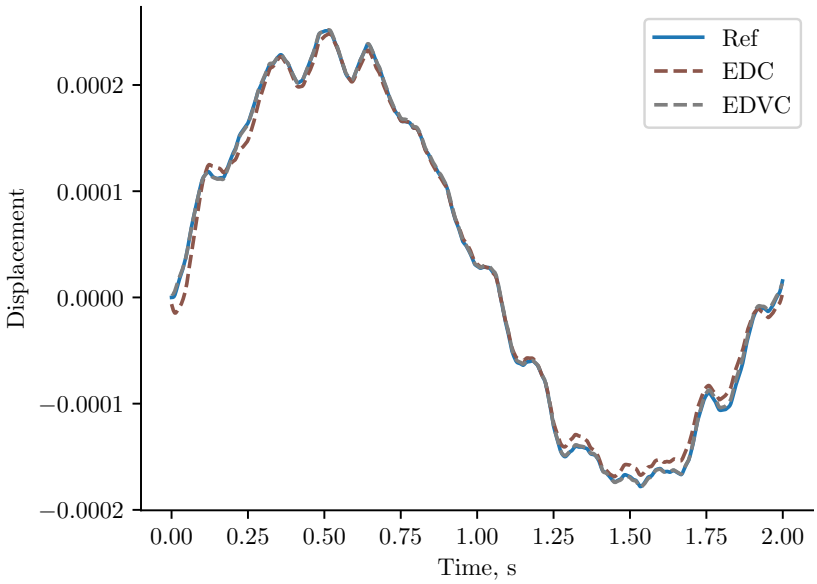

Figure 6.17: Comparison of the models against the reference solution with $A_0 = 0.1$ and $A_1 = 0.2$.

Twenty additional signals were generated to compare the models against the reference solution and the distribution of relative error from these additional samples are shown in Figure 6.18. The relative error is calculated by the MAE normalized by the peak-to-peak amplitude of the reference solution. In this case the Volterra series is superior to all the others and all the convolution models tend to have lower error compared to the effective dynamics models.

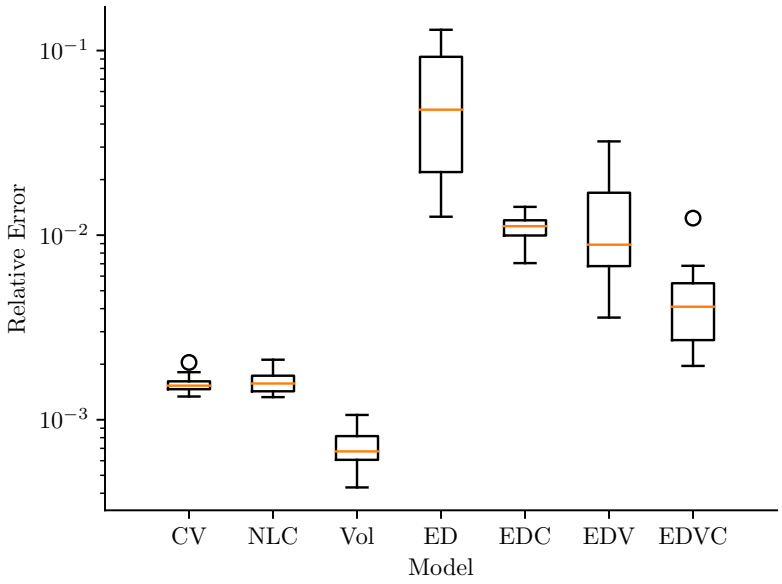

Figure 6.18: Distribution of relative error for each model using fifteen additional samples with $A_0 = 0.1$ and $A_1 = 0.2$. Outliers are defined as being beyond $1.5 \times IQR$, the interquartile range, away from the first and third quartile of the data.

Another simulation with a larger force amplitude, $A_0 = 0.5$ and $A_1 = 1.0$ is presented in Figure 6.19. This simulation is meant to excite the nonlinear dynamics of the system by moving away from the reference condition with oscillations within the range of linearity. The predicted output by the available models is compared against the reference solution in Figure 6.20. The linear (CV and NCF) and nonlinear (Vol) convolution-based models are accurate while the input is within the range of linearity $[-1.0, 1.0]$. The linearized stiffness calculated at the initial condition is a good approximation in this case and introducing the nonlinear correction factor adds high-frequency content that is not represented in the reference solution. On the other hand, the results of using the effective dynamics show good correlation with the reference signal throughout the simulation Moreover, the effective dynamics can also be corrected using a steady-state simulation to calculated the DC component of the signal, which greatly improves the accuracy of the model. In this case, the nonlinear

kernel identified using the effective dynamics approach improves the prediction accuracy compared to using a linear kernel only. The steady-state corrected linear and nonlinear solutions are shown in Figure 6.21 that capture the moderate amplitude response of the system away from the reference condition.

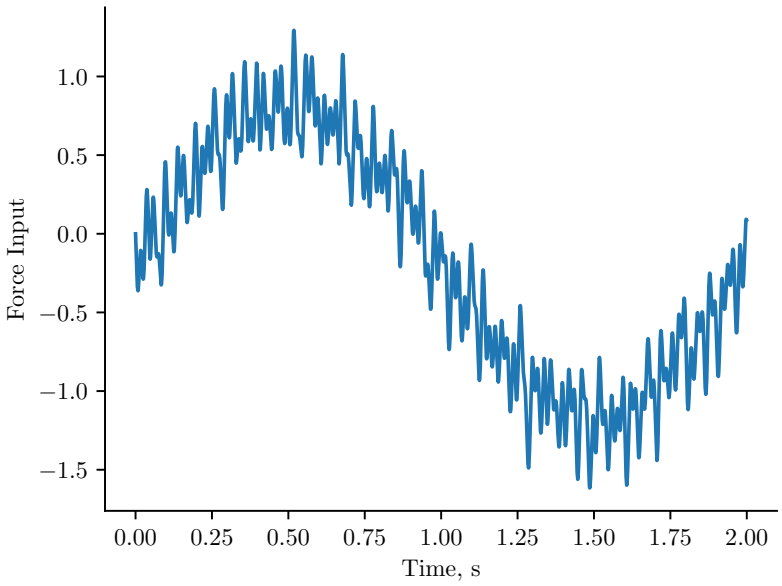

Figure 6.19: Force input with $A_0 = 0.5$ and $A_1 = 1.0$

The relative error is the MAE normalized by the peak-to-peak amplitude of the solution and is calculated on an additional 20 signals. The distribution of relative error for each model is presented in Figure 6.22. The linear and nonlinear convolution-based models all have low relative error, but it must be kept in mind that the nonlinear correction factor does not correlate well with the reference solution. The linear and nonlinear effective dynamics approaches tend to have higher error, but this can be corrected by introducing a steady-state correction for the signal zero-frequency component as shown by the relative error of EDC and EDVC.

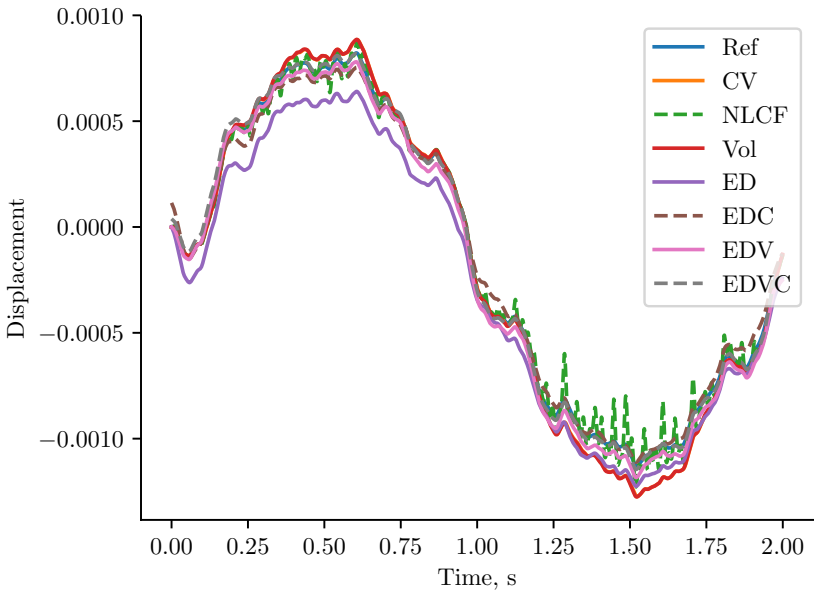

Figure 6.20: Comparison of the models against the reference solution with $A_0 = 0.5$ and $A_1 = 1.0$.

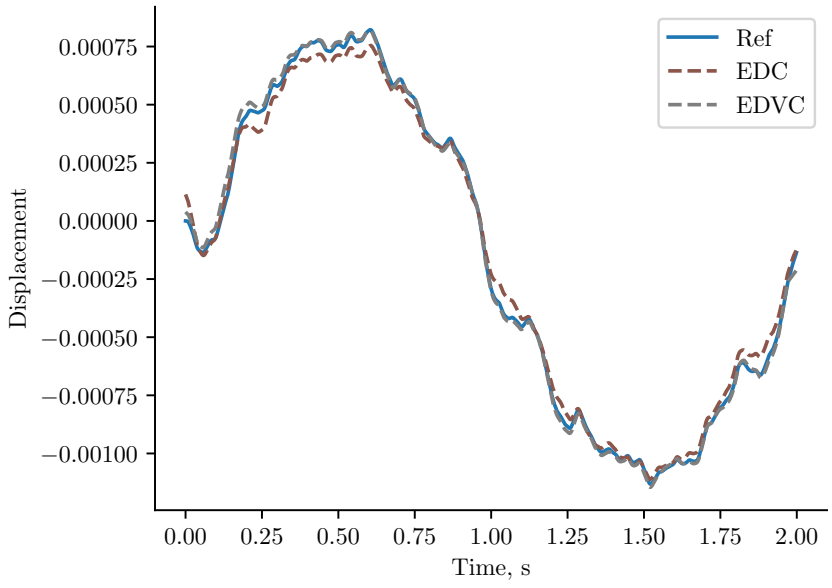

Figure 6.21: Comparison of the models against the reference solution with $A_0 = 0.5$ and $A_1 = 1.0$.

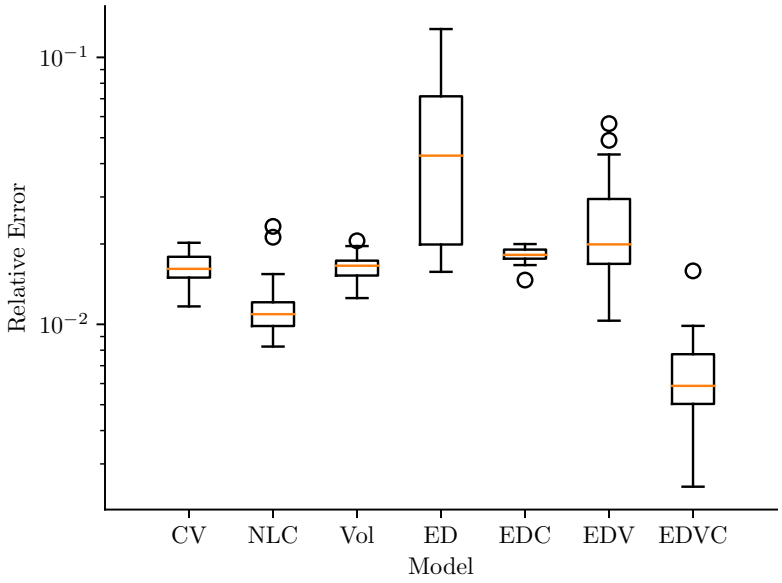

Figure 6.22: Distribution of relative error for each model using fifteen additional samples with $A_0 = 0.5$ and $A_1 = 1.0$. Outliers are defined as being beyond $1.5 \times IQR$, the interquartile range, away from the first and third quartile of the data.

The simulation is repeated with $A_0 = 1.0$ and $A_1 = 2.0$ then compared to the models. The input and the model predictions are presented in Figures 6.23 and 6.24. This test case is very difficult to model as it features very large amplitude oscillation along with a wide range of inputs, which is representative of the supersonic FSJI problem. The linear and nonlinear convolution-based models capture the overall trends, but show large deviations from the reference signal throughout. The nonlinear correction factor again introduces high-frequency content that leads to poor correlation with the reference solution. The linear and nonlinear effective dynamics models correlate very well with the reference solution, but there is a consistent offset that can be accounted for using a steady-state model. The nonlinear effective dynamics model with steady-state correction tends to have the least error and correlates well with reference solution. The steady-state corrected linear and nonlinear solutions are shown in Figure 6.25 that capture the large amplitude response of the system away from the reference condition.

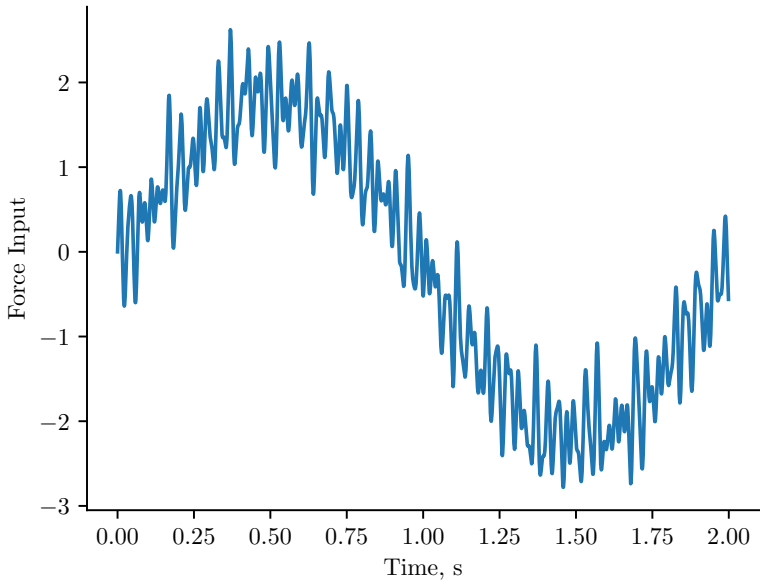

Figure 6.23: Force input with $A_0 = 1.0$ and $A_1 = 2.0$.

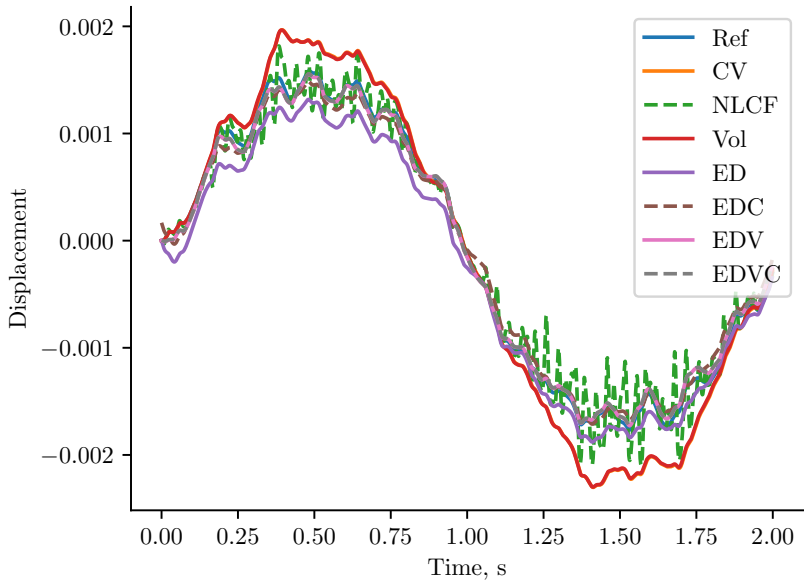

Figure 6.24: Comparison of the models against the reference solution with $A_0 = 1.0$ and $A_1 = 2.0$.

The distributions of relative error from the additional samples are shown in Figure 6.26. The methods that leverage the nonlinear steady-state solution, convolution with nonlinear correction factor (NLC) and the effective dynamics model with steady-state correction (EDC), are among those with lowest relative error. However, the effective dynamics model significantly reduces the error in this very dynamic test case with the nonlinear effective dynamics model with steady-state correction (EDVC) tending to have the lowest relative error.

Step response or Volterra models demonstrated superior performance in some of the test cases that were explored. Strategies to leverage these models for large deviations away from a reference point such as developing a kernel surrogate model could feasibly be constructed using several sample conditions. The approximation would then require convolution with each step response or set of kernels. At this time it is unclear how to transition between step responses and Volterra kernels smoothly

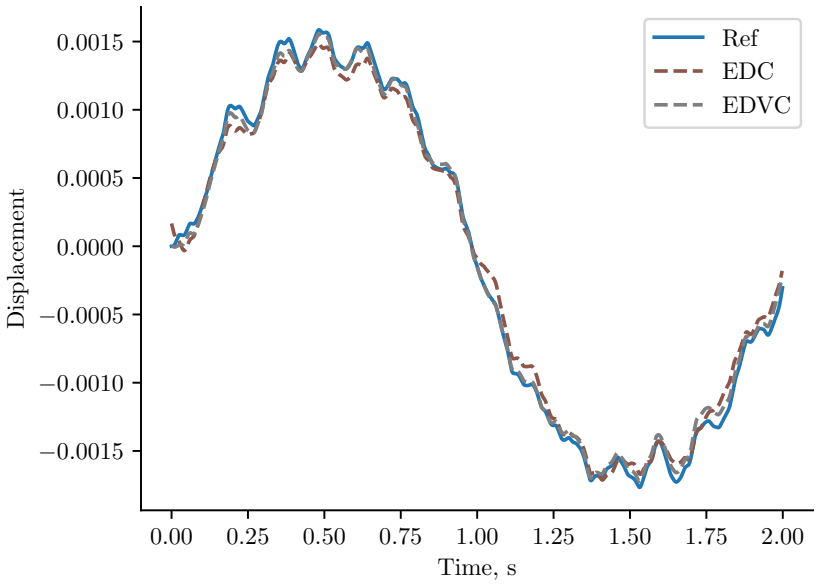

Figure 6.25: Comparison of the models against the reference solution with $A_0 = 1.0$ and $A_1 = 2.0$.

and accurately.

The results focus on a nonlinear mass-spring-damper system that was meant to challenge the current and newly developed dynamics modeling methods. None of the models were consistently accurate between the convolution-based models the effective dynamics approach. Of course, the linear convolution methods were very accurate for low amplitude or low frequency inputs and the effective dynamics approaches were more accurate with nonlinear training maneuvers. The benefit of the new approach is the ability to model the system dynamics in situations when other methods are inaccurate. If the typical operating condition involves high amplitude, high frequency, or moving reference conditions then the effective dynamics can be identified for these routine conditions either for modeling or analysis purposes.

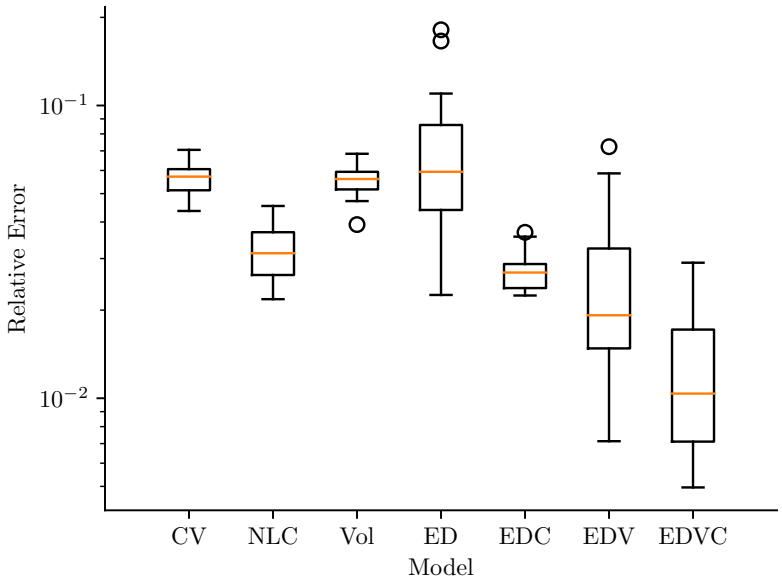

Figure 6.26: Distribution of relative error for each model using fifteen additional samples with $A_0 = 1.0$ and $A_1 = 2.0$. Outliers are defined as being beyond $1.5 \times IQR$, the interquartile range, away from the first and third quartile of the data.

6.4 Concluding Remarks

This chapter considered the unsteady FSJI that occurs for highly maneuverable, agile, HSVs. The coupled FSJI has a significant effect on the applied loads to the vehicle that must be modeled accurately to calculate the vehicle response. Flight simulation of the vehicle is desired to experiment with varying vehicle designs and aid the design and development process. The unsteady FSJI model must fit within a flight simulation framework, which requires an accurate, robust, and fast approach. A couple of methods that have been used for other unsteady aerospace applications are adapted for the unsteady FSJI problem.

One major challenge to modeling the unsteady loads applied to the maneuverable HSV is the wide range of a high dimensional input problem. Developing a model for a limited number of flight conditions is sufficient for conventional air vehicles,

but the whole flight envelope must be represented for a maneuverable vehicle with an undetermined trajectory. This adds more dimensions to the problem that is dependent on the fluid, structure, and jet states. The fluid, structure, and jet input parameters have nonlinear effects on the applied loads which adds an additional layer of complexity to the model. To address this wide range of input parameters over the entire flight envelope, the steady-state response is sparsely sampled before doing any unsteady sampling.

The convolution with nonlinear correction factor approach involves two layers of surrogate models, the step response and steady-state surrogates, to create a comprehensive surrogate model of the nonlinear unsteady applied loads. Verification of each modeling layer and the composite model is required to measure the level of accuracy relative to the true solution. The high-dimensionality of the problem imposes a significant cost for additional sampling for verification. Therefore, a cross-validation technique is used to measure the accuracy of each of the modeling sub-layers: the nonlinear steady-state model and linearized unsteady model. The full nonlinear unsteady model is compared to a select set of dynamic maneuvers meant to excite the unsteady FSJI effects on the vehicle applied loading.

Time-accurate dynamic simulations of the vehicle with dynamic fluid, structure, and jet inputs were presented to study the effect of a dynamic environment to the FSJI problem. These unsteady simulations were compared against the convolution-based modeling approach that was developed to highlight the nonlinear response. The model showed good correlation with the CFD solution by capturing the amplitude and unsteady effects at higher frequencies. The unsteady model based on the step responses of the vehicle contributes some additional information that is not represented in the steady model such as the transient jet interaction in response to turning the jet on and the amplification of the applied forces due to dynamic structural deformation. The jet interaction effect appears to be sensitive to unsteadiness in the flow such

that the steady-state model does not capture low-frequency inputs that well. The difference between the current unsteady modeling approach and the CFD solution may be addressed using a nonlinear representation as the unsteady model is unable to capture even moderate flow unsteadiness for strong jet interactions.

The effective dynamics approach was applied to a single degree of freedom mass-spring-damper model to compare to (linear and nonlinear) convolution methods using a nonlinear system. The results indicate that the convolution with nonlinear correction factor approach is accurate for quasi-steady and low amplitude inputs, but becomes inaccurate away from the refence point and for very dynamic inputs. The Volterra series was the most accurate model for small perturbations about a reference condition, but also became inaccurate away from the reference point. The linear or nonlinear effective dynamics can be calculated for dynamic inputs and used to accurately predict other maneuvers that may deviated from a known reference point. Multiple maneuvers were used to develop the effective dynamics model. The model out-performs the other approaches using a set of training points for the more extreme inputs. This approach can be applied to HSV dynamics modeling as well. The effective dynamics can be identified using multiple characteristic maneuvers throughout the flight envelope. During simulation, the effective dynamics based on the most-similar training maneuver can be used to approximate the nonlinear vehicle dynamics. The effective dynamics approach may be too complex for weakly nonlinear systems or quasi-steady conditions where convolution can be very accurate. However, the effective dynamics approach can be useful when other approaches breakdown due to extreme conditions with high-performance vehicles.

Overall, this work adds to the discussion of unsteady loads prediction of highly nonlinear, high-dimensional, strongly coupled problems using a maneuverable HSV as an example. A couple of modeling approaches from the literature are investigated to study the feasibility of using these approaches for this application. The model-

ing methods and approach developed is general and can be adapted for future use with multi-disciplinary problems. The nonlinear unsteady surrogate model of the FSJI for HSVs in particular enables flight simulation and aids the future design and development of high-performance vehicles.

CHAPTER 7

Fluid-Structure Interaction Effects on Vehicle Performance and Stability

This chapter begins to analyze the system-level quantities such as maneuverability, agility, and stability as part of the fifth research objective. The first section examines the impact of structural flexibility and stiffness distribution on high-speed vehicle performance and stability. The high-speed vehicle model that has been developed for numerical simulations is used with varying levels of overall flexibility in addition to modifications of the stiffness distribution. The vehicle models with varying structural properties are input into the flight simulation framework with the same applied forces. These simulations are then post-processed to calculate the change in vehicle maneuverability and agility.

The second section focuses on the aeroelastic stability of the high-speed vehicle with two configurations. The first is a state-of-the-art configuration with control fins near the vehicle nose and tail. The second configuration is an advanced concept with divert and attitude control jets as opposed to control fins. The two configurations are modeled in the flight simulation framework and the vehicle response to a small perturbation is used to determine the stability of the vehicle as a function of flight conditions and structural flexibility. These results are compared to weigh the gains in vehicle performance against the impact on vehicle stability for each structural flexibility and control system configuration.

7.1 Modeling Varied Flexibility and Stiffness Distribution

The first structural configuration aspect that is analyzed is the overall vehicle stiffness. This is studied using a vehicle with a uniform mass distribution and free-free vibration mode shapes similar to the analytical solution of a uniform free-free beam. The stiffness of these mode shapes is then scaled to study the effect of flexibility on vehicle response. The range of free-free vibration frequencies used for the first bending mode is 25-40 Hz. The *stiff* vehicle (40 Hz) is near the free-free vibration frequency of the Sidewinder vehicle[94] and the *flexible* vehicle (25 Hz) represents the vehicle material stiffness value roughly cut in half.

The second structural configuration aspect to be analyzed is the distribution of stiffness along the length of the vehicle. The internal structure of the vehicle is non-uniform in practice and this study investigates how different distributions of structural material or stiffness could lead to different responses. The internal structure of a high speed vehicle may have less support material surrounding the solid rocket fuel and more material surrounding the payload and control system. This variation in bending stiffness can be seen as either a change in thickness or material along the length of the vehicle. The bending stiffness distribution that is used to model the representative vehicle is shown in Figure 7.1. This distribution leads to a first bending mode shape with the inflection point aft of mid-length. A linear combination of the uniform and representative stiffness distribution shapes is used to derive several vehicle models. Each new set of vibration modes is mass normalized, the mass and inertia properties of the vehicle are kept constant at 85 kg uniformly distributed, and the low bending frequency associated with each is held constant to the lowest value of 25 Hz. Figure 7.2 shows the free-free vibration mode shapes of the uniform distribution vehicle *Configuration 1* and *2*. These two configurations are used as the bounds for generating

new free-free vibration mode shapes.

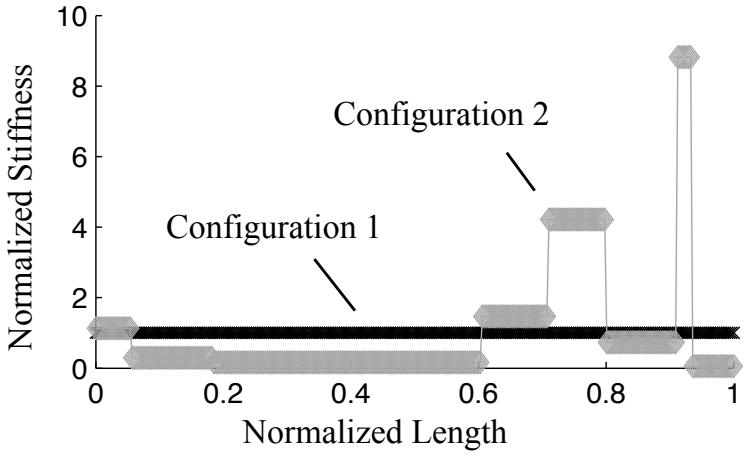

Figure 7.1: Normalized stiffness distributions of the uniform and representative vehicles.

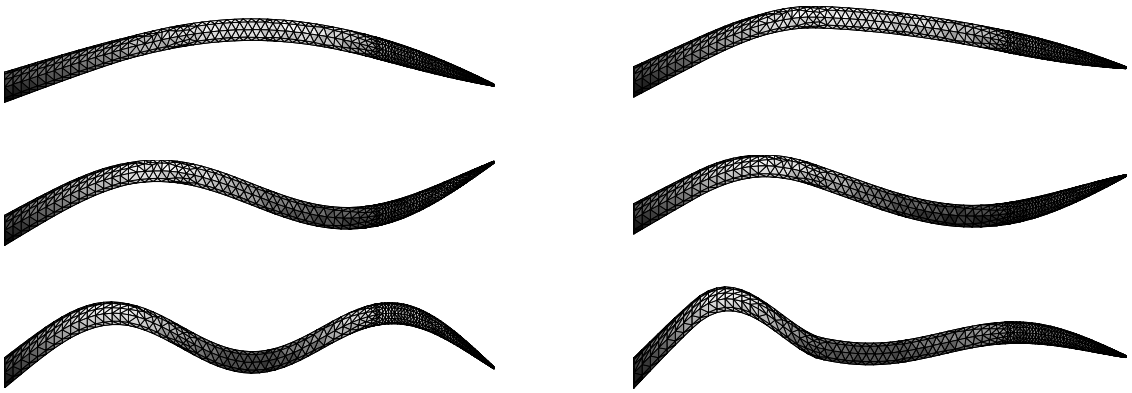

(a) Configuration 1

(b) Configuration 2

Figure 7.2: Free-free vibration mode shapes of the vehicle with uniform and representative mass and stiffness distributions.

These vehicles are modeled in the UM/HSV simulation framework using the baseline aerodynamics and jet interaction modules. This corresponds to shock-expansion aerodynamics with piston-theory for unsteady corrections and an ideal jet model that applies the jet thrust without the additional jet interaction with the supersonic flow. The results represent the expected trends in vehicle performance with varying stiffness and stiffness distribution, which is helpful in the early vehicle development phase.

More accurate modeling methods would be required to include FSJI dynamics during maneuvers.

7.2 Vehicle Performance and Static Stability

The vehicle response and performance during aggressive maneuvers are calculated using the reduced order vehicle and simulation framework. First, a steady aerodynamic analysis shows the variation of the aerodynamic loads for varying levels of vehicle deformation. Second, an open-loop simulation with the attitude jet as the control input shows how the vehicle response is affected by varying the total stiffness (i.e. first bending frequency from 40 Hz to 25 Hz) and varying the stiffness distribution from Configuration 1 to 2. New mode shapes for the different stiffness distributions are calculated as

$$\Phi_i = \Phi_{1i} + \sigma(\Phi_{2i} - \Phi_{1i}) \qquad \text{for } i = 1 \ldots n \tag{7.1}$$

where Φ_i is the i^{th} new shape, Φ_{1i} is the i^{th} Configuration 1 shape, and Φ_{2i} is the i^{th} Configuration 2 shape. The total number of mode shapes, n, used for the analysis is equal to 3 and corresponds to the first three free-free bending modes in the longitudinal plane. The configuration parameter σ ranges from 0 to 1 to create new models that are linear combinations of configurations 1 and 2.

7.2.1 Static aerodynamic results

The aerodynamic characteristics of the model were evaluated about a set of steady conditions to calculate the loads on the vehicle for the selected flight conditions. The loading on the vehicle was calculated over a range of angles of attack from 0 to 60 degrees at Mach 3 and 40,000 ft for varying levels of deformation and different deformation shapes. All of the forces are normalized by the freestream dynamic

pressure, a reference length of 3 m, and a reference area equal to 1 m^2. The static margin is also calculated as the center of pressure changes for each aerodynamic flow condition and deformation. The static margin is calculated as:

$$Static\ Margin = \frac{(x_{cp} - x_{cg})}{L_{ref}} \tag{7.2}$$

where L_{ref} is the reference length.

The change in static aerodynamic properties of the vehicle with varying degrees of deformation is studied first. The results shown in Figure 7.3 were obtained using Configuration 1 (Figure 7.2a).

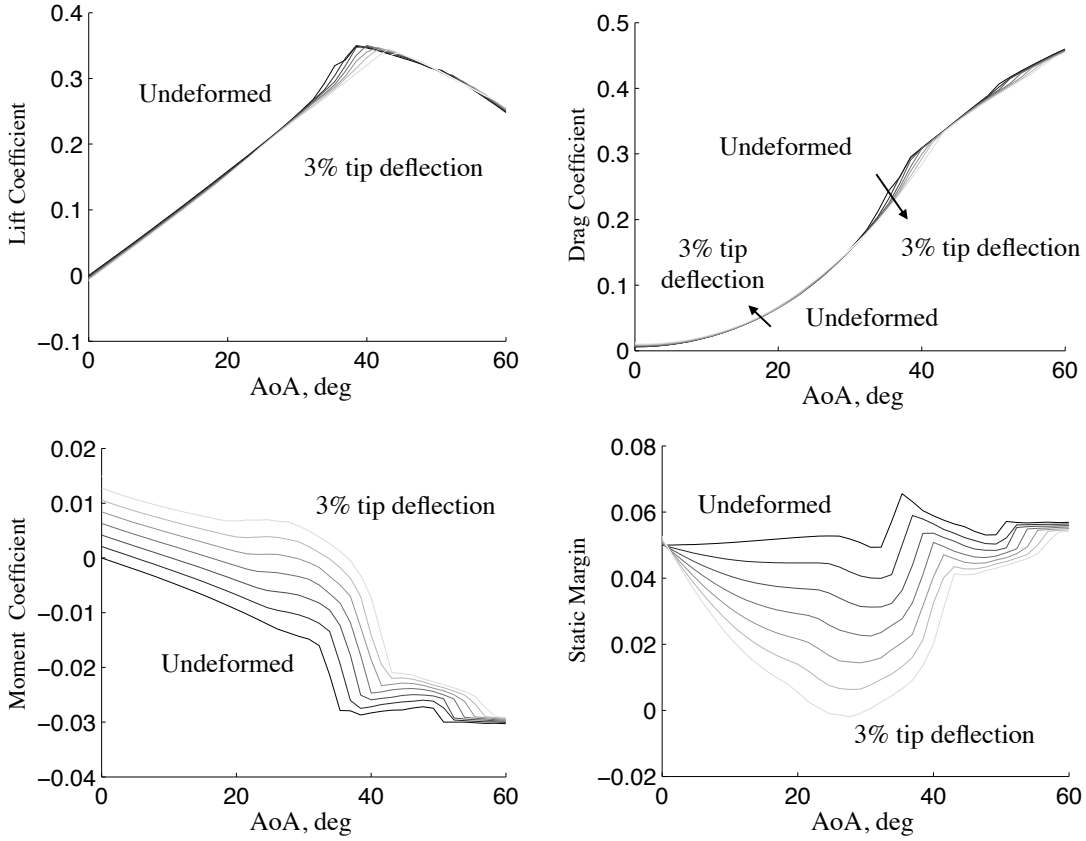

Figure 7.3: Flexible vehicle response with varying levels of deformation under static aerodynamic loading (Configuration 1)

Figure 7.3 shows that vehicles with larger deformation have lower lift, higher drag,

and higher moments about the center of gravity until about 30 to 35 degrees. This angle of attack is near the deflection angle for which an oblique shock will separate at Mach 3 in a two-dimensional flow. Beyond 35 degrees the trend for drag flips so that the vehicles with larger deformation have lower drag. At zero angle of attack the vehicle with higher deformation has a higher static margin. However, as the angle of attack and deformation are increased the static margin for the deformed vehicle is significantly decreased. This effect leads to deformed vehicles being more maneuverable at higher angles of attack.

As discussed above, the vehicle internal configuration can vary along the length and change the free-free vibration characteristics. The effects of the aerodynamic loading on the vehicle were studied as the stiffness distribution transitions to Configuration 2. The effects on lift, drag and moment about the center of gravity are shown in Figure 7.4 for varying stiffness distribution. Only the first bending mode was included here and each mode shape is mass normalized thus a constant energy value was used as opposed to a constant tip deflection. This is to explore the overall trends with the various models although more modes should be included for further investigation due to the impulsive nature of the inputs.

The results in Figure 7.4 show that Configuration 2 has lower lift, higher drag, and higher moment at low angles of attack compared to Configuration 1. The trend for drag flips and Configuration 2 has lower drag for angles of attack larger than 40 degrees. The static margin plot shows the variation in mode shape for vehicles with 1%, 3%, and 5% tip deflections. Configuration 2 has a higher static margin at lower angles of attack, but has a lower static margin than Configuration 1 as the angle of attack is increased. This further increases the maneuverability of the Configuration 2.

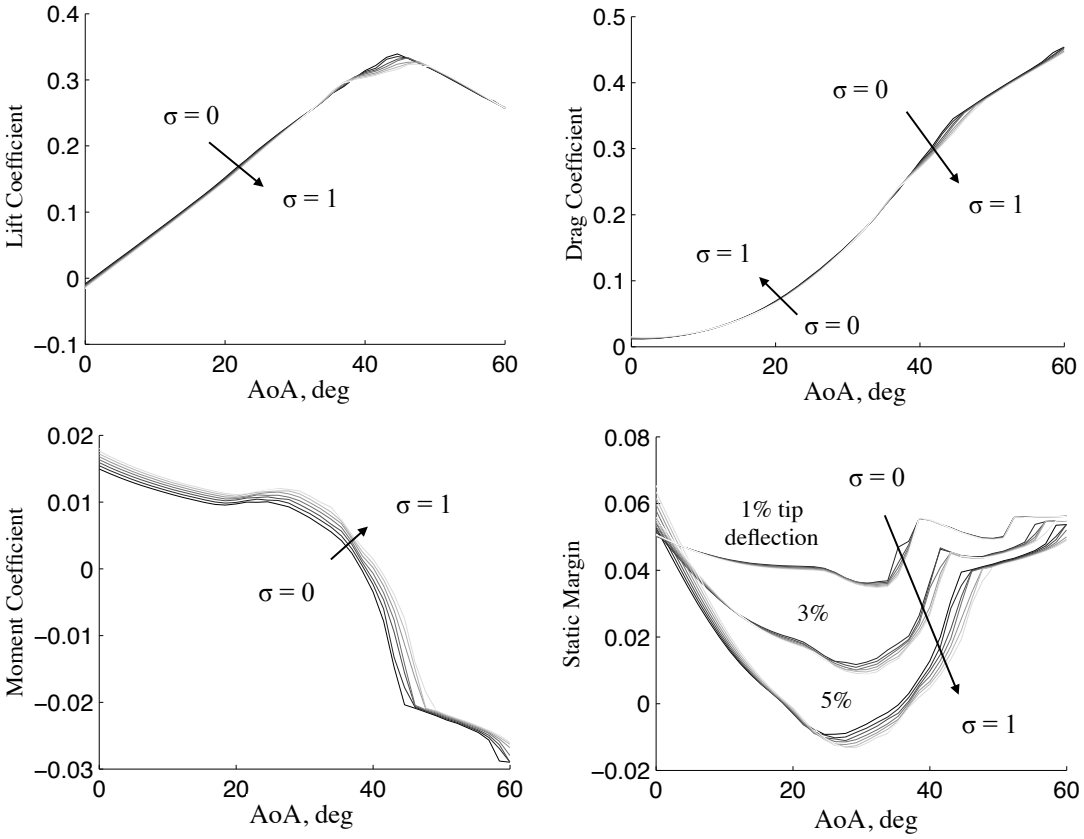

Figure 7.4: Flexible vehicle response under static aerodynamic loading with stiffness distribution varying from Configuration 1 ($\sigma = 0$) to 2 ($\sigma = 1$).

7.2.2 Vehicle response to attitude jet input

The ability to quickly change the flight path to intercept a target is critical to success of the air-to-air vehicle and is calculated in terms of maneuverability and agility. Maneuverability is defined here as the vehicle turn rate based on its flight path angle and the acceleration normal to the flight path. Agility has been calculated using the time rate of change of turn rate. These parameters were chosen based on a previous study[9] that compared the maneuverability and agility metrics across the industry. Two maneuvers were performed using the same attitude jet impulse with a short and long pulse duration. The maneuvers used the attitude jet characteristics shown in

Table 7.1 and applied according to

$$F_{DACS} = \begin{cases} \frac{I}{t_d} sin(2\pi f t) & 0 < t < t_d, \\ 0 & t > t_d. \end{cases} \tag{7.3}$$

Table 7.1: Properties of the attitude jet force applied to the vehicle.

Property	Value	Unit
Location	25	% length
Impulse, I	2500	N·s
Frequency, f	1	Hz
Short duration, t_d	0.5	s
Long duration, t_d	1.5	s

Choosing a range of stiffness values with the stiffness distribution of Configuration 1 shows the impact of vehicle structural properties on the overall performance. A series of vehicles with varying flexibility have been modeled and the responses to the short jet impulse are shown in Figures 7.5 and 7.6. The *stiff* vehicle corresponds to the first bending frequency of 40 Hz and the *flexible* vehicle to the first bending frequency of 25 Hz. Figures 7.7 and 7.8 show the vehicle response to the long duration impulse with varying levels of stiffness. This study is used to simulate a more complex maneuver to see if the trends for the short duration impulse still hold.

The results show that flexibility has an effect on the vehicle response to a jet impulse used to turn the vehicle. The performance metrics follow trends shown in the steady aerodynamics results section. The vehicles with higher deformation have higher maneuverability ($\dot{\gamma}$) and agility ($\ddot{\gamma}$), but have lower velocities at the end of the maneuver due to increased drag. The improvements in the vehicle maneuverability and agility are summarized in Table 7.2 for the short and long duration impulses.

The vehicle stiffness distribution was studied to calculate its effect on vehicle performance. All of the vehicles have the same inertia properties and stiffness values,

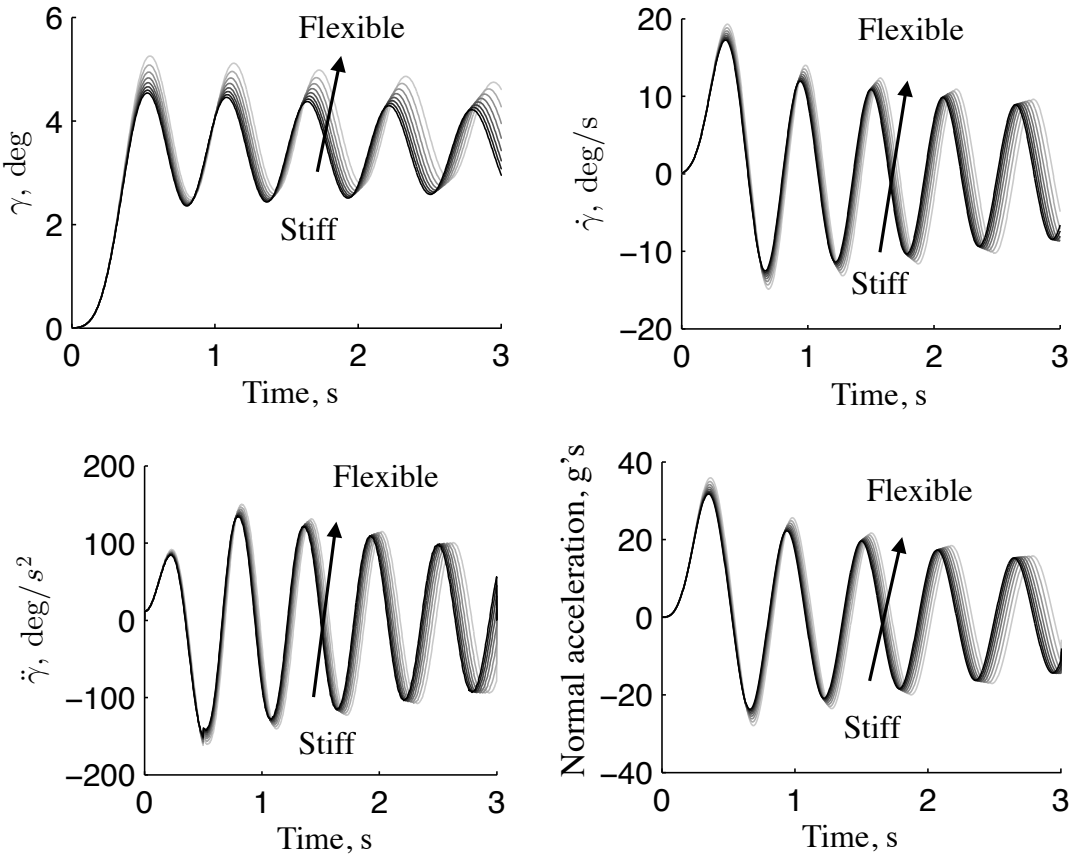

Figure 7.5: Performance results of the vehicle with varying stiffness in response to the short attitude jet impulse (Configuration 1 stiffness distribution).

Table 7.2: Summary of performance increases by reducing the vehicle stiffness from 40 Hz to 25 Hz.

Impulse duration	Normal acceleration	$\dot{\gamma}$	$\ddot{\gamma}$
Short	13.08%	11.92%	7.10%
Long	23.09%	21.48%	13.13%

which isolates the difference in the results to the free-free vibration mode shapes. The lowest free-free vibration frequency (25 Hz) was used for all models as the mode shape is varied between Configuration 1 and 2 shown in Figures 7.2a and 7.2b, respectively. This shows the effects of moving the inflection point of the vehicle deformation. Figures 7.9-7.12 show the vehicle responses to short and long duration impulses with varying free-free vibration mode shapes.

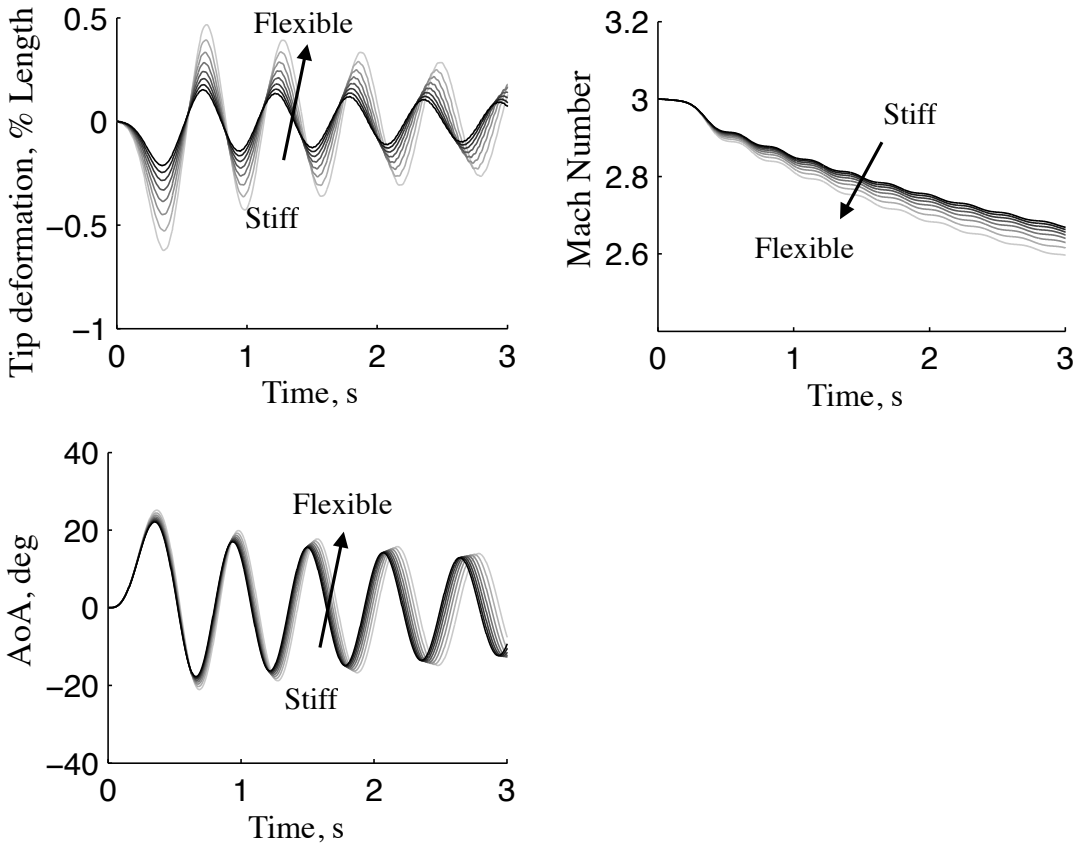

Figure 7.6: Structural and flight dynamics response of the vehicle with varying stiffness in response to the short attitude jet impulse (Configuration 1 stiffness distribution).

The results show that the vehicles with the Configuration 2 stiffness distribution are more maneuverable and agile, but have higher drag and lower velocities at the end of the maneuver than Configuration 1 vehicles. These results are in line with the steady aerodynamic results. The improvements in the vehicle maneuverability and agility are summarized in Table 7.3 for the short and long duration impulses.

Table 7.3: Summary of performance percent increases by transitioning from Configuration 1 to 2 for the 25 Hz case.

Impulse duration	Normal acceleration	$\dot{\gamma}$	$\ddot{\gamma}$
Short	2.58%	2.34%	2.45%
Long	5.20%	4.77%	3.06%

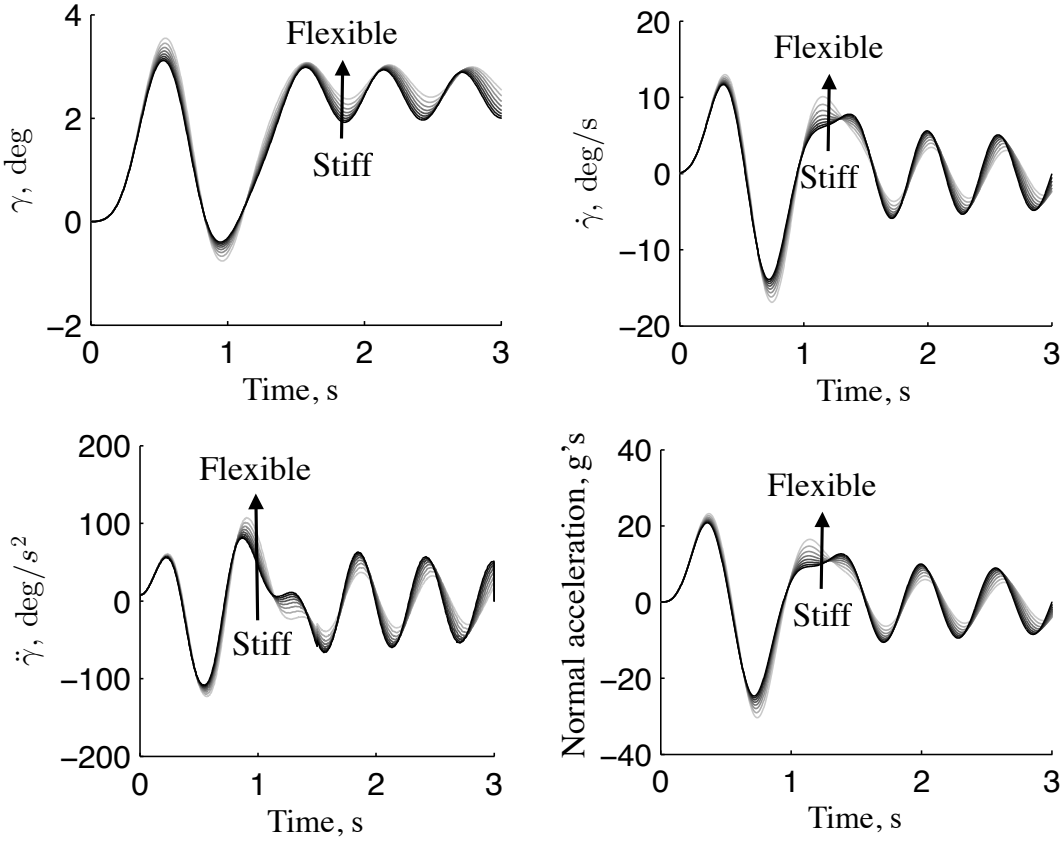

Figure 7.7: Performance results of the vehicle with varying stiffness in response to the long attitude jet impulse (Configuration 1 stiffness distribution).

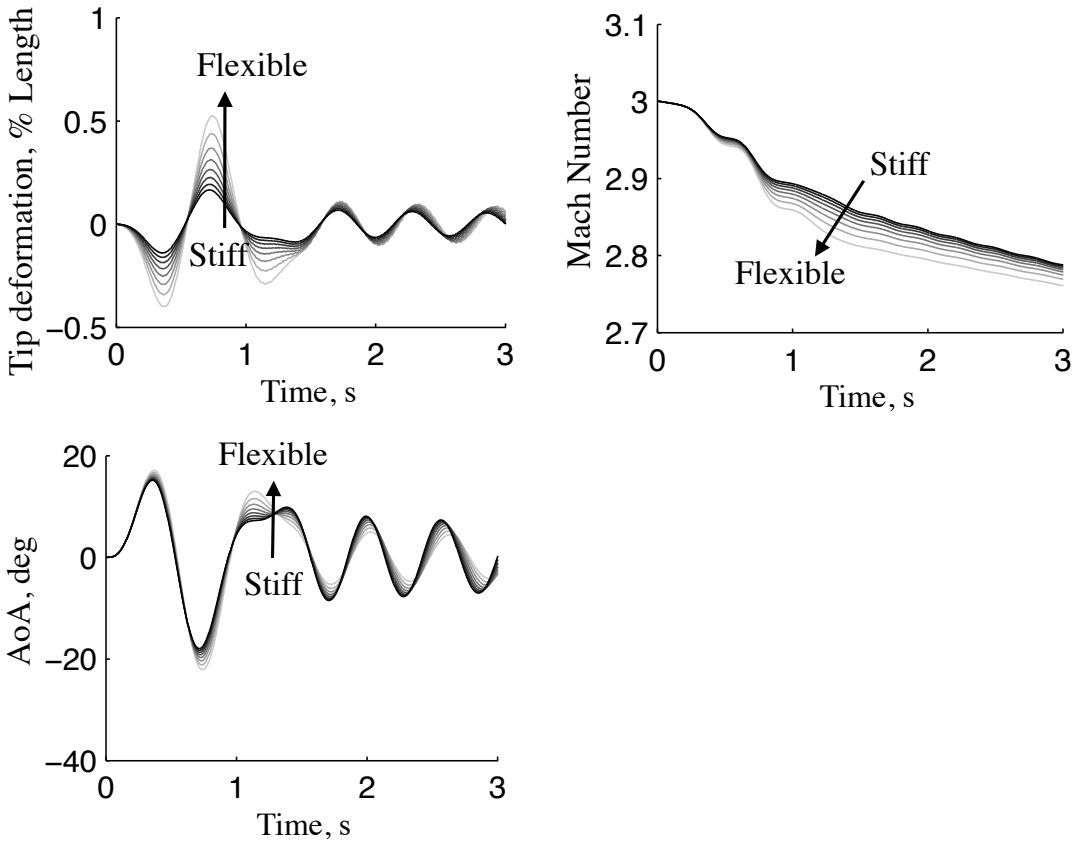

Figure 7.8: Structural and flight dynamics response of the vehicle with varying stiffness in response to the long attitude jet impulse (Configuration 1 stiffness distribution).

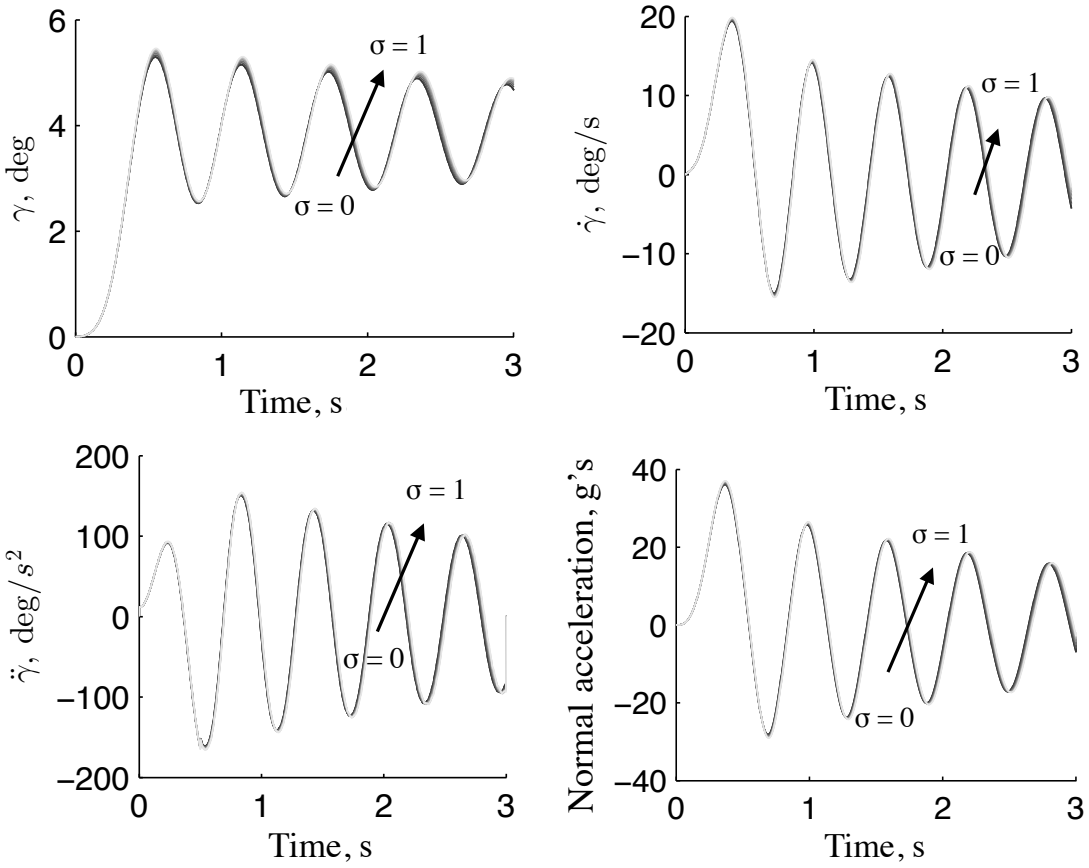

Figure 7.9: Performance results of the vehicle in response to the short attitude jet impulse with stiffness distribution varying from Configuration 1 to 2 with the first bending frequency equal 25 Hz.

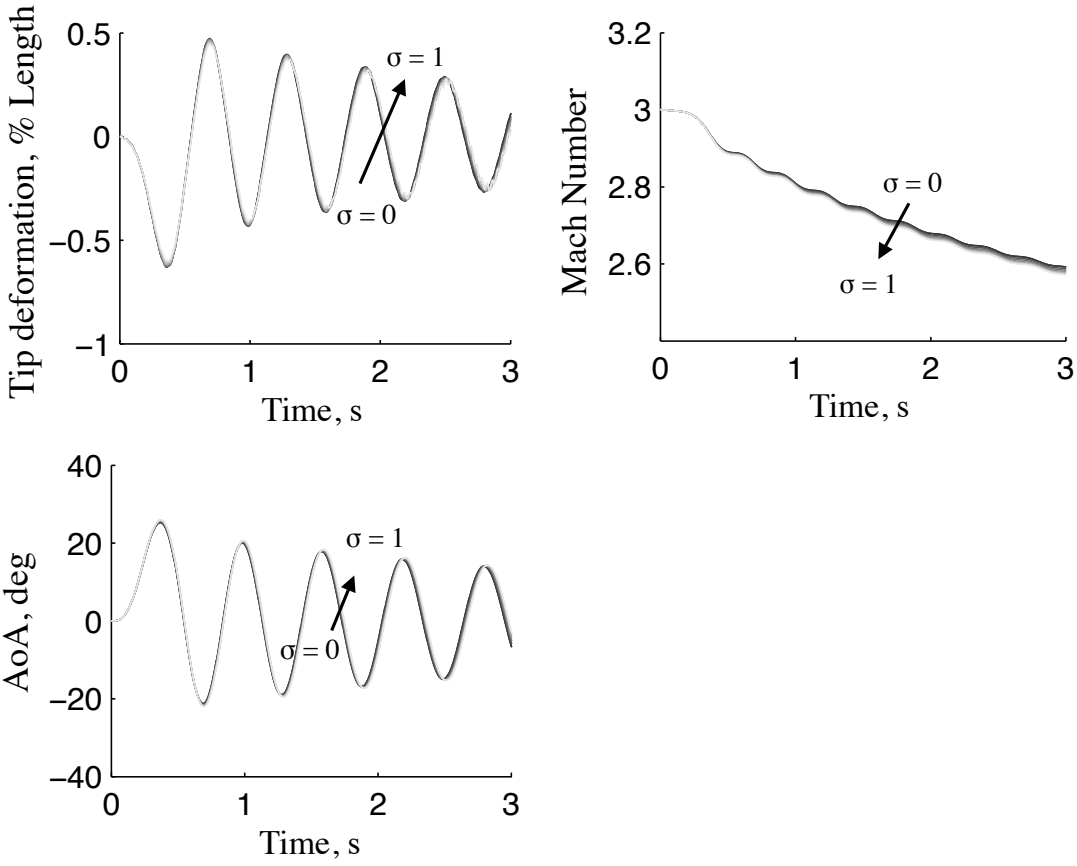

Figure 7.10: Structural and flight dynamics response to the short attitude jet impulse with stiffness distribution varying from Configuration 1 to 2 with the first bending frequency equal 25 Hz.

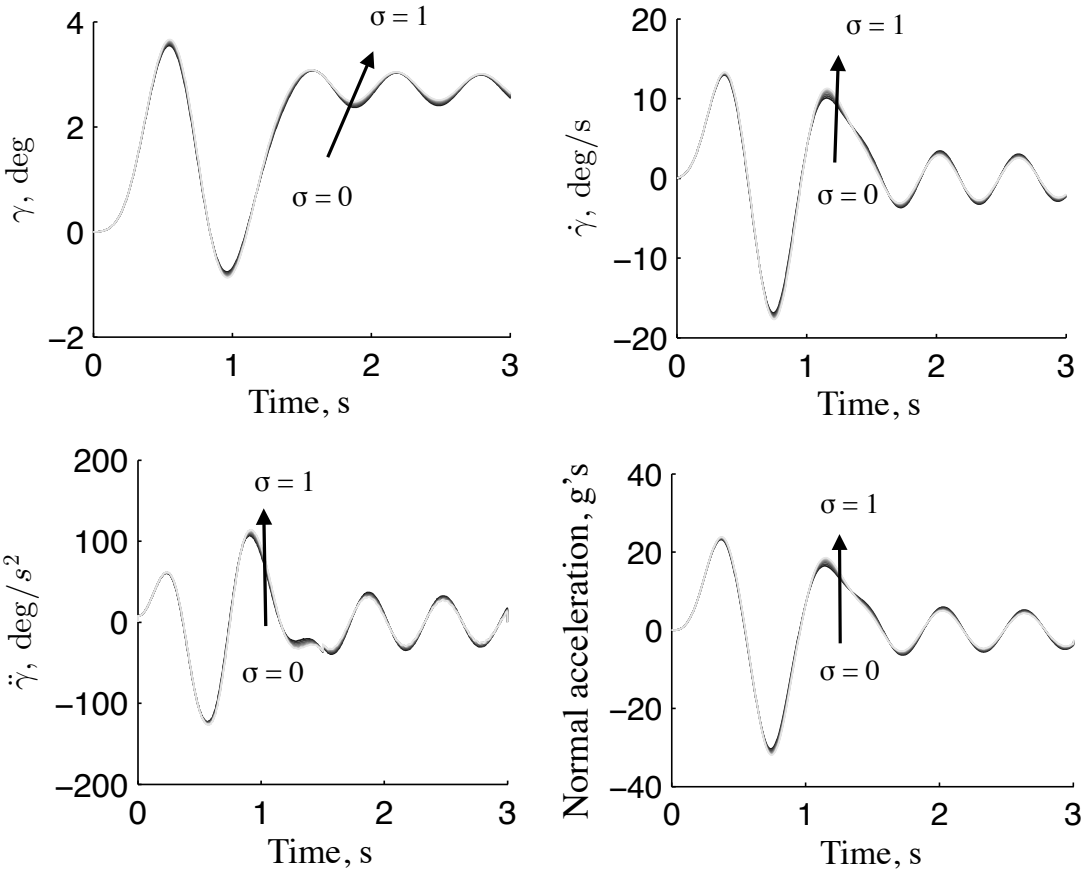

Figure 7.11: Performance results of the vehicle in response to the long attitude jet impulse with stiffness distribution varying from Configuration 1 to 2 with the first bending frequency equal 25 Hz.

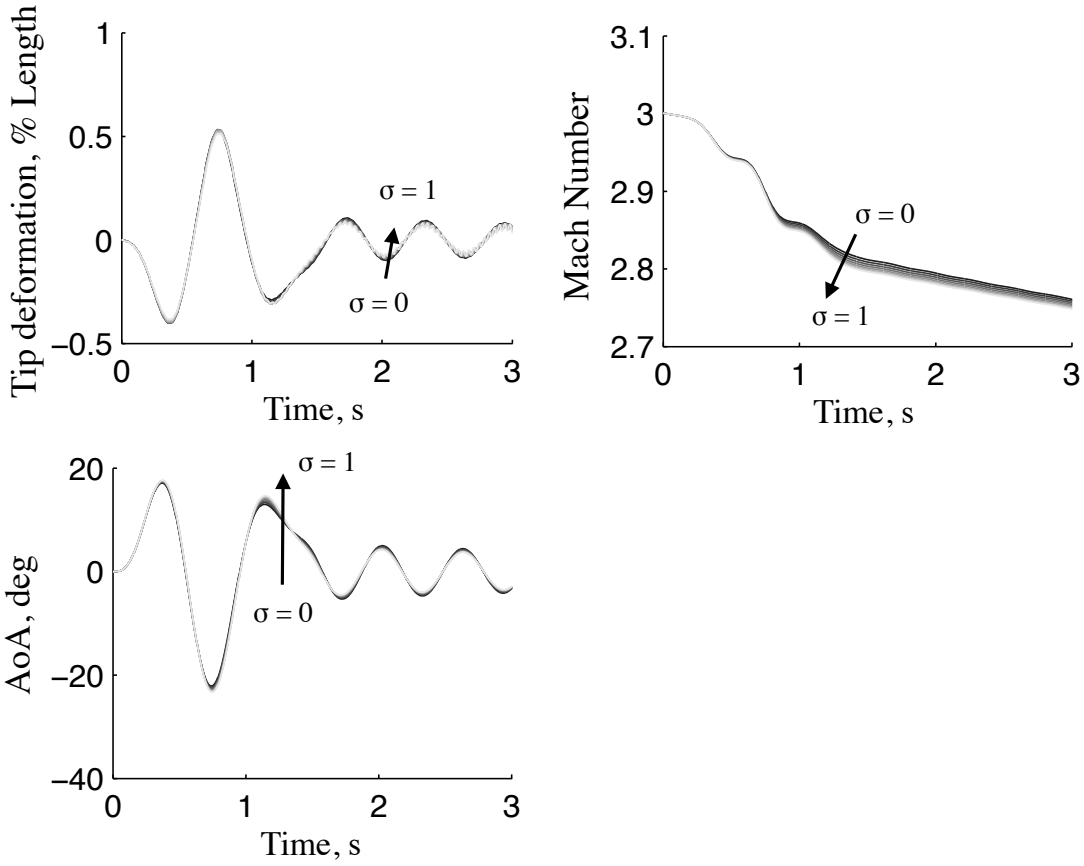

Figure 7.12: Structural and flight dynamics response to the long attitude jet impulse with stiffness distribution varying from Configuration 1 to 2 with the first bending frequency equal 25 Hz.

7.3 Dynamic Vehicle Stability

The dynamic stability of the state-of-the-art and advanced concept configurations is assessed over the flight envelope with varying levels of structural stiffness. Each vehicle is modeled in the UM/HSV simulation framework that captures the coupling between the vehicle aerodynamics, structural dynamics, and rigid-body dynamics. The equations of motion are updated at each time step and marched forward to calculate the vehicle response. The vehicle aerodynamics are modeled using a shock-expansion panel method to calculate the vehicle steady-state loads with a piston-theory correction for unsteady loads. The vehicle structures are modeled with the same uniform mass and stiffness distributions, which is represented in the framework with free-free vibration mode shapes shown in Figure 7.13.

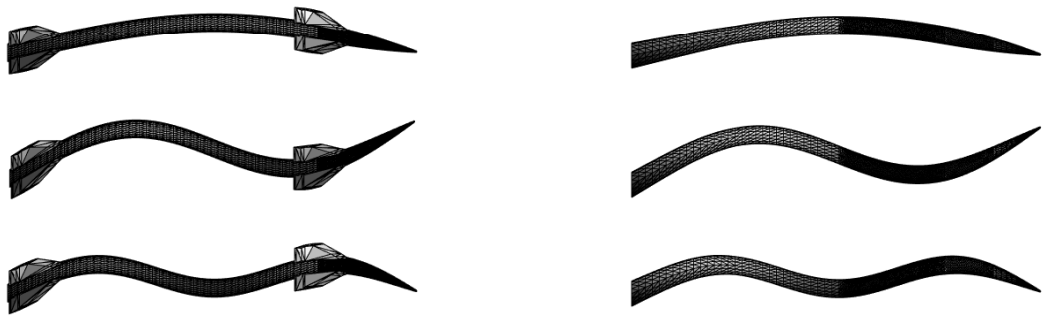

(a) State-of-the-Art Configuration (b) Advanced Concept Configuration

Figure 7.13: Free-free vibration mode shapes used to represent structural deformations during flight simulations.

The objective is to identify the coupled aeroelastic and flight dynamic stability boundary for each vehicle as a function of altitude, Mach number, and structural stiffness. The bounds for these parameters are listed in Table 7.4. An exhaustive search is not feasible and therefore adaptive sampling is used to expedite the process of identifying the stability boundary. A coarse sampling of the space is used initially to estimate the stability boundary and identify the next sample point that would

add the most information. These initial points are the 8 extreme values of the three-dimensional space and the process continues with *max-min* and *anti-locking* points as calculated using the CODES toolbox [85] until the stability boundary converges as determined by the EDSD algorithm with $\epsilon_1 = 4 \times 10^{-}3$ and $\epsilon_2 = 5 \times -4$ for the error tolerances. These points maximize the additional information gained as opposed to additional random samples. The first eight simulations are the corners of the three-dimensional parameter space and 92 additional *max-min* points are added to calculate the stability boundary of each configuration. The three-dimensional stability boundary is calculated by the SVM module of the CODES toolbox with the Gaussian kernel to represent the nonlinear boundary.

Table 7.4: Bounds for calculating vehicle stability.

Parameter	Lower Bound	Upper Bound	Units
Altitude	12	30	km
Mach	2	4	
Structural Stiffness	10	100	% Baseline Stiffness
Corresponding Frequency of First Bending Mode	13	40	Hz

The flutter boundary is calculated using time-domain simulation results of the vehicle configurations in free flight. After an initial time has passed at the initial flight condition, a small perturbation is imposed in the form of a point force in the positive-z direction to cause a nose-up attitude. The vehicle flight dynamic response is then monitored to determine if the vehicle is stable or unstable. Examples of stable and unstable responses are shown in Figures 7.14 and 7.15, respectively. An ARMA model with two autoregressive and one moving average coefficient is fit to the vehicle response to expedite the process and avoid manually or qualitatively assessing stability. Following the work of Pak and Friedmann [89], the ARMA model is then expressed as a linear system to calculate the eigenvalues where positive real parts of the eigenvalues indicate instability.

The stability boundary is shown for both configurations in Figures 7.16 and 7.17.

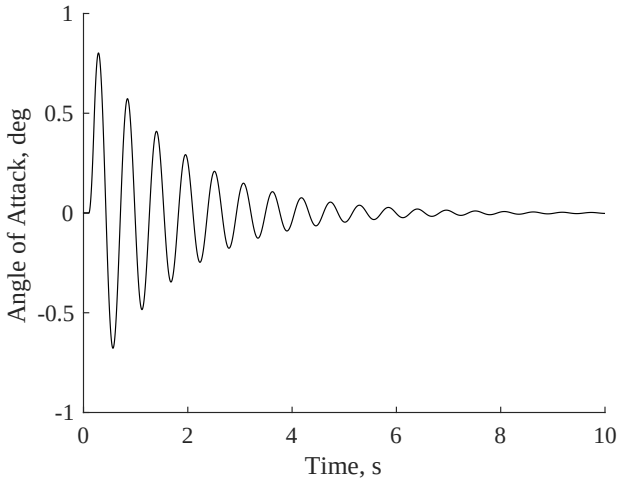

Figure 7.14: Sample responses of the advanced concept vehicle at 12-km altitude and Mach 3 with 100% of the baseline stiffness.

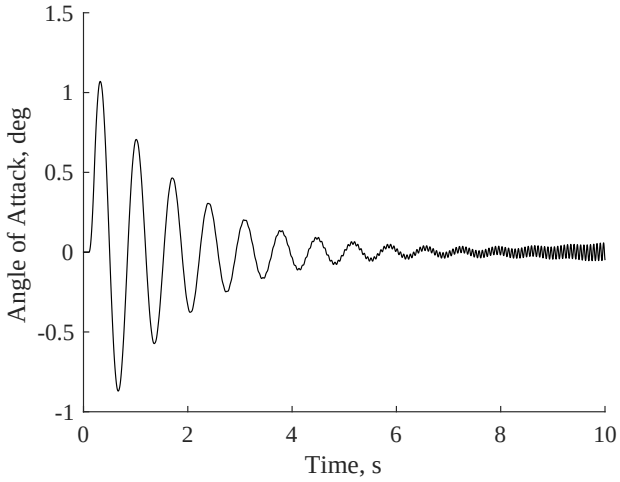

Figure 7.15: Sample responses of the advanced concept vehicle at 12-km altitude and Mach 3 with 10% of the baseline stiffness.

Figure 7.16 shows a view of the boundary in the three-dimensional space and 7.17 shows the boundary surfaces from the side to highlight the lack of Mach number dependence for the configurations. As altitude is decreased and stiffness is decreased for both configurations the system becomes unstable, which is to be expected. However, the state-of-the-art configuration becomes unstable for stiffness values and altitudes approximately 40% larger and 5 km higher, respectively, than the advanced configuration. The additional surface area of the control surfaces increases the aerodynamic

loads compared to the advanced concept and leads to instability for a larger portion of the parameter space. The state-of-the-art configuration is more sensitive to additional structural flexibility and the advanced concept is more robust to additional flexibility.

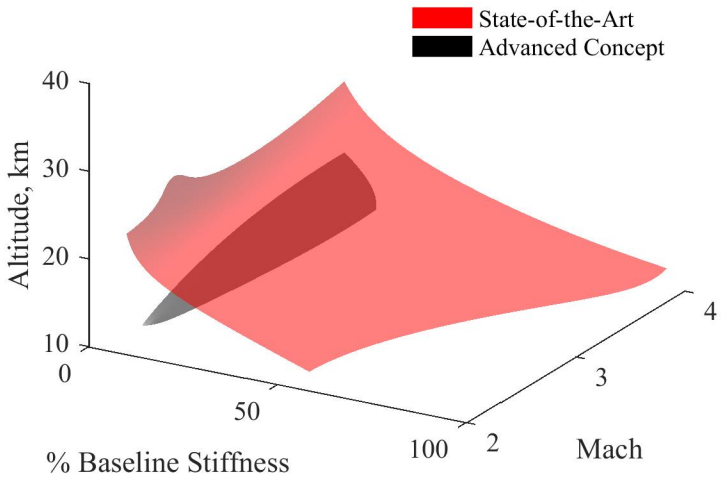

Figure 7.16: Three-dimensional view of the stability boundary calculated for both configurations dependent on Mach number, vehicle stiffness and altitude.

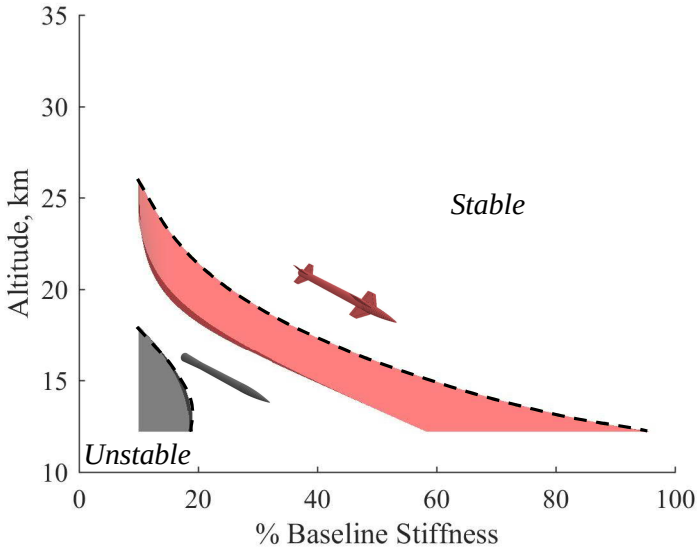

Figure 7.17: Side view of the stability boundary along the Mach-axis calculated for both configurations dependent on Mach number, vehicle stiffness and altitude.

7.4 Concluding Remarks

The focus of this chapter is the impact of flexibility, structural configuration, and reaction jet control inputs on the performance and stability of slender high speed vehicles. Analyzing the results shows that even very small deformations (1% of the vehicle length) have a significant impact on the aerodynamic loading and vehicle response. In addition, the shape of the vehicle deformation has an impact on the vehicle loading and response. The results add to the findings in the literature by showing that the slender vehicle is more maneuverable as the inflection point of the free-free vibration mode shape is moved aft.

The static aerodynamic results provide the motivation to consider vehicle stiffness as a design parameter for improving vehicle maneuverability and agility. Considering the vehicle model with uniform properties, the vehicles with larger deformation have higher moment coefficients throughout the range of angles of attack that was considered. Therefore, a flexible vehicle will either reach higher angles of attack for the same applied force or will require less applied force to maintain the same angle of

attack as compared to a stiffer vehicle. A similar effect is evident when considering the stiffness distribution of the vehicle. As the vehicle shape is transitioned from a uniform stiffness distribution (*configuration 1*) to the representative stiffness distribution (*configuration 2*), the moment coefficient about the center of gravity is increased for the range of angles of attack that were calculated. Therefore, for the same amount of energy applied to the structure the vehicles with inflection points located aft will reach higher angles of attack. During the trajectory the vehicle is likely to have low deformation at low angles of attack and larger deformation at higher angles of attack. The static margin was decreased in both cases either by increasing deformation or moving the inflection point of the deformation aft. Therefore, the flexible vehicle for either configuration show little to no effect on stability during minor maneuvers, but will have a positive benefit on maneuverability during aggressive maneuvers by moving the center of pressure forward.

The vehicle response to the attitude jet impulse follows similar trends to the static aerodynamic results for vehicles with varying stiffness values and distributions. Considering the short and long duration impulses applied to the uniform vehicle with varying stiffness the flexible vehicles have larger deformations which translates to higher maneuverability and agility calculated using the flight path angle. In addition, there is a phase shift that occurs in the vehicle response that stems from the flexible vehicles maintaining larger deformations for a longer time duration. Using the most flexible model then transitioning to the configuration 2 stiffness distribution further increases maneuverability and agility.

This work also compared vehicle configurations with control fins to slender axisymmetric flexible structures with attitude control jets. The dynamic stability of the finned and axisymmetric configurations was assessed using time domain flight simulations of various flight conditions and structural stiffness values. The results were used to calculate the stability boundary of each vehicle with respect to flight al-

titude, Mach number, and structural stiffness. Overall, the Mach number had a small effect on vehicle stability, but the boundary was strongly dependent on altitude and structural stiffness. As expected, lower altitudes and structural stiffness values lead to instability. However, the calculated stability boundary of the advanced concept was significantly lower than the state-of-the-art configuration. As vehicle flexibility is increased, the additional surface area of the control surfaces lead to higher aerodynamic loading. This effect must be taken into account as flexibility is introduced in the design and development of both configurations.

The results that have been presented show that vehicle maneuverability, agility, and stability are dependent on vehicle structural properties as well as outer mold line. The largest gains in performance are made as the structural configuration approaches a more flexible design. Additional gains are achieved by a structural configuration that moves the inflection point of the dominant deformation mode aft along the vehicle. Adding fins may increase surface area and maneuverability, but significantly reduces the stability region compared to the finless configuration. These results show that modeling the interaction between the aerodynamics, structural dynamics and flight dynamics can be reveal design trends that may ultimately improve performance.

CHAPTER 8

Fluid-Structure-Jet Interaction Effects on Vehicle Performance

This chapter focuses on the steady and dynamic loads due to FSJI as they relate to vehicle performance. Vehicles with and without fins are studied with varying flight conditions, structural deformation, and jet input. The jet interaction amplification factor is presented to quantify the multi-physics interaction effect on the steady-state loads. The step responses to changes in fluid, structure, and jet parameters are compared between the finned and finless configurations and provide insight to the performance impact due to dynamic inputs. These results, combined with the aeroelastic analysis of the previous chapter, fulfill the fifth research objective.

The numerical studies are based on the two vehicle configurations introduced in Section 3.2. They allow one to exploit multi-physics interactions for performance gains that can be concisely calculated by metrics such as the amplification factors. The baseline finned configuration is modeled as a rigid vehicle with only control surfaces available for attitude control. Each of the other vehicles, i.e. a finned and a finless configuration, introduce a combination of structural flexibility, attitude control jets, and removed control surfaces to add additional capability to the vehicle design. Table 8.1 provides a summary of the naming convention and characteristics of each concept. These design modifications introduce complex interactions between the fluid, structure, and jet components that is not taken into account in the baseline configu-

ration. Both vehicles are modeled with structural deformation and attitude control jets that represent the introduction of slenderness and alternative control systems. Given equal mass and inertia properties, the maneuverability and agility correspond directly to the forces applied to the vehicle. Therefore, the amplification of these forces due to multi-physics interactions is presented to highlight areas of improved performance relative to a conventional configuration.

Table 8.1: Summary of the vehicle configurations.

Concept	Configuration	Flexibility	Attitude Control
Baseline	Finned	Rigid	Fins
Conventional	Finned	Flexible	Fins + DACS
Advanced	Finless	Flexible	DACS

8.1 Steady-State Loads

The steady-state vehicle loads of the various configurations due to FSJI are presented in Figures 8.1–8.2. The flow angle of attack, structural deformation, and jet total pressure were the parameters varied from ±60 degrees, ±5% tip deflection, and up to 1 MPa, respectively. The lift coefficient and pitch moment coefficient are calculated using the aerodynamic and JI forces only and do not include the contribution due to jet thrust. The amplification factors due to JI, K, are calculated to highlight the regions of favorable and adverse conditions that affect the control authority. In addition, a support vector classifier has been fit to the data to visualize the boundary of increased and decreased control authority.

Examining the lift coefficient (Figure 8.1) and corresponding amplification factor, there is a decrease in control effectiveness at high angles of attack for both configurations. However, the finned configuration transitions from enhanced to reduced amplification factor at approximately +20 degrees angle of attack with the jet on the windward side of the vehicle. The advanced concept transitions from enhanced to

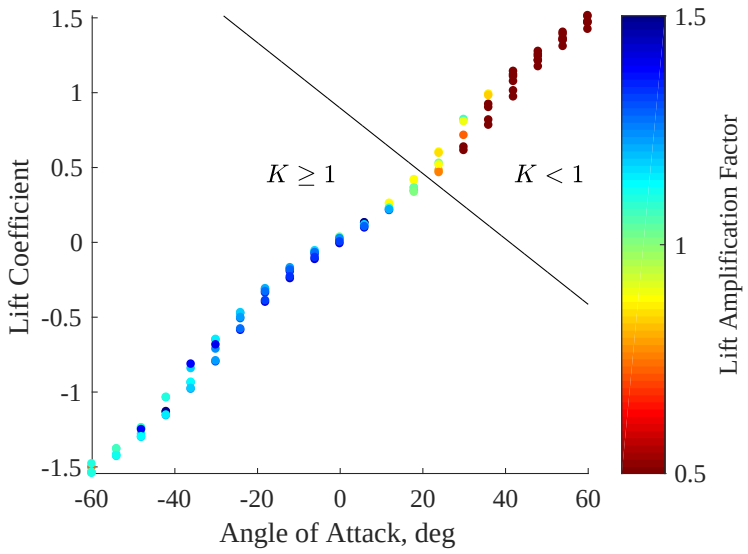

(a) Conventional Configuration

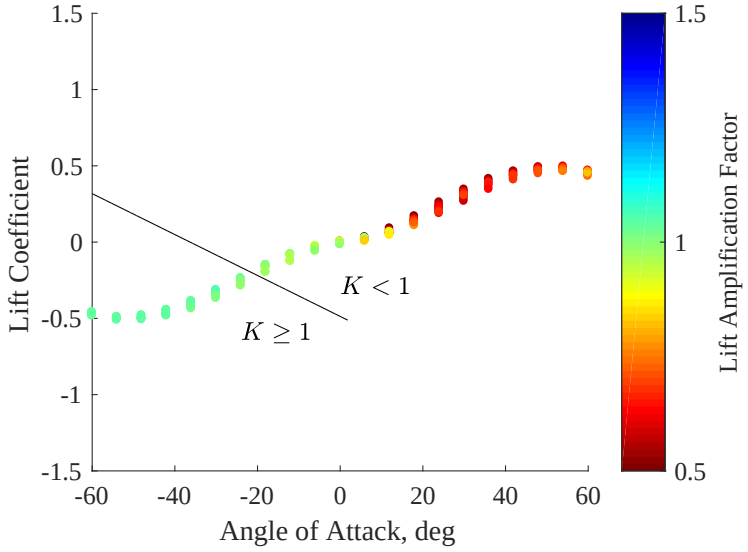

(b) Advanced Concept Configuration

Figure 8.1: Steady-state lift due to fluid-structure-jet interaction for the conventional and advanced concept configurations. Positive angles of attack correspond to the jet on the windward side of the vehicle.

reduced JI amplification around -20 degrees angle of attack when the jet is on the leeward side of the vehicle. Furthermore, the overall lift slope is approximately three times higher due to the presence of the control fins, which would directly translate to higher maneuverability although with a penalty due to increased drag.

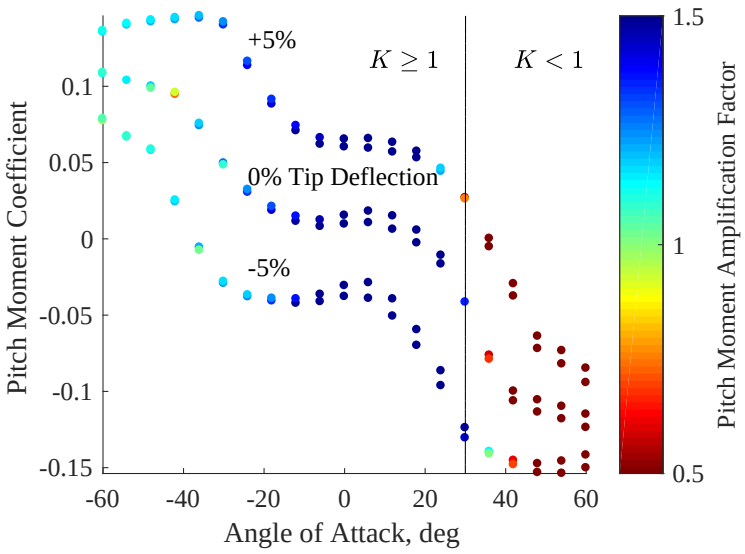

(a) Conventional Configuration

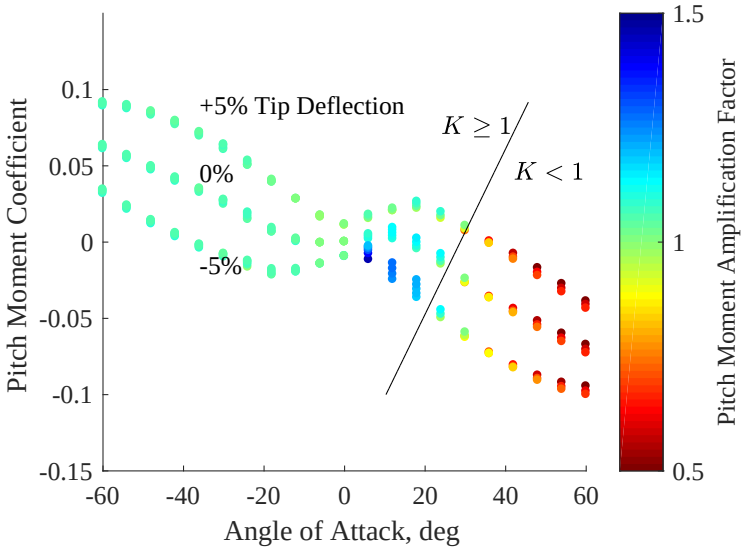

(b) Advanced Concept Configuration

Figure 8.2: Steady-state pitch moment due to fluid-structure-jet interaction for the conventional and advanced concept configurations. Positive angles of attack correspond to the jet on the windward side of the vehicle.

The effect of structural deformation is most clearly seen in the pitch moment coefficient values of both configurations (Figure 8.2). The pitch moment is increased in both cases for positive deformation and decreases for negative deformation. This effect is more pronounced in the advanced configuration at high angles of attack,

but is consistent for the conventional configuration throughout the range of angles of attack studied. The overall pitch moment derivative with respect to angle of attack is larger for the conventional configuration, but is nonlinear near zero angle of attack for both configurations. This could lead to significant differences in the static stability of each configuration and the control effort required to maintain high angles of attack while maneuvering.

The amplification of pitch moment due to JI for the conventional configuration is relatively insensitive to structural deformation whereas the advanced concept shows variation with structural deformation for small positive angles of attack. The JI has a significant effect for low angles of attack with the conventional configuration due to the increased area with high surface pressure from the flow separation and shocks in the flow. The amplification due to JI is reduced for high angles of attack and leads to a loss in control effectiveness at high angles of attack with the jet on the windward side. The pitch moment amplification due to JI for the advanced concept is relatively insensitive to angle of attack with negligible effect for negative angles of attack. There is a reduction in effectiveness at high angles of attack with the jet on the windward side, which is similar to the conventional configuration. At these conditions there are no control reversal conditions observed for either configuration, but the jet interaction effect can be exploited most strongly with the presence of control fins.

8.2 Dynamic Loads

The dynamic loads of the conventional and advanced concept configurations are analyzed using step inputs to the fluid, structure and jet input parameters via the angle of attack, structural deformation, and attitude jet total pressure. Each dynamic CFD simulation is started from a steady-state solution of the vehicle at Mach 3, 70,000 ft altitude, zero angle of attack, no structural deformation, and no attitude jet pressure.

The response of the vehicle lift and moment were calculated and used to calculate the JI amplification factors. The magnitudes of the step inputs are listed in Table 8.2. Figures 8.3–8.6 show the responses of the conventional and the advanced concept configurations to step inputs in the fluid, structure, and jet input channels, respectively. Figures 8.7–8.9 show the coupled step responses to simultaneous step changes in the fluid, structure, and jet parameters.

Table 8.2: Magnitudes of the step inputs used for the dynamic loads assessment.

Parameter	Value	Unit
Angle of attack	10	degrees
Structural deformation	1%	tip deflection, $\%L_{ref}$
Attitude jet total pressure	1	MPa

The results in Figure 8.3 show the vehicle response to a 10-degree step change in angle of attack for the advanced concept and conventional configuration. The responses are similar qualitatively, but the magnitudes of the conventional lift and moment coefficients are higher than the advanced configuration due to the presence of the the control fins. This trend is consistent throughout the step response and is consistent with the trends observed in the steady-state loads assessment.

Figure 8.4 shows the responses to a step change in the structural deformation of the vehicle. The deformation is imposed on the vehicle by amplifying the first longitudinal bending mode and holding that deformation constant for the duration of the CFD simulation. The magnitude of the conventional vehicle is larger in both the lift and pitch moment compared to the advanced configuration. However, there is a distinct jump that occurs as the flow travels down the length of the vehicle. The external flow is traveling Mach 3 and thus the flow initially at the nose travels the length of the vehicle at around $t = 1/3$ in nondimensional time. At this time the aft control fins have an additional effect on the lift and pitch moment whereas the finless advanced configuration has less unsteady effects due to structural deformation.

Figure 8.6 shows the amplification factor due to JI for the vehicle lift and pitch

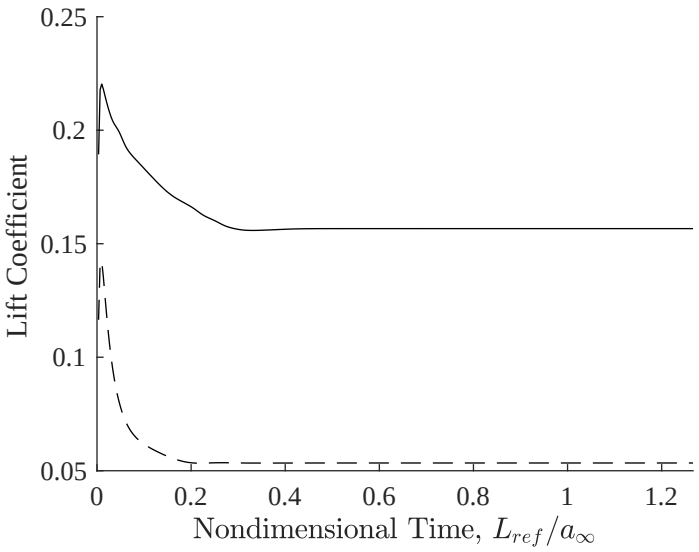

(a)

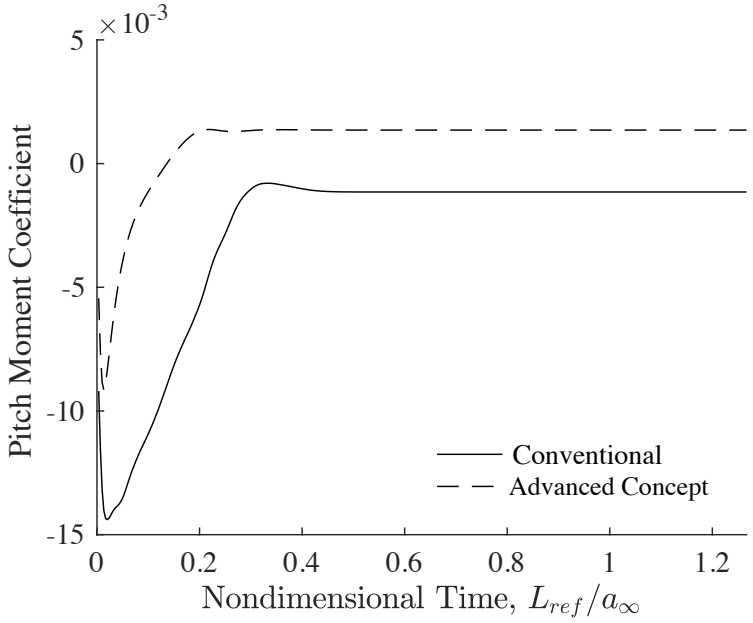

(b)

Figure 8.3: Vehicle responses to a 10-degree step change in angle of attack with no structural deformation or JI.

moment of each configuration. Each configuration is significantly affected by the JI with the external flow and the change in amplitude of the dynamic loads is significant compared to the steady-state value. The advanced configuration has a steady-state amplification in lift coefficient of about -10% with a range from approximately -30%

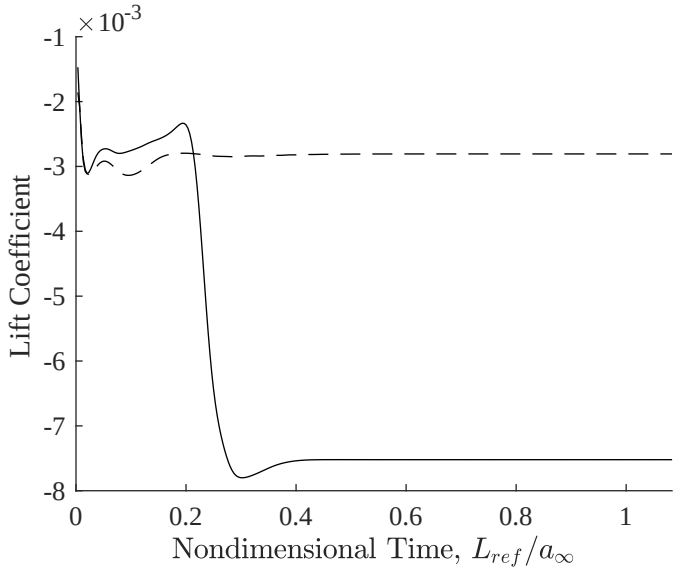

(a)

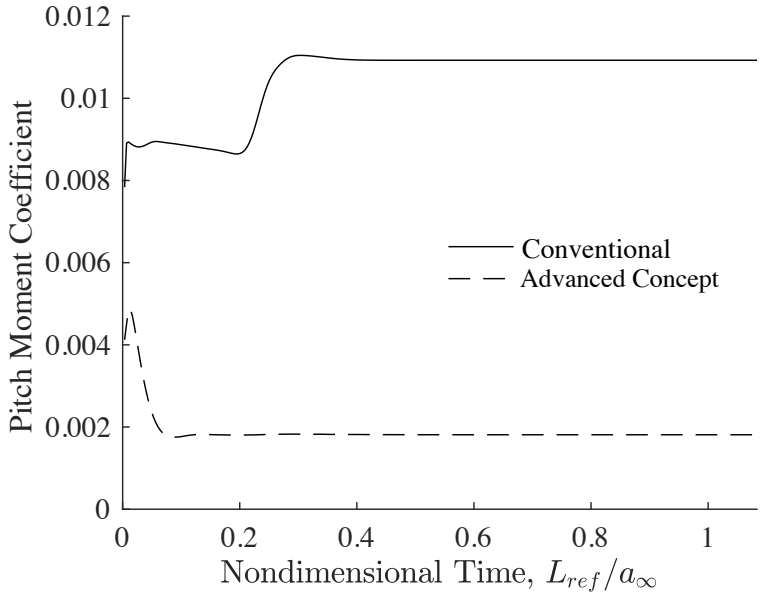

(b)

Figure 8.4: Vehicle responses to a 1% deflection nose-up step change in structural deformation with zero angle of attack and no JI.

to +10%. However, the conventional configuration has a steady-state amplification in lift due to JI of approximately 20% with peaks in the dynamic response up to 50%. The dynamics of the JI response must be taken into account in both cases, but especially the conventional configuration where significant gains are possible for short

pulses of the attitude control jet. The jet-fin interaction from Section 3.3 is presented again in Figure 8.5 to visualize how the high-pressure region in the jet interaction profile extends laterally onto the fins and increasing the applied loads.

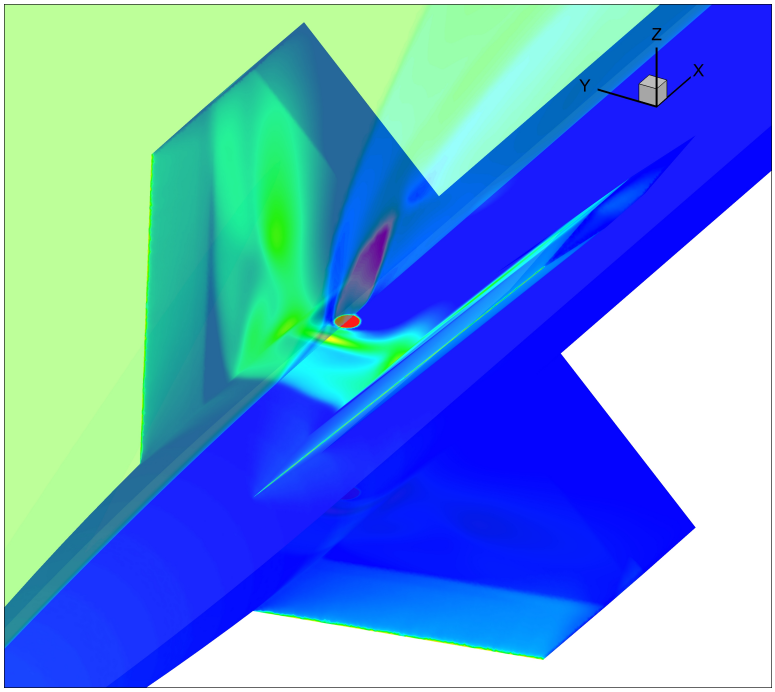

Figure 8.5: Visualization of Mach number contours in the longitudinal cut plane and normalized pressure $\bar{p}$ along the finned vehicle surface from the grid convergence study in Section 3.3.

The pitch moment of each vehicle is significantly affected by the dynamic loads due to JI. The conventional configuration steady-state amplification due to JI is approximately 200% due to the presence of the fins. The advanced concept pitch moment is less affected by JI with a dynamic peak-to-peak amplitude of approximately 20%. In each case the transient loads due to JI take time to reach a steady-state value. However, the effects of jet interaction are highly dependent on the local geometry near the jet exit.

Figure 8.7 shows the vehicle response to simultaneous step changes to the fluid and jet parameters. The amplification of the lift and pitch moment due to jet interaction are presented to highlight the effect of jet interaction and the change due to

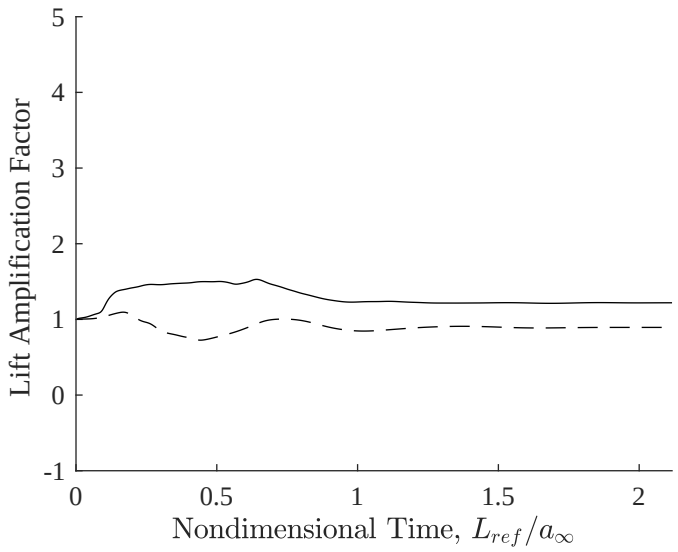

(a)

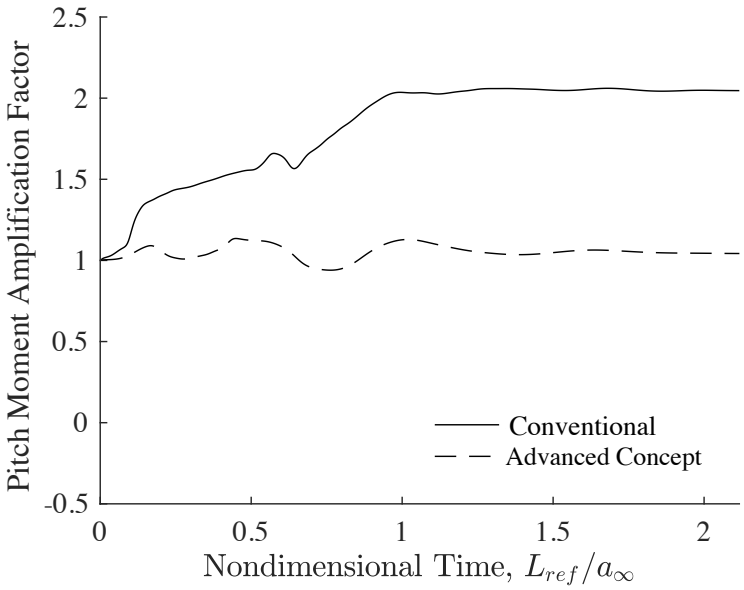

(b)

Figure 8.6: Vehicle responses to a 1-MPa step change in jet total pressure with zero angle of attack and no structural deformation.

body angle of attack. The responses are significantly different than Figure 8.6 where the vehicle was at a zero degree angle of attack. The lift of each configuration reaches approximately the same steady-state value, but the magnitude of the dynamics reach approximately 400%. This corresponds to a significant increase in control effective-

ness. However, the variation in lift for the advanced concept leads to degradation and slight reversal of the applied load due to the fluid and jet interaction dynamics.

The dynamic response of vehicle pitch moment of each configuration shows a significant variation due to fluid-jet dynamics compared to the results shown in Figure 8.6 with JI-only. The two configurations experience degradation of the effective pitch moment due to JI and before reaching similar steady-state values as in the JI-only case. The conventional configuration pitch moment amplification factor actually has a control reversal immediately after the step input. Overall, the conventional configuration is better suited to exploit steady-state jet interaction, but these dynamic simulations reveal that the advanced concept could leverage the coupled fluid-jet dynamics for better performance.

Figure 8.8 shows the vehicle responses to simultaneous step changes in structural deformation and attitude jet total pressure, which show similar trends to the JI-only case shown in Figure 8.6. However, the pitch moment amplification factor is significantly different immediately after the step input due to the addition of structural deformation. Both configurations experience degraded pitch moments due to the coupled structure-jet dynamics. However, the advanced concept reaches higher amplification factors approximately 40% above the JI-only dynamic response. The pitch moment is more significantly affected by structural deformation, which continues a trend throughout the numerical results. The change to the lift coefficient amplification factor is not significant, but larger levels of structural deformation may lead to more significant changes in the dynamic response.

Figure 8.9 shows the responses of the two configurations to the coupled step changes in fluid, structure, and jet responses. Overall, the responses are quite similar to those in Figure 8.7, which suggest that the impact of structural deformation is much smaller for determining vehicle loads. There is a difference at the beginning of the response that shows further degradation of the applied pitch moment due to

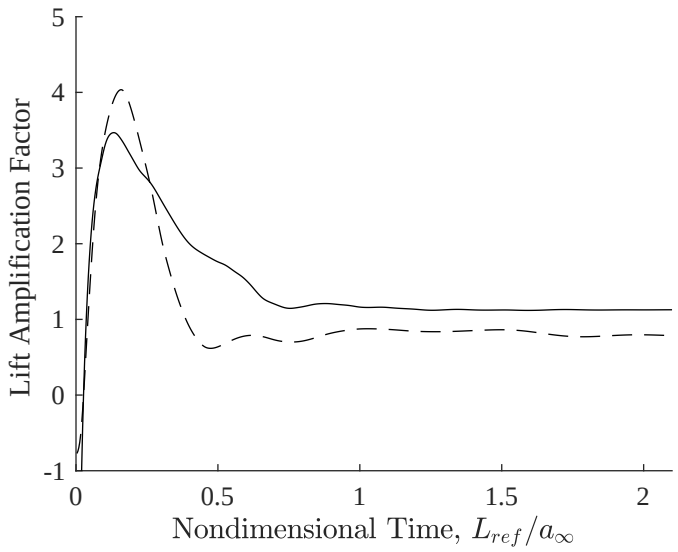

(a)

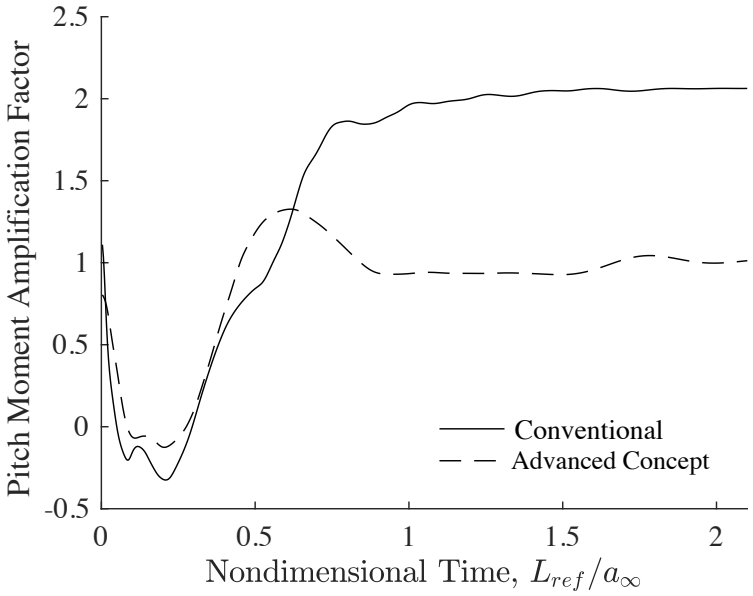

(b)

Figure 8.7: Vehicle responses to a 10-degree step change in angle of attack, 1-MPa step change in attitude jet total pressure and no structural deformation.

jet interaction and structural deformation. This effect is more pronounced in the conventional configuration.

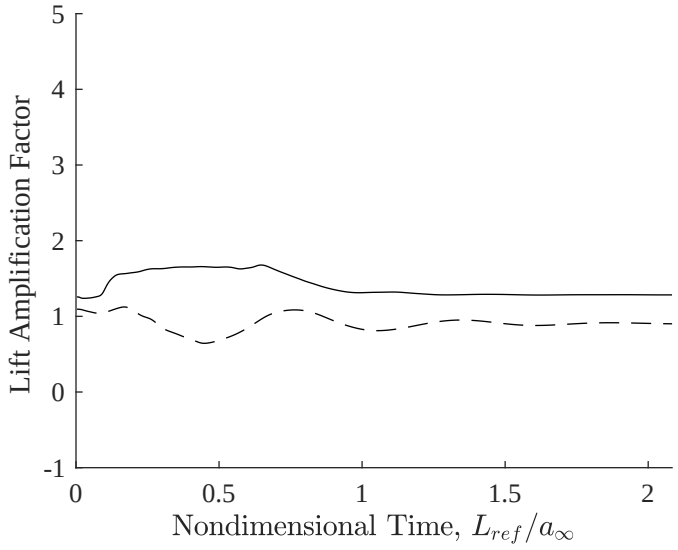

(a)

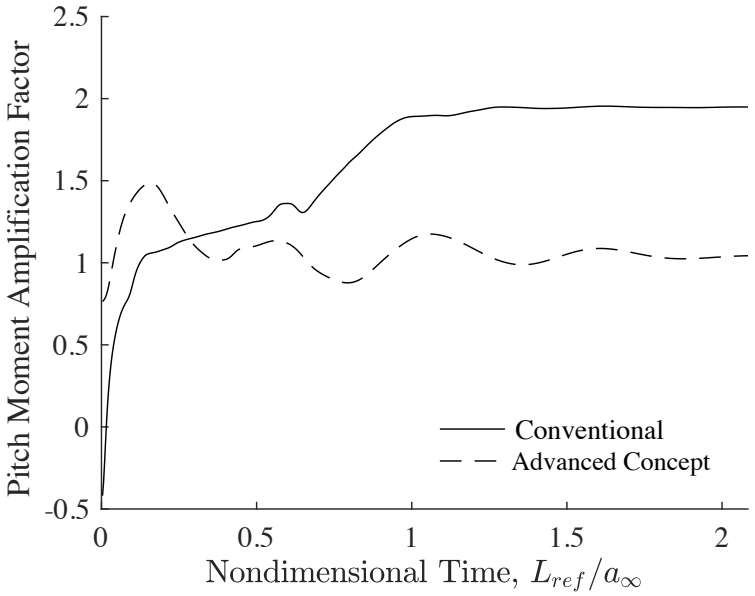

(b)

Figure 8.8: Vehicle responses to a 1% step change in structural deformation, a 1-MPa attitude step change in attitude jet total pressure with zero angle of attack.

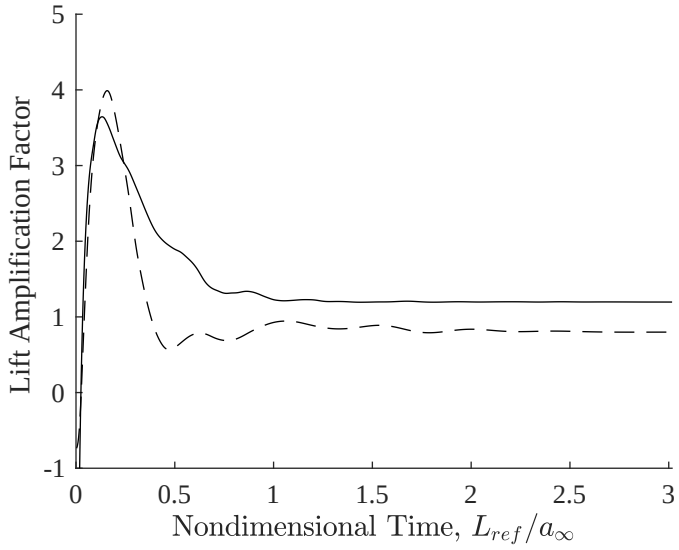

(a)

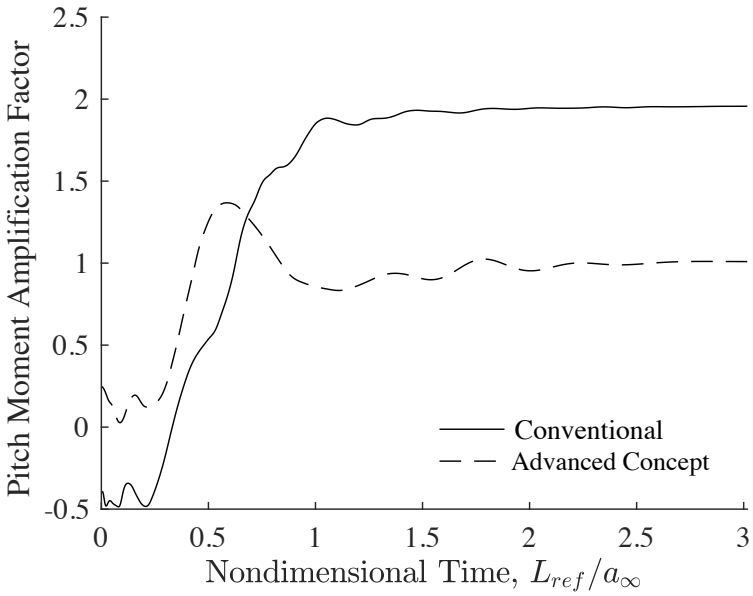

(b)

Figure 8.9: Vehicle responses to a 10-degree step change in angle of attack, 1% step change in structural deformation, and 1-MPa attitude step change in attitude jet total pressure.

8.3 Concluding Remarks

This chapter considered the state-of-the-art, conventional finned configuration and an advance, finless axisymmetric configuration with structural flexibility and attitude control jets. The impact of each vehicle characteristic and their various combinations were considered by taking into account the steady and unsteady nonlinear multi-physics interaction effects.

The steady-state loads of the conventional and advanced concept configurations were analyzed over a range of angle of attack, structural deformation, and attitude jet total pressure. The results showed a significant variation in the jet interaction loads due to changes in angle of attack, which is largely based on the jet located on the windward or leeward vehicle side. The studied flow conditions did not lead to a control reversal condition, but a significant variation in control effectiveness due to jet interaction. The structural deformation significantly affected the pitch moment of each configuration by increasing the magnitude along the same direction as the deformation (i.e., tip-down deformation leads to pitch-down moment). The change in the applied loads due to jet interaction was most significant for the conventional configuration due to the presence of control fins near the jet exit. The high pressure region that develops ahead of the jet exit due to flow separation and passing through the normal shock extends laterally onto the control fins, which then leads to an increase in the surface area affected and an increase in the applied loads. This effect lead to a relatively consistent reduction in control effectiveness of approximately 50% for low angles of attack. The flow separation effect is not present for either configuration at large positive angles of attack. For both configurations at large positive angles of attack the flow separation effect is not present, but there is a portion of the body that is shadowed by the jet exhaust leading to lower surface pressure and a decrease in the control effectiveness. At large negative angles of attack (jet on leeward side) there is flow separation near the jet exit that leads to an amplification of the control

effectiveness. Overall, the conventional configuration is most significantly affected by fluid-structure-jet interaction effects and increased aerodynamic loads due to the presence of control fins. However, the sensitivities with respect to fluid and structure parameters are higher, which may lead to an increase in stability and decrease in agility.

The dynamic loads of the two configurations were analyzed using step responses to changes in the fluid, structure, and jet parameters. Specifically, the angle of attack, structural deformation of the first bending mode, and total pressure of the attitude jet were the varied parameters. These were used in isolation and in combination to examine the unsteady loads due to coupled FSJI. Overall, dynamic jet interaction has significant effects on both configurations that led to large amplification factors for lift and pitch moment as well as longer response times compared to the step responses without jet interaction. The amplification factors for lift and pitch moment for the two configurations highlight the importance of dynamic jet interaction modeling. The step responses including jet interaction have amplitudes that range from significant amplification of the applied force to degradation or reversal of the applied force. These effects could lead to exploiting jet interaction, but if not properly modeled or accounted for could lead to adverse effects on vehicle performance. Similar to the steady-state loads assessment, the conventional configuration is strongly affected by jet interaction with the control fins. The fins near the attitude jet exit lead to larger amplification factors overall compared to the advanced concept configuration, but also lead to more severe degradation and reversal of the applied forces. Therefore, the conventional configuration might benefit from longer duration pulses from the attitude jet to leverage the large steady-state amplification factors and mitigate the adverse dynamic JI effects. On the other hand, the opposite would benefit the advanced concept. The step responses indicate that shorter duration jet pulses with the advanced concept could leverage the large amplitude dynamic JI effects compared

to the relatively small amplification at steady state.

In summary, this chapter focused on the effects of fluid-structure interaction, jet interaction, and the coupled effect of FSJI on slender high-speed vehicles. The addition of control surfaces near the attitude jet nozzle exit was introduced to examine the effect on performance of two configurations with and without control surfaces. Overall, the numerical results reveal that there are opportunities to exploit FSJI for both configurations. The conventional configuration with control surfaces is more effective at leveraging the effects of jet interaction, but additional structural flexibility has a more significant effect on vehicle stability compared to the advanced concept as shown in Chapter 7. Conversely, the advanced concept is more robust to additional flexibility and there are still opportunities to leverage FSJI as identified in the steady-state and dynamic loads analyses.

CHAPTER 9

Concluding Remarks

This chapter summarizes the key findings from the previous chapters along with insights and interpretations based on these results. The key contributions of this dissertation are presented based on the dissertation objectives and supporting results throughout the previous chapters. A discussion of broader impacts relates these key contributions back to the original motivation for this work. Finally, new research questions have arisen throughout the course of this dissertation and recommendations for future research are provided.

9.1 Summary

This dissertation focused on the fluid-structure-jet interactions of a high-speed vehicle, which are due to considering slender vehicles with attitude control jets. These configurations introduce structural deformation and jet interaction with the supersonic freestream flow. Specifically, how FSJI affects the loads applied to the vehicle, development of FSJI modeling methods, and how those interactions can effect the vehicle performance were investigated. The analysis and results demonstrate how these interactions can be leveraged for improved designs and performance.

In order to investigate the effects of FSJI on flight performance for maneuvering vehicles, simulations are the most effective way of achieving it. The UM/HSV simulation framework was used in this dissertation to incorporate FSJI. The enhanced

framework couples the aeroelastic and rigid-body degrees of freedom with the jet interaction effects. Several JI modeling methods were presented that were implemented in the UM/HSV framework. The first was a semi-empirical method that was newly developed using insights provided from the literature and verified using computational and experimental results. Next, a CFD-based Kriging surrogate method was adapted to modeling the pressure distribution due to supersonic JI by reducing the vehicle surface grid into a vector space that reduced the Kriging model size. The combination of the two previous methods led to a multi-fidelity approach that leverages the simplicity behind the semi-empirical model with the accuracy of the high-fidelity CFD solution at selected sample points.

Two approaches to capture the unsteady component to the vehicle maneuver loads were presented. The first was the linear convolution with nonlinear correction approach that had been used previously for aerodynamic modeling. This method identifies the system dynamics using step responses that are calculated *a priori* and are convolved with the vehicle input history to approximate the dynamic response. The nonlinear correction factor is based on the steady-state model of the vehicle loads. This approach had not been used previously to model dynamic FSJI. The next approach was newly developed to calculate the effective dynamics for aggressive maneuvers when other modeling strategies become inaccurate. The effective dynamics approach is based on the Volterra series, identifying the corresponding nonlinear kernels in the frequency domain as a least-squares problem. This formulation removes the need to identify step responses *a priori* and instead uses a representative maneuver that excites the relevant degrees of freedom.

Beyond the steady and unsteady modeling methods, some post-processing methods were included to efficiently calculate the vehicle performance and stability across a high-dimensional input domain. SVMs were used to calculate the boundary between two regions. For example, SVMs were used to identify increased or decreased

control effectiveness and the stability boundary for two and three-dimensional domains. Explicit Design Space Decomposition (EDSD) was used in combination with the SVM to identify the next best points to sample and quickly converge to the boundary. Two methods were used to calculate the vehicle stability from the time-domain vehicle response that is output from the flight simulation. The Autoregressive Moving-Average (ARMA) was used to monitor a single degree of freedom from the simulation output, such as angle of attack or deformation, and fit to a linear model using multiple autoregressive coefficients. The second approach, Dynamic Mode Decomposition (DMD), takes the simulation output and calculates the modes and frequencies without any model fitting. The DMD approach can track all the structural degrees of freedom in addition to the rigid-body velocities and calculate the modes, frequency, and damping.

New vehicle models were developed to feature FSJI as well as explore high-speed intercept vehicle design trends that could improve performance. Slender structures and attitude jets were the primary features to introduce fluid-structure and jet interaction. The structural stiffness, stiffness distribution, and fin configuration were additional modifications that were made to incorporate state-of-the-art and advanced concept designs. These models enabled a more systematic approach to studying FSJI effects that had been lacking in the literature.

The jet interaction modeling methods that were developed were then applied to the representative configurations for verification. The semi-empirical JI method and CFD-based surrogate were both included in the flight simulation to compare the effect of varying model fidelity. The finless vehicle configuration was then used to apply the multi-fidelity modeling approach to JI. Cross-validation results demonstrated the feasibility and convergence of the multi-fidelity approach.

The sensitivity of FSJI to variations in flight conditions and control inputs was presented using the representative vehicles. This analysis highlighted several key con-

ditions such as jet-fin interaction, dynamic fluid-jet interaction, Mach and altitude conditions that had a significant effect on the vehicle transient and steady-state loads. These results including deformation, aggressive flight conditions, and a large flight envelope contribute to the missile and jet interaction literature. The dynamic analysis in particular fills a gap in the literature regarding rigid-body motion, structural vibration, and dynamic jet input effects on the vehicle loads.

The FSJI dynamics were shown to be very sensitive to perturbations in the flight conditions and could have a wide variation from control amplification to reversal. Therefore, modeling methods were developed and tested using the representative vehicle and a nonlinear mass-spring-damper system as test cases. The linear convolution with nonlinear correction factor proved to be accurate for quasi-steady inputs involving jet interaction, but more dynamic test cases caused the model to become inaccurate. The transient jet interaction was shown to be particularly sensitive to changes in angle of attack such that it is difficult to identify the system dynamics or to transition between known reference points. A new method, the effective dynamics approach, was developed to account for these cases when steady-state and linear convolution models are inaccurate. The most direct way to demonstrate the effectiveness and limitations of the effective dynamics approach was the nonlinear mass-spring-damper model. The method is out performed by the convolution models for small perturbations about a single reference condition, which is to be expected. The step response and the Volterra kernels approach the exact solution for small perturbations about the reference condition and the effective dynamics model approaches the exact solution for small perturbations about the representative maneuver. As the system input was increased to develop a nonlinear response or as the reference condition was moved throughout the simulation, the effective dynamics approach became the most accurate using representative maneuvers at the new conditions. Representative maneuvers can be used to calculate the dynamics in highly nonlinear and unsteady

regimes and approximate similar maneuvers. This directly applies to the FSJI that is highly sensitive to changes in flight conditions, angles of attack and jet input.

Flight simulations were conducted with the various vehicle models to study maneuverability, agility, and stability with the addition of vehicle flexibility. These results moved beyond the steady-state and dynamic loads analysis to understand the system-level affect of fluid-structure interaction. The additional flexibility was shown to improve vehicle maneuverability and agility with a slight drag penalty due to additional deformation. Stiffness distribution could be tuned to further improve performance. A representative stiffness distribution was applied that moved the center of pressure forward. This is one way to leverage the vehicle flexibility with an existing structural architecture. Vehicle stability was analyzed using the flight simulation response of the conventional configuration and advanced concept configurations. The flight simulation response to a small perturbation was recorded with varying structural stiffness, Mach number, and altitude. The structural stiffness and Mach number were the most sensitive parameters for both vehicle models. The difference in the flutter boundary between the two configuration proved to be significant with the advanced concept configuration having the larger stable region.

Finally, the steady-state and dynamic FSJI analysis of the conventional and advanced configurations provided some guidelines for leveraging the complex physical interaction for improved performance. Although the divert and attitude jets were added to potentially replace control fins, the jet-fin interaction proved to significantly increase the control effectiveness of the jet. The additional surface area increases the aerodynamic loading and could be used for improved maneuverability, but this would also require more control effort to compensate for the additional pitch moment. A balance can be struck between the two configurations by reducing the fin size to only the jet interaction profile. This new fin size would really depend on the expected Mach and jet pressure regime, but could take advantage of jet interaction while minimizing

box-size profile.

Overall, this dissertation has addressed several FSJI gaps in the literature that existed previously. Modeling methods were developed to include the relevant physical interactions needed to simulate maneuvering intercept vehicles in flight. These methods were then applied to create representative vehicle models that served as a test bed for exploring FSJI effects on vehicle flight response. The steady-state and dynamic sensitivity to a wide range of flight conditions including aggressive maneuver conditions fills another previous gap in the literature. Finally, flight simulation results of multiple vehicle configurations were compared to identify flight regimes and design trends that leverage the FSJI effects.

9.2 Key Contributions

This dissertation provides the following key contributions to the scientific community. The contributions are a collection of novel insights and methods related to the FSJI of maneuverable and slender intercept missiles.

1. Created a new semi-empirical modeling method of JI for three-dimensional problems. This method allows the rapid prediction of the resulting pressure distribution as a function of arbitrary freestream flow and jet conditions. This method helps fill the gap in JI modeling methods.

2. Developed an improved approach to handling high-dimensional input and output data for multi-fidelity modeling of vehicle loads. This facilitates modeling the surface pressure distribution with low and high-fidelity models for FSJI. This method contributes to JI modeling for complex geometry.

3. Enhanced an existing aero-thermo-elastic-propulsive simulation framework (UM/HSV) to enable effective numerical investigations of FSJI problems in a variety of vehicle configurations.

4. Obtained high-fidelity results of the steady and dynamic FSJI across the vehicle flight envelope that highlight the sensitivity and nonlinearity of the problem. Results support quantification of the performance effect due to FSJI at extreme and dynamic flight conditions for various vehicle geometries.

5. Developed a new method of extracting the dynamic vehicle loads model from the high-fidelity FSJI solution that can be applied for aggressive maneuvers when other modeling methods may be inaccurate.

6. Achieved deeper insight how the physical FSJI can be exploited to improve vehicle performance and stability. Comparison of conventional and advanced concept high-speed vehicle configurations reveals the trade-offs throughout the design space and flight envelope.

9.3 Broader Impacts

Supersonic intercept vehicles operate in a very high energy environment and various configurations may introduce multi-physics interactions such as fluid-structure interaction or supersonic jet interaction. These are additional effects that can be leveraged during vehicle design and development to increase versatility, agility, maneuverability, and compatibility. These characteristics combine to create an advantage and maintain air superiority over current and future threats. One major benefit of this dissertation is the identification of how to exploit fluid-structure-jet interaction effects for performance gains. In addition, the techniques used throughout are general to a wide range of multidisciplinary high-speed vehicle configurations and applicable to develop and evaluate future vehicle concepts, particularly ones flying in and out of the atmosphere.

High-speed intercept vehicles in this dissertation are considered to operate over a wide range of altitudes, Mach number, and perform aggressive maneuvers. This

combines multiple capabilities into a single versatile high-performance vehicle. These qualities are enabled by the divert and attitude control jets that can maintain effectiveness at high angles of attack and low dynamic pressure conditions compared to control surfaces. Increasing the altitude range adds a capability to the air-launched vehicle that is typically reserved for sea and land-based vehicles. The high angle of attack capability adds to the maneuverability of the vehicle and enables intercept of targets that may be outside the aircraft field of view (off-boresight). In the terminal phase of flight, rapid-fire jets allow for agile end-game maneuvers similar to current missile defense platforms. Jet interaction with the external flow changes the applied loads to the vehicle, but modeling methods have been developed in this dissertation to approximate the steady-state and unsteady jet interaction and its effect on high-speed vehicle loads. These surrogate models are robust, accurate, and fast enough to simulate the impact of jet interaction on high-speed flight vehicles.

Increased slenderness can improve aerodynamic performance and compatibility with modern aircraft architecture. For example, a slender high-speed vehicle may be moved from wing-mounted launchers to an internal bay launcher that recovers the stealth characteristics of a fifth-generation fighter aircraft. However, this higher slenderness increases flexibility of the structure and leads to larger deformation under applied loads. Modeling methods were developed and flight simulations were conducted of flexible high-speed vehicles that account for the fluid-structure interaction effects. The results showed that maneuverability and agility were improved in addition to the compatibility aspect.

The numerical results in this dissertation highlight the vehicle configurations that are most sensitive to and can best leverage FSJI. The flight simulation of high-speed vehicles with FSJI is also a unique capability that allows researchers to explore the high-speed vehicle design space. An intelligent combination of attitude control jets, slenderness, and control surfaces may lead to next generation vehicles with superior

agility, maneuverability, versatility, and compatibility.

9.4 Recommendations for Future Research

Additional research directions to pursue based on the results of this dissertation are presented here. The first few paths focus on the fluid and structural model fidelity. This dissertation was focused on developing the methods and models needed for system-level analysis, which sacrificed some model fidelity. Another approach is to extend the applications of the methods and results in this dissertation to other vehicle types and flight regimes. The final avenue of future research may explore the control techniques of a nonlinear flow-controlled elastic structure.

Numerical results of steady-state and dynamic FSJI effects were presented throughout that significantly varied compared to undeformed conditions or jet-off conditions. However, some results showed small differences and the lessons learned from these results may be impacted by the uncertainty in the models. More rigorous study to quantify the uncertainty of the models and the confidence intervals associated with the results should be carried out in future work.

Another point of emphasis is to look at canonical test cases with high-fidelity solutions of the fluid and structure. Previous experimental studies focused primarily on flat-plate configurations, but a more relevant geometry would be a cylinder at non-zero angle of attack. The turbulent boundary layer separation is known to be a key factor for determining the pressure distribution along a flat plate. However, the RANS modeling used here does not solve for these turbulent fluctuations that may interact with the structural dynamics. A high-fidelity structural analysis method could be extended to examine the local structural deformation and dynamics due to the jet interaction. At this smaller scale, Large Eddy Simulation (LES) becomes more feasible to model the flow and large-scale turbulence structures. A refined

finite element representation of the structure would be ideal to capture as much of the structural response as possible. This high-fidelity approach would pair well with an experimental model of a compliant panel with jet interaction. Experimental jet interaction results have been vital to validating the computational modeling of the fluid, but may need to be revisited for the coupled FSJI problem. The lower-order methods can then be verified from the high-fidelity results. Finally, a simpler geometry extends the applicability to a variety of applications such as supersonic combustion and re-entry vehicle structural panels in the hypersonic regime.

Thermodynamics may need to be taken into account for hypersonic vehicles using jets for attitude control. The aerothermodynamics associated with a jet in crossflow was not addressed in this dissertation, but the surface heat flux and temperature may affect the jet interaction load distribution. The jet flow properties such as temperature, pulse duration, and location would need to be considered again with the thermoelastic response of the structure. The next generation of aerospace vehicles will certainly take advantage of advanced materials and manufacturing techniques to develop unconventional designs, configurations, and structural properties. As the complexity of the structure increases, this must be taken into account with the FSJI problem to study system-level effects on stability and performance.

The FSJI problem should be considered at the subsonic through transonic regimes as well. Flow control actuators have been proposed for a variety of applications such as high-lift wing configurations, drag reduction, and improve flow stability. The fluid dynamics analysis of these applications are maturing to the point that the interaction with the structural dynamics and flow control devices should be considered. This is especially critical for slender structures and high-aspect-ratio structures with large displacements where the additional jet interaction effects may significantly alter the applied load and aeroelastic response. Experimental data of a canonical case in this flow regime would be beneficial as well to develop modeling methods need for full

vehicles analysis.

Another research direction is to leverage the modeling methods for FSJI dynamics to investigate control techniques to exploit flow control of flexible structures. This is a complex problem due to the dynamic nature of the devices and the nonlinear effects on pressure distribution, which can lead to aeroelastic instability or improved control effectiveness. Control techniques that address the nonlinearity of the system may provide insight that was not available by conventional configurations without the complex physical interactions.

Overall, there are opportunities to explore the intersection of the aeroelastic and jet interaction problems for new and interesting research questions. Separately, each research area may be mature enough to offer some established methods and insights, but new methods and results are necessary when introducing more complexity to the system.

BIBLIOGRAPHY

[1] VanderWyst, A., Shelton, A., and Martin, C., "A Computationally Efficient, Multi-fidelity Assessment of Jet Interactions for Highly Maneuverable Missiles," *34th AIAA Applied Aerodynamics Conference*, AIAA Aviation Forum, AIAA 2016-4333, Washington, D.C., June 2016. doi:10.2514/6.2016-4333.

[2] Spaid, F. W. and Zukoski, E. E., "A Study of the Interaction of Gaseous Jets from Transverse Slots with Supersonic External Flows," *AIAA Journal*, Vol. 6, No. 2, February 1968, pp. 205–212. doi:10.2514/3.4479.

[3] Kawai, S. and Lele, S. K., "Large-Eddy Simulation of Jet Mixing in Supersonic Crossflows," *AIAA Journal*, Vol. 48, No. 9, September 2010, pp. 2063–2083. doi:10.2514/1.J050282.

[4] Klock, R. J., *Efficient Numerical Simulation of Aerothermoelastic Hypersonic Vehicles*, Ph.D. thesis, University of Michigan, Ann Arbor, Michigan, 2017. doi:2027.42/138502.

[5] Spaid, F. W. and Cassel, L. A., "Aerodynamic Interference Induced by Reaction Controls," Tech. Rep. AGARD-AG-173, Advisory Group for Aerospace Research and Development, Paris, France, December 1973. url:www.dtic.mil/dtic/tr/fulltext/u2/775209.pdf.

[6] Roger, R. P., "The Aerodynamics of Jet Thruster Control for Supersonic/Hypersonic Endo-Intercepters: Lessons Learned," *37th AIAA Aerospace Sciences Meeting and Exhibit*, AIAA 1999-0804, Reno, Nevada, January 1999. doi:10.2514/6.1999-804.

[7] Ebrahimi, H. B., "Numerical Simulation of Transient Jet-Interaction Phenomenology in a Supersonic Freestream," *Journal of Spacecraft and Rockets*, Vol. 37, No. 6, November–December 2000, pp. 713–719. doi:10.2514/2.3634.

[8] Naumann, K. W., Ende, H., George, A., and Mathieu, G., "Stationary and Time-Dependent Effects in the Near Interaction of Gaseous Jets and Supersonic Crossflow," *29th AIAA Fluid Dynamics Conference*, AIAA 1998-2972, Albuquerque, NM, June 1998. doi:10.2514/6.1998-2972.

[9] Bitten, R., "Qualitative and Quantitative Comparison of Government and Industry Agility Metrics," *Journal of Aircraft*, Vol. 27, No. 3, 1989, pp. 276–282. doi:10.2514/3.45930.

[10] Costello, M. and Argarwalla, R., "Improved Dispersion of a Fin Stabilized Projectile Using a Passive Movable Nose," *Atmospheric Flight Mechanics Conference*, AIAA 2000-4197, Denver, CO, August 2000. doi:10.2514/6.2000-4197.

[11] Youn, E. B. and Silton, S. I., "Numerical Study on Bending Body Projectile Aerodynamics," *34th AIAA Applied Aerodynamics Conference*, AIAA 2016-4331, Washington, D.C., June 2016. doi:10.2514/6.2016-4331.

[12] Yao, S., Wu, Z., and Yang, C., "Trajectory Simulation of Flexible Missiles and the Effect of Flexibility on Hit Precision," *AIAA Atmospheric Flight Mechanics Conference*, AIAA 2014-0888, National Harbor, Maryland, January 2014. doi:10.2514/6.2014-0888.

[13] Crimi, P., "Aeroelastic Stability and Response of Flexible Tactical Weapons," *AIAA 22nd Aerospace Sciences Meeting*, AIAA 1984-0392, Reno, Nevada, January 1984. doi:10.2514/6.1984-392.

[14] Platus, D. M., "Aeroelastic Stability of Slender, Spinning Missiles," *16th Atmospheric Flight Mechanics Conference, Guidance, Navigation, and Control and Co-located Conferences*, AIAA 1989-3393, Boston, MA, August 1989. doi:10.2514/6.1989-3393.

[15] Beal, T. R., "Dynamic Stability of a Flexible Missile under Constant and Pulsating Thrusts," *AIAA Journal*, Vol. 3, No. 3, March 1965, pp. 486–494. doi:10.2514/3.2891.

[16] Chae, S. and Hodges, D. H., "Dynamics and Aeroelastic Analysis of Missles," *44th AIAA/ASME/ASCE/AHS Structures, Structural Dynamics, and Materials Conference*, AIAA 2003-1968, Norfolk, Virginia, April 2003. doi:10.2514/6.2003-1968.

[17] Zukoski, E. E. and Spaid, F. W., "Secondary Injection of Gases into a Supersonic Flow," *AIAA Journal*, Vol. 2, No. 10, October 1964, pp. 1689–1696. doi:10.2514/3.2653.

[18] Billig, F. S., Orth, R. C., and Lasky, M., "A Unified Analysis of Gaseous Jet Penetration," *AIAA Journal*, Vol. 9, No. 6, June 1971, pp. 1048–1058. doi:10.2514/3.49916.

[19] Werle, M. J., Driftmyer, R. T., and Shaffer, D. G., "Jet-Interaction-Induced Separation: The Two-Dimensional Problem," *AIAA Journal*, Vol. 10, No. 2, February 1972, pp. 188–193. doi:10.2514/3.6558.

[20] Young, C. T. K. and Barfield, B. F., "Viscous Interaction of Sonic Transverse Jets with Supersonic External Flows," *AIAA Journal*, Vol. 10, No. 7, July 1972, pp. 853–854. doi:10.2514/3.50233.

[21] Demuren, A. O., "Modeling Jets in Cross Flow," Tech. Rep. NASA-CR-194965, NASA, Langley Research Center, Hampton, Virginia, August 1994. url:ntrs.nasa.gov/archive/nasa/casi.ntrs.nasa.gov/19950005517.pdf.

[22] Margason, R. J., "Fifty Years of Jet in Cross Flow Research," *Computational and Experimental Assessment of Jets in Cross Flow*, Advisory Group for Aerospace Research & Development, AGARD-CP-534, Winchester, UK, November 1993. url:www.dtic.mil/dtic/tr/fulltext/u2/a275733.pdf.

[23] Broadwell, J. E., "Analysis of the Fluid Mechanics of Secondary Injection for Thrust Vector Control," *AIAA Journal*, Vol. 1, No. 5, May 1963, pp. 1067–1075. doi:10.2514/3.1726.

[24] Taylor, G., "The Formation of a Blast Wave by a Very Intense Explosion. I. Theoretical Discussion," *Proceedings of the Royal Society of London*, Vol. 201, March 1950, pp. 159–174. *JSTOR*, www.jstor.org/stable/98395.

[25] Sakurai, A., "On the Propagation and Structure of the Blast Wave, I," *Journal of the Physical Society of Japan*, Vol. 8, No. 5, September–October 1953, pp. 662–669. doi:10.1143/JPSJ.8.662.

[26] Sakurai, A., "On the Propagation and Structure of the Blast Wave, II," *Journal of the Physical Society of Japan*, Vol. 9, No. 2, March–April 1954, pp. 256–266. doi:10.1143/JPSJ.9.256.

[27] Warfield, M. J., "Calculation of Supersonic Interacting Jet Flows," *27th Aerospace Sciences Meeting*, AIAA 1989-0666, Reno, Nevada, January 1989. doi:10.2514/6.1989-666.

[28] Graham, M. J. and Weinacht, P., "Numerical Simulation of Lateral Control Jets," *37th AIAA Aerospace Sciences Meeting and Exhibit*, AIAA 1999-0510, Reno, Nevada, January 1999. doi:10.2514/6.1999-510.

[29] Sahu, J., Fresconi, F., and Heavey, K. R., "Unsteady Aerodynamic Simulations of a Finned Projectile at a Supersonic Speed With Jet Interaction," Tech. Rep. ARL-TR-6960, U.S. Army Research Laboratory, Aberdeen Proving Ground, Maryland, June 2014. url:www.arl.army.mil/arlreports/2014/ARL-TR-6960.pdf.

[30] DeSpirito, J., "Turbulence Model Effects on Cold-Gas Lateral Jet Interaction in a Supersonic Crossflow," *Journal of Spacecraft and Rockets*, Vol. 52, No. 3, May–June 2015, pp. 836–852. doi:10.2514/1.A32974.

[31] DeSpirito, J., Kennedy, K. D., Mikkelsen, C. D., and Chaplin, R. A., "Predictions of a Supersonic Jet-in-Crossflow: Comparisons Among CFD Solvers and with Experiment," *32nd AIAA Applied Aerodynamics Conference*, AIAA Aviation Forum, AIAA 2014-2736, Atlanta, Georgia, June 2014. doi:10.2514/6.2014-2736.

[32] DeSpirito, J., "Lateral Jet Interaction on a Finned Projectile in Supersonic Flow," *50th AIAA Aerospace Science Meeting including the New Horizons Forum and Aerospace Exposition*, AIAA 2012-0413, Nashville, Tennessee, January 2012. doi:10.2514/6.2012-413.

[33] DeSpirito, J., "Factors Affecting Reaction Jet Interaction Effects on Projectiles," *29th AIAA Applied Aerodynamics Conference*, AIAA 2011-3031, Honolulu, Hawaii, June 2011. doi:10.2514/6.2011-3031.

[34] DeSpirito, J., "Transient Lateral Jet Interaction Effects on a Generic Fin-Stabilized Projectile," *30th AIAA Applied Aerodynamics Conference*, AIAA 2012-2907, New Orleans, Louisiana, June 2012. doi:10.2514/6.2012-2907.

[35] Gnemmi, P., Adeli, R., and Longo, J., "Computational Comparisons of the Interaction of Lateral Jet on a Supersonic Generic Missile," *AIAA Atmospheric Flight Mechanics Conference and Exhibit*, AIAA 2008-6883, Honolulu, Hawaii, August 2008. doi:10.2514/6.2008-6883.

[36] Cassel, L. A., "Applying Jet Interaction Technology," *Journal of Spacecraft and Rockets*, Vol. 40, No. 4, July–August 2003, pp. 523–537. doi:10.2514/2.3992.

[37] Ferrante, A., Matheou, G., and Dimotakis, P. E., "LES of an Inclined Jet into a Supersonic Turbulent Crossflow: Synthetic Inflow Conditions," *48th AIAA Aerospace Sciences Meeting Including the New Horizons Forum and Aerospace Exposition*, AIAA 2010-1287, Orlando, Florida, January 2010. doi:10.2514/6.2010-1287.

[38] Ziefle, J. and Kleiser, L., "Large-Eddy Simulation of a Round Jet in Crossflow," *36th AIAA Fluid Dynamics Conference and Exhibit*, AIAA 2006-3370, San Francisco, California, 2006. doi:10.2514/6.2006-3370.

[39] Randolph, H., Chew, L., and Johari, H., "Pulsed Jets in Supersonic Crossflow," *Journal of Propulsion and Power*, Vol. 10, No. 5, September 1994, pp. 746–748. doi:10.2514/3.23790.

[40] Génin, F. and Menon, S., "Dynamics of Sonic Jet Injection into Supersonic Crossflow," *Journal of Turbulence*, Vol. 11, No. 4, March 2010, pp. 1–30. doi:10.1080/14685240903217813.

[41] Morton, S. A., McDaniel, D. R., Sears, D. R., Tillman, B., and Tuckey, T. R., "Kestrel - A Fixed Wing Virtual Aircraft Product of CREATE Program," *47th AIAA Aerospace Sciences MeetingIncluding The New Horizons Forum and Aerospace Exposition*, AIAA 2009-338, Orlando, Florida, January 2009. doi:10.2514/6.2009-338.

[42] Skujins, T. and Cesnik, C. E. S., "Reduced-Order Modeling of Unsteady Aerodynamics Across Multiple Mach Regimes," *Journal of Aircraft*, Vol. 51, No. 6, November–December 2014, pp. 1681–1704. doi:10.2514/1.C032222.

[43] McNamara, J. J., Crowell, A. R., Friedmann, P. P., Glaz, B., and Gogulapati, A., "Approximate Modeling of Unsteady Aerodynamics for Hypersonic Aeroelasticity," *Journal of Aircraft*, Vol. 47, No. 6, November–December 2010, pp. 1932–1945. doi:10.2514/1.C000190.

[44] Crowell, A. R. and McNamara, J. J., "Model Reduction of Computational Aerothermodynamics for Hypersonic Aerothermoelasticity," *AIAA Journal*, Vol. 50, No. 1, January 2012, pp. 74–84. doi:10.2514/1.J051094.

[45] VanderWyst, A. S., Shelton, A. B., Martin, C. L., Neergaard, L. J., and Witeof, Z. D., "Reduced Order Models for Generation of Large, High Speed Aerodynamic Databases with Jet Interactions," *57th AIAA/ASCE/AHS/ASC Structures, Structural Dynamics and Materials Conference*, AIAA SciTech Forum, AIAA 2016-0464, San Diego, California, January 2016. doi:10.2514/6.2016-0464.

[46] Baker, M. L., Alston, K. Y., and Munson, M. J., "Integrated Hypersonic Aeromechanics Tool (IHAT)," *9th AIAA/ISSMO Symposium on Multidisciplinary Analysis and Optimization*, AIAA 2002-5512, Atlanta, Georgia, September 2002. doi:10.2514/6.2002-5512.

[47] Pasiliao, C. L., Sytsma, M. J., Neergaard, L. J., Witeof, Z. D., and Trolier, J. W., "Preliminary Aerothermal Structural Simulation," *14th AIAA Aviation Technology, Integration, and Operations Conference*, AIAA 2014-2292, Atlanta, Georgia, June 2014. doi:10.2514/6.2014-2292.

[48] Klock, R. J. and Cesnik, C. E. S., "Aerothermoelastic Simulation of Air-Breathing Hypersonic Vehicles," *55th AIAA/ASME/ASCE/AHS/SC Structures, Structural Dynamics, and Materials Conference*, AIAA 2014-0149, National Harbor, Maryland, January 2014. doi:10.2514/6.2014-0149.

[49] Raveh, D. E. and Mavris, D. N., "Reduced-Order Models Based on CFD Impulse and Step Responses," *42nd AIAA/ASME/ASCE/AHS/ASC Structures, Structural Dynamics, and Materials Conference*, AIAA 2001-1527, Anaheim, California, April 2001. doi:10.2514/6.2001-1527.

[50] Zaide, A. and Raveh, D. E., "Numerical Simulation and Reduced-Order Modeling of Airfoil Gust Response," *AIAA Journal*, Vol. 44, No. 8, August 2006, pp. 1826–1834. doi:10.2514/1.16995.

[51] Kitson, R. C. and Cesnik, C. E. S., "Aeroelastic Modeling and Simulation of High-Speed Flexible Vehicles," *15th Dynamics Specialists Conference*, AIAA SciTech Forum, AIAA 2016-1324, San Diego, California, January 2016. doi:10.2514/6.2016-1324.

[52] Kitson, R. C. and Cesnik, C. E. S., "High Speed Vehicle Fluid-Structure-Jet Interaction Analysis and Modeling," *58th AIAA/ASCE/AHS/ASC Structures, Structural Dynamics, and Materials Conference*, AIAA SciTech Forum, AIAA 2017-0405, January 2017. doi:10.2514/6.2017-0405.

[53] Kitson, R. C. and Cesnik, C. E. S., "Unsteady Fluid-Structure-Jet Interactions of Agile High-Speed Vehicles," *AIAA Atmospheric Flight Mechanics Conference*, AIAA Aviation Forum, AIAA 2017-3549, Denver, CO, June 2017. doi:10.2514/6.2017-3549.

[54] Kitson, R. C. and Cesnik, C. E. S., "Unsteady Fluid-Structure-Jet Interaction Modeling Methods for Agile High-Speed Vehicles," *AIAA Atmospheric Flight Mechanics Conference*, AIAA Aviation Forum, AIAA 2017-4356, Denver, CO, June 2017. doi:10.2514/6.2017-4356.

[55] Kitson, R. C. and Cesnik, C. E. S., "Fluid-Structure-Jet Interaction Modeling and Simulation of High-Speed Vehicles," *Journal of Spacecraft and Rockets*, Vol. 55, No. 1, 2017, pp. 190–201. doi:10.2514/1.A33895.

[56] Kitson, R. C. and Cesnik, C. E. S., "Unsteady Fluid-Structure-Jet Interactions of Agile High-Speed Vehicles," *Journal of Spacecraft and Rockets*, 2017, pp. 1–14. doi:10.2514/1.A34092.

[57] Kitson, R. C. and Cesnik, C. E. S., "Multidisciplinary Effects on High-Speed Vehicle Performance and Stability," *2018 AIAA/ASCE/AHS/ASC Structures, Structural Dynamics, and Materials Conference*, AIAA SciTech Forum, AIAA 2018-1208, Kissimmee, Florida, Jan. 2018. doi:10.2514/6.2018-1208.

[58] Kitson, R. C. and Cesnik, C. E. S., "Fluid-Structure-Jet Interaction Effects on High-Speed Vehicle Performance and Stability," *Journal of Spacecraft and Rockets*, *In Review* 2018.

[59] Frendreis, S. G. V. and Cesnik, C. E. S., "3D Simulation of Flexble Hypersonic Vehicles," *AIAA Atmospheric Flight Mechanics Conference*, AIAA 2010-8229, Toronto, Ontario, Canada, August 2010. doi:10.2514/6.2010-8229.

[60] Falkiewicz, N. J., Cesnik, C. E. S., Crowell, A. R., and McNamara, J. J., "Reduced-Order Aerothermoelastic Framework for Hypersonic Vehicle Control Simulation," *AIAA Journal*, Vol. 49, No. 8, August 2011, pp. 1625–1646. doi:10.2514/1.J050802.

[61] Craig Jr., R. R. and Kurdila, A. J., *Fundamentals of Structural Dynamics*, John Wiley & Sons, Inc., 2006.

[62] Dreyer, E. R., Grier, B. J., and McNamara, J. J., "Towards Characterization of Relevant Fidelity Modeling of Loads for Maneuvering Hypersonic Vehicles," *2018 AIAA/ASCE/AHS/ASC Structures, Structural Dynamics, and Materials Conference*, AIAA 2018-1207, Kissimmee, Florida, January 2018. doi:10.2514/6.2018-1207.

[63] Martin, J. D. and Simpson, T. W., "Use of Kriging Models to Approximate Deterministic Computer Models," *AIAA Journal*, Vol. 43, No. 4, April 2005, pp. 853–863. doi:10.2514/1.8650.

[64] Zhang, M. and He, L., "Combining Shaping and Flow Control for Aerodynamic Optimization," *AIAA Journal*, Vol. 53, No. 4, April 2015, pp. 888–901. doi:10.2514/1.J053277.

[65] Sun, X., Huang, W., Guo, Z., and Yan, L., "Multiobjective Design Optimization of Hypersonic Combinational Novel Cavity and Opposing Jet Concept," *Journal of Spacecraft and Rockets*, Vol. 54, No. 3, May–June 2017, pp. 662–671. doi:10.2514/1.A33801.

[66] Biedron, R. T., Carlson, J., Derlaga, J. M., Gnoffo, P. A., Hammond, D. P., Jones, W. T., Kleb, B., Lee-Rausch, E. M., Nielsen, E. J., Park, M. A., Rumsey, C. L., Thomas, J. L., and Wood, W. A., "FUN3D Manual 12.9," Tech. Rep. TM-2016-219012, NASA, Langley Research Center, Hampton, Virginia, February 2016. url:fun3d.larc.nasa.gov/papers/FUN3D_Manual-12.9.pdf.

[67] McKay, M. D., Beckham, R. J., and Conover, W. J., "A Comparison of Three Methods for Selecting Values of Input Variables in the Analysis of Output from a Computer Code," *Technometrics*, Vol. 21, No. 2, May 1979, pp. 239–245. doi:10.2307/1268522.

[68] Halton, J. H. and Smith, G. B., "Algorithm 247: Radical-inverse quasi-random point sequence," *Communications of the ACM*, Vol. 7, No. 12, December 1964, pp. 701–702. doi:10.1145/355588.365104.

[69] Klock, R. J. and Cesnik, C. E. S., "Nonlinear Thermal Reduced-Order Modeling for Hypersonic Vehicles," *AIAA Journal*, Vol. 55, No. 7, July 2017, pp. 2358–2368. doi:10.2514/1.J055499.

[70] Lillian, C. S., McDaniel, D. R., and Morton, S. A., "An Efficient Method of Computing Maneuvering Aircraft Surface Loads Using CFD, Proper Orthogonal Decomposition, and System Identification," *49th AIAA Aerospace Sciences Meeting including the New Horizons Forum and Aerospace Exposition*, AIAA 2011-1177, Orlando, Florida, January 2011. doi:10.2514/6.2011-1177.

[71] McNamara, J. J. and Friedmann, P. P., "Aeroelastic and Aerothermoelastic Analysis in Hypersonic Flow: Past, Present, and Future," *AIAA Journal*, Vol. 49, No. 6, June 2011, pp. 1089–1122. doi:10.2514/1.J050882.

[72] Thomas, J. P., Dowell, E. H., and Hall, K. C., "Three-Dimensional Transonic Aeroelasticity Using Proper Orthogonal Decomposition-Based Reduced-Order Models," *Journal of Aircraft*, Vol. 40, No. 3, May–June 2003, pp. 544–551. doi:10.2514/2.3128.

[73] Silva, W. A., "Application of Nonlinear Systems Theory to Transonic Unsteady Aerodynamic Responses," *Journal of Aircraft*, Vol. 30, No. 5, September–October 1993, pp. 660–668. doi:10.2514/3.46395.

[74] Boyd, S., Tang, Y. S., and Chua, L. O., "Measuring Volterra Kernels," *IEEE Transactions on Circuits and Systems*, Vol. CAS-30, No. 8, August 1983, pp. 571–577. doi:10.1109/TCS.1983.1085391.

[75] Marzocca, P., Librescu, L., and Silva, W. A., "Volterra Series Approach for Nonlinear Aeroelastic Response of 2-D Lifting Surfaces," *42nd AIAA/ASME/ASCE/AHS/ASC Structures, Structural Dynamics, and Materials Conference*, AIAA 2001-1459, Seattle, WA, April 2001. doi:10.2514/6.2001-1459.

[76] MathWorks, Natick, Massachusetts, *MATLAB Documentation*, r2018a ed.

[77] Bicken, G., Carey, G. F., and Stearman, R. O., "Frequency Domain Kernel Estimation for 2nd-order Volterra Models Using Random Multitone Excitation," *VLSI Design*, Vol. 15, No. 4, 2002, pp. 701–713. doi:10.1080/106514021000123 18.

[78] Balajewicz, M., Nitzsche, F., and Feszty, D., "Application of Multi-Input Volterra Theory to Nonlinear Multi-Degree-of-Freedom Aerodynamic Systems," *AIAA Journal*, Vol. 48, No. 1, January 2010, pp. 56–62. doi:10.2514/1.38964.

[79] Zukoski, E. E., "Turbulent Boundary-Layer Separation in Front of a Forward-Facing Step," *AIAA Journal*, Vol. 5, No. 10, October 1967, pp. 1746–1753. doi:10.2514/3.4299.

[80] Zettl, D., Dreyer, E. R., Grier, B. J., McNamara, J. J., and Pasiliao, C. L., "Rapid Steady-State Pressure Prediction for Ultra High-Speed Vehicles," *15th Dynamics Specialists Conference*, AIAA 2016-1323, San Diego, California, January 2016. doi:10.2514/6.2016-1323.

[81] Forrester, A. I. J., Sóbester, A., and Keane, A. J., "Multi-fidelity optimization via surrogate modelling," *Proceedings of the Royal Society of London A: Mathematical, Physical and Engineering Sciences*, Vol. 463, No. 2088, December 2007, pp. 3251–3269. doi:10.1098/rspa.2007.1900.

[82] Kennedy, M. C. and O'Hagan, A., "Predicting the output from a complex computer code when fast approximations are available," *Biometrika*, Vol. 87, No. 1, March 2000, pp. 1–13. *JSTOR*, www.jstor.org/stable/2673557.

[83] Lophaven, S. N., Nielsen, H. B., and Sondergaard, J., "DACE Matlab Kriging Toolbox," Tech. Rep. IMM-TR-2002-12, Informatics and Mathematical Modelling Technical University of Denmark, August 2002.

[84] Tinsley, H. E. A. and Brown, S. D., *Handbook of Applied Multivariate Statistics and Mathematical Modeling*, Academic Press, 2000.

[85] Lacaze, S. and Missoum, S., "CODES: A Toolbox For Computational Design," Version 1.0, 2015. url:codes.arizona.edu/toolbox.

[86] Basudhar, A. and Missoum, S., "An improved adaptive sampling scheme for the construction of explicit boundaries," *Structural and Multidisciplinary Optimization*, Vol. 42, No. 4, May 2010, pp. 517–529. doi:10.1007/s00158-010-0511-0.

[87] Dribusch, C. and Missoum, S., "Construction of Aeroelastic Stability Boundaries Using a Multi-Fidelity Approach," *53rd AIAA/ASME/ASCE/AHS/ASC Structures, Structural Dynamics and Materials Conference*, AIAA 2012-1803, Honolulu, Hawaii, April 2012. doi:10.2514/6.2012-1803.

[88] McNamara, J. J. and Friedmann, P. P., "Flutter-Boundary Identification for Time-Domain Computational Aeroelasticity," *AIAA Journal*, Vol. 45, No. 7, July 2007, pp. 1546–1555. doi:10.2514/1.26706.

[89] Pak, C. G. and Friedmann, P. P., "New Time-Domain Technique For Flutter Boundary Identification," *AIAA Dynamics Specialists Conference*, AIAA 1992-2102, Dallas, Texas, April 1992. doi:10.2514/6.1992-2102.

[90] Schmid, P. J., "Dynamic mode decomposition of numerical and experimental data," *Journal of Fluid Mechanics*, Vol. 656, August 2010, pp. 5–28. doi:10.1017/S0022112010001217.

[91] Pointwise, Inc., Fort Worth, Texas, *Pointwise V18.0R3*, 2016. url:www.pointwise.com/doc/user-manual/.

[92] Dowdy, M. W. and Newton, J. F., "Investigation of Liquid and Gaseous Secondary Injection Phenomena on a Flat Plate with M = 2.01 and M = 4.54," Tech. Rep. TR-32-543, Jet Propulsion Laboratory, California, December 1963.

[93] Ashley, H. and Zartarian, G., "Piston Theory - A New Aerodynamic Tool for the Aeroelastician," *Journal of the Aeronautical Sciences*, Vol. 23, No. 12, 1956, pp. 1109–1118. doi:10.2514/8.3740.

[94] Shutty, M. A., *Dynamic Modeling and Modal Analysis of an Air-to-Air Missile*, Naval Postgraduate School, September 1991. doi:10945/25858.